The Thesis Committee for Maxwell Elliott Pommer
Certifies that this is the approved version of the following thesis:

Quantitative Assessment of Pore Types and Pore Size Distribution Across Thermal Maturity, Eagle Ford Formation, South Texas

APPROVED BY
SUPERVISING COMMITTEE:

Supervisor:

Kitty L. Milliken

Charles Kerans

Peter B. Flemings

Quantitative Assessment of Pore Types and Pore Size Distribution Across Thermal Maturity, Eagle Ford Formation, South Texas

by

Maxwell Elliott Pommer, BA

Thesis

Presented to the Faculty of the Graduate School of

The University of Texas at Austin

in Partial Fulfillment

of the Requirements

for the Degree of

Master of Science in Geological Sciences

The University of Texas at Austin

August, 2014

Dedication

For Richard and Ann Geesaman

Acknowledgements

Support for this project was provided by Shell Exploration and Production Inc. as a part of the Shell/University of Texas Unconventional Research (SUTUR) Project 3: "Characterization of Mudrocks by Quantitative Analysis of High-resolution SEM Images". I would like to acknowledge our friends at Shell for the support, samples and data necessary to complete this task. In particularly, I would like to thank Aysen Ozkan and Robert Dombrowski who made this project possible.

In addition, I would like to thank my advisor Kitty Milliken for sharing with me a small portion of her wealth of knowledge, and love of science. Also Nick Hayman for bringing a new perspective, my professors for broadening my horizons, and Patrick Smith for teaching me how to prepare and image samples. Most importantly, I would like to thank my friends and family for their love and support.

Abstract

Quantitative Assessment of Pore Types and Porosity Distribution Across Thermal Maturity, Eagle Ford Formation, South Texas

Maxwell Elliott Pommer, MSGeoSci

The University of Texas at Austin, 2014

Supervisor: Kitty L. Milliken

Scanning electron microscopy of Ar-ion milled samples from the Eagle Ford Formation, South Texas shows that the character and abundance of porosity changes significantly across burial conditions as a result of compaction, cementation, bitumen generation, and generation of secondary porosity within organic matter (OM). Samples displaying a range of compositions and maturities are imaged and quantified to provide insight into the effects of these processes.

Porosity in low-maturity samples (Ro~0.5%) is volumetrically dominated (0.1% - 12.5% bulk volume, average 6.2%) by relatively large, mostly interparticle, primary mineral-associated pores (median sizes range 35.9-52.7 nm). Larger pores are generally associated with coccolith debris that is commonly aggregated into pellets. Porosity and pore size correlate directly with calcite abundance and inversely with OM volumes. OM is dominantly detrital kerogen "stringers" that range in size and have spatial distributions

and character suggestive of detrital origin. Destruction of primary porosity in low-maturity samples has occurred due to compaction of ductile kerogen and clays and, to a minor degree, as a result of cementation and infill of early bitumen.

Smaller, secondary OM-hosted pores (median size range 11.1-14.9 nm) volumetrically dominate porosity (0.02%-3.6% bulk volume, average of 1.36%), in most high-maturity samples (Ro~1.2%-1.3%). Mineral-associated pores are present, but are typically smaller (median size range from 20.3-40.6 nm) and less abundant (0.0%-10.0% bulk volume, average of 2.5%) than at low maturity. Abundant mineral-associated porosity is present locally in samples where incursion of primary pore space by bitumen has not occurred. OM within high-maturity samples is distributed more evenly throughout the rock fabric, occupying spaces similar in size and morphology to primary interparticle pores, coating euhedral crystals (probable cements), and filling intraparticle porosity. These observations, and positive correlation between calcite and OM volumes (OM-hosted pore volume included) in samples with dominantly OM-hosted pore networks, suggests that a large portion of OM within high-maturity samples is diagenetic in origin and has filled primary pore space. Destruction of primary porosity in high-maturity samples has occurred through cementation, bitumen infill, and, possibly greater compaction. Additional porosity, however, has been generated through maturation of OM.

Table of Contents

List of Tables

List of Figures

INTRODUCTION

The Eagle Ford Formation, South Texas is a coccolithic, organic matter-rich mudrock. This study quantifies pores detected utilizing field-emission scanning electron microscopy (FE-SEM) and integrates this data with bulk analyses and qualitative observations of rock character. Primary goals of this study include: 1) developing petrographic techniques to measure porosity at a variety of scales, and 2) gaining insight into controls on porosity, pore type abundance, and pore size distribution across burial conditions. Results of the study indicate that pore networks can be dominated by either primary mineral-associated pores or by secondary porosity within organic matter (OM), depending on the composition of the detrital grain assemblage and its response to variable physical and chemical conditions.

Geologic Setting

The Eagle Ford Formation in South Texas is Cenomanian-Turonian in age, ranges from 40 - 400 ft thick, and extends laterally at least 250 mi to the East Texas Basin (Donovan and Staerker, 2010; Hentz and Ruppel, 2010). Stratigraphically, in South Texas the Eagle Ford was deposited onto the Buda Limestone (Cenomanian) and is overlain by the Austin Chalk (Coniacian-Santonian), spanning across the Cenomanian/Turonian boundary and oceanic anoxic event (OAE 2) (Donovan and Staerker, 2010; Driskill et al., 2013). It was deposited during the maximum transgression of the Western Interior Seaway onto a broad shallow shelf (Donovan and Staerker 2010, Driskill et al 2012). Extensive OM preservation occurs due to lack of sediment dilution by silicate input, and low-oxygen environments during sediment deposition (as

interpreted from geochemical and paleontological studies) (Aurthur and Sageman, 2004; Driskill et al., 2012).

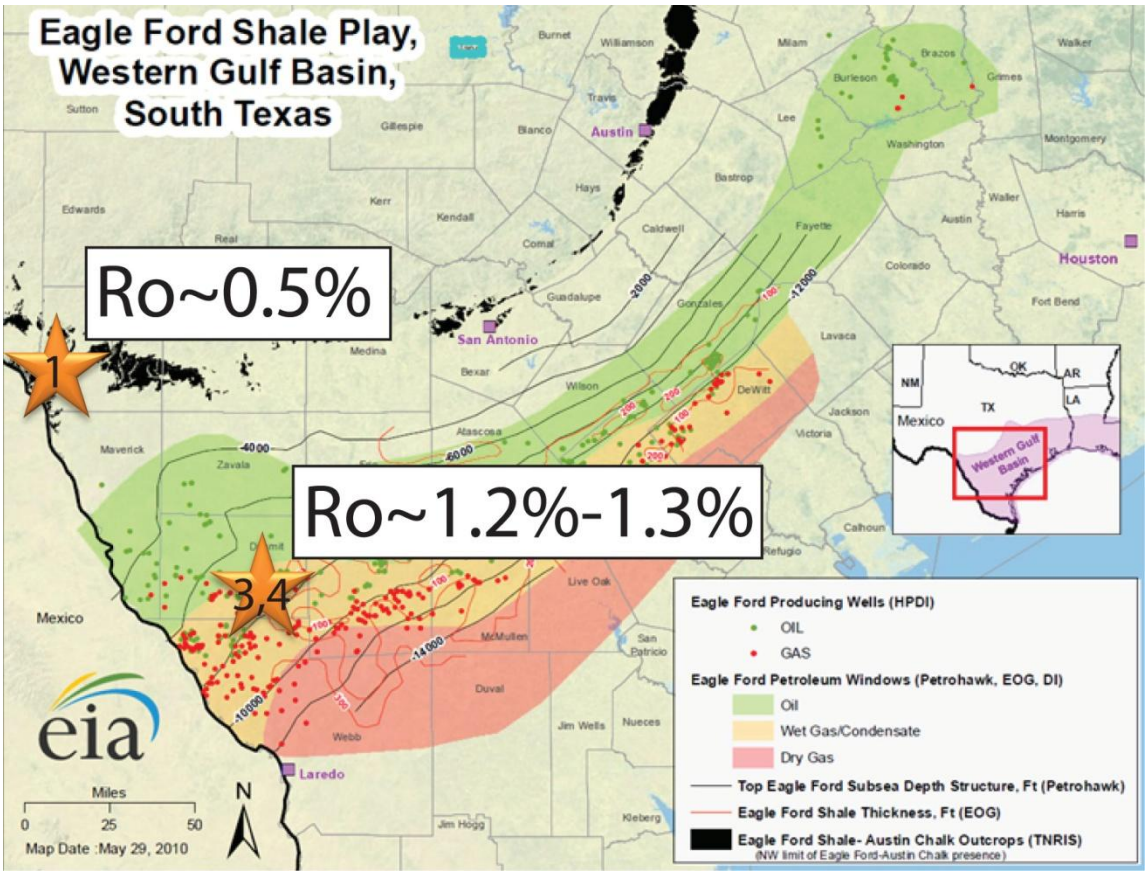

Figure 1: Map of the South Texas Eagle Ford Play, sample location (stars) and maturity outcrops, oil and gas windows, structural contours and wells drilled by June 2010 are shown. Altered from U.S. Energy Information Administration, (2014).

Individual members within the Eagle Ford have been studied extensively in different areas. In the study area (South Texas) the Eagle Ford can be broken into the Upper Eagle Ford (UEF) and the Lower Eagle Ford (LEF) on the basis of lithology and log character, (Donovan and Staerker, 2010; Driskill et al., 2013; Fairbanks, 2010; Harbor, 2011; Hentz and Ruppel, 2010; Workman and Grammer, 2013). Samples from

the UEF have relatively high volumes of clay, carbonate and terrestrial components and low volumes of OM, whereas samples from the LEF are more heterogeneous, have variable amounts of calcite and clay and generally contain significantly higher volumes of OM (Tables 2 and 3). Sun et al. (2014), using the same sample set examined here, shows in that OM from the LEF is more strongly marine than within the UEF. This corresponds with a distinct change in OM character that is observed and measured across these intervals (Figures 20, 28, 58).

Porosity in Mudrocks

Pore types and porosity distribution within OM-rich mudrocks have been studied extensively utilizing SEM microscopy in conjunction with other techniques (Ambrose et al., 2010; Bernard et al., 2013; Curtis et al., 2012b; Desbois et al., 2009; Fishman et al., 2013; Houben et al., 2013b; Loucks et al., 2012.; Milliken et al., 2013). These studies show a tremendous heterogeneity in pore network character, which varies with burial conditions and composition (Loucks et al., 2012; Milliken et al., 2013).

Large pore volumes are present in near surface sediment (up to ~80%) (Mondol et al. 2007), consisting of primary interparticle and intraparticle pores (Loucks et al., 2012; Milliken et al., 2014). A large amount of primary pore space is destroyed during early compaction, especially within mudrocks composed of ductile components, most commonly kerogen and clay particles (Figure 63) (Loucks et al., 2012; Milliken et al., 2014; Mondol et al., 2007). Large, rigid, grains shelter large pores from strain, preserving primary pore space during burial (Figures 37, 49, 51) (Day-Stirrat et al., 2010; Milliken and Day-Stirrat, 2013; Milliken et al., 2014; Schneider et al., 2011). Primary pores within OM were reported in trace amounts in kerogen under near surface conditions and early burial (Fishman et al., 2012; Milliken et al., 2014; Reed et al., 2013).

Mineral-hosted pore volume decreases in abundance with burial through cementation, compaction, and infill of primary porosity by secondary OM (bitumen) as suggested by others (Bernard, 2012; Fishman, 2013; Milliken et al., 2013; Milliken and Day-Stirrat, 2013). Within the Eagle Ford, destruction of pore space by authigenic mineral growth occurs as early mineral precipitates (pyrite, kaolinite, and calcite), as well as late burial cements (dominantly calcite and quartz), (Figures 29 - 44) (Fishman et al., 2013).

Secondary pores within OM are in samples with thermal maturities greater than Ro~0.6% at the onset of peak oil generation and have been described extensively as a component of mudrock reservoirs (Loucks et al., 2012, Curtis et al., 2012a). Fishman et al. (2013) shows Eagle Ford samples in the oil window (Ro~0.7%) with weakly developed pores within OM and well-developed pores in samples from the gas-condensate window, suggesting that OM-hosted porosity varies as a function of thermal maturity from the oil window into the gas window (Ro~0.7%-1.2%). Milliken et al. (2013) shows that in the Marcellus, within the gas window, between Ro~1.0% to the dry gas window (Ro~2.1%), OM-hosted pore size and volume does not show a dependence on thermal maturity, but rather that the abundance of OM more strongly controls the OM-hosted pore volume. It has also been suggested that heterogeneity between OM type and chemistry influences OM-hosted pore development (Fishman et al., 2013; Loucks et al. 2012; Milliken et al., 2013).

Quantitative Pore Analysis in Mudrocks

SEM IMAGING

Several researchers have conducted quantitative assessments of pore volumes and size distributions using image analysis software on two-dimensional SEM images from polished cross-sections utilizing manual trace and automated techniques, combined with bulk measurements e.g., point counts, dry-helium porosity, x-ray diffraction, and many others (Houben et al., 2013a; Driskill et al., 2013; Milliken et al., 2013). Automated techniques commonly apply a combination of grayscale threshold limitations and edge detection software to determine porosity and detect pores more efficiently than manual techniques (Curtis et al., 2010; Houben et al., 2013a; Houben et al., 2013b). Pores detected with automated techniques can be classified manually after detection (Houben et al., 2013a; Houben et al., 2013b). Houben et al. (2013a), states that "...thresholding + edge detection gives similar results to manual detection with respect to pore size distribution", but shows data that suggest that porosity calculated with thresholding and edge detection was under-estimated relative to the manual trace by approximately 40%. (Houben, et al., 2013a).

This study utilizes manual trace methods in favor of automated techniques to apply a pore classification scheme, avoid artifact pores, and because images' gray levels within pores significantly overlap with gray levels within sample defects and on OM and mineral surfaces (Figures 48, 49, 51, and 54) (Milliken et al., 2013). Similar problems occur with edge-detection software (Houben et al., 2013a). Secondary electron images, preferable when imaging pores because of the need to analyze topographical information (Huang et al., 2013), often have depth of fields significantly deeper than most pores in mudrocks (Figures 48, 51, and 54). In addition, classification of specific pore volumes, either OM-hosted or mineral associated, allows for populations of those pore types to be

measured at different magnifications and later integrated as calculated cumulative populations, allowing quantification of a broad scale of pore size (see *Quantification of Pore-Size Distributions* and *Pore-Size Distributions* for more detail).

OTHER TECHNIQUES

Other non-petrographic techniques used to quantify pore size distribution in mudrocks include: measuring ratios of adsorbed gas to free gas in (e.g., N_2 adsorption) and calculating pore throat radii from pressures changes associated with the injection of a non-wetting fluid phase, e.g., mercury injection porosimetry (MIP) (Burdine, 1950; Bolton, 2000; Clarkson, 2012; Ji et al., 2012; Kaneko, 1994, Nelson 2009). Nuclear magnetic resonance (NMR), small angle neutron scattering, and three-dimensional imaging techniques have also been used recently, each with their own limitations (Hall and Mildner, 1983; Kaneko, 1994; Knackstedt et al. 2009; Sondergeld et al., 2010). Nitrogen gas-adsorption is used to characterize pores between ~1-300 nm, however it fails to measure large pores, which can contribute up to ~87% of measured pore space in a sample (Figure 66) (Barrett et al., 1951; Milliken et al., 2013; Zhang et al., 2014). In addition, MIP techniques require impractically high pressures (> 60,000 psi) in order to inject mercury into miniscule pores beyond the theoretical limit of 3.6 nm (Kulia et al., 2012; Kulia and Prasad, 2013).

Related Studies

As with previous studies (Milliken et al., 2013; Houben et al., 2013b.), additional techniques were applied to petrographically characterize samples, geochemically characterize OM, and quantifiably measure pores beyond the limit of detection by field-emission scanning-electron microscopy. Thin-sectioned samples were petrographically

analyzed by Ergene (2014) utilizing conventional light microscopy, cathodo-luminescence, and broad scale SEM. In addition, N_2 adsorption was performed by Zhang et al. (2014), effectively quantifying pores between ~1 nm and 300 nm, many of which can be below the detection limit of FE-SEM (Milliken et al. 2013). Sun et al. (2014) utilizes various organic-geochemical techniques to characterize OM source and composition.

METHODS

Sampling and Sub-Sampling

Eighteen core plugs were obtained from three wells in the South Texas Eagle Ford Formation across thermal maturity. Samples include: seven "low maturity" samples from the early oil-window Well 1 (Ro~0.5%, ~100m), four "high maturity" samples from the wet-gas window Well 3 (Ro~1.2%, ~2,500 m), and seven "high maturity" samples from the wet-gas Well 4 (Ro~1.3%, ~2,800 m) (Figures 1 and 2). Samples were selected across stratigraphy to highlight heterogeneity in lithology, TOC, and geochemistry.

Each core plug was sub-sampled three times. From each sample: ~1 cm^3 piece was taken for Ar-ion cross-section polishing and FE-SEM imaging, ~10 grams were taken for thin section preparation by Spectrum Petrographics, and 3) nitrogen adsorption, heavy oil analysis, and porosity measurements were obtained with the remaining ~20 - 40 grams. This study focuses on FE-SEM imaging of Ar-ion cross-section polished samples to observe trends in pore abundance, character and size distribution.

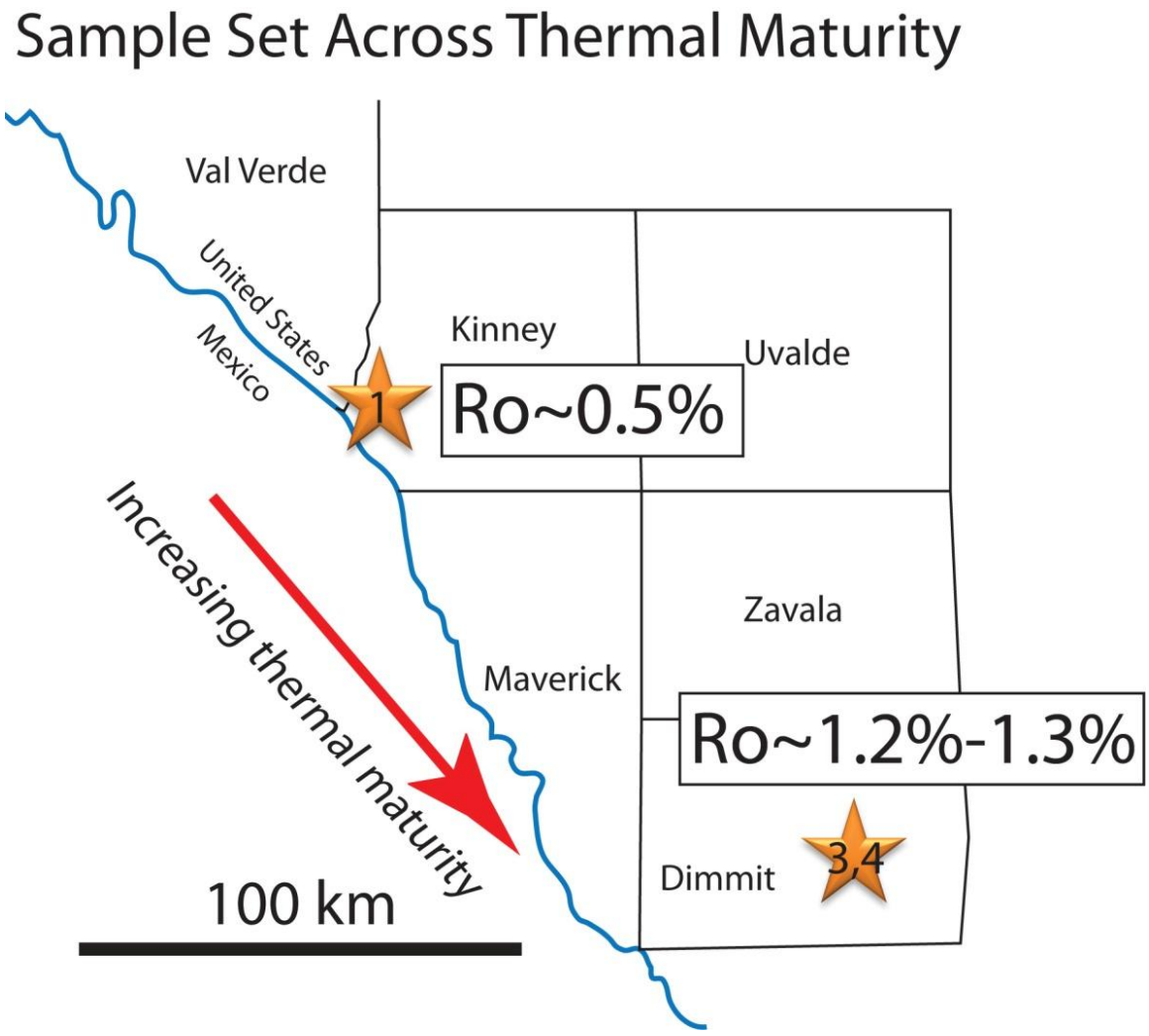

Figure 2: Location of South Texas Eagle Ford Formation wells sampled in this study, and approximate vitrinite reflectance as calculated from biomarkers by Sun et al. (2014). Stars indicate location of Well 1, Well 3, and Well 4.

Sample Preparation

Ar-ion milling (AIM) polishes surfaces independent of hardness, creating a pristine two-dimensional surface (Loucks et al., 2009; Loucks et al., 2012; Reed and Loucks, 2007) (Figures 3 and 4). This preserves petrologic features within both rigid minerals and soft organic components, minimizing artifacts associated with mechanical

polishing. Artifacts associated with thin section preparation can lead to misidentification of porosity. Examples of these artifacts include: artifact moldic pores from grain plucking and general topographic irregularities associated grinding with grit and powders and embedment of grit or swarf (Loucks et al., 2009; Loucks et al., 2012; Pittman, 1992). Additionally, pores in thin sections are impregnated with epoxy. Imaged surfaces were prepared by AIM polishing using a Leica EM TIC020 Triple Ion Beam Miller. Samples were milled for 8 to 10 hours using an accelerating voltage of 8 kV, and a current of 2.8 mA.

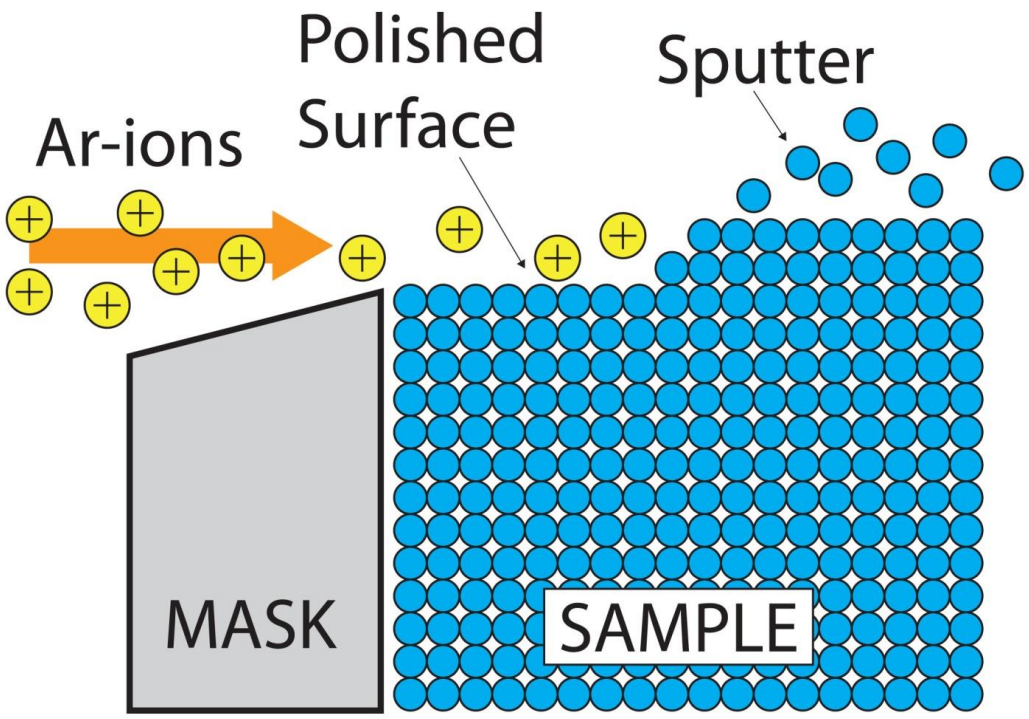

Figure 3: Schematic diagram of Ar-ion cross-section polishing process. Samples are oriented so polished surface is fixed perpendicular to bedding plane.

A thin, conductive coating of Ir applied to each sample reduces charging and increases image quality in SEM images. Two different machines were used to apply conductive coating: a GATAN 682 Precision Etching Coating system and a Leica EM ACE600 High Vacuum Coater.

Artifacts from the milling and coating process are visible with the FE-SEM. Grooves and curtaining (Figure 5), caused by uneven ablation by argon ions on milled surfaces vary in abundance and distribution. Coating irregularity, or "spotting" is present in samples coated with the Leica EM ACE600, and is likely resultant of contamination during the coating process (Figure 6A). At high magnification (greater than ~100,000x), cracked and scaly Ir coating is visible on mineral surfaces (Figures 6B and 10). The mechanism behind this is poorly understood, but likely related to contrasting electrostatic properties of different materials during the coating process (Milliken et al., 2013).

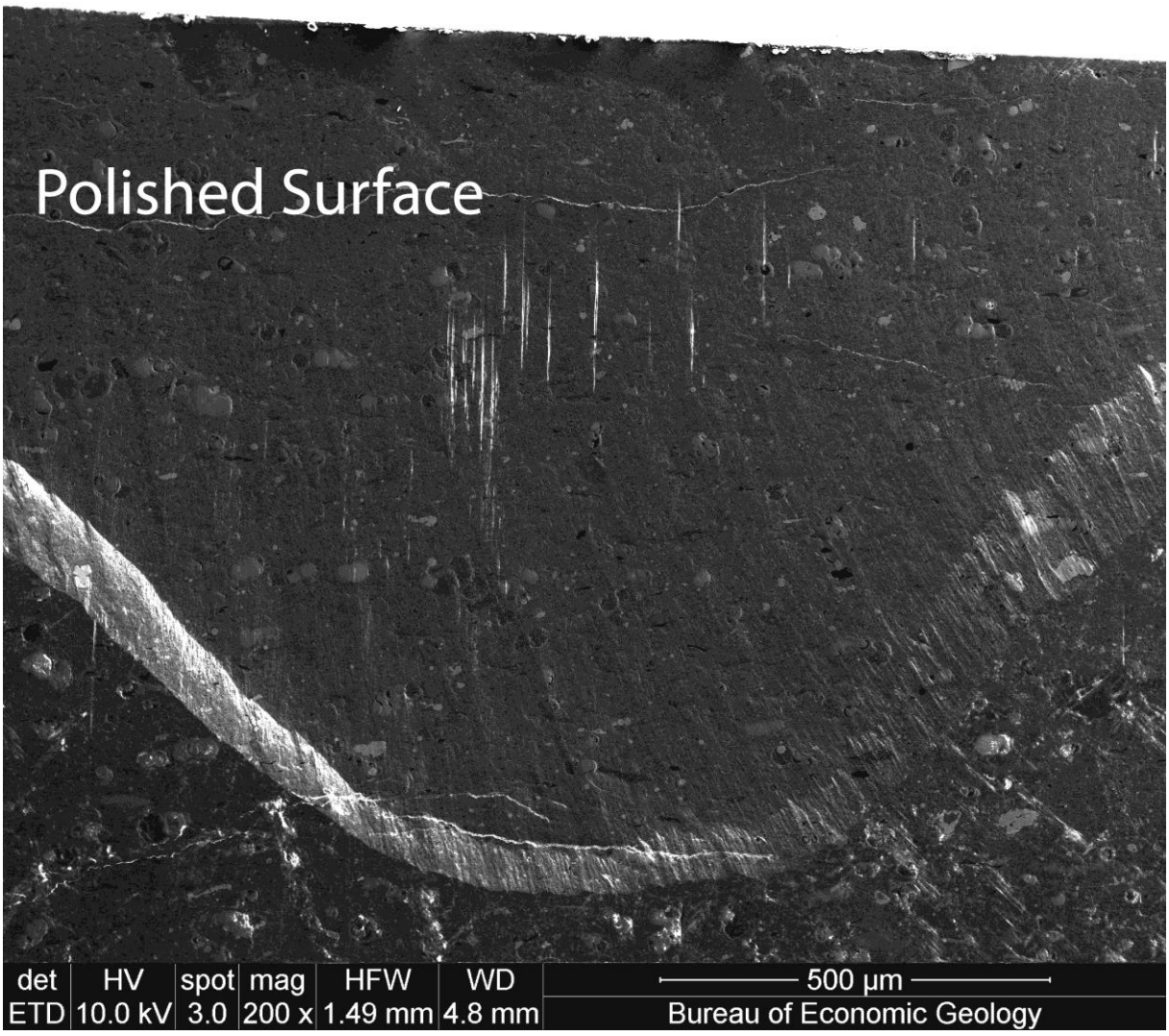

Figure 4: Secondary electron (SE) image of an Ar-ion cross-section polished surface from the Leica EM TIC020 Triple Ion Beam Miller. Well 4 sample 1-90.

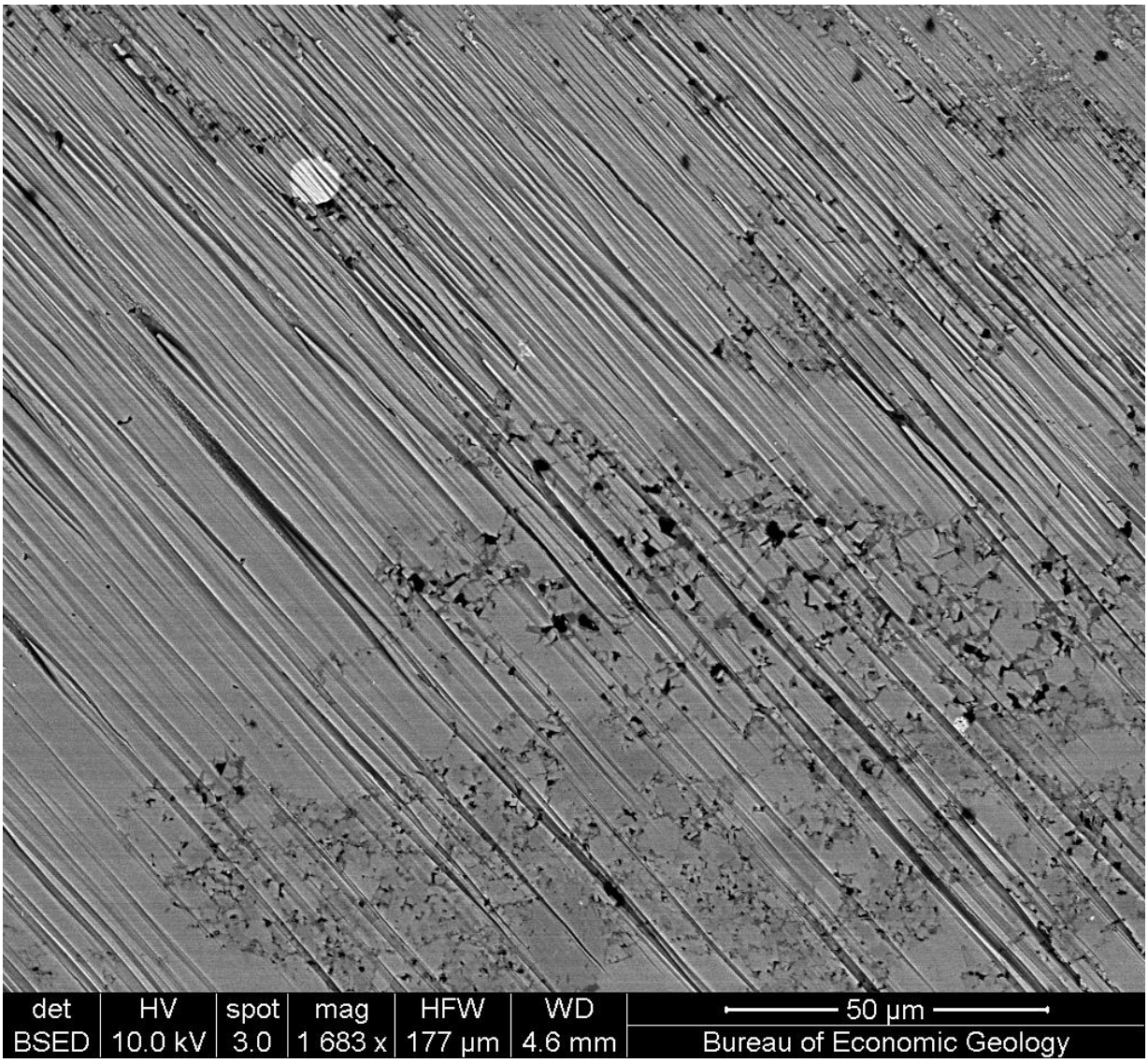

Figure 5: Back scattered electron (BSE) image of unidirectional grooves induced by Ar-ion cross-section polishing with Leica EM TIC020 Triple Ion Beam Miller. Well 4 sample 1-80.

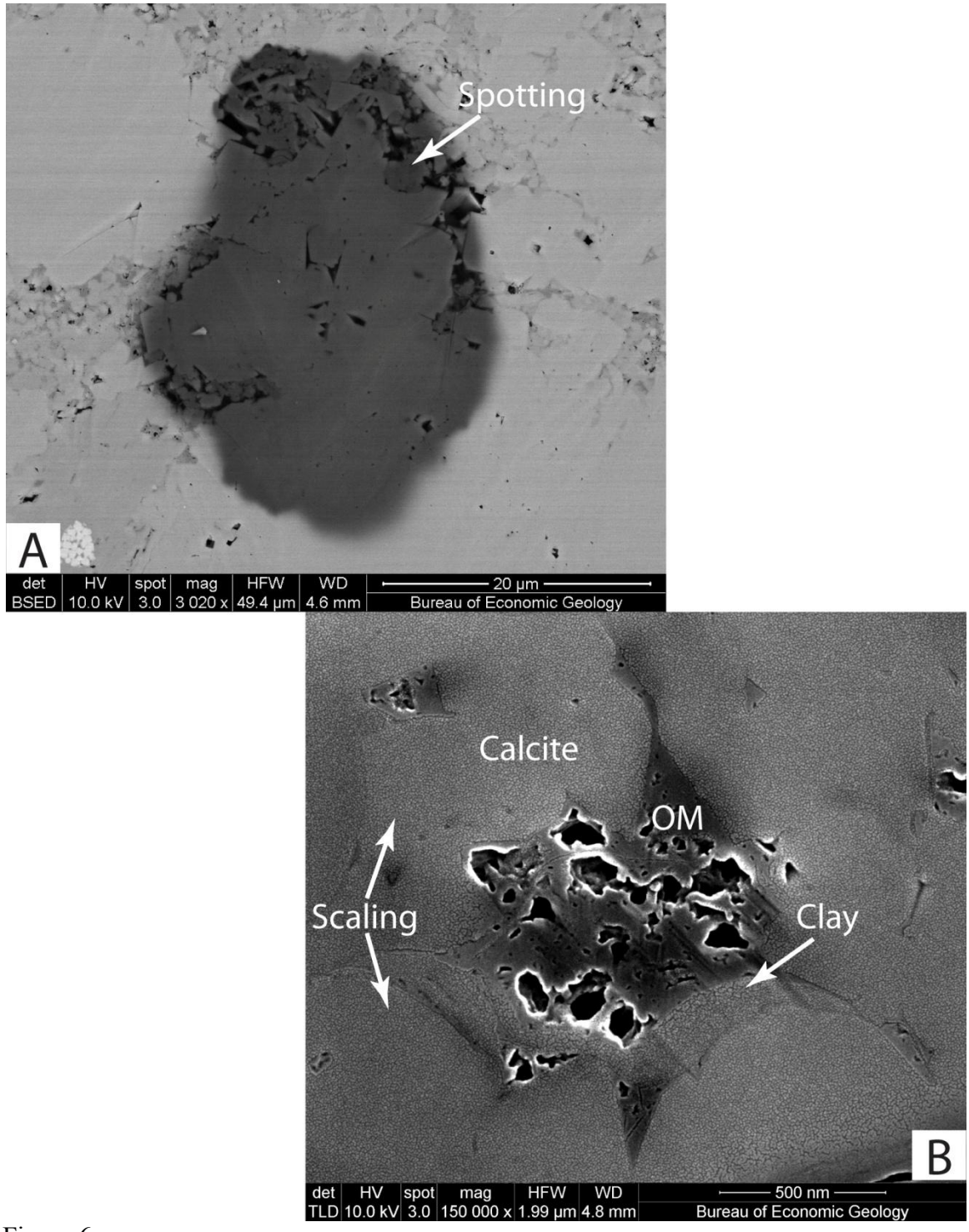
Spotting
A
det HV spot mag HFW WD
BSED 10.0 kV 3.0 3 020 x 49.4 µm 4.6 mm
20 µm
Bureau of Economic Geology
Calcite
OM
Scaling
Clay
B
det HV spot mag HFW WD
TLD 10.0 kV 3.0 150 000 x 1.99 µm 4.8 mm
500 nm
Bureau of Economic Geology

Figure 6

Figure 6: BSE and SE images of artifacts of Ir coating process including: A) "spotting" related to contamination during the coating process with the Leica EM ACE600 (Well 4 sample 1-80), and B) "scaling" related to differential electrostatic properties of mineral and OM surfaces during coating with the GATAN 682 Precision Etching Coating system (Well 4 sample 1-75). Here scaling coats calcite and clay surfaces.

Imaging

A FEI Nova NanoSEM 430, a Field-Emission Scanning Electron Microscope (FE-SEM) was used to collect images. Detectors utilized in this study include: back-scattered electron (BSE), secondary electron (SE), and SE through-the-lens detector (TLD). Additionally energy dispersive spectroscopy (EDS) was utilized to map elemental abundance. BSE, SE, and TLD images were acquired at accelerating voltages of 10-15 kV and a spot size (sample current) of 3, approximately mid-range of the current for the instrument. EDS images were acquired at an accelerating voltage of 15 kV, and a spot size of 5 to increase the signal received by the detectors. Working distances range from 4.2 - 10 mm depending on which detector was in use. Images were initially collected at a pixel count of 1024x943, but later images were collected at a higher pixel count of 2048x1886 in favor of higher resolution. This adjustment increased minimum detection from ~6 nm to ~4 nm. Images were obtained at a variety of scales and configurations to capture both qualitative and quantitative data.

QUANTITATIVE IMAGING:

The size distribution of observed pores is significantly greater than can be visualized or quantified at a single magnification. Pores measured in this study range from 3.6 nm - 3056.5 nm in equivalent circular diameter (ECD). In order to capture a statistically valid sampling of the full range of imagable pore sizes, images were collected at 10,000x, 50,000x, and 150,000x (instrument magnification). This range observed as much of the pore network as possible, cataloguing the distribution of porosity, organic matter, mineralogy and particles. Pores smaller than 4 nm are below the detection limit of

imaging methods utilized in this study. In order to characterize the rock fabric and aid in identification of skeletal aggregates, areas were also imaged at 1,500x.

Two 10,000x (machine magnification) SE, BSE, and EDS maps were generated for each milled sample. The areas represented by these images were randomly chosen representations of "bulk matrix", avoiding inclusion of anomalously large allochems. These images were collected at a magnification estimated to be low enough to encompass small scale heterogeneity, and high enough to differentiate components and capture a majority of the mineral-associated pore volume. The BSE images were point counted (350 pts) using the image measurement program JMicrovision© (JMv; Roduit, 2008; Milliken et al., 2013). Resolution of these images allowed for pores ~40 nm and larger to be quantified. This range encompasses greater than 94% of mineral-associated porosity within low-maturity samples and greater than 85% of mineral-associated porosity within high-maturity samples with significant mineral porosity (as measured by trace at 50,000x) (Figure 68). Pores within OM are generally too small to discern at this magnification. Horizontal field width at this magnification is 29.8 μm and pixel size is 14.6 nm with a 2048X1886 pixel count.

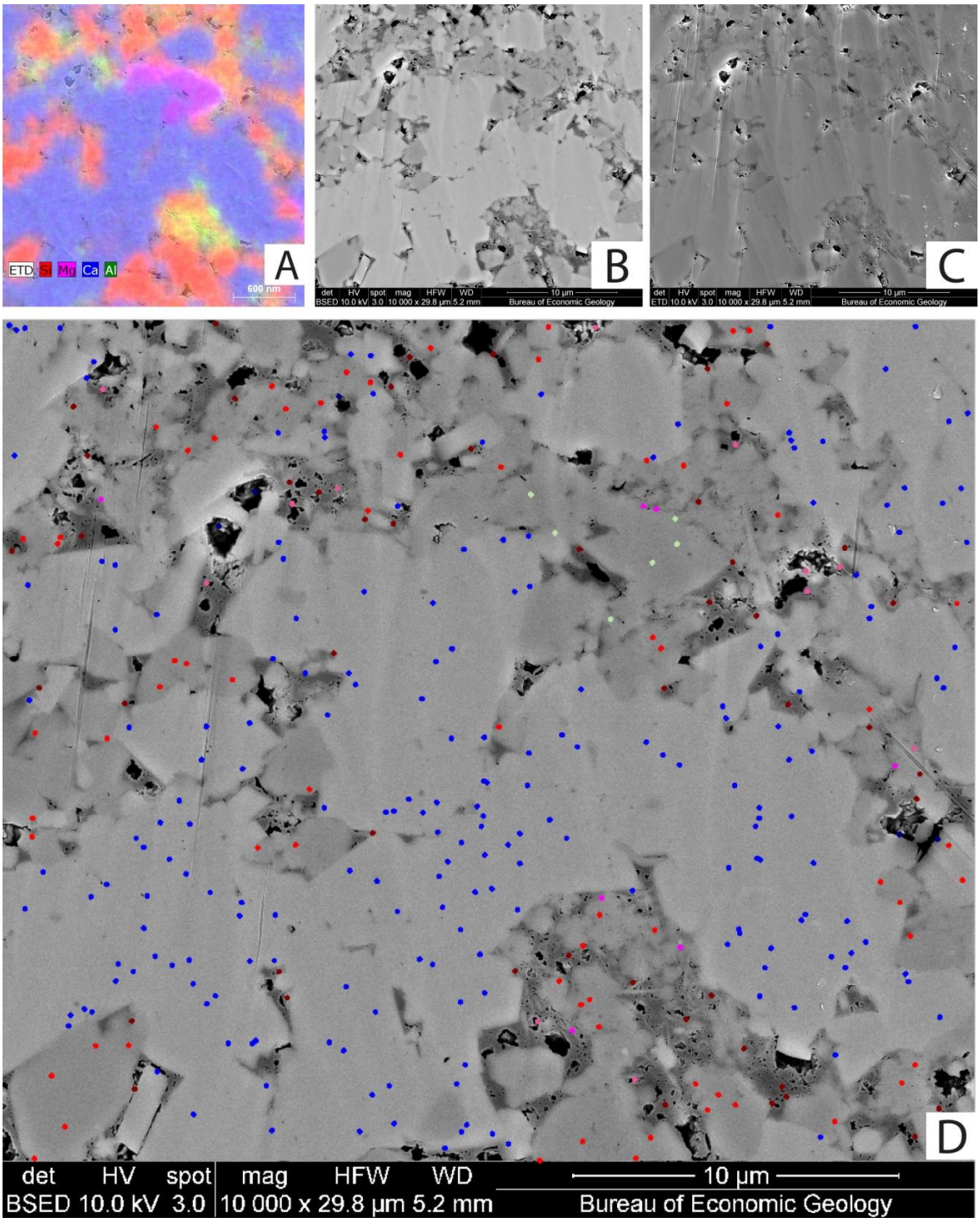

Figure 7: Example of different image types of the same area including: A) EDS map, B) BSE image, and C) SE image, and D) BSE image at 10,000x with point count (350 pts) overlain. Well 4 sample 1-80.

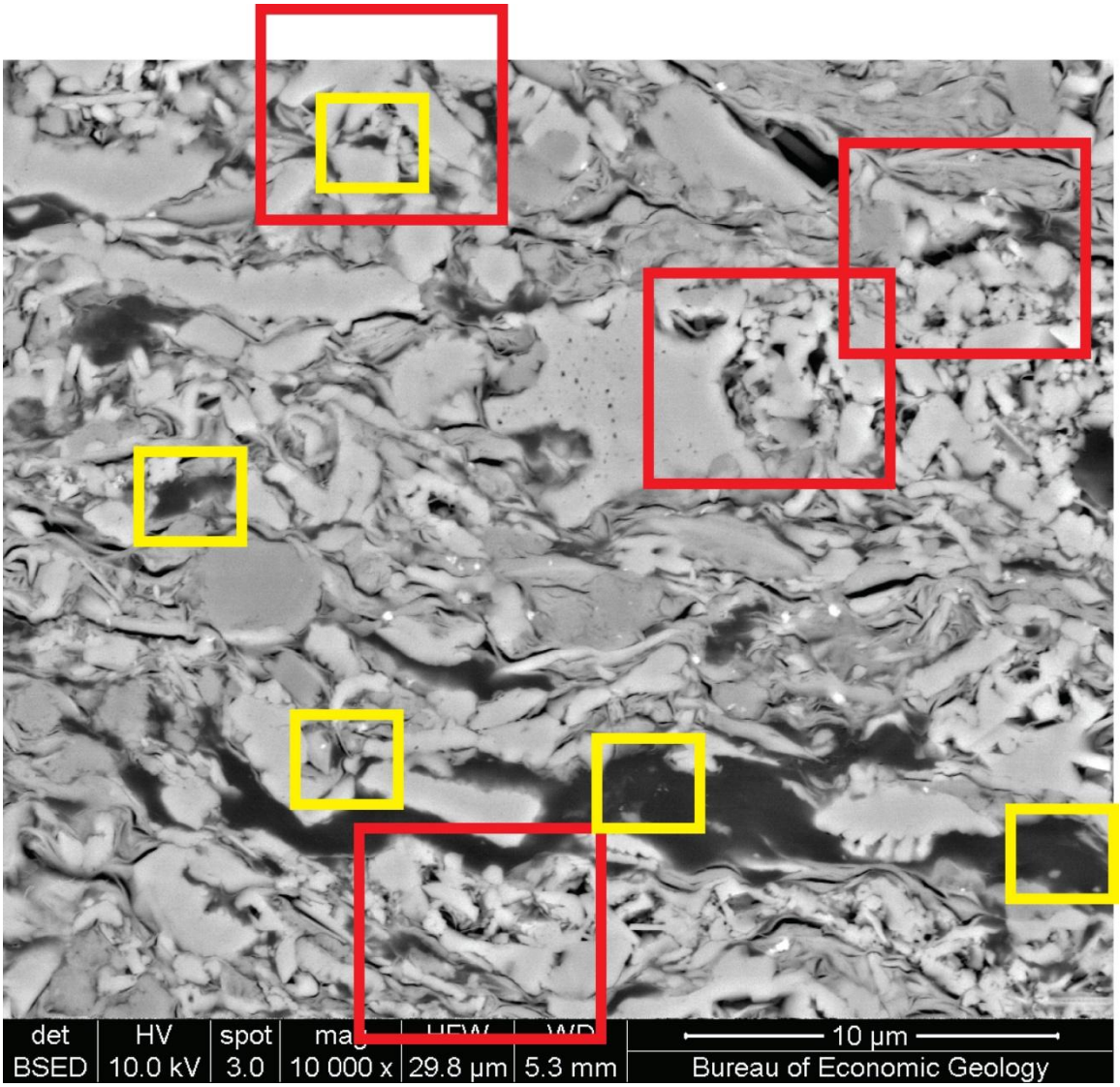

Figure 8: Example of BSE image at 10,000x with randomly selected quantified areas. Areas randomly selected to quantify mineral-associated pores are traced in red, and areas randomly selected to quantify OM-hosted pores in yellow. Well 1 sample 16.

Within both images captured at 10,000x, eight TLD images per sample were captured at 50,000x. Porous areas were chosen randomly from the two 10,000x BSE images using JMv. The distribution of mineral-associated pores by type, pore size, shape, etc., were quantified from these images. Resolution of these images allowed for pores ~9

nm and larger to be quantified. Horizontal field width at this magnification is 5.97 µm, and pixel size is 2.9 nm with a 2048X1886 pixel count.

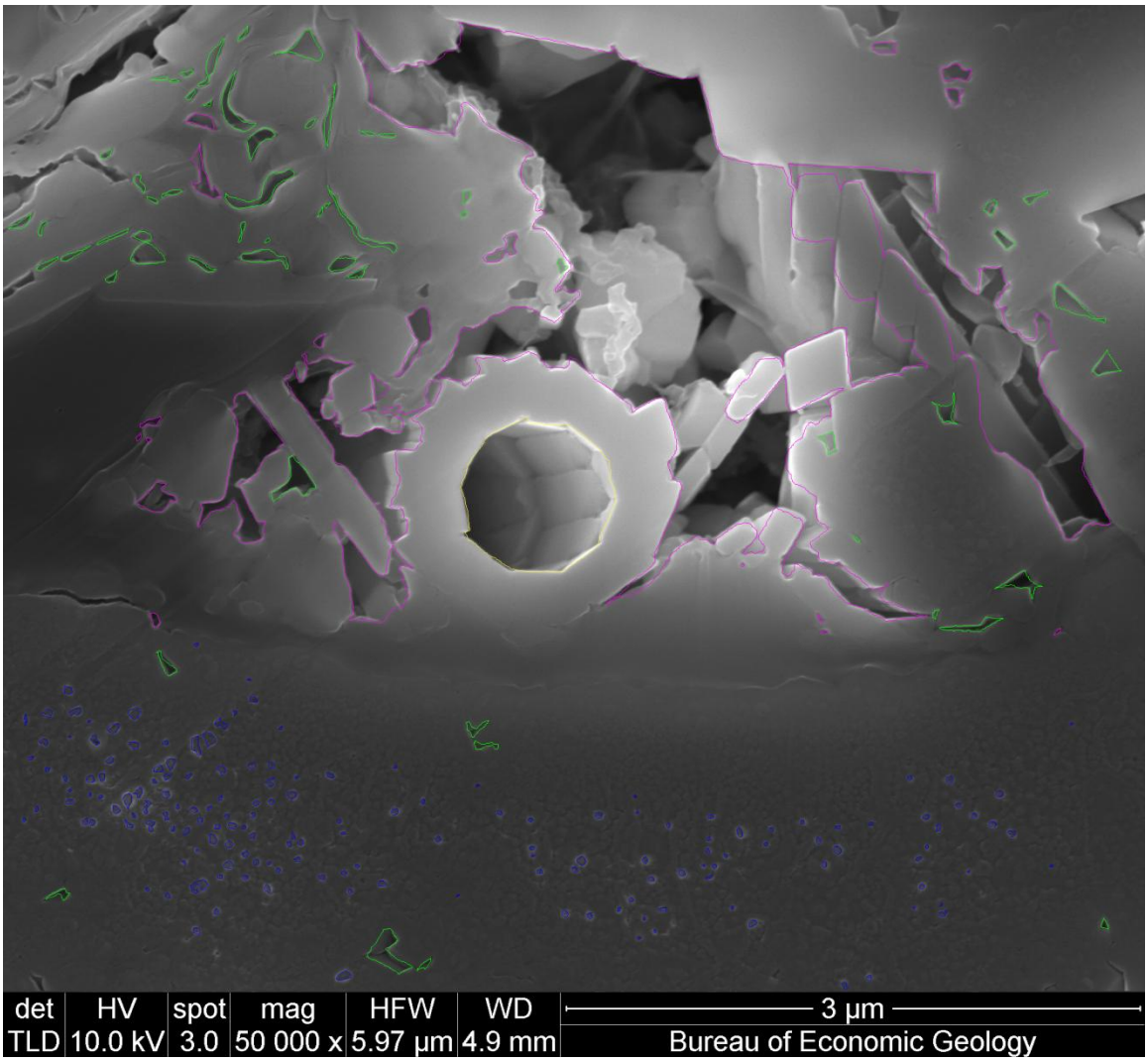

Figure 9: Example of TLD image at 50,000x with overlain pore boundary trace. Well 1 sample 16.

In addition to the 8 images collected at 50,000x per sample, 10 high-resolution TLD images of OM were collected at 150,000x. OM was chosen at random using JMv from within the two 10,000x BSE images and centered to image as much OM as possible.

These images were used to quantify the porosity of OM, as well as distribution of OM-hosted pores by type, abundance, size, shape, etc. Resolution of these images allowed for pores ~4 nm and larger to be quantified. Horizontal field width at this magnification is 1.99 and pixel size is 0.97 nm with a 2048X1886 pixel count.

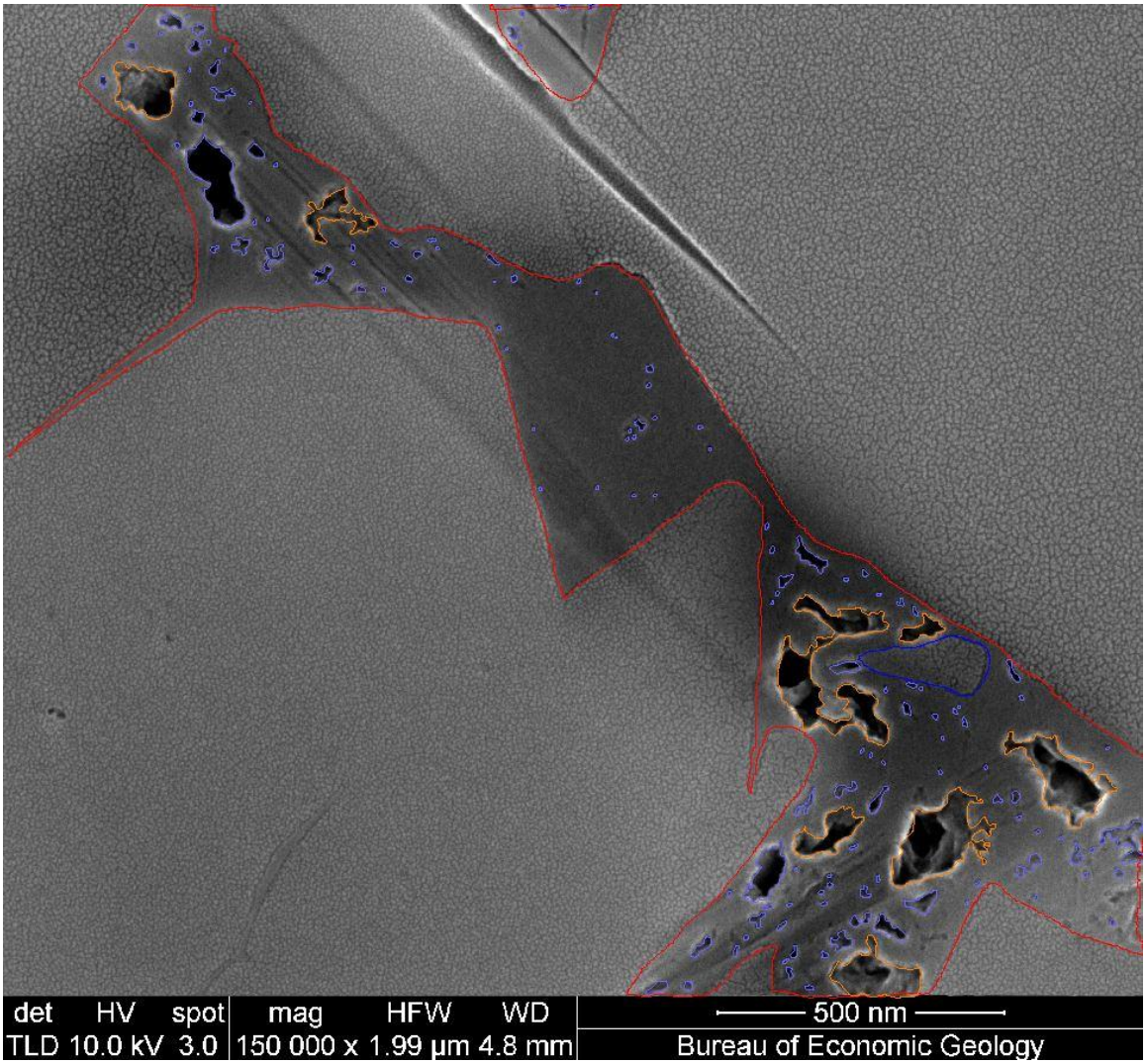

Figure 10: Example of 150,000x TLD image with overlain trace of OM, minerals surrounded by OM and OM-hosted pore boundaries. Note scaling of Ir coat on calcite surface. Well 4 sample 1-75A.

QUALITATIVE IMAGING:

In order to make observations about pore type, distribution, and abundance, it was necessary to utilize BSE, SE, TLD, and EDS detectors under a variety of conditions on samples prepared with a variety of techniques. Qualitative observations presented in this study were made using dominantly BSE, SE, TLD, and EDS images of AIM samples. Machine magnifications ranged from 300X to 300,000X under the same working conditions as quantitative images. In addition to this, 8 samples were imaged on a freshly broken, Ir-coated bed-parallel, surface to highlight skeletal grain diversity and textures of diagenetic trends (Figure 11). This includes, but is not limited to coccolith occurrence and diversity, cements (calcite, albite, pyrite, kaolinite, etc.), and OM texture.

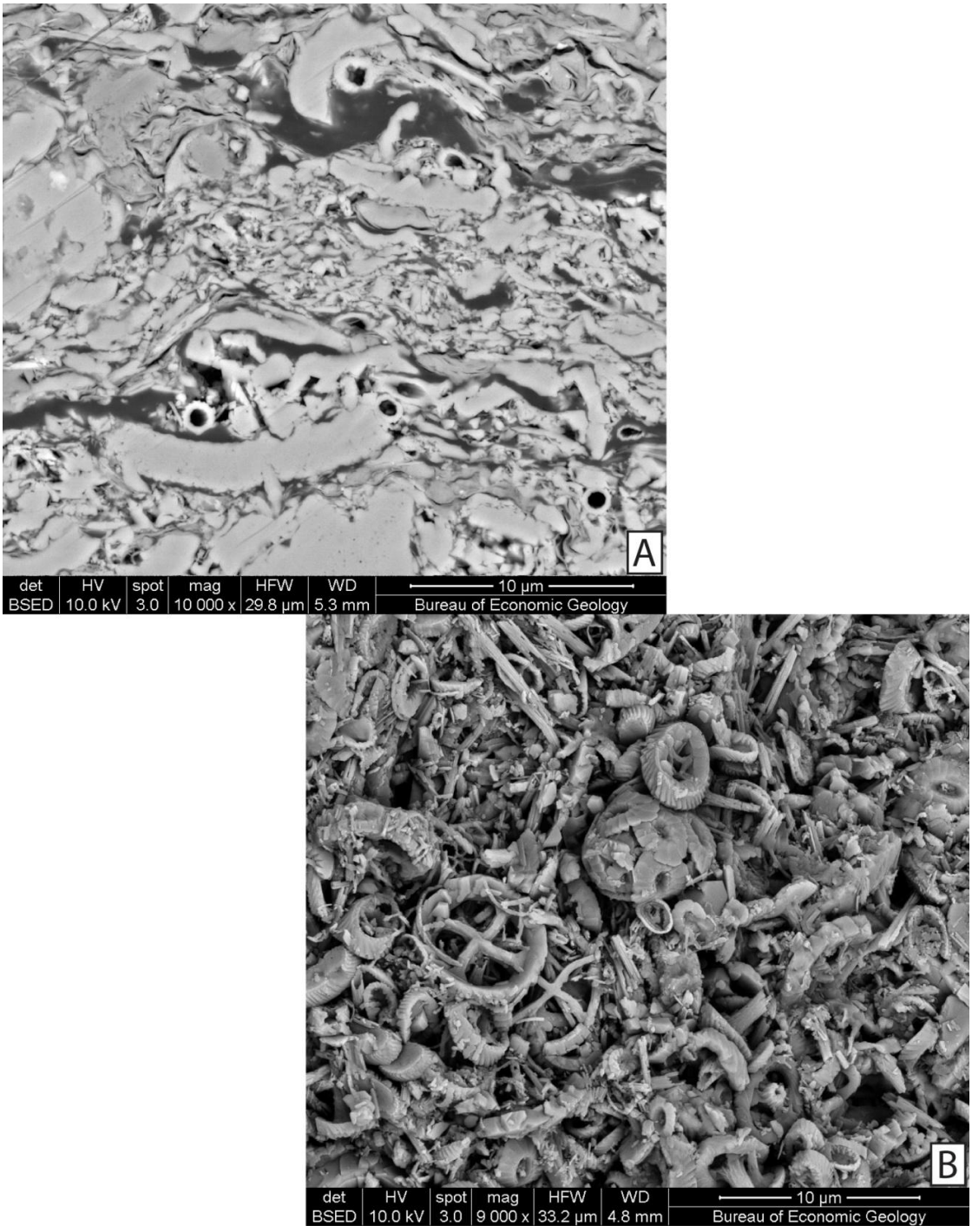

Figure 11: Example images of A) AIM and B) broken surface images of the same sample at similar magnifications. Note abundance of coccoliths and skeletal-hosted porosity in both images. Well 1 sample 16.

Quantitative Methods

Images from 18 samples were point counted and manually traced to quantify compositions, porosity values by type and pore size distributions. BSE images collected at 10,000x were point counted, using JMv (350 pts) (Figure 7). Point counts yielded: measured volume percentages of mineral-associated pores (including OM-mineral interface-pores), mineralogy, and OM volume (including OM-hosted porosity), or $\mathbf{TOC_{BV\%w/OM\phi}}$. Point counted mineral components include: quartz, sodium feldspar, potassium feldspar, calcite, phyllosilicates (clays and micas), OM, pyrite, kaolinite, dolomite, apatite, and titanium oxide (Table 2).

Pore boundaries of pores within 50,000x and 150,000x TLD images were interpreted manually using a digital tracing screen (Wacom Cintiq pen display) and quantified using JMicrovision©. JMv renders interpreted shapes as objects for which it calculates a wide range of size and shape parameters e.g., area, perimeter, length, width, equivalent circular diameter, and eccentricity. Manual interpretation of pore boundaries was favored over automated because: gray levels within pores overlaps significantly with gray levels on mineral surfaces, pore edges are often not sharp enough to be detected, and automated interpretation does not allow for categorization of pore type and recognition of induced porosity (Milliken et al., 2013). Classification of pores was based upon objective parameters to avoid interpretive bias.

Objects traced at 50,000x were classified as follows (Table 1; Figures 50-56; see *Mineral-associated Pore Types* for more detail):

- Pores between mineral particles (inter-mineral)

- Inter-mineral pores within aggregates (intra-pellet inter-min)
- Pores between OM and mineral surfaces (OM-mineral interface)
- OM-mineral interface pores within aggregates (intra-pellet interface)
- Pores within skeletal cavities (intra-skeletal)
- Intra-skeletal pores within aggregates (intra-pellet intra-skeletal)
- Small "inclusion" pores within mineral particles (intra-inclusion)
- Pores within or between clay particles (clay-hosted)
- Moldic pores associated with dissolution of mica and/or kaolinite (mica-associated mold)

These measurements generate values of the size, shape and abundance of type of mineral-associated pores.

OM-hosted pores as well as OM boundaries were interpreted within 150,000x images. Objects traced at 150,000x include (Table 1; Figure 57; see *Organic Matter Hosted Pore Types* for more detail):

- OM boundaries
- Mineral within OM
- Simple OM-hosted pore
- Complex OM-hosted pore

These measurements generate values for the area of OM, and OM-hosted porosity, as well as size, shape, and classification distributions by area and number.

QUANTIFICATION OF POROSITY

The porosity of OM in each sample was calculated as follows:

$$\mathbf{OM_{\phi}} = 100^{*} (\mathbf{A_{\phi OM}})/(\mathbf{A_{OM}}) \quad \text{(Eq. 1)}$$

Where $\mathbf{A_{OM}}$ is measured OM area, $\mathbf{A_{\phi OM}}$ is measured OM-hosted pore area, and $\mathbf{OM_{\phi}}$ is the porosity of OM within the imaged area.

Given the measured mineral-associated porosity and volume of OM ($\mathbf{TOC_{BV\% w/OM\phi}}$) from the point counts, the calculated $\mathbf{OM_{\phi}}$ the volume percentage of OM-hosted pores (**ϕOM**), and total visible porosity ($\mathbf{\phi_{VIS}}$) can be calculated as follows:

$$\mathbf{\phi OM = OM_{\phi} * TOC_{BV\% w/OM\phi}} \quad \text{(Eq. 2)}$$

$$\mathbf{\phi VIS = \phi OM + \phi MIN} \quad \text{(Eq. 3)}$$

Key values and distributions obtained by these methods include: mineral-associated porosity by volume percent (**ϕMIN**), the porosity of OM (**OMϕ**), bulk volume percent of OM-hosted porosity (**ϕOM**), the bulk volume percent of observed OM including OM-hosted porosity ($\mathbf{TOC_{BV\% w/OM)}}$), and the bulk volume percent of OM ($\mathbf{TOC_{BV\%-OM\phi}}$). Additionally the bulk volume taken up by each specific pore type (**ϕType A)** for OM-hosted pore types (Eq. 4) and for mineral-associated pore types (Eq. 5) is calculated by as follows:

$$\mathbf{(\phi OM)^{*} (A_{\phi Type}/A_{\phi OM}) = \phi Type\ A} \quad \text{(Eq. 4) or:}$$

$$\mathbf{(\phi MIN)^{*}(A_{\phi Type}/A_{\phi MIN}) = \phi Type\ A} \quad \text{(Eq. 5)}$$

Where traced area of a specific pore type ($\mathbf{A_{\phi Type)}}$, area of traced OM-hosted

porosity is ($\mathbf{A_{\phi OM}}$), area of measured mineral-associated pores are ($\mathbf{A_{\phi MIN}}$).

QUANTIFICATION OF PORE SIZE DISTRIBUTIONS

Given the data collected from point counts of BSE images at 10,000x and areal trace measurement of TLD images at 50,000x and 150,000x, distributions of pore sizes can be generated. Size distributions by frequency percent and volume percent are calculated for cumulative measured pores and by specific type. Data is presented as cumulative distributions by area to highlight relative contribution to pore volume, and or in binned histograms to highlight numerical abundance (Figures 65-72, and 74-76). Size is most commonly expressed as equivalent circular diameter (ECD) in nanometers (nm).

Statistically valid populations of a specified pore type (e.g., mineral-associated or OM-hosted) are measured from randomly selected pores imaged at a constant magnification within a sample. However, measured populations of OM-hosted pores or mineral-associated pores likely represent disproportionate amounts of the bulk porosity. Relative numerical abundance of OM-hosted and mineral-associated pores can be calculated by scaling number percent of respective OM-hosted or mineral-associated pores by a "scaling factor". "Scaling factors" for mineral-associated pore types ($\mathbf{SF_{MIN}}$) or for OM-hosted pore types ($\mathbf{SF_{OM}}$) are calculated as follows.

$$\mathbf{SF_{MIN}} = \frac{(\phi MIN/\ \phi VIS)}{(A_{\phi MIN}/A_{\phi TOT})} \qquad \text{(Eq. 4)}$$

$$\mathbf{SF_{OM}} = \frac{(\phi OM/\ \phi VIS)}{(A_{\phi OM}/A_{\phi TOT})} \qquad \text{(Eq. 5)}$$

Similarly, it is possible to integrate OM-hosted and mineral-associated pore populations into a single distribution as follows:

1) Bin the values of OM-hosted and mineral-associated pores by area for both populations. In this case area-equivalent intervals of 10 nm ECD were used (Figure 12A).
2) Scale the number percent of each bin by $\mathbf{SF_{MIN}}$ or $\mathbf{SF_{OM}}$ for respective populations.
3) Normalize the (now scaled) number percent values for both populations (Figure 12B).
4) Add the values of the scaled number percentages (OM-hosted and mineral-associated) for each bin to yield a binned size distribution of all measured pores (Figure 12B).
5) Area percentages of each bin can be back-calculated, with a relatively higher error than mineral-associated or OM-associated populations due to binning.

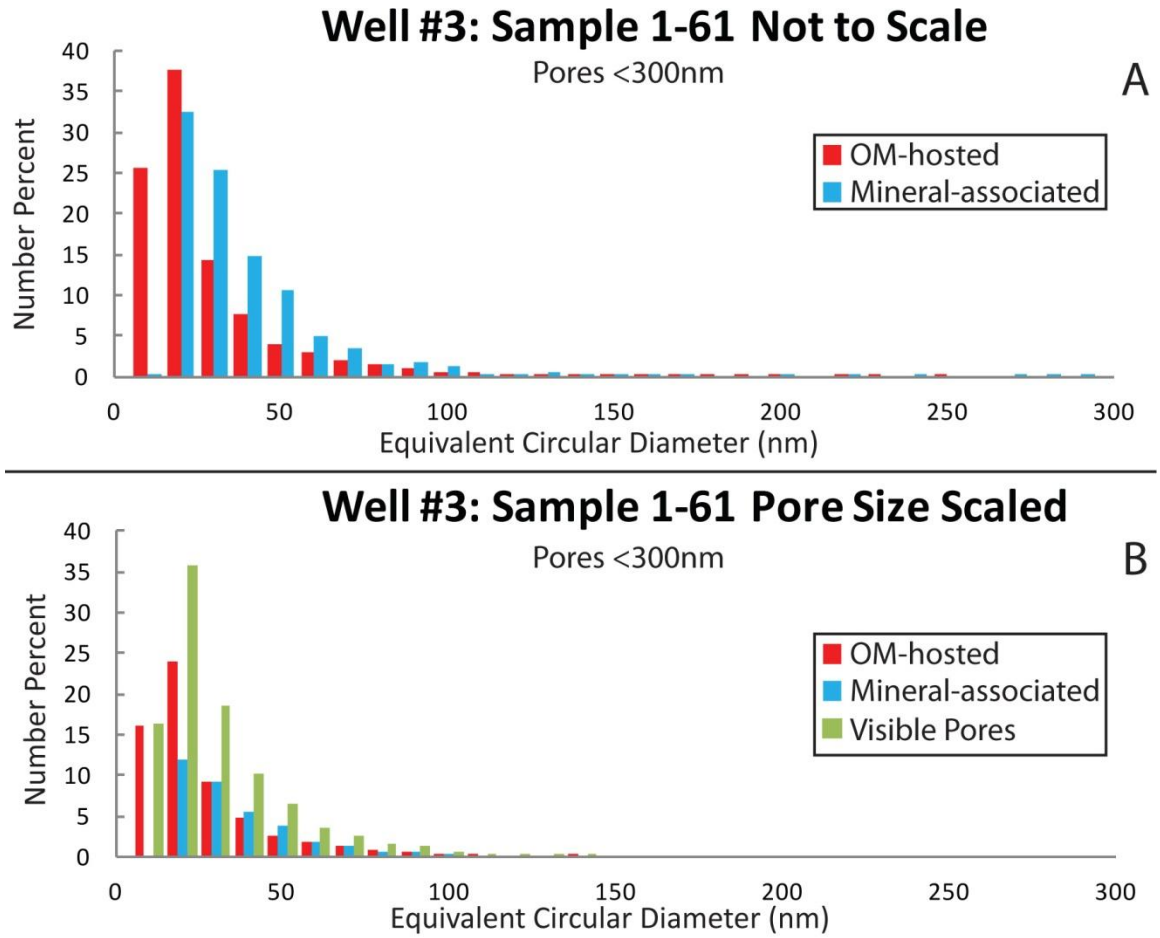

Figure 12: Histograms (pores < 300 nm) showing number percent plotted against equivalent circular diameter from Well 3 sample 1-61 in 10 nm bins. A) OM-hosted and mineral-associated populations plotted as number percentages of their respective populations. b) OM-hosted, mineral-associated, and all visible pores plotted as relative (calculated) number percentages of the total pore population.

ERROR

Using a complex, relatively new methodology that integrates a variety of different methods, including point counts and manual tracing, results in error uncertainty. While carefully thought out methodical imaging, randomizing and quantification techniques

keep human error to a minimum, error deriving from a limited quantified area, point counting, and trace techniques is unavoidable. Error associated with point counting has been studied extensively, and is a function of the amount of points counted and the abundance of the component counted (Folk, 1980; Van der Plas and Tobi, 1965). Error associated with trace methodology is uncertain. Theoretically, a perfect trace of an image would represent the sample aerial abundances that an infinite point count would provide. Thus, it can be inferred that error in volume calculations from trace data is significantly less than point counting. Error most likely arises from pixel resolution and human tracing precision of pore margins. Further research is necessary to make estimates of error associated with manual-trace methodology.

Probably the largest challenge in minimizing error in these types of studies is picking working magnifications that statistically represent as much porosity as possible, while still allowing for reliable characterization of components. Because of practical constraints and the fine-grained nature of mudrocks, the investigated area is typically small, consisting of several areas within the ~1 mm^2 investigated milled surface. Klaver et al. (2012) and Houben et al., (2013b) estimate representative areas of ~140 x 140 μm^2 and ~100 x 100 μm^2 respectively. Lithology and grains however vary significantly between this study. In this study a large portion of the ~500 nm^2 - 1 mm^2 milled surface was investigated at relatively low-magnification, but only two randomly selected areas from different parts of the milled surface ~ 30 x 30 µm are quantified. Considerations from Houben et al. (2013b) and Klaver et al. (2012), suggest that a larger quantified area would be preferable and error might be affected accordingly. Given these considerations,

point-count volume measurements are preferred over bulk rock for correlation with pore data because they represent the same areas. Qualitatively, imaged areas are wide enough that they encompass the majority of scale heterogeneity and associated porosity, except within foraminifer tests that are typically larger than ~50 µm. The addition of a low-magnification trace of that specific pore type (~1,000x) would account for this.

QUALITATIVE RESULTS: COMPONENTS AND PROCESSES

Overview

Mudrocks examined in this study are composed primarily of coccolith debris, siliciclastic minerals, other skeletal debris, kerogen, authigenic minerals and secondary OM (bitumen). Spatial distribution of detrital components suggest that aggregates of calcite, kerogen and clay are present in varying abundances. Increasing pressure and temperature with burial depth alters the detrital grain assemblage and primary pore network via: cementation, compaction, OM maturation, and to a lesser degree replacement and dissolution. Major authigenic components include pyrite, calcite, clay minerals, apatite, and bitumen.

Possible classification of detrital grain assemblages in this study include, but are not limited to: argillaceous carbonate mudstones to packstones (Dunham et al., 1962), marls to chalky marls (Longman et al., 1998), and marls to calcareous tarls as discussed in Ergene (2014) and Milliken (personal communication, November 13, 2013). Each of these classifications has both advantages and disadvantages. Dunham classification accounts for heterogeneity in fabric and typically silt size and larger grain assemblage, but fails to account for abundance and diversity of siliciclastic components. Extra modifiers are necessary to comprehensively describe samples (e.g., argillaceous, quartz-rich, OM-rich, etc.), but do not account for subtle compositional heterogeneity. Longman classification accounts for a spectrum of clay and carbonate content, key controls on porosity in coccolithic mudrocks, but does not account for other silicates and carbonate minerals and requires a modifier to account for rock-fabric heterogeneity, e.g., pelleted, laminated, or bioturbated. The classification presented by Ergene (2014) and Milliken

(personal communication, November 13, 2013) is applicable here because it accounts for a diverse mixed assemblage of detrital grains. However it, like Longman's classification, requires a textural modifier.

The following presents qualitative observations about the grain assemblage, pore type assemblage, and diagenesis within Ar-ion cross-section polished and broken surface samples. Components are identified from their morphology, distribution, association, and elemental composition (using BSE, and EDS detectors). Where cements are present, particularly calcite and quartz, distinction of authigenic and detrital components is not always possible. For additional details see the related study by Ergene (2014).

Detrital Grains

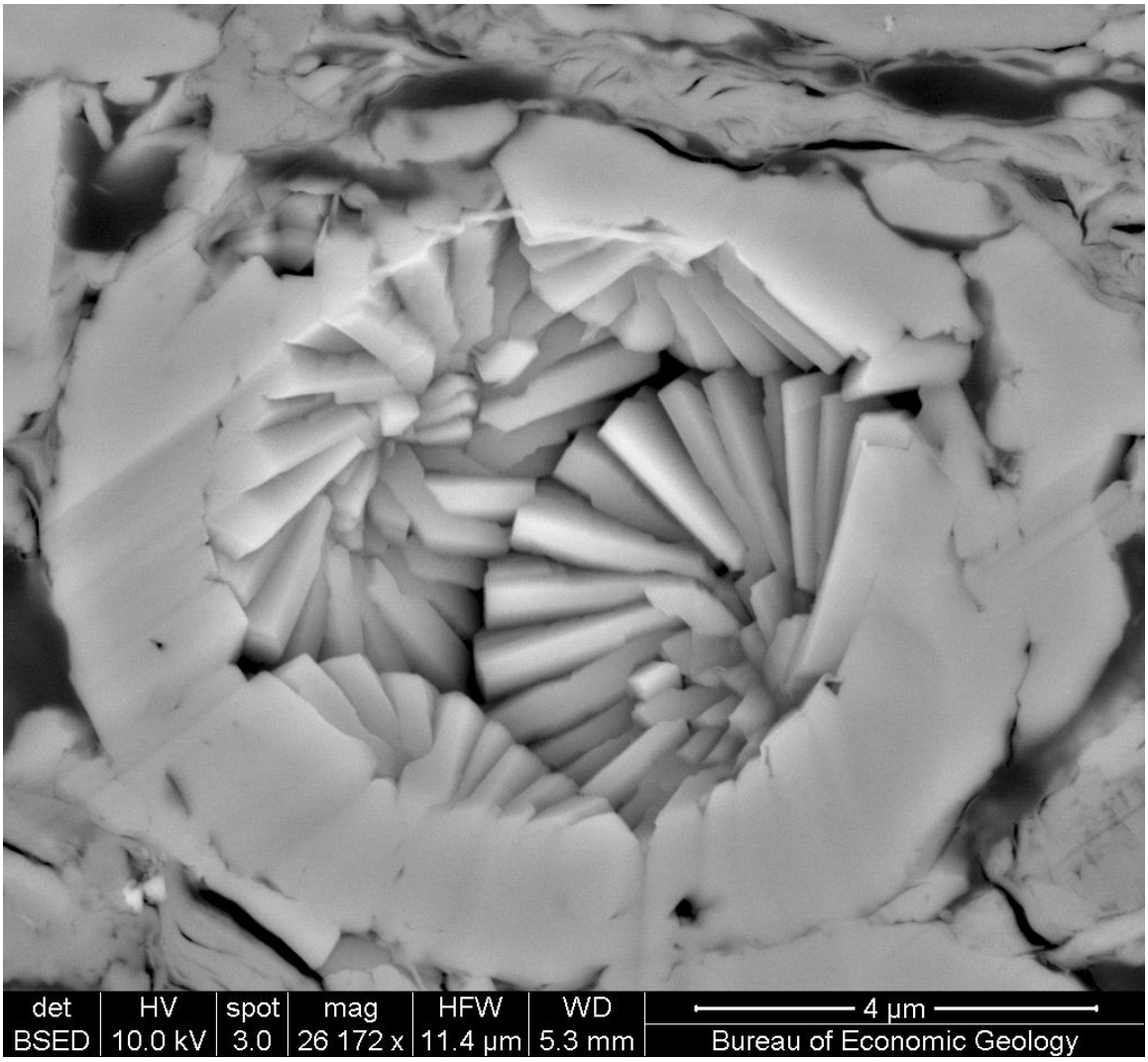

Figure 13: BSE image of intact coccosphere. Well 1 sample 16.

Samples contain complex grain assemblages with a wide range of detrital components observed in both low maturity and high-maturity samples. Components of extrabasinal and intrabasinal origins are present in all samples, in varying abundances and compositions.

EXTRABASINAL GRAINS

Extrabasinal components within the study set include siliciclastic grains (e.g., quartz, feldspars, micas and clays), and terrestrial OM. These components are of terrestrial origin, are the product of weathering and sedimentary processes, and compose between 27.2% and 42.6% of the bulk volume of samples (Tables 2 and 3). Silicate components are distinguished from carbonate components by their distinctive habits, darker BSE signal, and in most cases the presence of a Si signal in EDS maps. Terrestrial OM is distinguished by its dark BSE signal, discrete arcuate margins, and rigid structure (Figure 20).

Quartz is present in all samples, ranging in abundance from 0.9% to 21.7% of the bulk volume, a large portion of which is in the form of detrital grains at low maturities. A strong Si signal and lack of Al in EDS generally identifies quartz, in addition to its discrete, equant, and rounded to euhedral grain shape. Distinction of authigenic from detrital quartz, however, can be extremely difficult. Quartz particles commonly occur as micron scale particles (~1-10 μm), but can range into sub-micron sizes. Some of the microcrystalline quartz particles exhibit crystal growth faces, suggesting an authigenic genesis. A large portion exhibit irregular shape and are likely detrital (Figure 14).

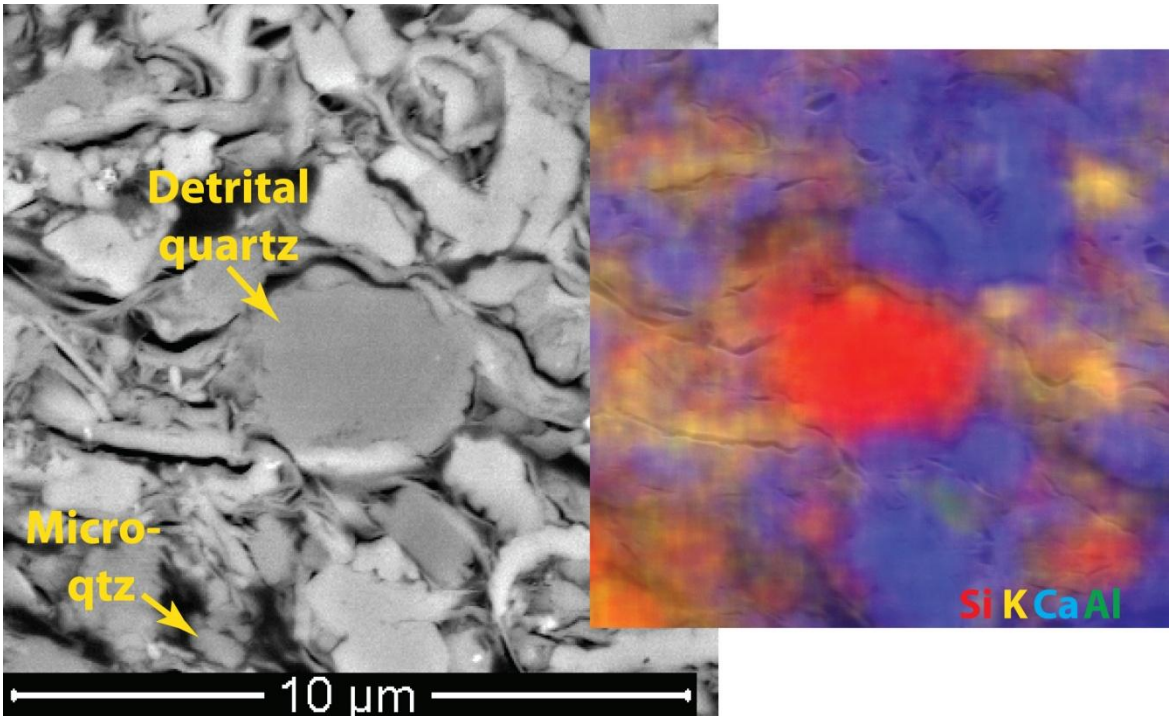

Figure 14: BSE image and EDS map of corresponding area. Detrital quartz grain, microcrystalline quartz (~400 nm), in addition to clays, and coccolithic debris. Sample Well 1 sample 16.

Potassium feldspar is present in low-maturity samples ranging from 0.6% - 5.6% of the bulk volume, but is present only in trace amounts at high maturity. It can be identified by the presence of Si, Al, and K signal in EDS map, as well as "blocky" grain shape, and partial dissolution along cleavage planes (Figure 15). Molds associated with clays, often display similar shapes and can be observed in other samples (Figure 56). Partial to full dissolution at low maturity and absence at high maturity reflects instability under burial conditions, as noted by others in both sandstones and mudrocks (Land et al., 1997; Milliken, 1992; Milliken et al., 1989).

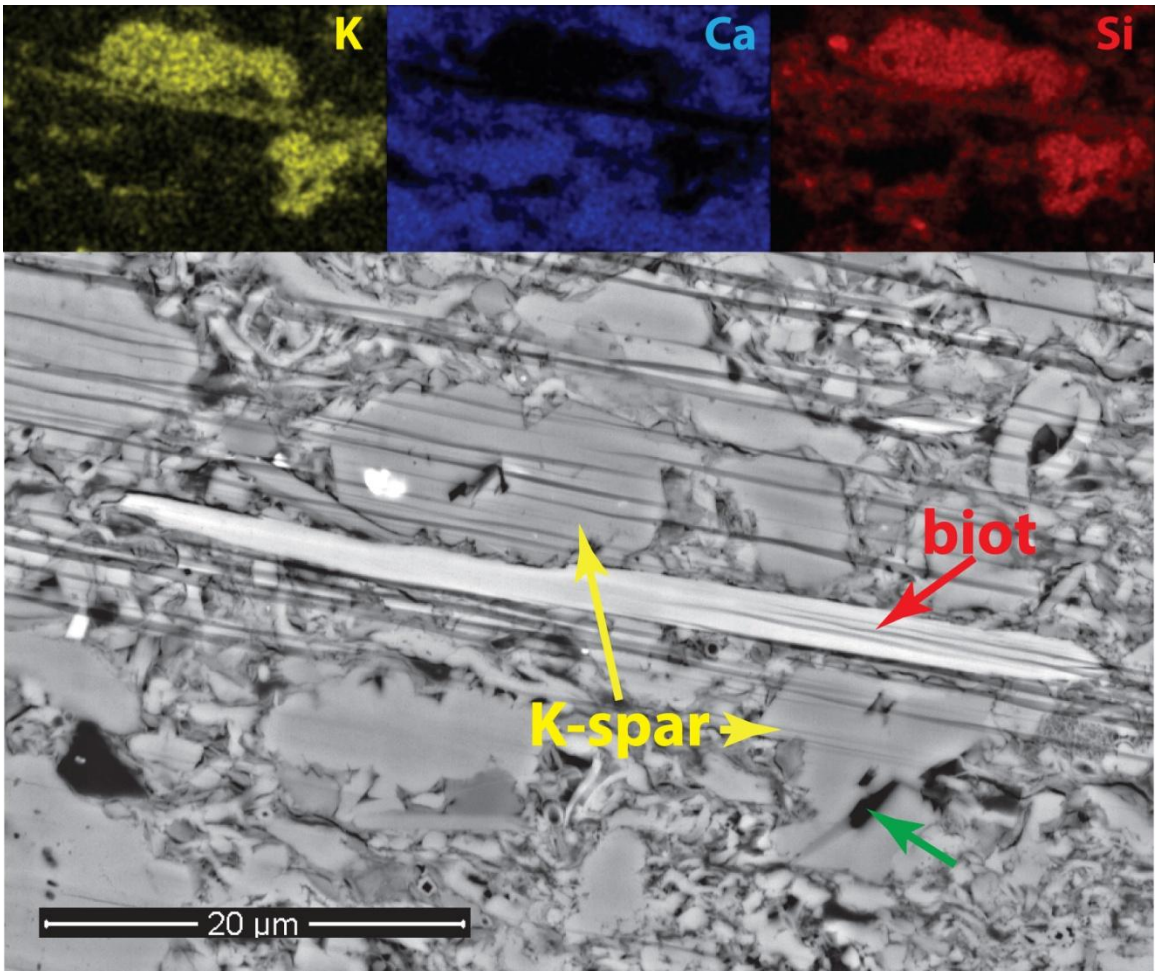

Figure 15: BSE and EDS images showing potassium feldspar (K-spar), and biotite (biot). Note: Feldspar shows distinctive blocky grain shape and partial dissolution along cleavage planes (green arrow). Biotite shows elongate grain shape and bright BSE signal. Well 1 sample 19.

One granitic rock fragment was observed in Well 1 sample 23, and consists of quartz, feldspar and biotite in the form of a large irregular, subrounded grain (Figure 16).

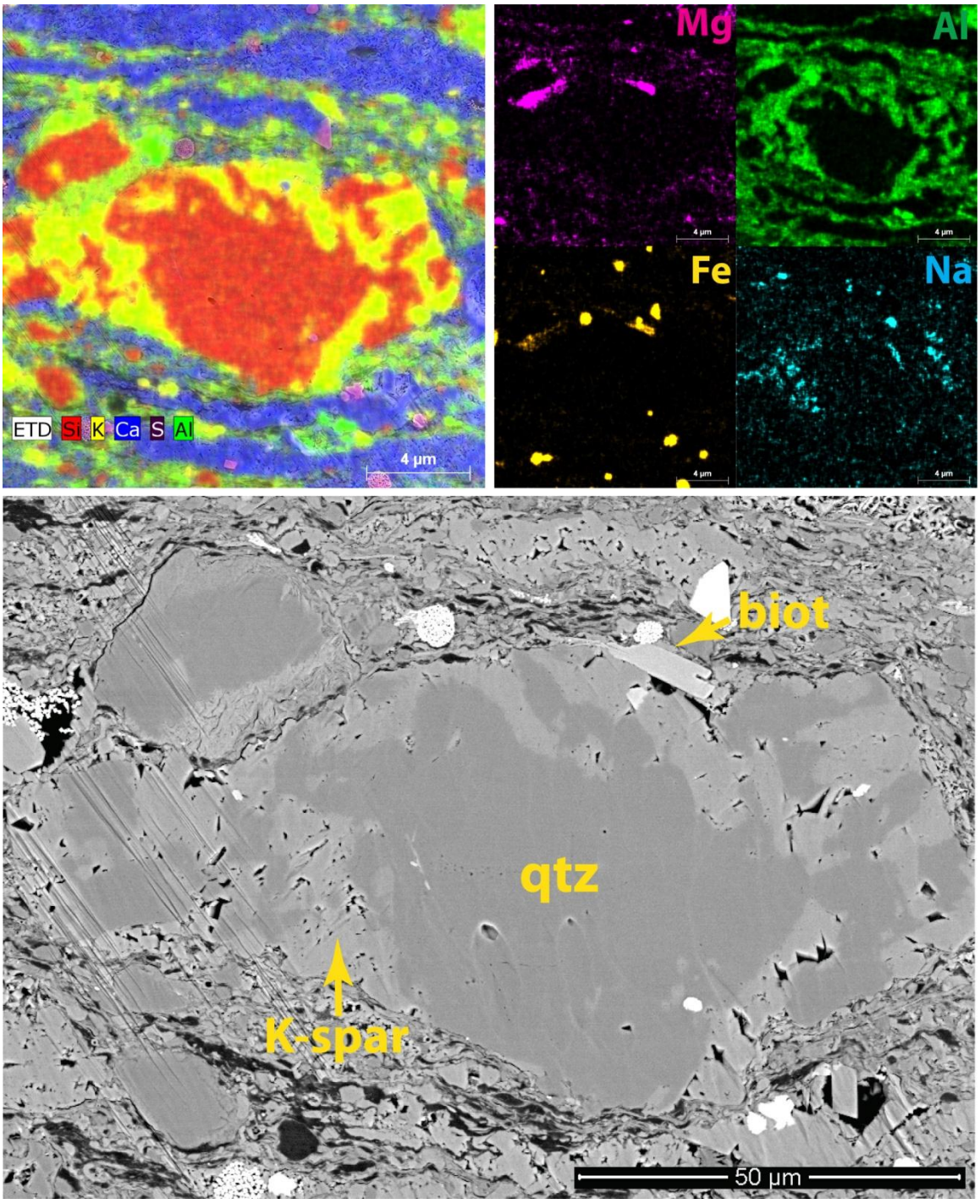

Figure 16: BSE image and EDS maps of corresponding area. Partially weathered granitic rock fragment composed of quartz (qtz), potassium feldspar (k-spar), biotite (biot). Well 1 sample 23.

Phyllosilicates are present in all samples, and range in abundance from 2.3% - 34.4% of the bulk volume. These samples displayed both clay minerals and micas, distinguished primarily on size and shape. Mica grains are larger than clay-size and exhibit distinct cleavage. Authigenic clays, predominantly kaolinite and Mg-bearing phyllosilicates, are discussed in *Diagenetic Processes and Components*.

Micas (biotite and muscovite) are present in most samples, and are easily distinguished by their elongate grain shape, platy cleavage, relatively bright BSE signal (especially biotite), and distinctive EDS signals. Bent, exfoliated, partially dissolved and "exploded" micas are observed in several samples as a result of compaction, weathering and precipitation of clay minerals (Figure 17).

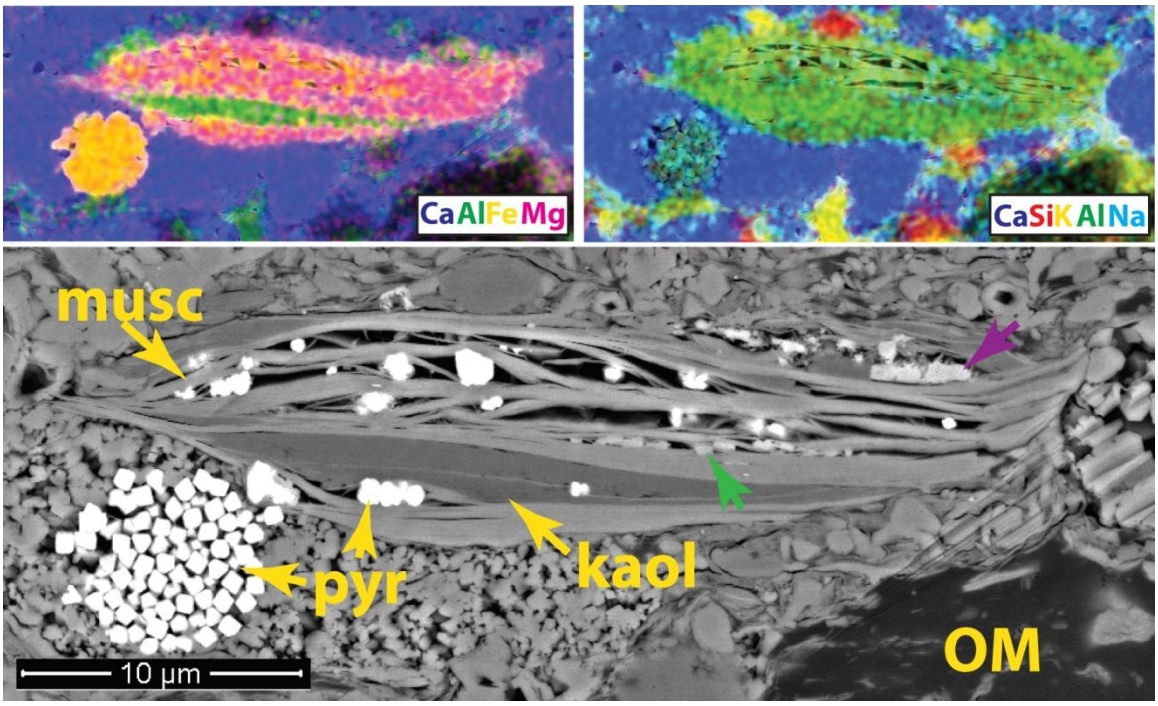

Figure 17: EDS and BSE image showing bent and "exploded" muscovite grain with authigenic kaolinite (kaol), pyrite (pyr), apatite (green arrow) in inter-plate pores. Also Pyrite framboid (pyr), kerogen (OM), and authigenic anatase (purple arrow). Well 1 sample 23.

Detrital clay is present in all samples. XRD data and EDS spectra show mixed-layer smectite/illite at both low and high maturities. Elemental maps show Si, Al, K and sometimes Mg, and Fe signals from detrital clay. Quantification of illite/smectite cannot be determined from EDS spectra. Detrital clay at low maturity is prone to desiccation induced shrinkage pores, resultant from sample preparation, and consists of irregular ductile platelets ~1-3 μm in length that are mashed between other grains. At high maturity, fewer shrinkage pores are observed, and both straight clay platelets, typically ~500 nm in length, and irregular clay platelets, ~1-3 μm in length, are present (Figure 18). Spatially, detrital clays occur within OM and silicate-rich seams between carbonate aggregates, as interstitial "matrix" between skeletal and silicate grains, and less commonly, clumped into detrital clasts (Figure 19). With a few rare exceptions, recognition of detrital clay clasts is difficult, especially within high-maturity samples where clays have been altered both physically and chemically. Clay platelets are observed within OM-mineral aggregates in both low and high-maturity samples (Figure 28).

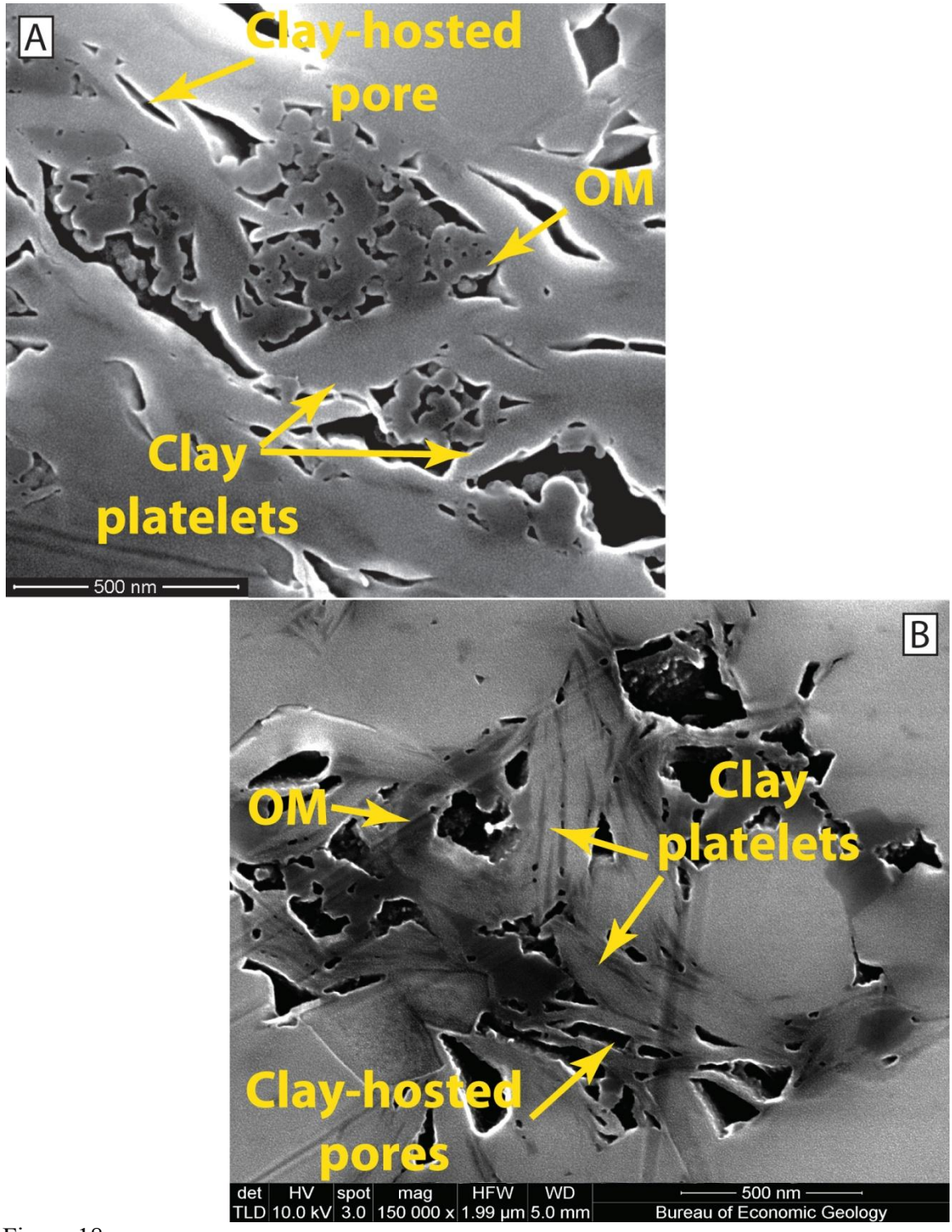
A
Clay-hosted pore
OM
Clay platelets
500 nm
B
OM
Clay platelets
Clay-hosted pores
det HV spot mag HFW WD
TLD 10.0 kV 3.0 150 000 x 1.99 µm 5.0 mm
500 nm
Bureau of Economic Geology

Figure 18

Figure 18: SE images showing clay platelets, and associated OM in A) low maturity where clay platelets are irregular and ~1 μm in length, and B) high maturity Well 3 sample 1-66 where clay platelets are straight, and ~500 nm in length.

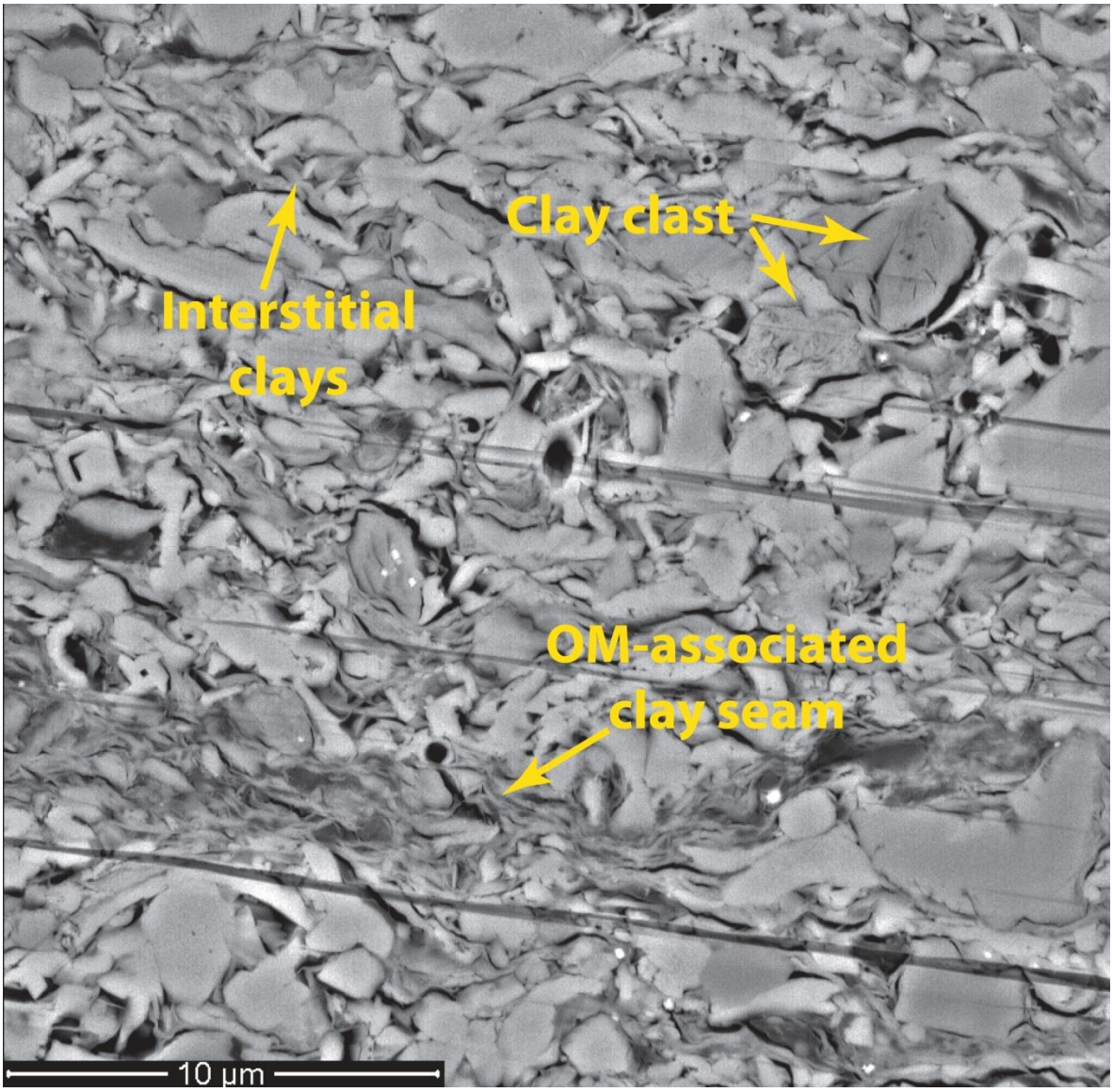

Figure 19: BSE image showing distribution of detrital clay platelets in a low-maturity sample. Clay platelets are observed as; interstitial "matrix" between skeletal and silicate grains, OM-rich seams, and as more discrete micron-scale clasts composed of disorganized clay platelets. Note abundance of shrinkage pores, particularly at margins of clay clast. Well 1 sample 19.

Terrestrial kerogen is present in most samples in minor amounts. Large (>10µm), rigid OM grains with discrete arcuate margins is interpreted as "woody" OM, indicative of terrestrial origins (Figure 20) (Milliken et al., 2013). Additionally, small particles of

non-discrete, clay-associated porous kerogen are potentially indicative of a more terrestrial origin, based upon factors including: 1) association with woody OM and siliciclastics in particularly intimate interworking with clay platelets (Figures 19 and 20), 2) biomarker signals from samples of this interval (Sun et al., 2014), and 3) relative stability of the OM-hosted pore network across thermal maturity (Tables 3, 4, and 7; Figures 62, 74).

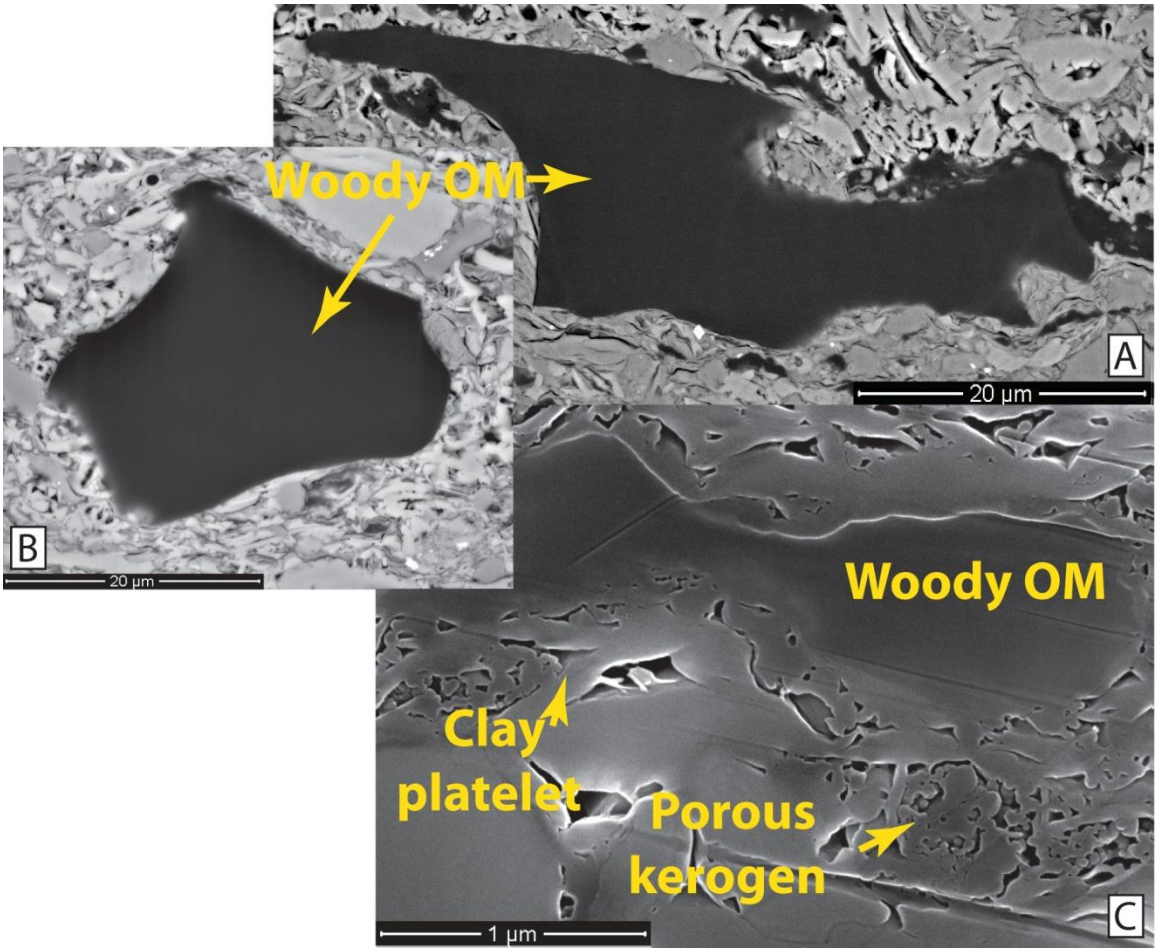

Figure 20: BSE and SE images of terrestrial OM including large (~3-40um), discrete particles of rigid OM grains with arcuate margins (A, B and C), and C) porous kerogen interworked with clay platelets interpreted as terrestrial with primary pores. Well 1 sample 11 (A) and Well 1 sample 19 (B&C).

INTRABASINAL GRAINS

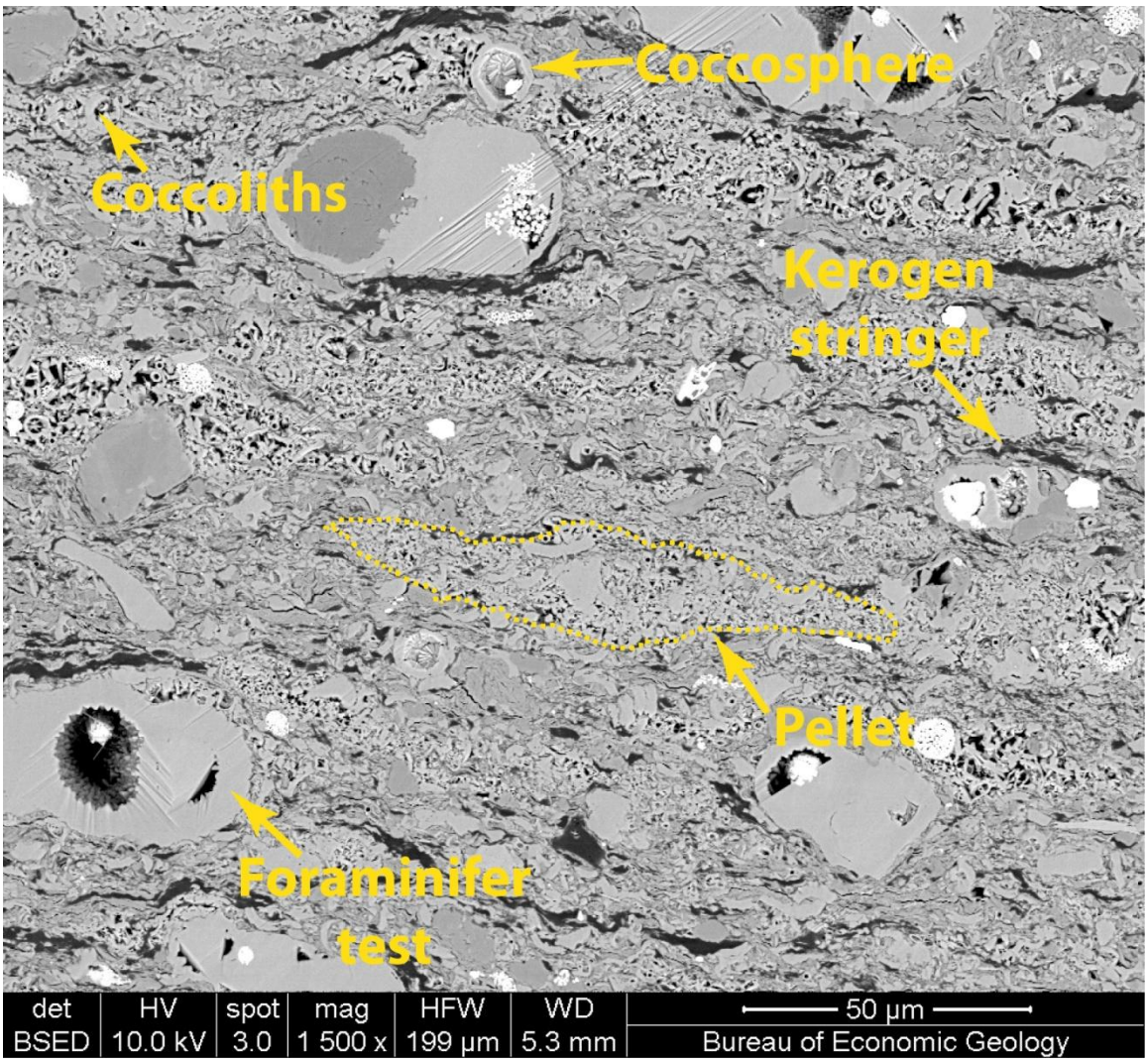

Figure 21: BSE image showing typical intrabasinal components including: coccolithic fecal pellets, foraminifer tests, coccoliths, coccospheres, and marine kerogen stringers. Well 1 sample 16.

Observed intrabasinal components composing a large portion of the detrital grain assemblage include skeletal debris and kerogen. At low maturity, intrabasinal components constitute between 50.6% and 66.1% of the bulk volume, including components of minor early cements (Tables 1 and 2). Carbonate skeletal debris is

dominantly coccolithic, although other calcareous allochems are present, including planktic and benthic foraminifer tests (mostly globigerinids), inoceramid fragments, echinoid fragments, and pithonellid calcispheres (Figures 13, 21, 22, 23, and 24). Irregular, ovoid-shaped aggregates of carbonate skeletal debris are abundant and interpreted as fecal pellets due to their shape, size, composition, and distribution (Honjo, 1976; Macquaker et al., 2010; Turner et al., 2002; Turner, 2002). Organomineralic aggregates are present in most samples (Figure 28). Siliceous and phosphatic skeletal debris are present in minor amounts.

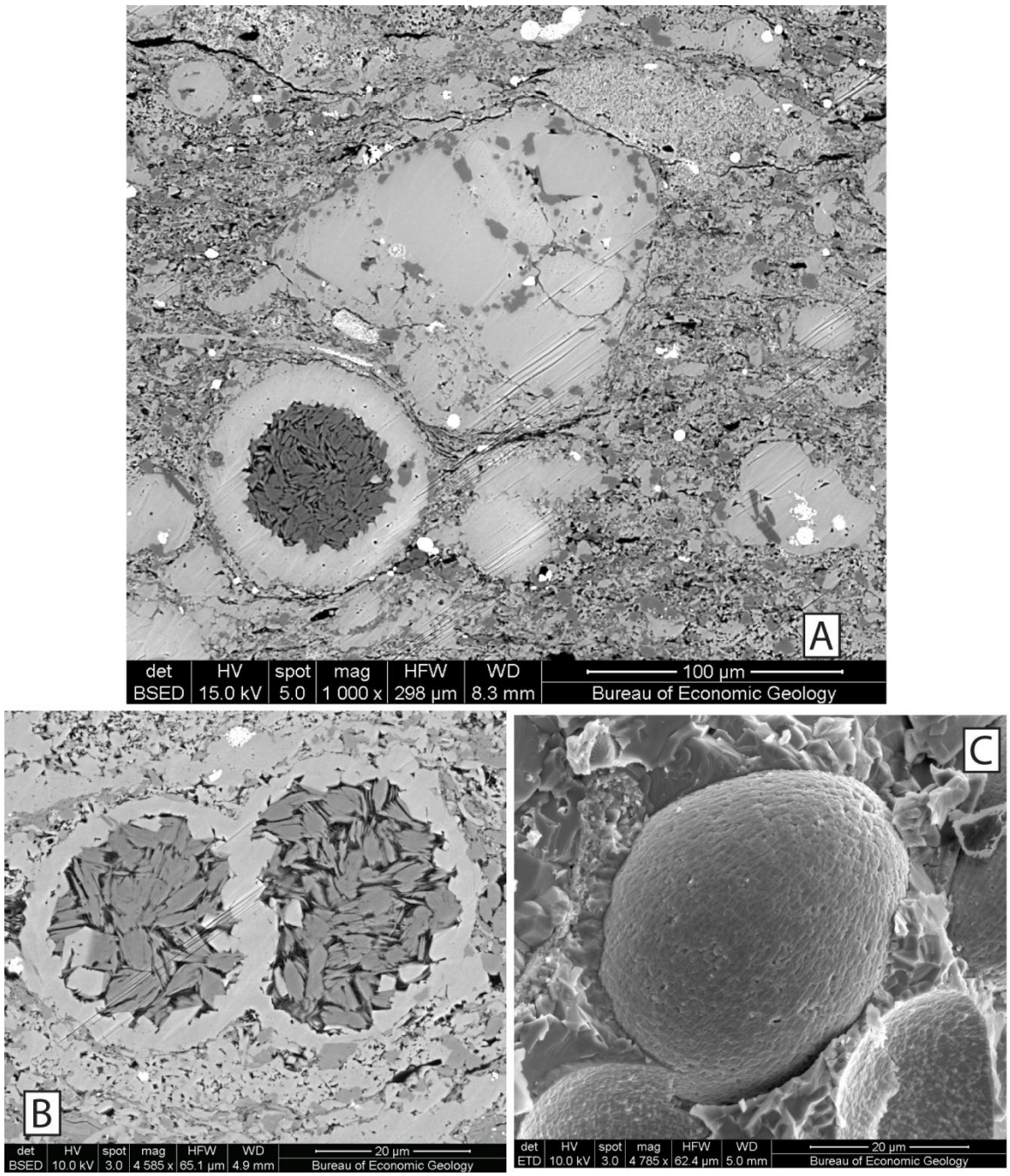
A
det HV spot mag HFW WD
BSED 15.0 kV 5.0 1 000 x 298 µm 8.3 mm
100 µm
Bureau of Economic Geology
B
det HV spot mag HFW WD
BSED 10.0 kV 3.0 4 585 x 65.1 µm 4.9 mm
20 µm
Bureau of Economic Geology
C
det HV spot mag HFW WD
ETD 10.0 kV 3.0 4 785 x 62.4 µm 5.0 mm
20 µm
Bureau of Economic Geology

Figure 22

Figure 22: BSE and SE images of foraminifers and a calcisphere. A) BSE image of biserial foraminifer with re-crystallized test, and calcite cement fill. Also single test chamber with diagenetic clay and bitumen fill. Note deformation of clays and OM between foraminifer tests (Well 3 sample 1-136), B) BSE image of foraminifer with authigenic clay and bitumen fill. Test is re-crystallized calcite (Well 4 sample 1-75), and C) SE image of pithonellid calcisphere, note characteristic egg-like shape and replaced test (quartz and calcite) (Well 1 sample 2).

Coccoliths and associated nannoliths compose a majority of the skeletal debris within the sample set and exhibit tremendous diversity. Coccolithic grains range widely in morphology and size. Coccolithic grain types include: intact coccospheres typically ~10µm - 20µm, disaggregated individual plates ~1-10µm in size, spines ~10-20µm in diameter, and indiscernible debris as small as ~100 nm (Figures 11B, 13, 21, 23, 24 and 25). Aggregates of coccolithic debris, likely fecal pellets, are present in some samples, hosting significant portions of porosity (up to 6.9% of the bulk volume) at low maturity (Table 4; Figure 21). In low-maturity samples, the majority of porosity is located between, or within, coccolithic grains (Table 4, Figure 62, 70 and 81). This occurrence is likely related to the irregular shape of coccolithic grains, chemical and physical stability, volumetric abundance and spatial proximity to other coccolithic grains.

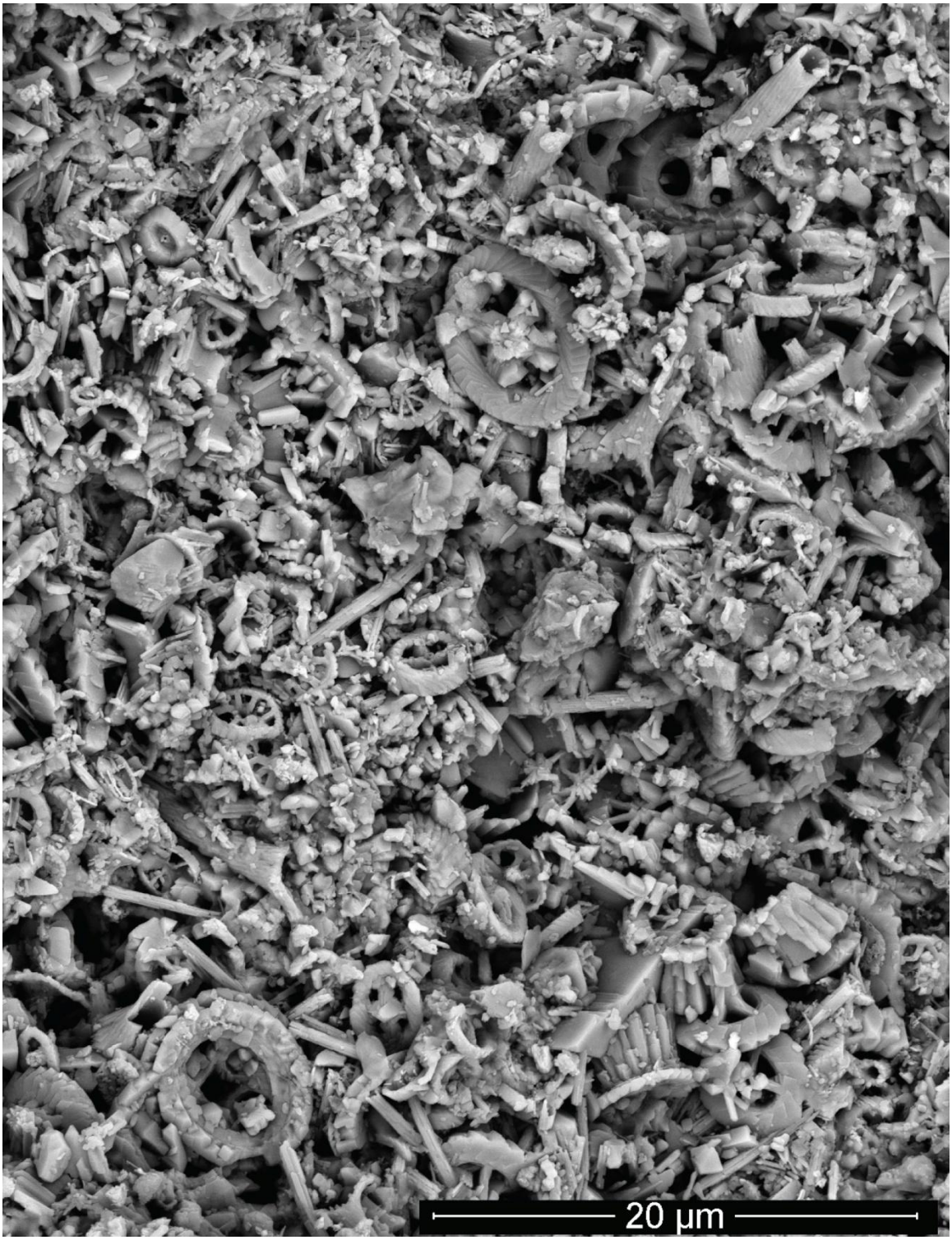

Figure 23: BSE image of coccolith and nannolith debris. Well 1 sample 11.

This study identifies more than 30 distinct heterococcolith and nannolith morphologies in low-maturity samples (Figure 25). A majority of these morphologies represent distinct species or families. However, individual species, e.g., *Lithastrinus floralis,* can show a wide variety of morphologies, a consistent observation with other datasets (Barrier 1980). Heterococcolith components are most common, and consist of circular to elliptical discs or rings containing one or more concentric radial arrays (cycles) of elaborate crystals-units (Bown 1998) (Figure 13, 25). Distinguishing characteristics include: plate shape, symmetry, characteristics of the central area, the number of cycles, size, and crystal unit habit (Haq & Boersma 1978). Identified types of coccoliths include: *Ellipsagelosphaera*, *Prediscospaera cretacea*, *Biscitum ellipticum*, *Watznaria barnesae*, *Cribosphaera ehrenbergi*, Zygodiscids, *Sollasites horticus*, etc. (Figure 25) (Bown, 1998; Haq & Boersma, 1978; Lord et al., 1982).

Nannolith forms include elongate rods with cylindrical or bladed habits that exhibit star-shaped, rhombohedral, or cross-shaped cross-sections (Figure 23 and 24). These are commonly observed as spines (rhabdoliths) and protrude from coccolith plates (Figure 23) up to ~20 μm in length, potentially as a defense mechanism against predators for the organism (Bown, 1998). Elongate crystals ~1μm in length exist as well, and are of an indistinct origin (Figures 23 and 24).

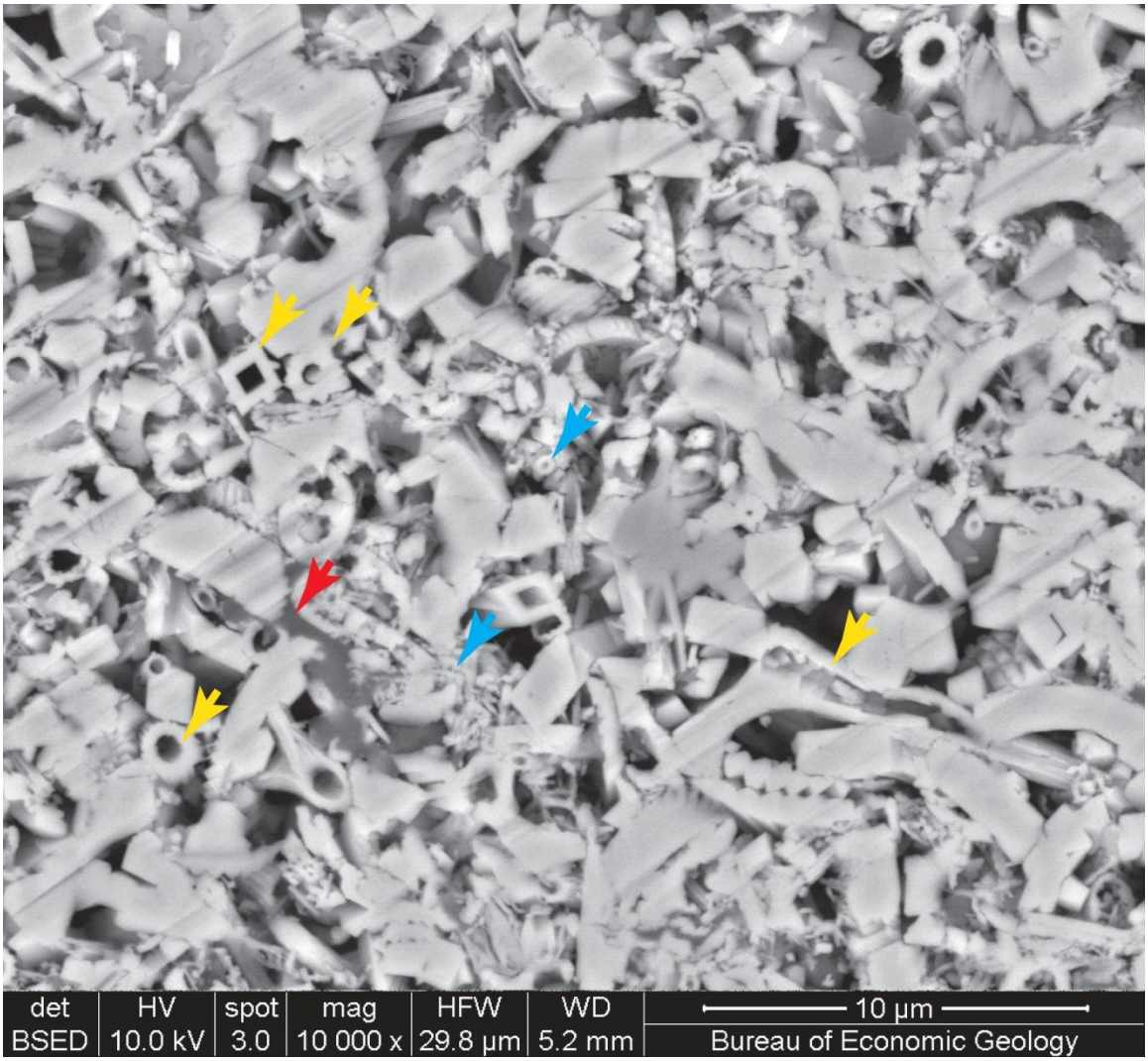

Figure 24: BSE image showing coccolithic debris within a skeletal carbonate aggregate. Abundant rhabdoliths with cirular, rhombohedral and star shaped cross sections (yellow arrows). Note abundant sub-micron skeletal debris (blue arrows) and intra-pellet kerogen smashed between coccolith grains (red arrow). Well 1 sample 8.

Family, Genera, or species		19B 81.3m	18B 88.8m	16B 98.m	11B 115.5m	8B 128.9m	4B 139.9m	2B 149.5m
Watznauria/ Ellipsa-gelsphaera	1	X	X	Ⓧ	Ⓧ	(?)	Ⓧ	X
Zygodiscus? *(Lord 113)*	2	X	X	X	X	X	X	X
Prediscosphaera cretacea (Lord 69)	3	X	X	X	X	X	X	X
Tubodisceae *(Lord 109)*	4	X	X	?	X	?	?	
Biscitum ellipticum (Lord 111)	5	X	Ⓧ	Ⓧ	X	X	Ⓧ	X
Lithraphraditeds carniolensis (Lord 68)	6	X	X	X	X	X	X	X
Actinozygus? *(Lord 71)*	7			X				
Stephanolithaceae Stradnerlihis?	8		X	X	X			
Stephanolithion lafitti (Bown 105)	9	X		X	X			?
Podorahabdus dietzmanni (Lord 103)	10				X			
Parhabdolithus angustus (Lord 69)	11				X			
Lithastrinus *(Lord 125)*	12				X			
???	13			X				
Staurolites ellipticus? (Lord 117)	14			X				
Cribrospaera ehren-bergi (Lord 119)	15			X	?	?		
Corrolithion?	16		X	X				
Chasmolithos?	17		X	X				
???	18			X				
Sollasites horticus (Lord 71)	19		X	X				
???	20	X		X				
Stradnerlithus geometricus?	21			X	X			
Rhagodiscus?	22			X	X			
Eiffelithus *(Lord 117)*	23			X	X			
MORE		1	3	9	4	0	0	1

Well #1 Coccolith and Nannolith Diversity

Figure 25

Figure 25: Biostratigraphic checklist of some observed coccolith morphologies within Well 1, where minimal cementation of coccolithic grains has occurred. Interpreted family, genera or species of observed coccolith morphology is plotted against sample name and depth, with occurrence of individual coccolith or nannolith noted as an X and occurrence of an intact coccosphere noted as an O. Question marks indicate uncertainty in observation and coccolith type. Data based primarily off of broken surface imaging at wide angle with high-pixel count (Figure 23).

Non-calcareous skeletal fragments, in particularly radiolarian debris, were identified by characteristic shape, and replacement by pyrite and early calcite cement (Figure 26).

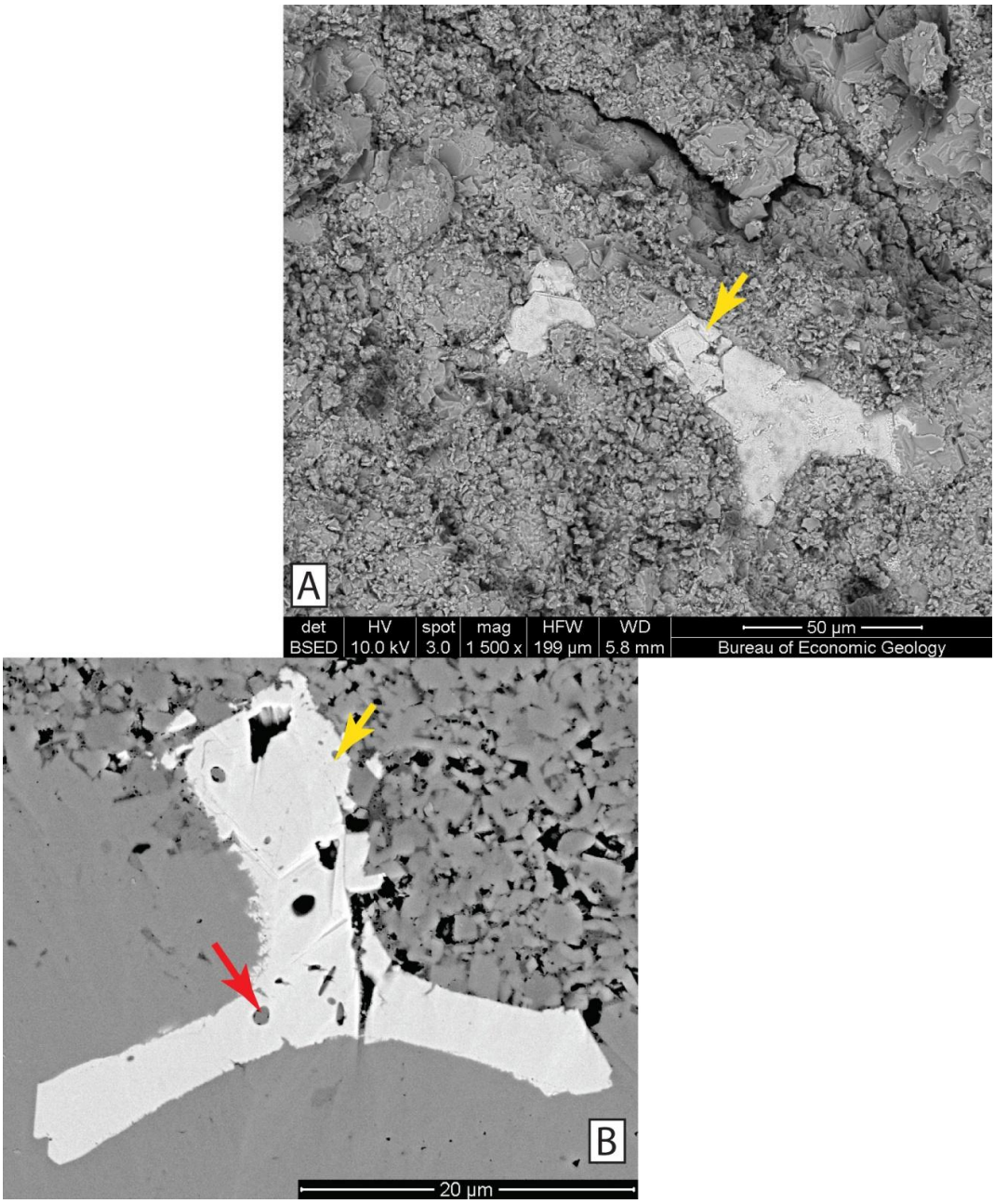

Figure 26: BSE images of possible replaced radiolarian spines (yellow arrows). A) Broken surface image showing possible spine with calcite and sparry calcite replacement and B) possible spine replaced with pyrite. Note inclusion of mineral phase (red arrow). Well 4 sample 1-80.

Phosphatic skeletal debris is present as a minor component in most samples, occurring as both large, elongate bone fragments and smaller grains (Figure 27). Bone fragments show a distinct banded microstructure, often retaining an elongate shape, and a phosphate EDS signal and can host minor primary intraparticle porosity (Figure 27).

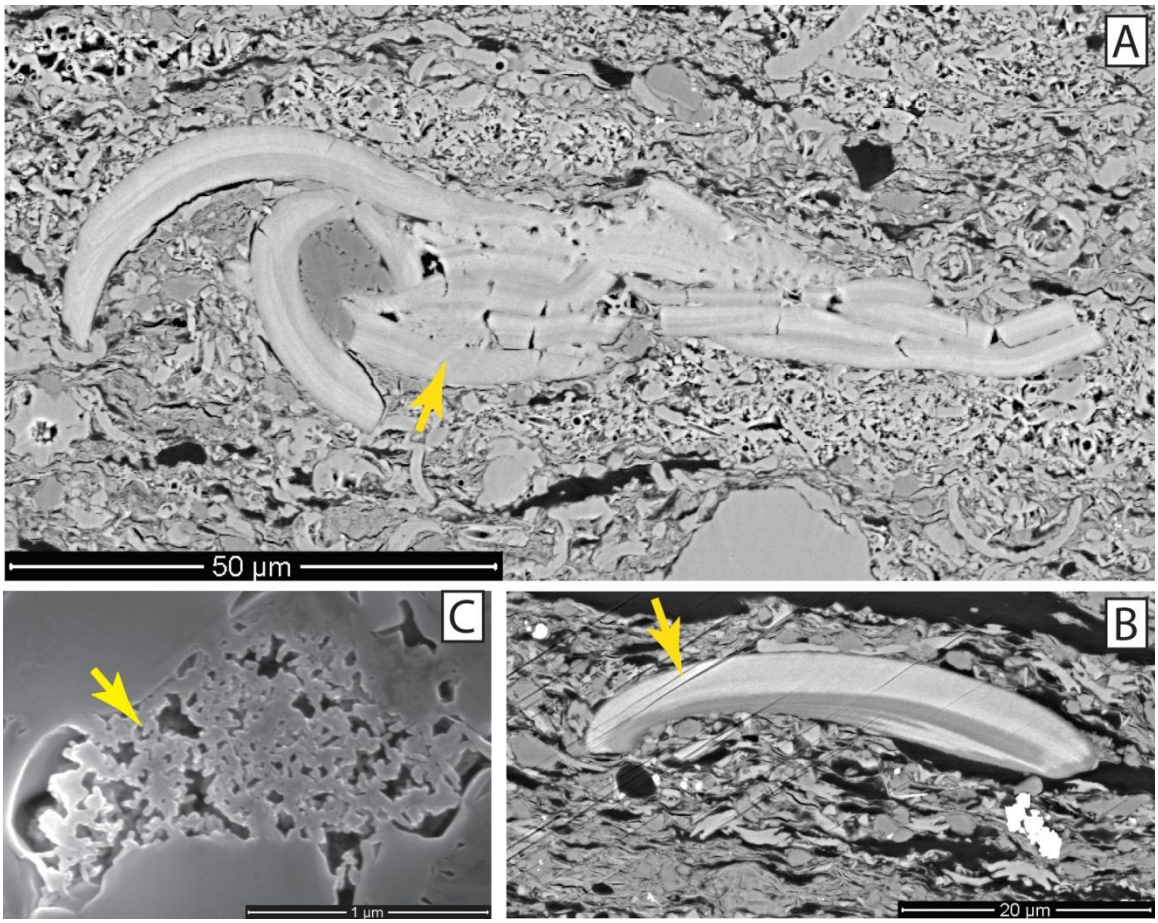

Figure 27: BSE and SE images of phosphatic skeletal debris. Note: elongate grain shape and banded microstructure in A and B and intra-particle porosity within phosphatic grain in C. Well 1 sample 16 (A), Well 1 sample 1 (B), and Well 1 sample 8 (C).

Marine kerogen is present in all samples, in varying amounts. Marine kerogen occurs commonly as: large discrete spatially isolated kerogen stringers, small stringers

interstitial with clay and/or other grains, organomineralic aggregates, and non-distinct OM filling intergranular space (Milliken et al., 2014; Macquaker et al., 2010) (Figure 19 and 28). Detrital marine kerogen is identified by its morphology, dark BSE signal, amorphous structure, and sometimes size and spatial isolation. Marine kerogen is easily identified in exemplary cases, especially in low-maturity samples, however a large proportion of OM in these samples is of an ambiguous origin, lacks discrete particle margins and fills inter-granular space at both low and high maturity.

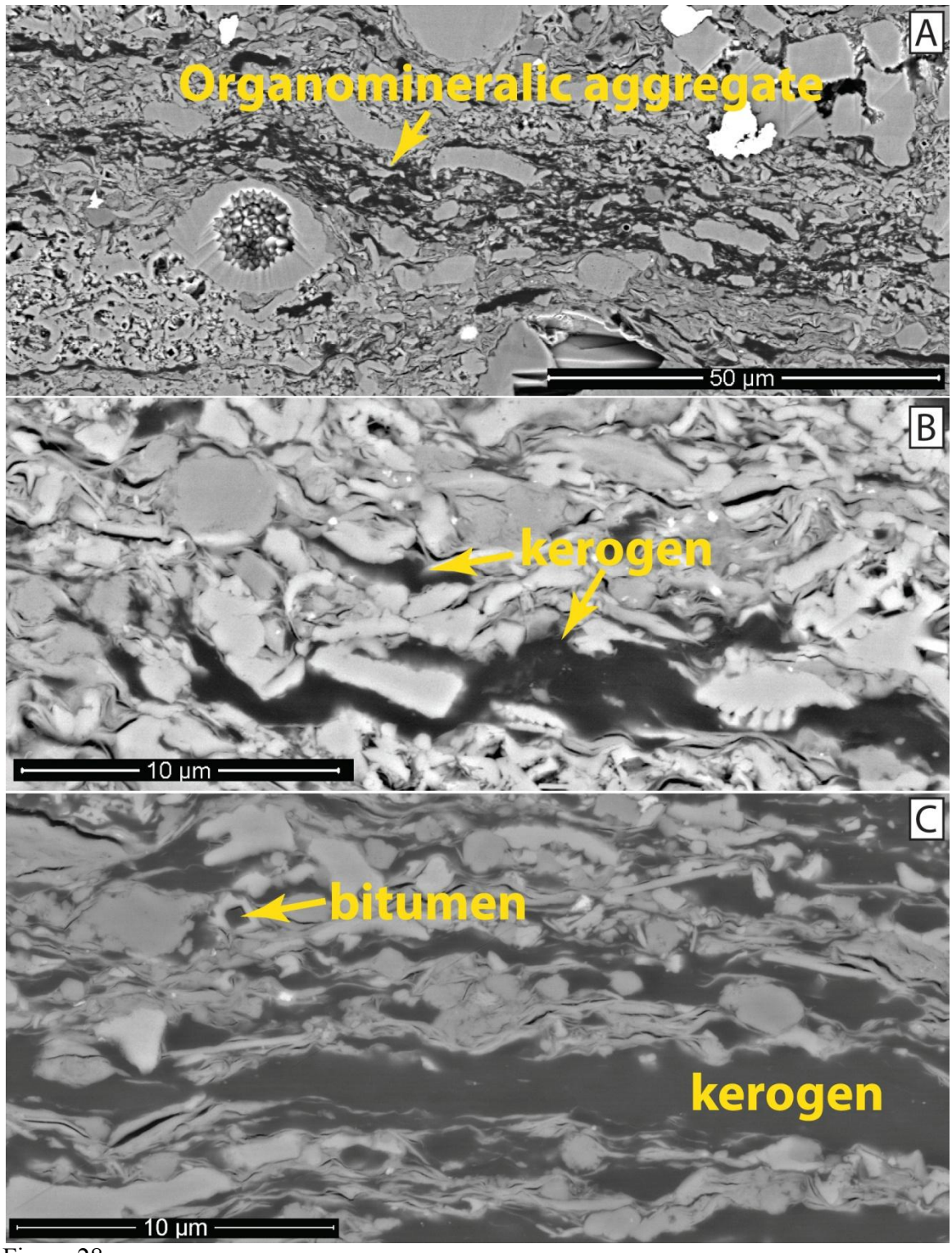
A
Organomineralic aggregate
50 µm
B
kerogen
10 µm
C
bitumen
kerogen
10 µm
Figure 28

Figure 28: BSE images of marine kerogen. A) organomineralic aggregate consisting of a large stringy kerogen particle with included mineral debris (Well 1 sample 16). B) Stringy kerogen mashed between coccolithic grains, and smaller bits of non-discrete kerogen intermixed with matrix components (Well 1 sample 16). C) Large kerogen stringers, non-discrete OM makes up much of the matrix (>30%), bitumen fills intra-particle pores (Well 1 sample 1).

Diagenetic Processes and Components

Diagenetic processes and components are a major control on reservoir quality. Cementation, compaction, maturation of OM, dissolution, and replacement are all processes that influence the character and abundance of porosity within the sample set. These processes occur throughout burial history ranging from syn-depositional, to deep burial diagenetic environments. The following presents an assessment of diagenetic components and processes observed at a pore scale within samples across thermal maturity.

AUTHIGENIC MINERALS

Calcite, quartz, pyrite, kaolinite, and apatite occur most commonly as pore-filling cements, but can also occur as replacements of detrital grains (Figures 29-45). Dolomite and albite most commonly occur as replacements in both low maturity and high-maturity samples. Mg-bearing phyllosilicate is interpreted here as a replacement of kaolinite in high-maturity samples. Sphalerite and celestite are observed in the low maturity well samples. Titanium dioxide, most likely anatase or possibly detrital rutile, occur in trace amounts within many of the samples.

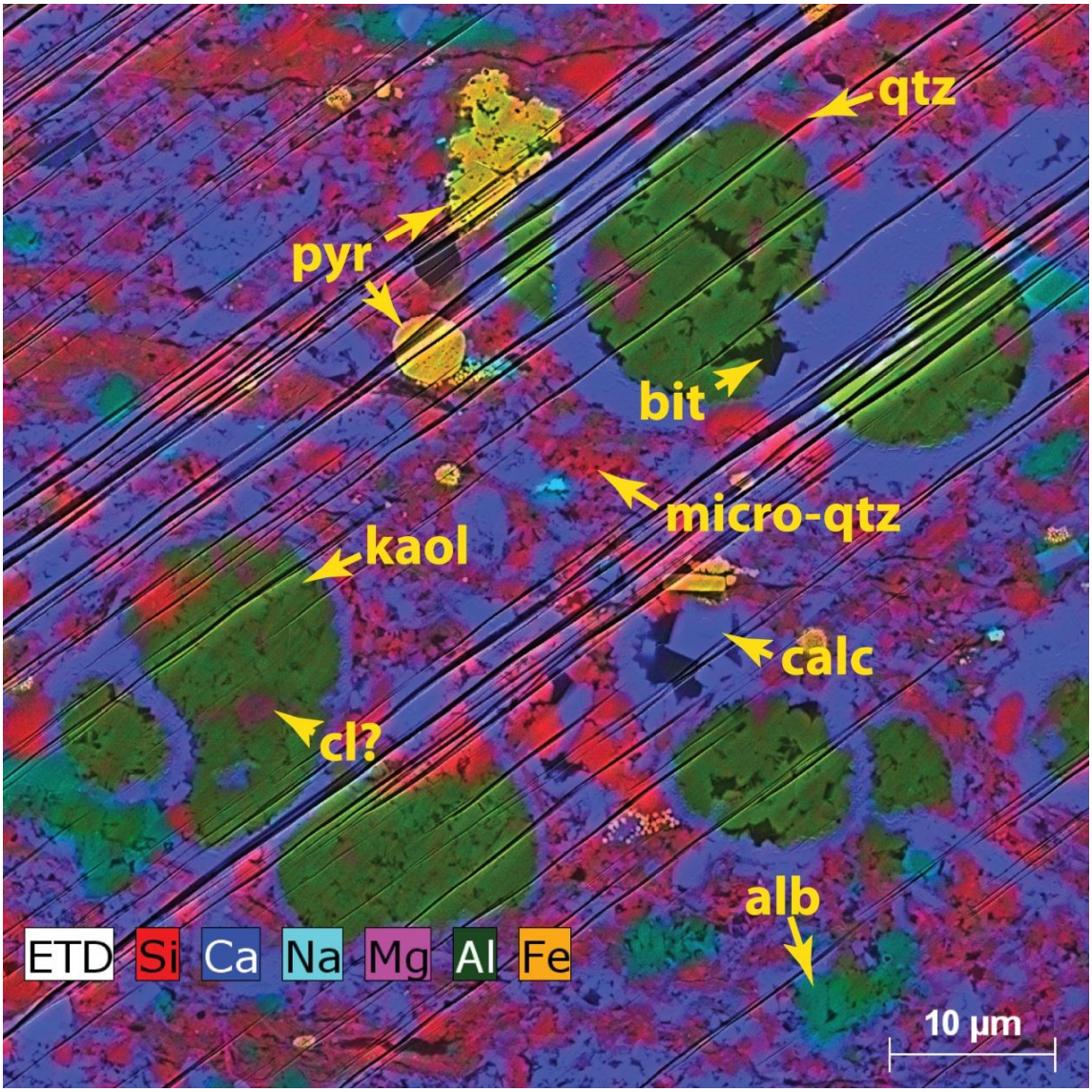

Figure 29: EDS map showing authigenic cement and replacement phases including: framboidal, euhedral and replacement pyrite (pyr), micro-crystalline quartz (micro-qtz), albite grain replacement (alb), rhombohedral calcite crystals (calc), kaolinite booklets (kaol), Mg-bearing phyllosilicate (cl?). Bitumen (bit) is present as well. Well 4 sample 1-123.

Syn-Depositional & Early Burial Cementation

Pyrite occurs in all samples most commonly as euhedral crystals and/or framboids. These crystals are dispersed throughout the rock matrix and rarely form as a replacement mineral (Figures 26, and 29). Pyrite precipitation results from the reaction of sulfide (S^{2-}) with Fe (II) in sediment pore space and Fe (III) produced by bacterial reduction (Berner, 1970; Berner, 1985). Pyrite morphology provide information on geochemical and environmental conditions during precipitation, such as oxygenation, sedimentation rate and OM reactivity (Lovley, 1991; Passier et al., 1997; Suits, 1998; Taylor and Macquaker, 1999; Wignall and Newton, 1998; Wilkin et al., 1996). Precipitation during deposition or very early burial is suggested by: interparticle pores between pyrite particles, and OM and clay particles bent or draped around pyrite particles (Figure 30). Pyrite framboids occur within foraminifer tests, suggesting precipitation from early pore water (Figure 30A, 30C, 46). Micron-scale crystals occur scattered throughout the matrix in addition to filling primary pore spaces (Figure 30). Pyrite precipitation pre-dates bitumen, and pre-dates or precipitate synchronously with early kaolinite and calcite (Figure 30, 45, and 46).

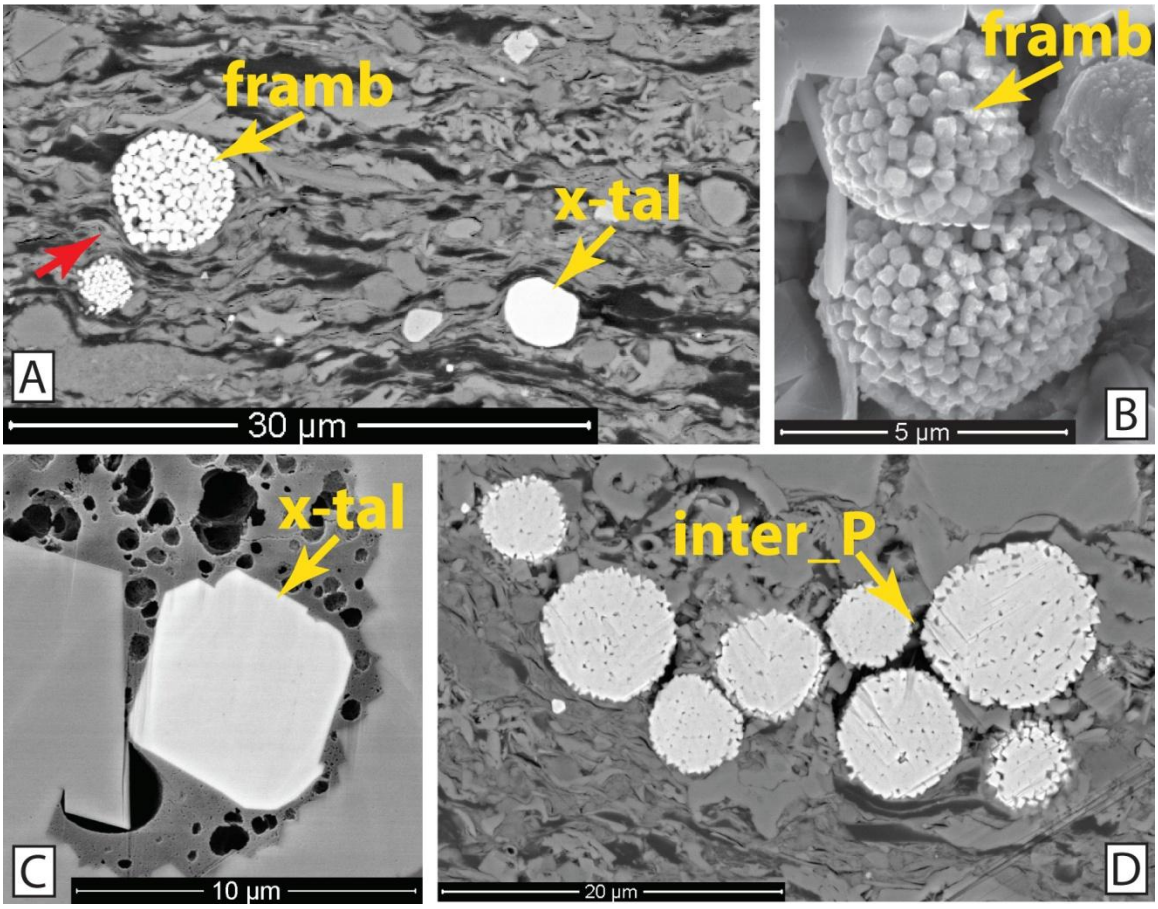

Figure 30: BSE and SE images of pyrite cement morphologies including: A) BSE image showing isolated euhedral pyrite crystal (x-tal), and pyrite framboids (fram) (Note: OM and clay platelets bent around pyrite particles (red arrow), B) SE image showing pyrite framboid within foraminifer test, C) BSE image showing euhedral crystal within foraminifer test, and D) BSE image showing pyrite framboids with inter-framboid porosity (inter_P). (Well 1 sample 1 (A), Well 1 sample 23 (B), Well 4 sample 1-80 (C) and Well 1 sample 11 (D).

Early-formed calcite occurs in all samples as isopachous microspar, displaying equant crystals inside foraminifer tests. They can also form poikilotopic crystals in large, primary pores and appear as a replacement of unstable skeletal debris such as radiolarians and calcispheres (Figure 31). Coccolithic debris is relatively inert, and shows little to no associated cementation within low-maturity samples.

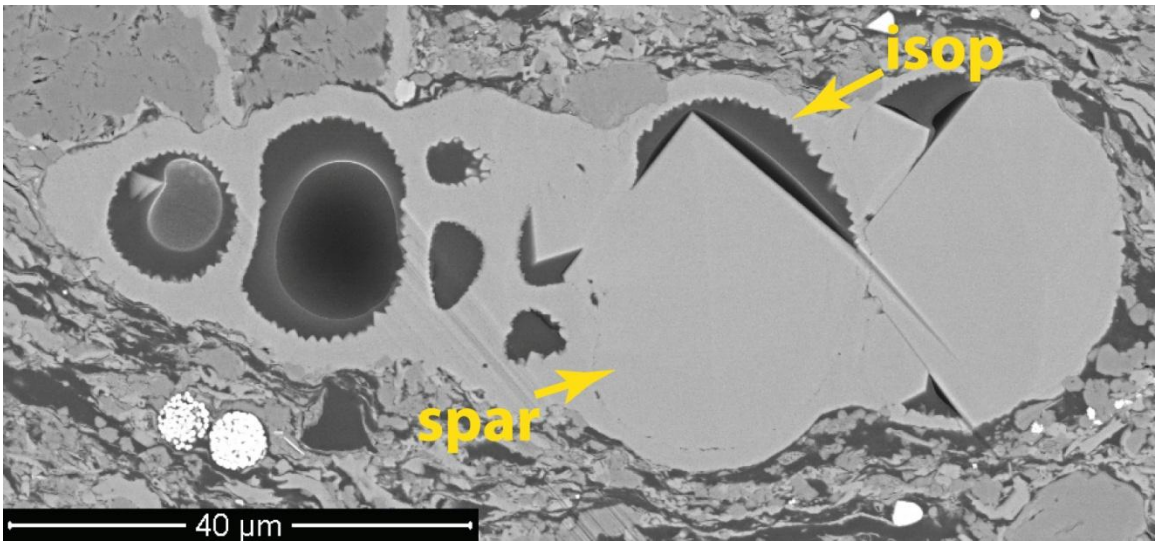

Figure 31: BSE images illustrating early calcite cements including: isopach microspar (isop) and large, sparry calcite crystals in-filling primary intra-particle pores of a foraminifer test. Primary intraparticle pore space has been filled with bitumen after the precipitation of calcite cement. Well 1 sample 4.

Dolomite occurs in small amounts, ranging from 0.0% to 5.7% of the bulk volume and averaging ~1% in Well 1 and Well 4. Dolomite occurs as: isolated euhedral crystals, replacement of foraminifer tests and other grains, and as crystals within foraminifer tests (Figures 32, 36). It is identified by its Mg and Ca EDS signals, and distinctive crystal habit. Crystals are euhedral and can appear partially weathered, forming "patchy" partial replacement zones with calcite (Figure 32). Dolomite is likely organogenic, as noted in other OM-rich mudrocks (e.g., Barnett Shale) and OM-rich modern sediments (Mazzullo, 2000; Milliken et al., 2012).

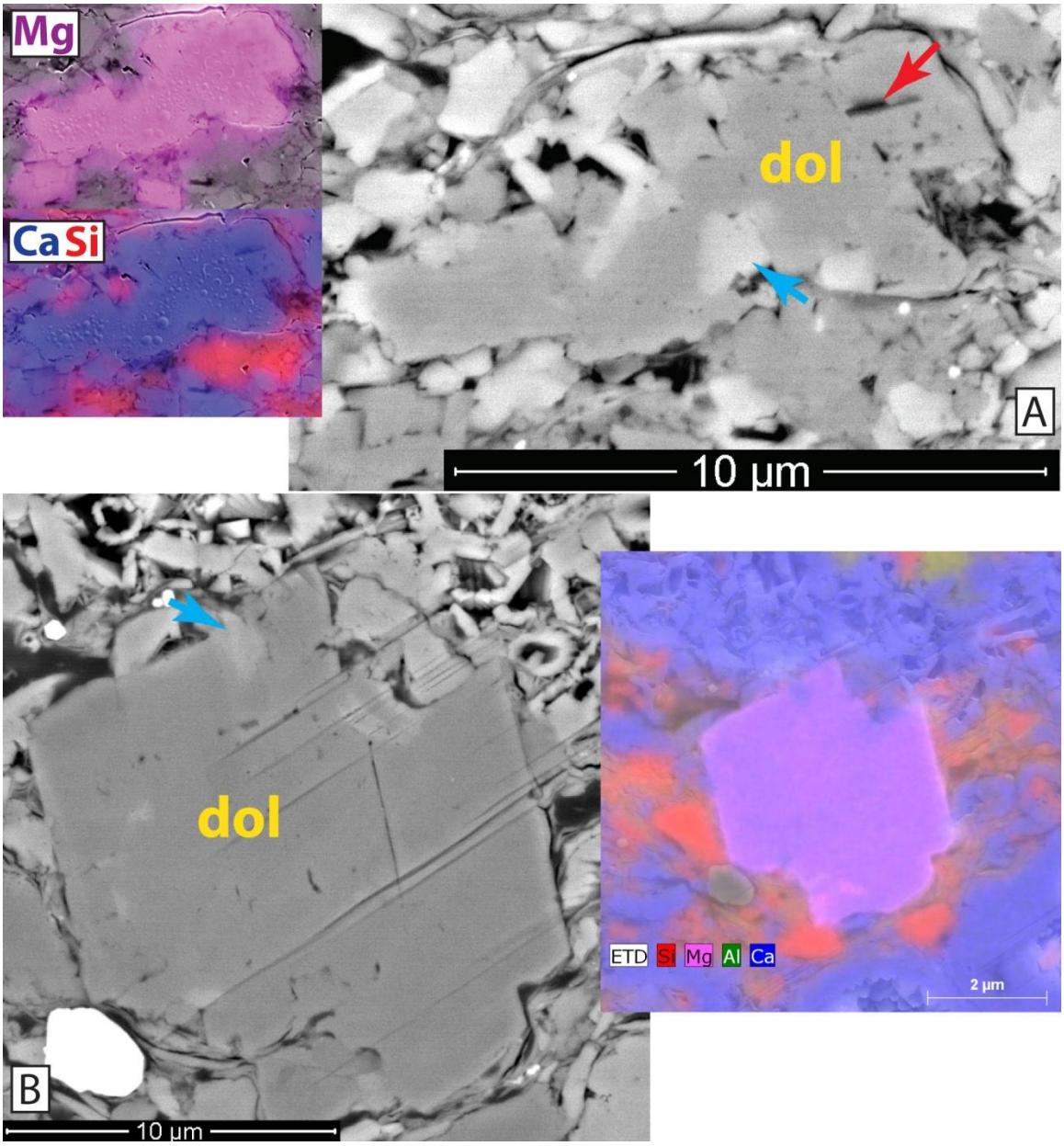

Figure 32: BSE images and EDS maps of corresponding areas showing dolomite crystals distinguishable by distinct rhombohedral shape and cleavage, dissolution along cleavage planes (red arrow). Note: remnant calcite within dolomite (blue arrows) indicative of partial dolomitization. Well 4 sample 1-5 (A) and Well 1 sample 8 (B).

Kaolinite occurs in many samples at both low and high maturity, most commonly filling intraparticle pores within foraminifer tests. Less commonly, kaolinite can occur within inter-particle pores and filling pore space within bent muscovite platelets (Figures 17 and 33). Kaolinite occurs most commonly as stacked "books" of pseudo-hexagonal platelets ~4 μm in diameter, displaying strong Al and Si EDS signals (Figure 17 and 33). Precipitation of kaolinite occurs relatively early, before bitumen infill and contemporaneously to after early calcite spar. Foraminifer test with cement fills show a lack of compactional collapse, suggestive of an early origin. Kaolinite genesis is likely related to alteration of volcanic ash composed of unstable smectitic bentonites, or due to the weathering of feldspars and other Al-rich silicates in an organic-rich environment under early burial conditions (Deer et al., 1992; Pevear, 1991; Pollastro, 1981).

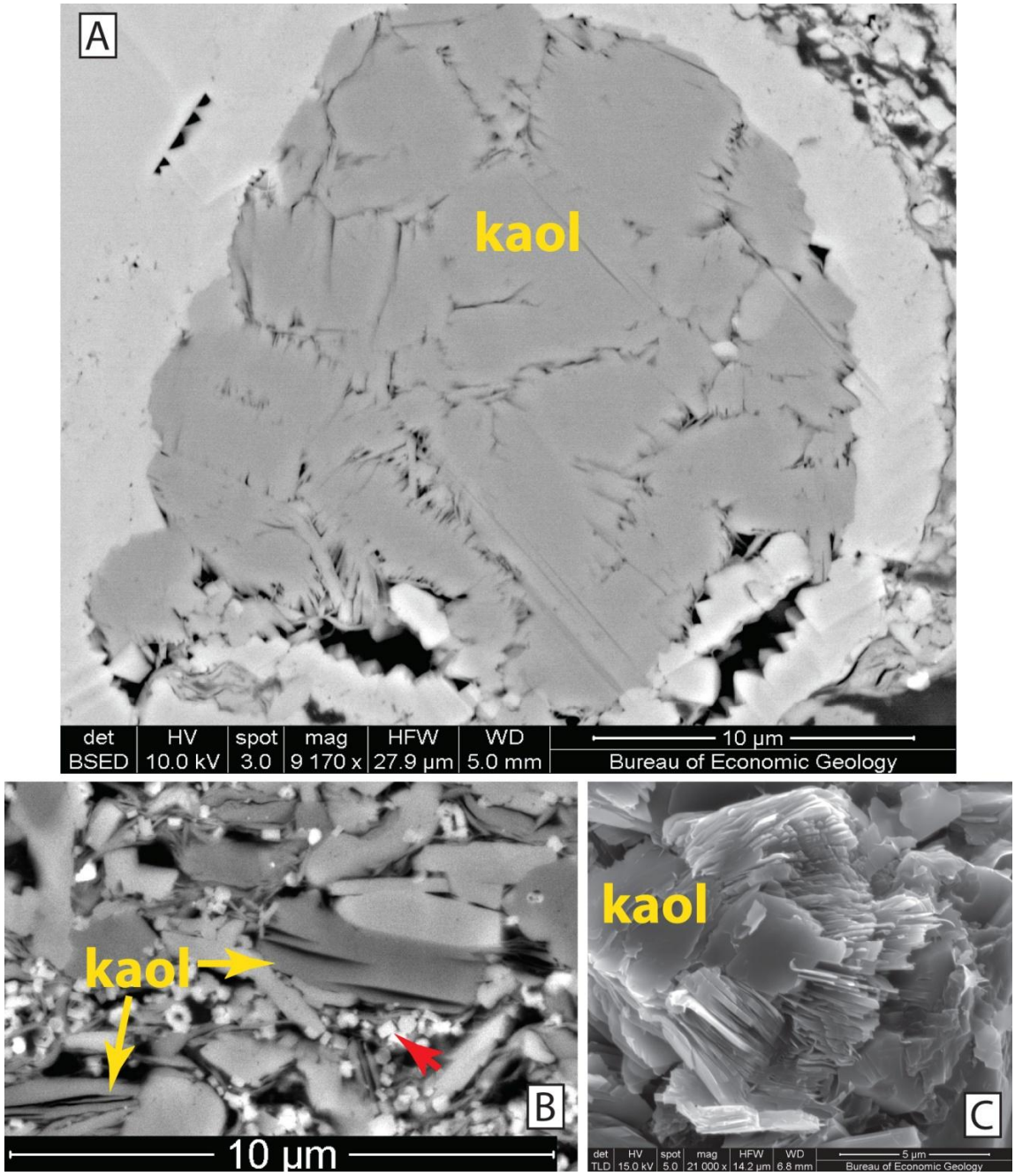

Figure 33: BSE and SE images showing authigenic cement habit. A) BSE image of polycrystalline kaolinite booklets filling foraminifer test. B) BSE image of kaolinite booklets filling inter-particle pore space. Note micro-crystalline apatite (red arrow). C) SE image of kaolinite in broken surface sample. Well 1 sample 11 (A), Well 3 sample 1-136 (B), and Well 1 sample 2 (C).

Late Burial Cementation

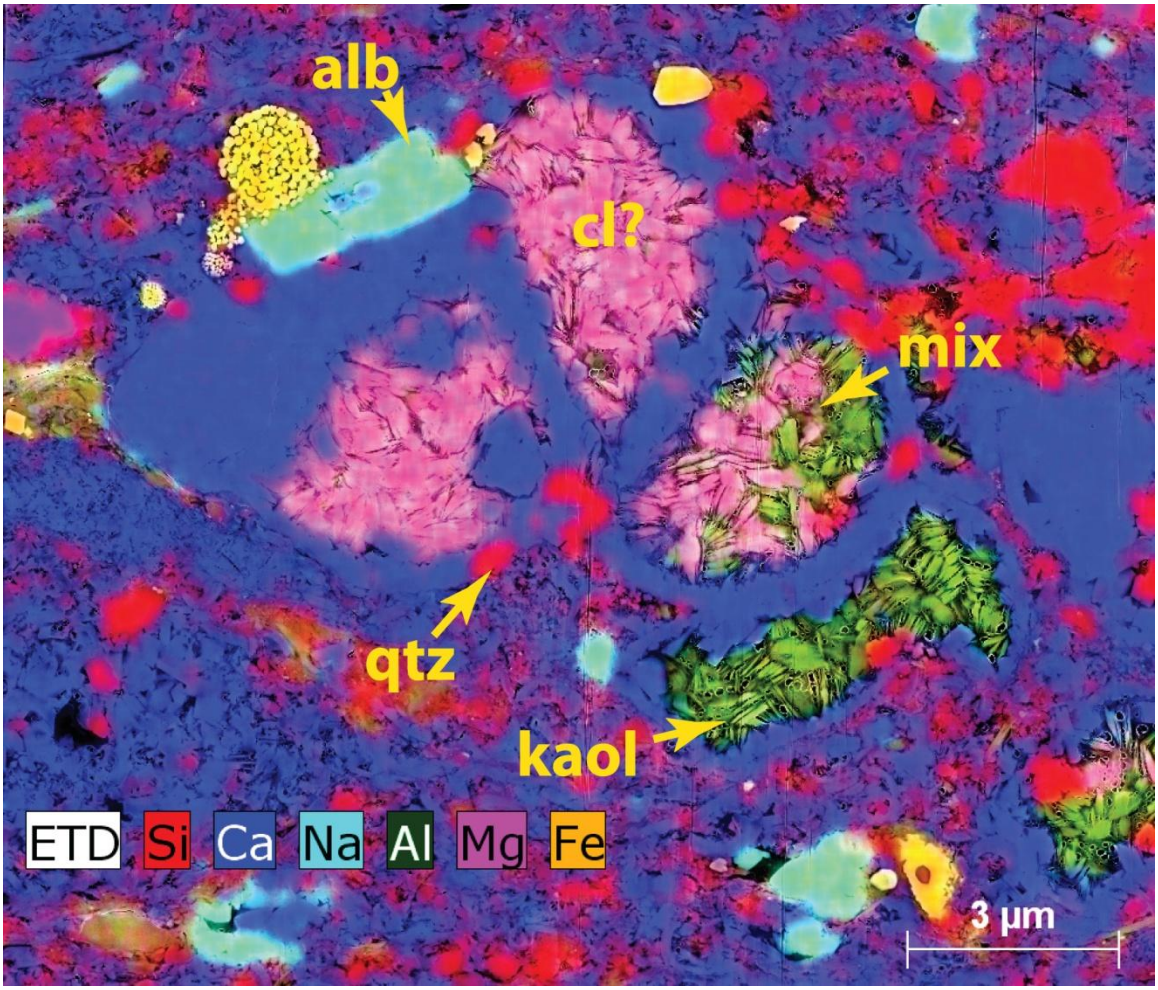

Figure 34: Example of common authigenic phases at high maturity, including; quartz crystals interstitial to the matrix and replacing foraminifer test, kaolinite partially altered to Mg-bearing phyllosilicate (cl?), albite occurring large grain-replacing crystals. Sample Well 4 sample 1-90.

An unidentified Mg-bearing phyllosilicate is present in many of the high-maturity samples. Mineralogy is most likely the chlorite group Mg end-member clinochlore, but there are many other possibilities such as palygorskite or amesite (Deer et al., 1992). Only Mg, Al, and Si were present in the EDS spectra (Figure 39), distinguishing the mineral from ubiquitously iron-rich chlorite in Gulf Coast sediments (Ahn and Peacor,

1985; Burton et al., 1987). Its distribution, occurrence, and habit are typically similar to that of kaolinite, and it is distinguished compositionally by the presence of Mg, as observed in EDS spectra and maps and by a slightly darker BSE signal (Figure 34, 35, 36, and 39). The Mg-bearing phyllosilicate occurs most commonly as stacked “books”, possibly pseudomorphic to kaolinite with more "frayed", irregular, and tapered plate ends (Figures 34, 35, and 39). Intimate and "spotted" co-occurrences with kaolinite are observed in three samples (Figure 34). In two high-maturity samples, this mineral occurs as a replacement associated with dolomite and mimics the crystalline shape of the replaced particle (Figure 36).

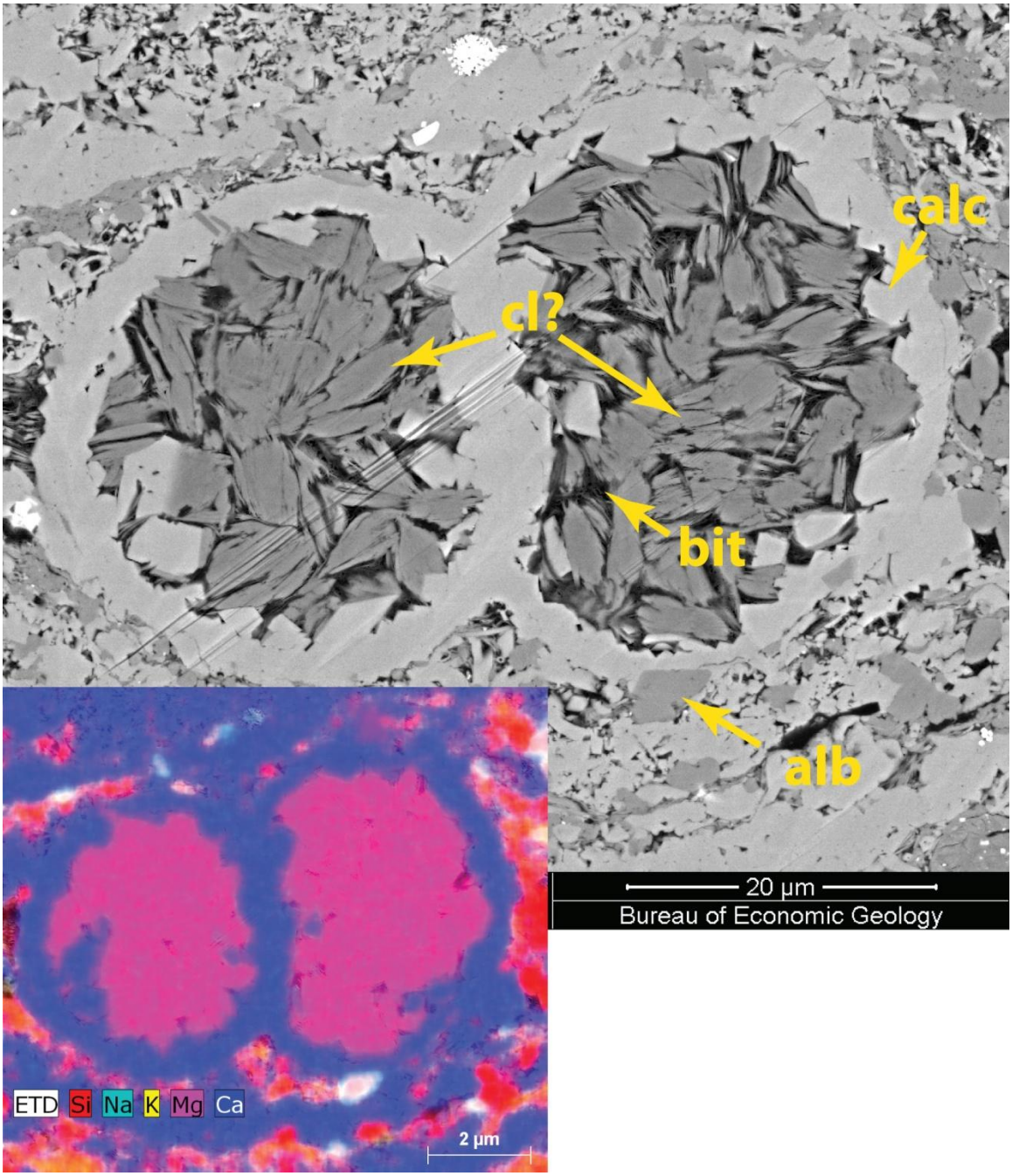

Figure 35: BSE image and EDS map of corresponding area showing re-crystallized foraminifer test, Mg-bearing phyllosilicate and later bitumen infill. Note: albite crystal partially replacing foraminifer test. Well 4 sample 1-75.

It is unclear if this mineral is precipitated with, or as an alteration product of, kaolinite. Other Gulf Coast studies have documented an inverse relationship of chlorite and kaolinite with depth (Burton et al., 1987). Bjorlykke and Aagaard (1992) suggest that chlorites appear to form from a kaolinitic precursor in North Sea siliciclastic rocks. Burton et al. (1987) documented kaolinite and iron-rich chlorite precipitation from fluid, and iron-rich chlorite as a pseudomorph after quartz in Gulf Coast sediments. The research also argued that the intermixture of chlorite and kaolinite along with the pseudomorphous habit of chlorite is suggestive of the chlorite replacement of kaolinite. However, both the chemical reaction producing chlorite from kaolinite and the reaction in which chlorite is generated by illitization, are driven by iron, an element not present in this mineral. Additionally, this reaction is reliant on the intermediary mineral phase berthierine, which is also not present (Ahn and Peacor, 1985; Burton et al., 1987). Regardless of mineral nomenclature and reaction pathway, an excess of magnesium would have to be present to alter kaolinite in our sample set. It is also possible that occurrence of this mineral only in down-dip wells could reflect chemical variability in marine and/or early burial pore waters, suggesting that kaolinite and Mg-bearing phyllosilicate co-occur and were precipitated directly from solution.

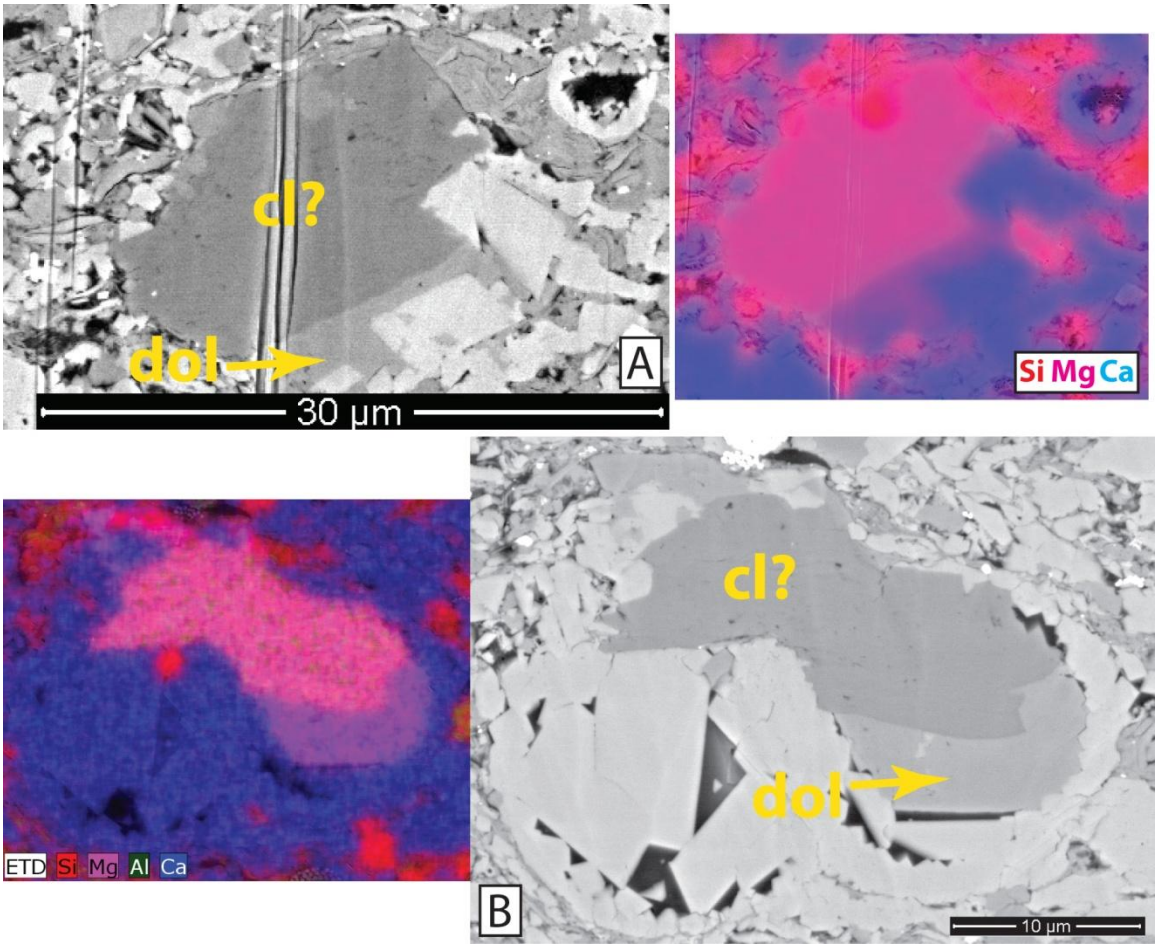

Figure 36: BSE images and EDS maps of corresponding areas showing Mg-bearing phyllosilicate replacement and associated dolomite. Note: shape of clay cement mimics replaced particle. Well 4 sample 1-75 (A), and Well 4 sample 1-100 (B).

Calcite overgrowths and re-crystallization are abundant in high-maturity samples and occur as interlocking rhombohedral overgrowths and as a replacement of carbonate skeletal debris (Figures 37, and 83-85). Calcite cementation appears to most strongly affect the more coccolithic and calcite-rich samples, suggesting it the process is strongly destructive of inter-particle porosity. Carbonate aggregates at high maturity show extensive calcite cementation (Figure 37). Paragenetically, extensive calcite cementation

occurs as a relatively late process throughout deep burial, similar to trends observed in "chalks" (Adelseck et al., 1973; Mapstone, 1975; Scholle, 1977).

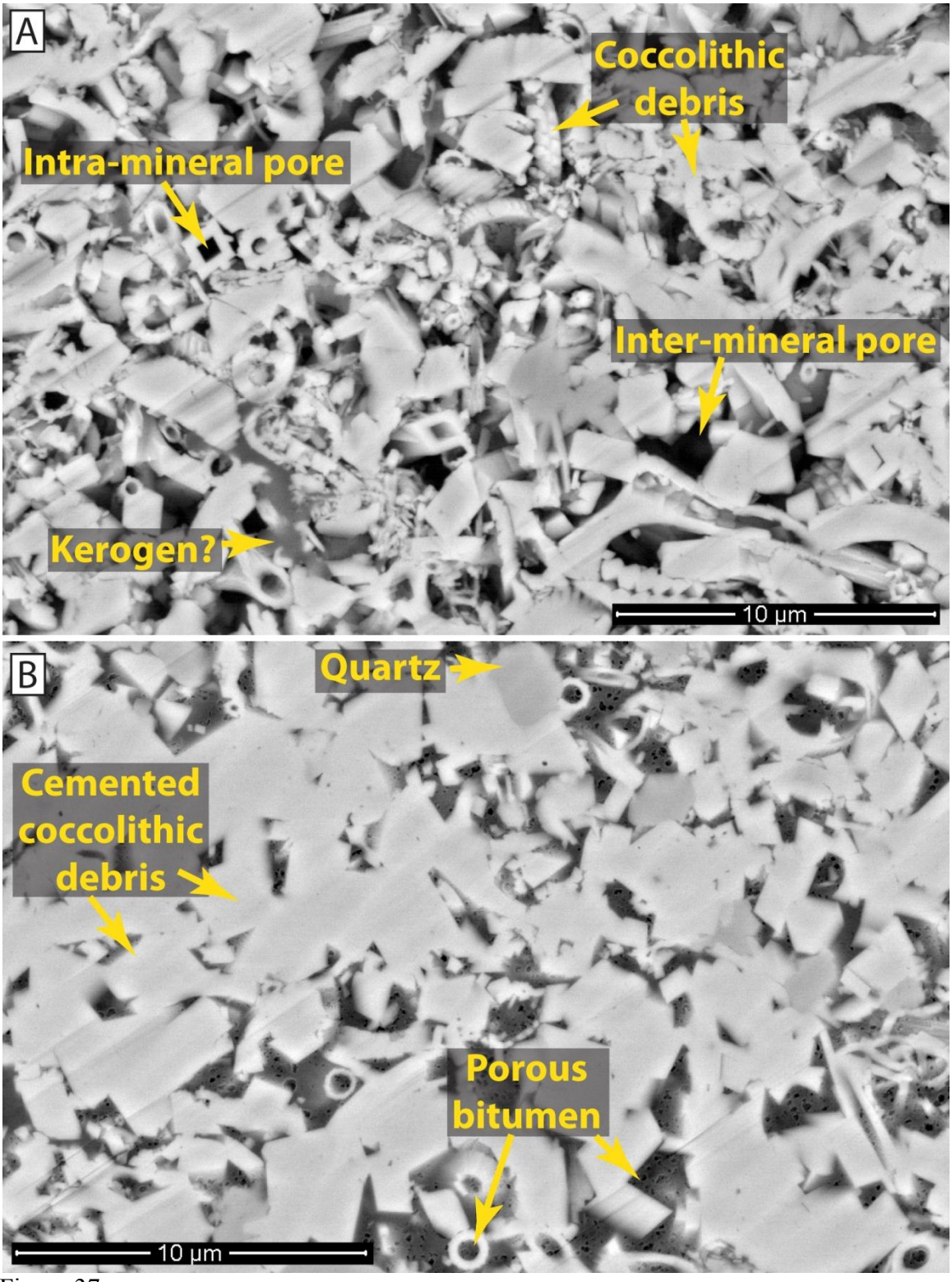
A
Coccolithic debris
Intra-mineral pore
Inter-mineral pore
Kerogen?
10 µm
B
Quartz
Cemented coccolithic debris
Porous bitumen
10 µm
Figure 37

Figure 37: BSE images at similar magnification and lithotype showing coccolith debris within carbonate aggregates. A) Low maturity showing distinct, diverse coccolithic grains, inter-coccolith pores, and intra-rhabdolith pores. OM present as isolated patches compacted between grains interpreted to be marine kerogen because of spatial isolation and apparent deformation by compaction between coccolithic grains Well 1 sample 8. B). High-maturity sample showing coccolithic debris with intergrown, uniformly shaped, rhombohedral calcite-cement. Nano-porous OM pervasively distributed between and within grains and cement interpreted as bitumen because it coats authigenic mineral growth, fills interparticle pores, and pervasively fills pore-shaped spaces Well 4 sample 1-75.

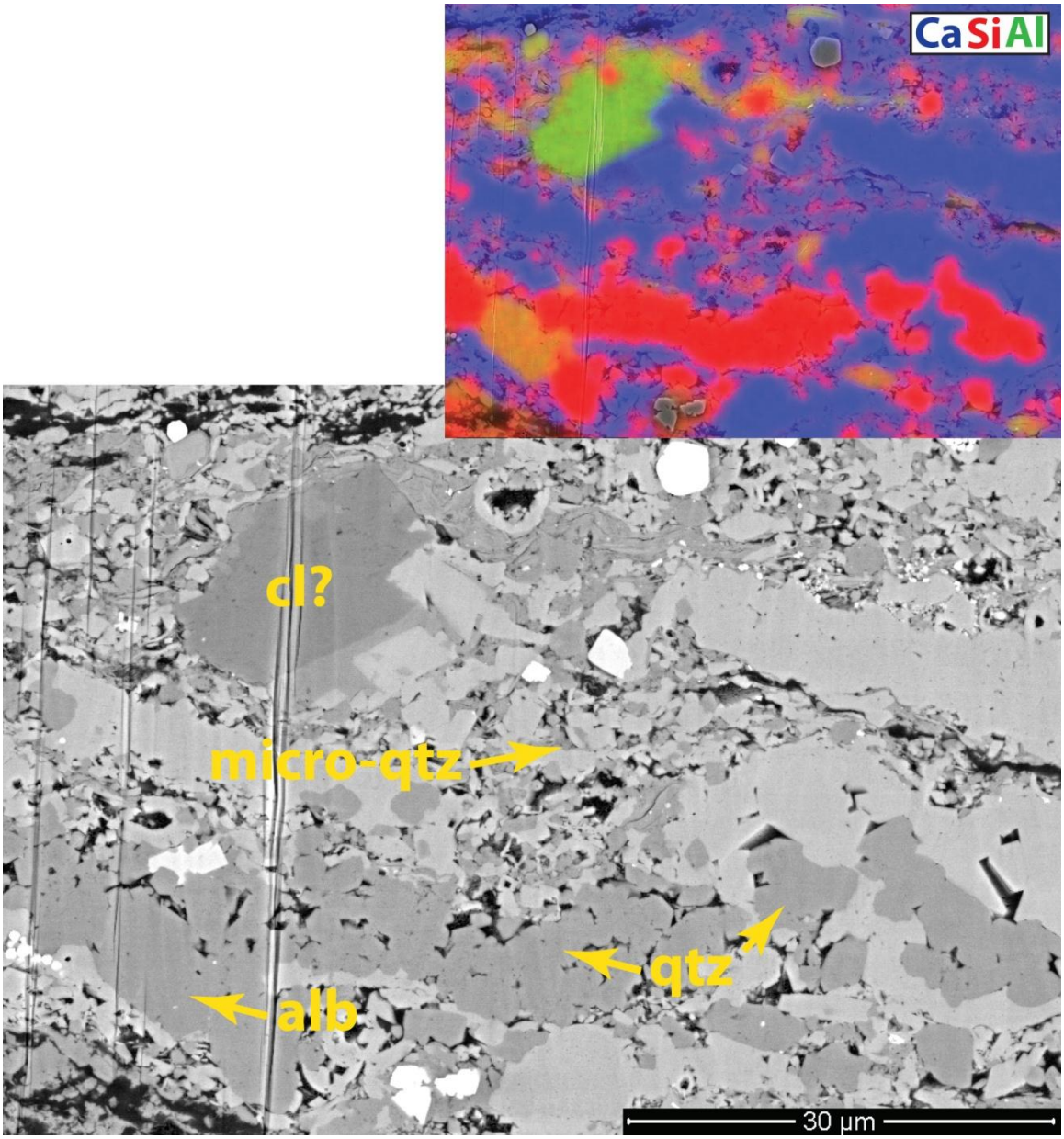

Figure 38: EDS map and BSE image showing euhedral micron scale quartz crystals (qtz) filling primary intraparticle pore space within foraminifer test, albite, Mg-bearing phyllosilicate replacing dolomite. Well 4 sample 1-75.

Quartz cement occurs to a minor degree within low maturity-samples but is extensive within most high-maturity samples. At high maturity, 14.5% of the bulk

volume is quartz, the majority of which appears to be authigenic (Table 2; Figures 38 and 43). Authigenic silica generally occurs as overgrowths on detrital quartz grains, and as microcrystalline quartz crystals ~200 nm - 2 μm (Figures 38 and 43). Euhedral quartz crystals occurs in minor amounts as replacement of siliceous and carbonate skeletal debris such as radiolarian and foraminifer tests (Figures 22 and 43).

Direct measurement of illite/smectite ratio is not possible with the techniques used in this study. However, a significant increase in illite content is interpreted to occur with burial. An increase in potassium content, reduction in occurrence of shrinkage pores, and a decrease in volume suggest that illitization has strongly affected smectitic clays in high-maturity samples.

Authigenic apatite occurs in most high-maturity samples in trace amounts, but is only volumetrically significant in a few samples (up to 8.86%) (Table 2). Phosphatic crystals occur as pore-filling and elongate micro-crystals typically ~200 nm - 500 nm in length. Large replacement and pore-filling crystals can form up to ~30 μm (Figures 39 and 40). Phosphatic micro-crystals are typically dispersed throughout interparticle pore space and throughout detrital clay (Figure 40). Absence of authigenic this phase at low maturity suggests that apatite is a later cement. Bitumen coats apatite micro-crystals in Well 3 sample 1-136. This sample has abundant microcrystalline apatite, composing 8.9% of the bulk volume (Table 2; Figure 40, 56A, and 56B).

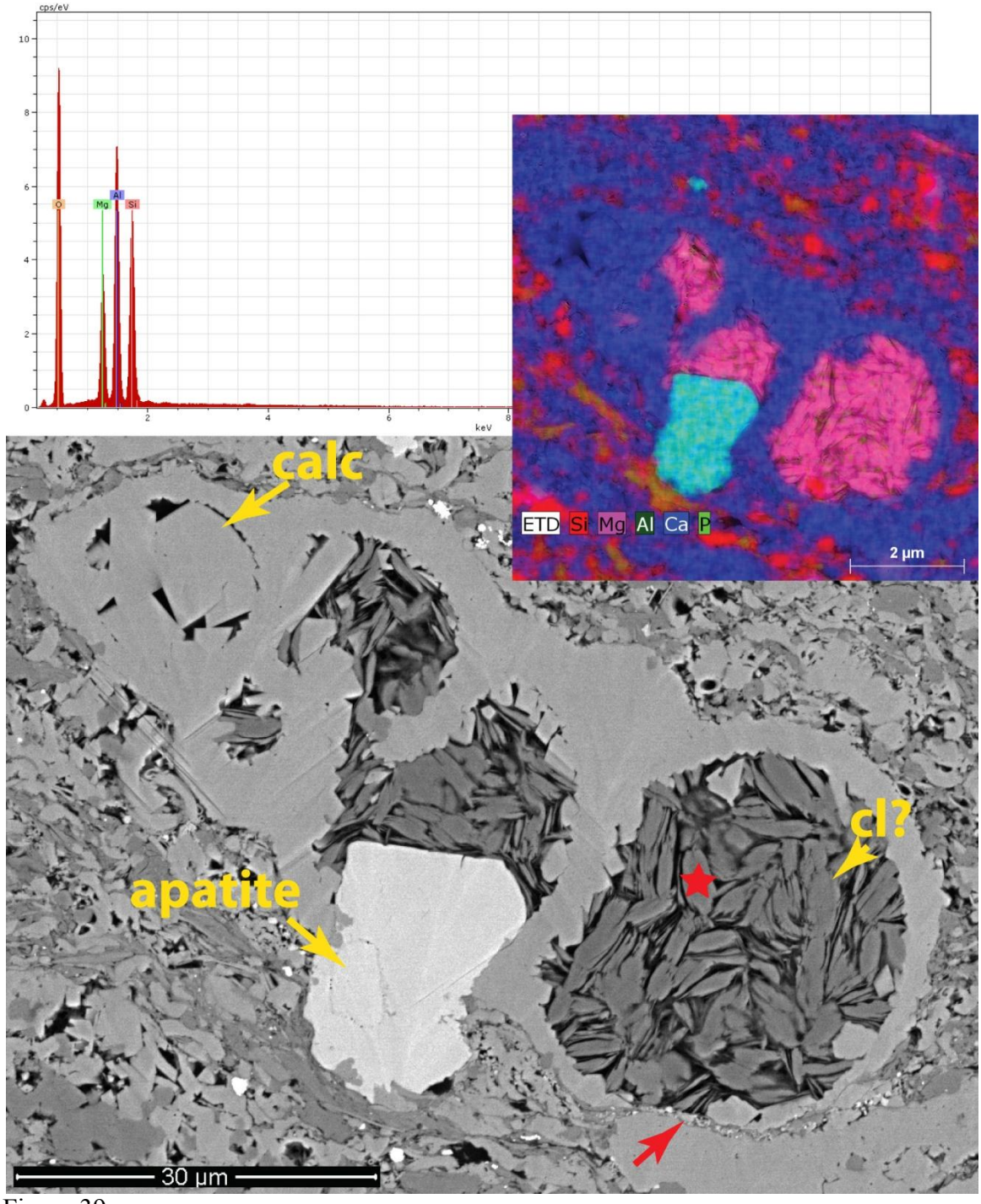

Figure 39

Figure 39: BSE image and corresponding EDS map showing foraminifer test with authigenic calcite spar, kaolinite, Mg-bearing phyllosilicate (cl?), and large, fabric destructive authigenic apatite crystal. Also EDS spectra of Mg-bearing phyllosilicate (taken at red star). Note: dissolution along test margin at grain contact (red arrow). Well 4 sample 1-100.

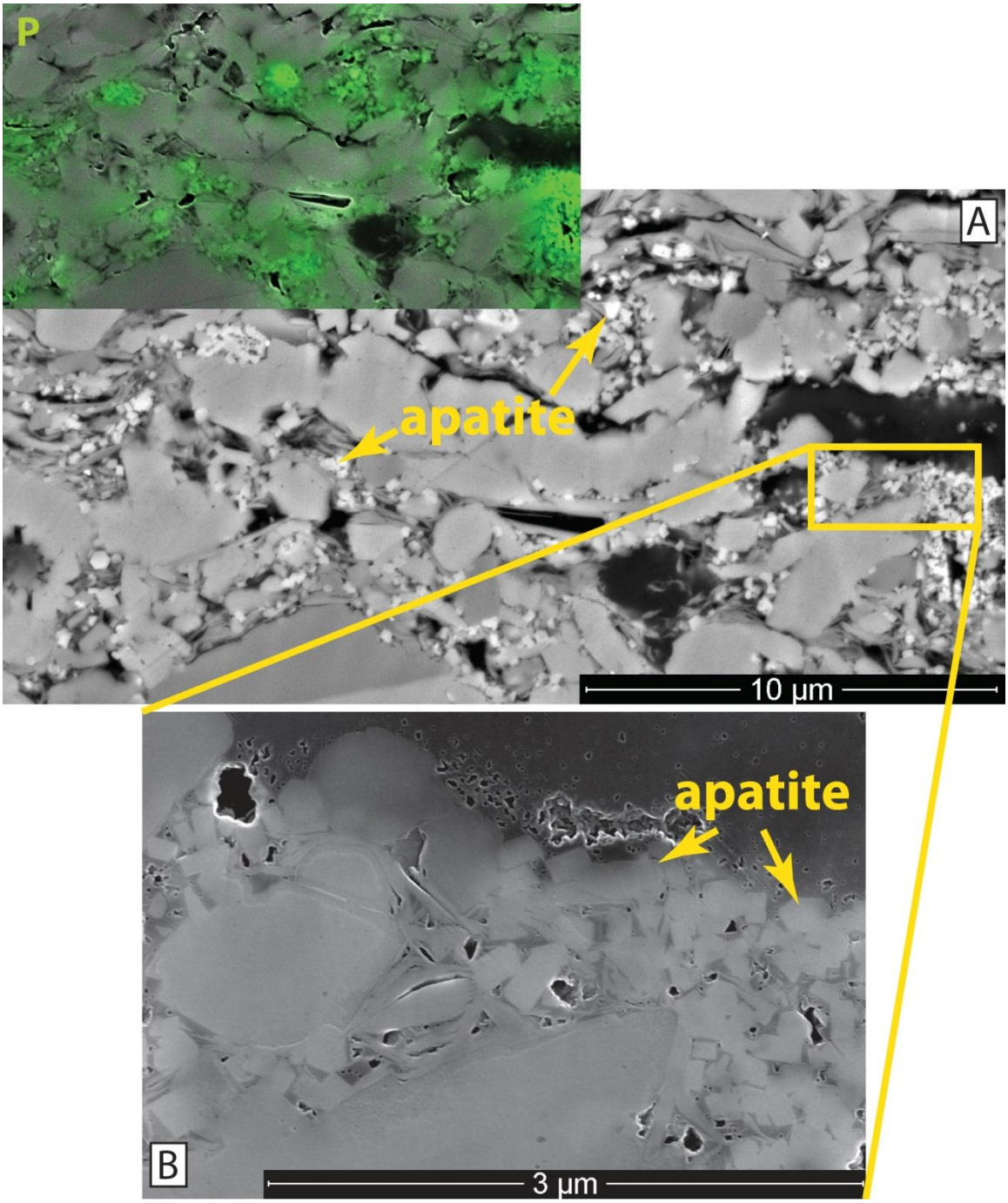

Figure 40: EDS map, BSE image (A), and SE image (B) showing authigenic apatite (elongate square tipped hexagonal crystals ~100-600 nm). Note OM coating apatite micro-crystals in B. Well 3 sample 1-136.

Atypical authigenic mineral phases occur in trace abundances at both low and high maturity. Anatase, or possibly rutile, is observed in several samples, as noted by the presence of Ti, bright BSE signal, and ragged appearance (Figure 41). Sphalerite is present in Well 1 sample 23 (low maturity, UEF) and is distinguished by its Zn and S EDS signal (Figure 42). Celestite is observed in Well 1 sample 8, partially filling a foraminifer test, and is recognized by distinctive Sr and S peaks in EDS spectra (Figure 42). Baker and Bloomer (1988) described authigenic celestite in calcareous nonnofossil oozes and chalks, associated with Sr generated from calcite dissolution-reprecipitation reaction.

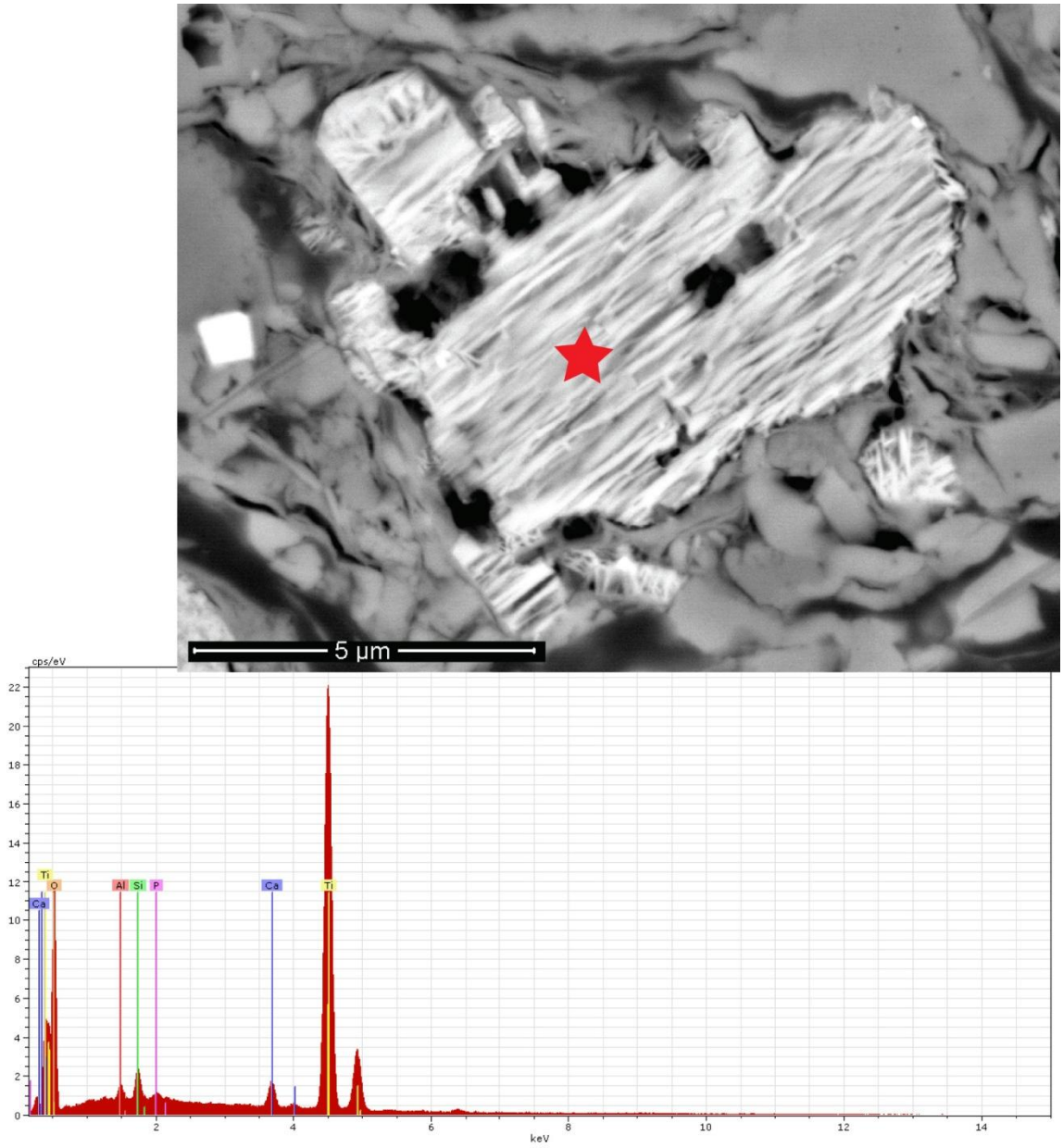

Figure 41: BSE image of anatase or rutile and corresponding EDS spectra (taken at star). Well 1 sample 8. Note ragged appearance and moldic pores suggesting the grain is either a detrital rutile grain or anatase replacement.

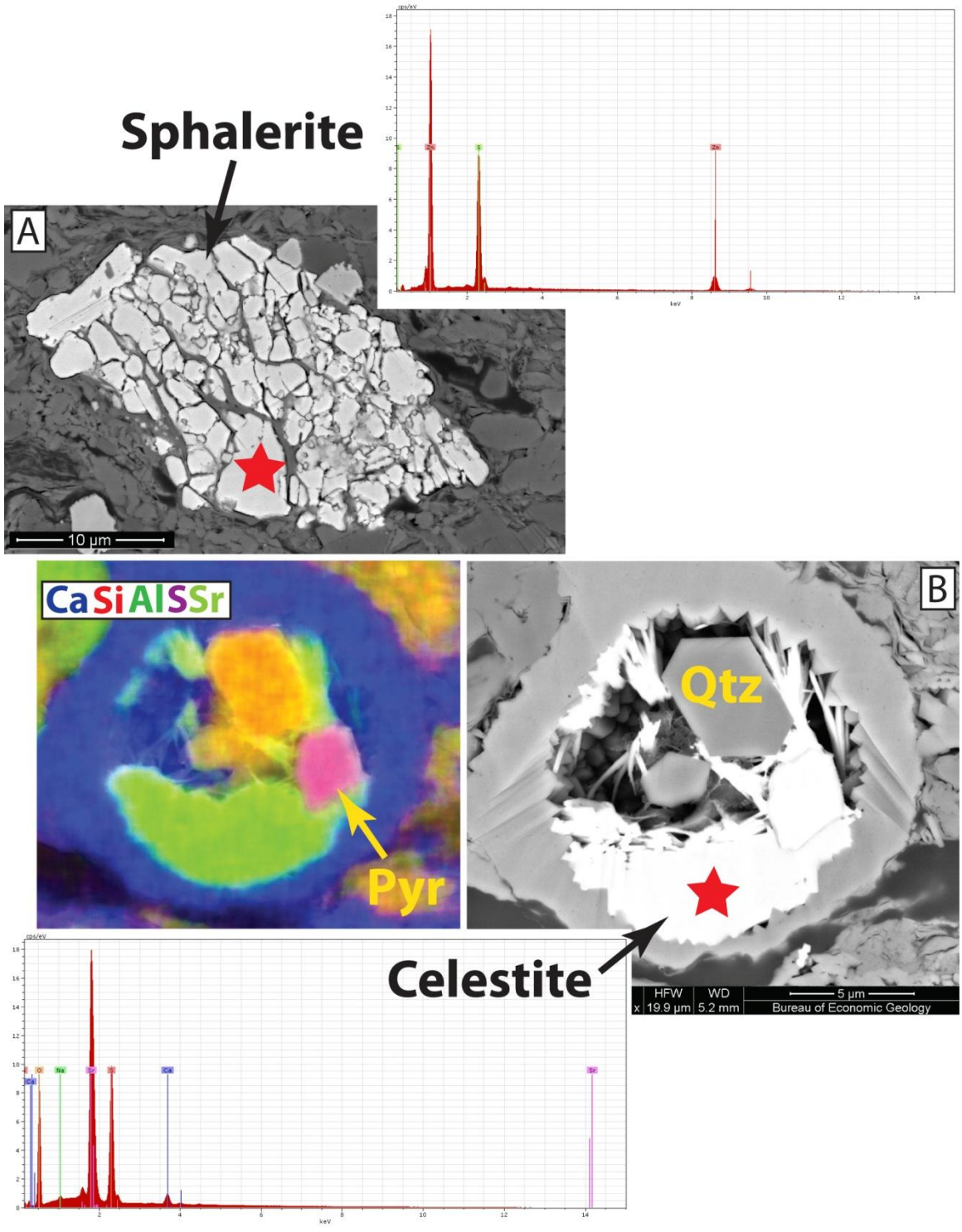

Figure 42: BSE images and EDS maps showing: A) sphalerite (Well 1 sample 23), and B) celestite, pyrite and quartz. Well 1 sample 8.

Dissolution and Replacement

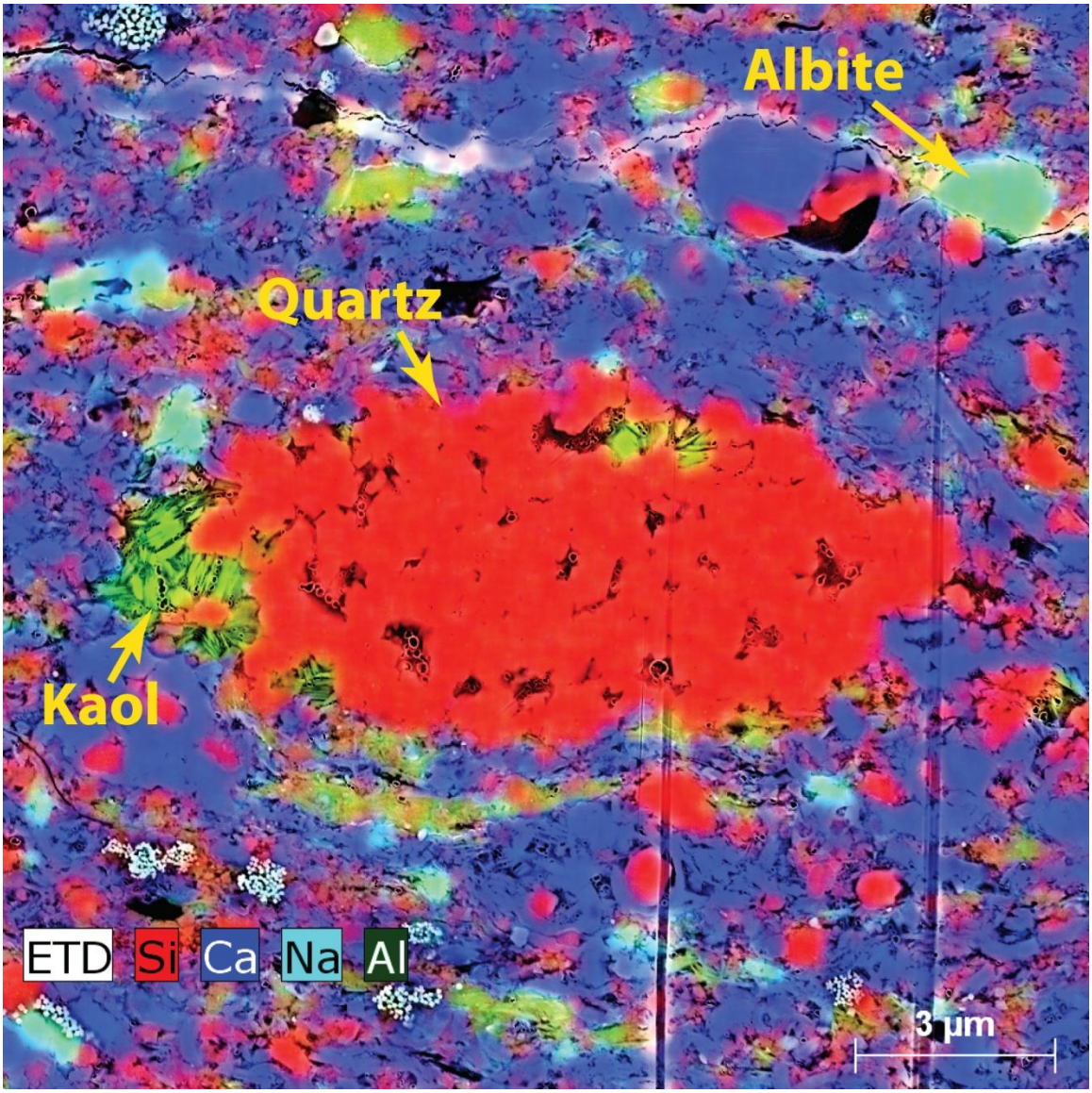

Figure 43: EDS map showing quartz replacing a dissolved grain (most likely a radiolarian), note abundant albite replacing smaller grains in the matrix. Well 4 sample 1-90. Albite could be partially detrital.

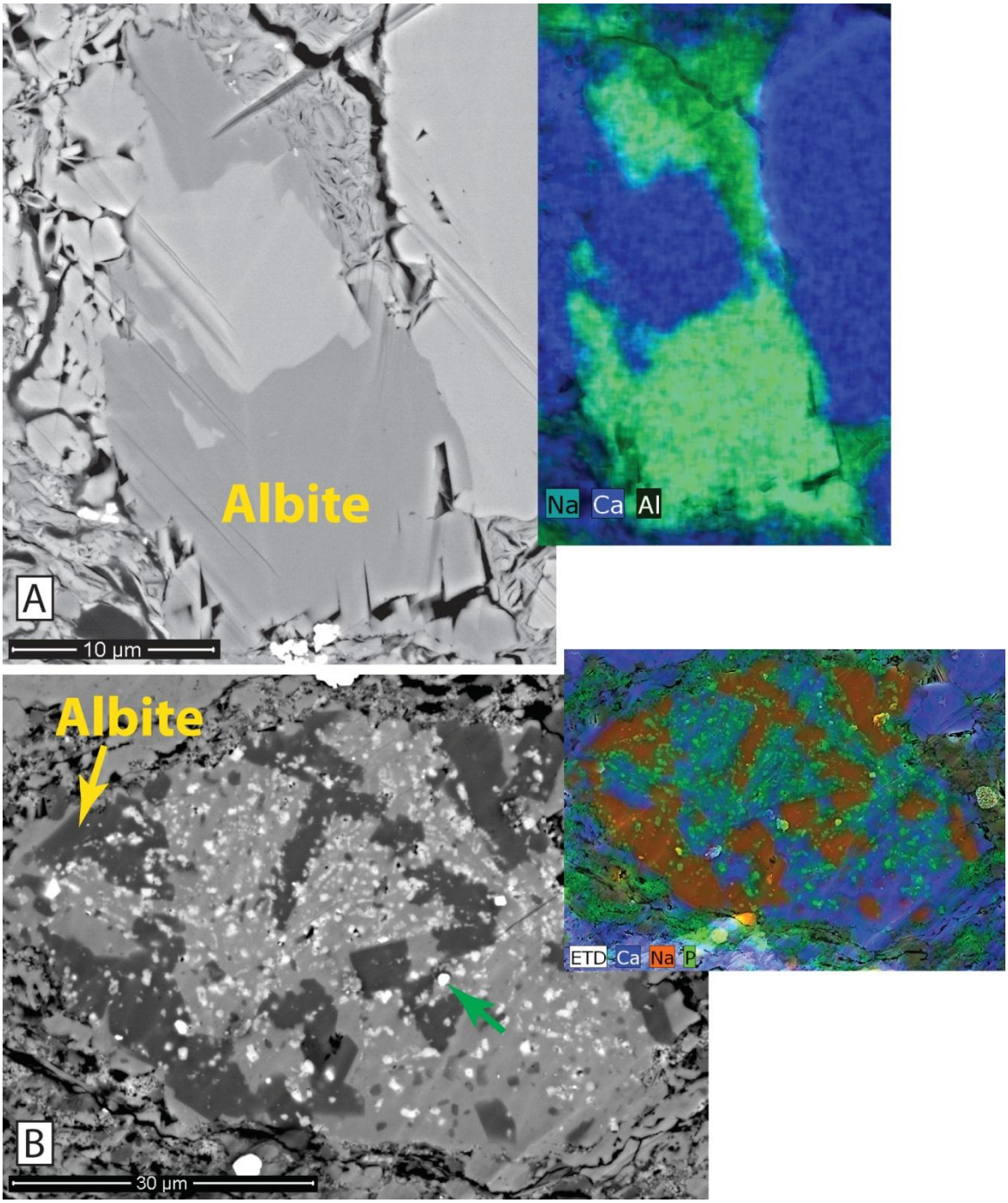

Figure 44: BSE images and EDS maps of albite including A) albite replacing carbonate grain (Well 1 sample 16), B) albite, micro-apatite (green arrow) and calcite replacing grain (Well 3 sample 1-136). Note sodium in B is mapped in orange to distinguish from apatite.

Extensive evidence of grain dissolution and/or replacement is present in both low and high-maturity samples. Dissolved grain types include: siliceous skeletal debris, non-coccolithic skeletal carbonate debris, feldspar, and micas (Figures 45 and 56). Dissolution of radiolaria and other un-stable skeletal debris likely occurs early, as is suggested by the relative paragenesis of the replacing mineral phase. Pyrite, sparry calcite are common replacements for radiolaria. Apparent dissolved feldspar and carbonate grains are observed at both low and high maturity, suggesting that dissolution begins during early burial. Increased abundance of albite with depth, and presence of minute amounts of potassium feldspar suggests that albitization occurs across depth, as documented in other sediment (Milliken et al., 1992).

Observed "exploded micas" in low-maturity samples suggest that mica alteration by kaolinite occurs before the oil-window (i.e., before bitumen mobilization), most likely with the other kaolinite. Pevear (1991) shows that kaolinite preferentially precipitates on mica plates, mimicking its crystal habit. Beyond physical bending, however, this process does little to alter the mica. Evidence of later dissolution of muscovite and/or kaolinite is observed in Well 3 sample 1-136, and includes "mica-shaped" pores within fully to partially dissolved muscovite after bitumen (Figure 56).

Dissolution of foraminifer tests, likely associated with generation of organic-acids associated with OM maturation, is observed in low-maturity samples with early bitumen generation. High-maturity samples display this as well, also associated with bitumen (Figure 45). In low-maturity samples where bitumen has been generated, foraminifer tests are partially to fully dissolved, and the tests cavities are filled with cement and bitumen. This suggests that dissolution occurred after early cement phases. Dissolution associated with bitumen is likely a result of OM-acid generation from the kerogen degradation process (Bernard et al., 2012a, Bernard et al., 2012b) (Figure 45). These observations

correspond with Seewald (2003), who shows that generation of organic acids can occur before, during, and after main stage bitumen generation. This is observed in this study's high-maturity samples as well. At high maturity, however, the tests' dissolution occurs more isolated to grain contacts, suggesting pressure solution (Figure 45) (Milliken and Land, 1993).

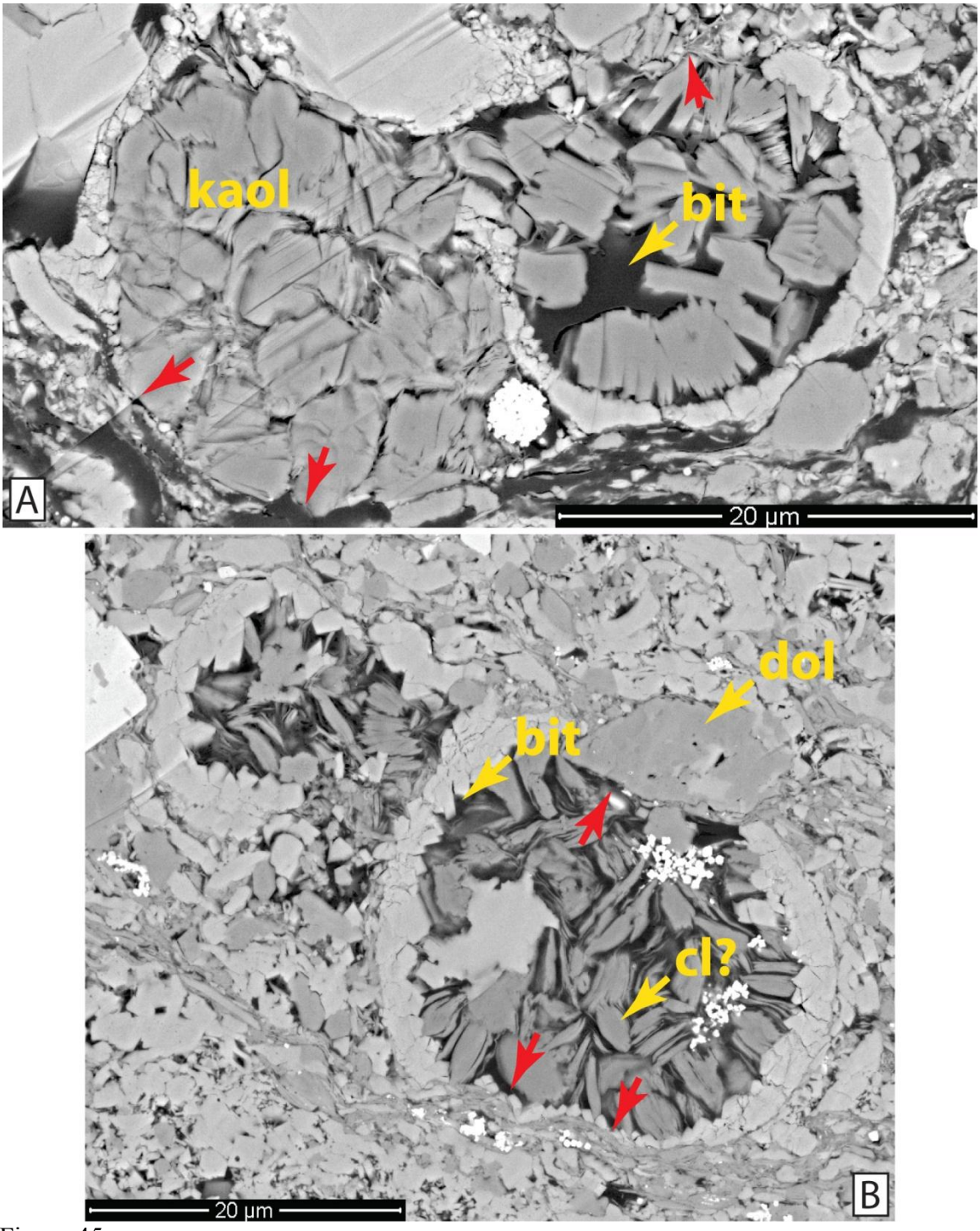

Figure 45

Figure 45: BSE images showing partially dissolved foraminifer tests (red arrows point to dissolved test). Clay-cementation and bitumen in-fill pre-date test dissolution. A) Low-maturity sample showing partially dissolved test with kaolinite, and partial bitumen (bit) fill. B) High-maturity sample showing partially dissolved test with preferential dissolution along clay seams and grain contacts, and Mg-bearing phyllosilicate calcite, and bitumen infill. Note: Dissolution at high maturity are more localized to points of pressure on the tests. Well1 sample 4 (A), and Well 4 sample 1-100.

ORGANIC-MATTER MATURATION

Results of this study show that maturation of organic matter is a controlling factor of distribution and character of porosity. Diagenetic products of kerogen maturation that significantly impact porosity include: bitumen, organic acids, and volatile fluids. Results indicate: occlusion of porosity occurs by bitumen infill, and generation of porosity occurs within OM. Hydrocarbon maturation is a function of chemical and physical conditions, and the composition of detrital OM as described by Milliken et al. (2013), and Seewald (2003).

Maturation of hydrocarbons directly correlates with increasing depth. Increasing PT conditions, in addition to a dynamic chemical environment, make it thermodynamically favorable to break weaker bonds in large molecules within detrital kerogen to form bitumens (Seewald, 2003). As maturation continues, oil and gas are commonly generated from bitumen. In some cases, however, volatile hydrocarbons can be generated directly from kerogen (Seewald, 2003). As bonds break, a volume expansion occurs, and elevated pressures lead to expulsion of smaller, mobile hydrocarbons (Seewald, 2003). Pores develop within OM, in spaces where bubbles of volatiles have nucleated and grown (Milliken et al., 2013).

Petrographic observations and geochemical data suggest that within most low-maturity samples, the vast majority of OM is non-porous, amorphous, and is chemically meta-stable (Sun et al., 2014). However, where they occur, primary pores are present in low volumes, composing between 0.20% - 0.35% of the bulk volume. Primary pores are largely isolated to the Upper Eagle Ford where biomarkers suggest a larger proportion of terrestrial kerogen (Sun et al., 2014). Kerogen is very ductile and susceptible to compaction as suggested by: strong inverse correlation between TOC and visible porosity

(Figure 61), and kerogen "mashed" between more rigid grains partially infilling primary pore space (Figures 28 and 50) (Milliken et al., 2014).

Bitumen generation within low-maturity samples from the Lower Eagle Ford occurs where OM with high sulfur contents make it kinetically favorable to break bonds in kerogen to form a mobile, bitumen phase (Seewald et al., 2003; Sun et al., 2014). At low maturity, bitumen occurs as amorphous, non-porous, and primary-pore-filling OM (Figure 46A, and 82). It lacks discrete shapes of particles and is or was a mobile liquid that permeated into pore space (Figures 46A and 82) (Milliken et al., 2014). "Bubble" shaped pores occur between OM and mineral surfaces, are often isolated on a crystal point or corner occurring where a second fluid phase was present (Figure 46,48, and 52) of “bubble” morphology suggest many of these pores are a non-wetting phase on calcite surfaces and are likely artifacts of water droplets bound by capillary and/or surface tension. Water is not necessary to degrade kerogen, however, it acts as reactant and strongly influences the reaction pathway of OM (Seewald 2003). Water retards the cracking of long bitumens to form gas and is essential in processes resulting in the generation of liquid oil (Seewald 2003).

Petrographic observations and geochemical biomarker analysis suggest that bitumen is present in all high-maturity samples in varying amounts (Figures 47 and 84-86) (Sun et al., 2014). Contrasting the amorphous, non-porous bitumen observed at low maturity, bitumen within high-maturity samples shows extensive development of complex micro-structure and OM-hosted porosity. While there is significant heterogeneity, significant proportions of interpreted bitumen has developed a "vermicular" or " brainy" network of interlocked "worms" that encrust mineral surfaces, especially calcite (Figures 47 and 48). In samples where this type of texture is present, small pores occur between the "worms" (Figure 47 and 48).

Bitumen is present in all high-maturity samples, as well as low-maturity samples with abundant sulfur-rich OM (Sun et al., 2014). With the techniques applied here, bitumen can be confidently distinguished from kerogen where it coats authigenic mineral growth or where it in-fills primary intra-particle porosity. However, the distinction is only clear in exemplary cases. The majority of bitumen likely occurs as amorphous OM, filling space between mineral grains (Figure 47C, 84, and 85). As suggested by Milliken et al. (2013), observation of heterogeneity and character of OM within samples from across stratigraphy and maturity suggests that relative abundances of OM composition are a strong control generation of bitumen and secondary porosity within OM.

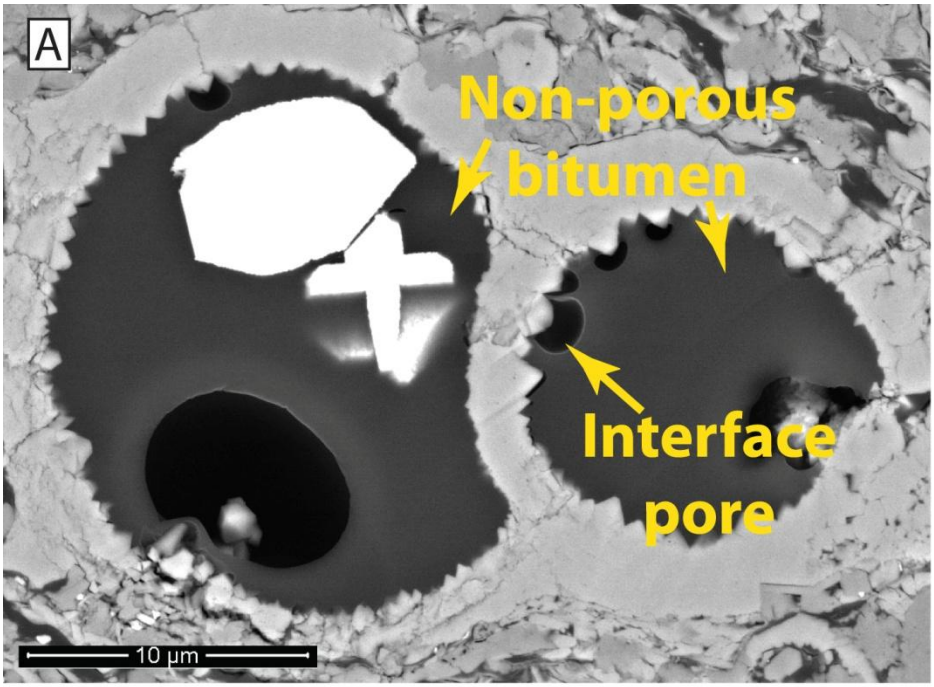
A
Non-porous
bitumen
Interface
pore
10 µm

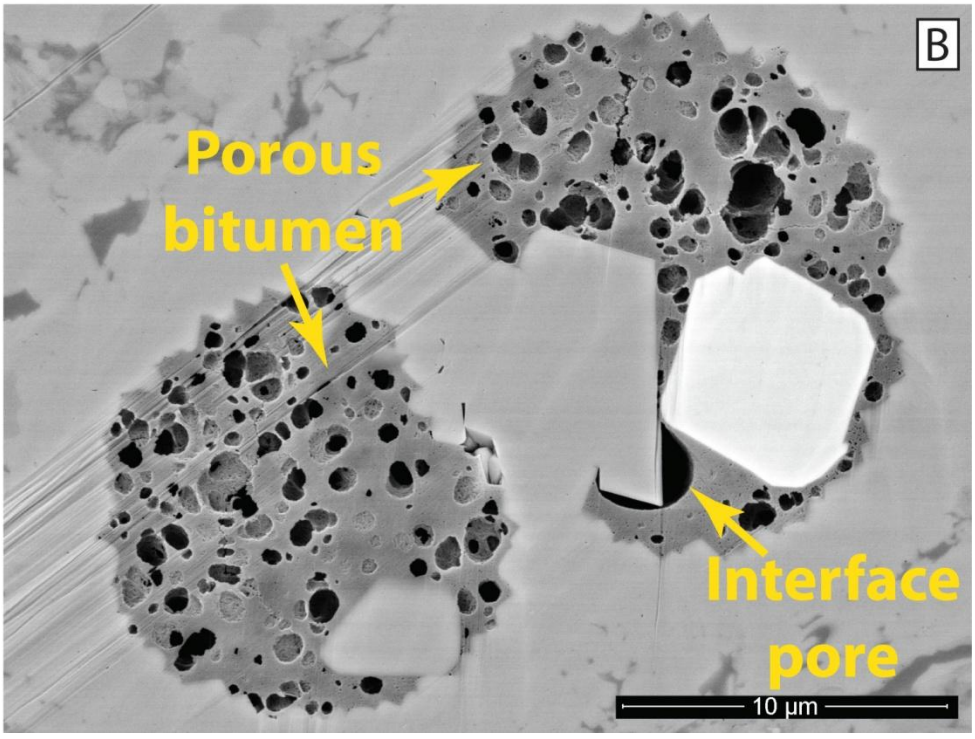
B
Porous
bitumen
Interface
pore
10 µm

Figure 46

Figure 46: BSE images of bitumen fill of foraminifer test. Bitumen in-fills primary pore space and coats authigenic mineral growth. Note presence of OM-mineral interface pores on crystal points. A) Non-porous amorphous bitumen (Well 1 sample 4), B) porous bitumen with complex "spongy" pore network (Well 4 sample 1-123).

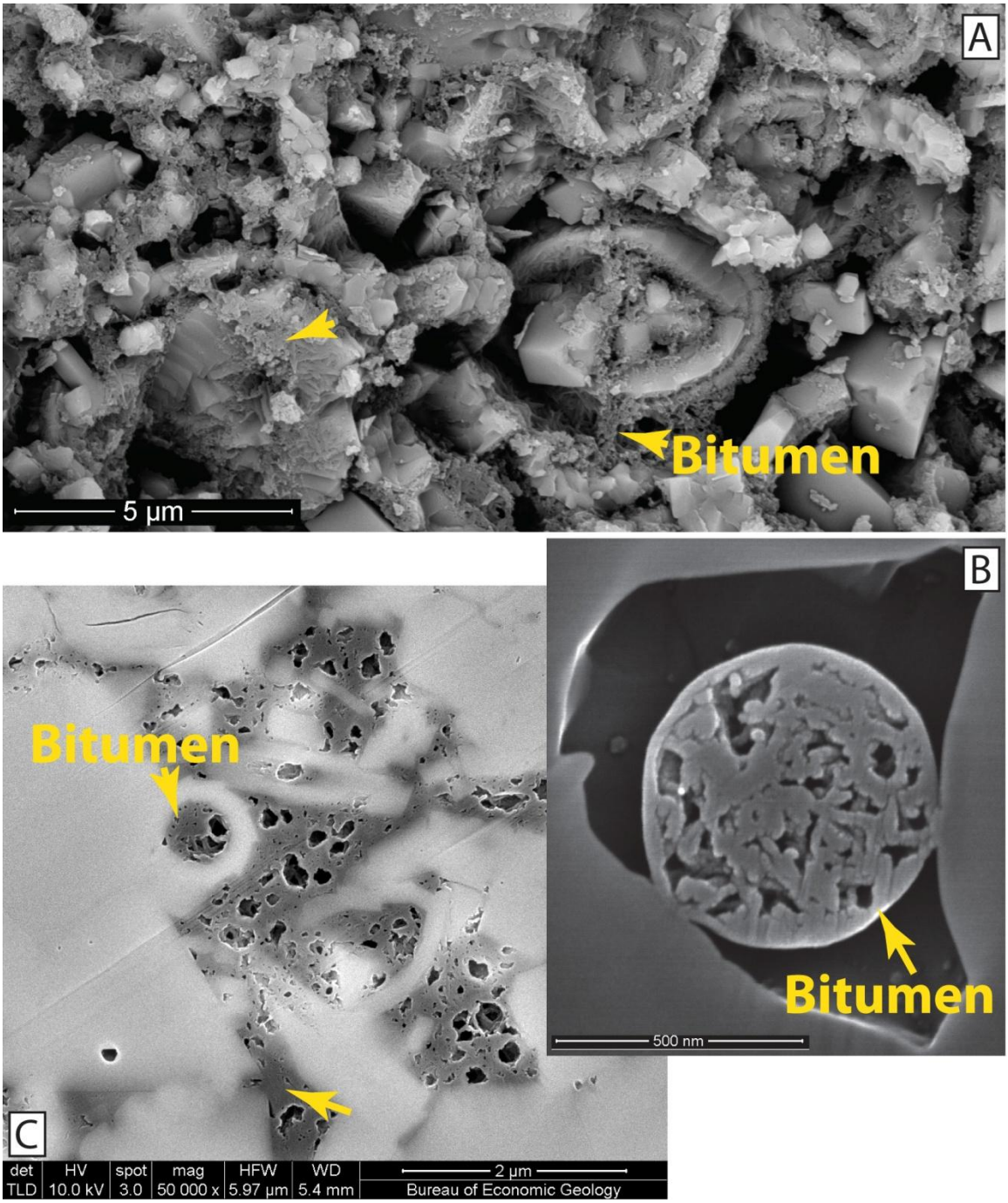
A
Bitumen
5 µm
B
Bitumen
500 nm
Bitumen
C
det HV spot mag HFW WD
TLD 10.0 kV 3.0 50 000 x 5.97 µm 5.4 mm
2 µm
Bureau of Economic Geology
Figure 47

Figure 47: BSE images and TLD images of bitumen as: A) vermicular grain encrustation (Well 4 sample 1-80), B) pervasive fill of primary pore space (coats cements and fills intra-skeletal pores) (Well 4 sample 1-75), and C) tiny (~500 nm) bead of vermicular bitumen included in calcite cement (Well 4 sample 1-80).

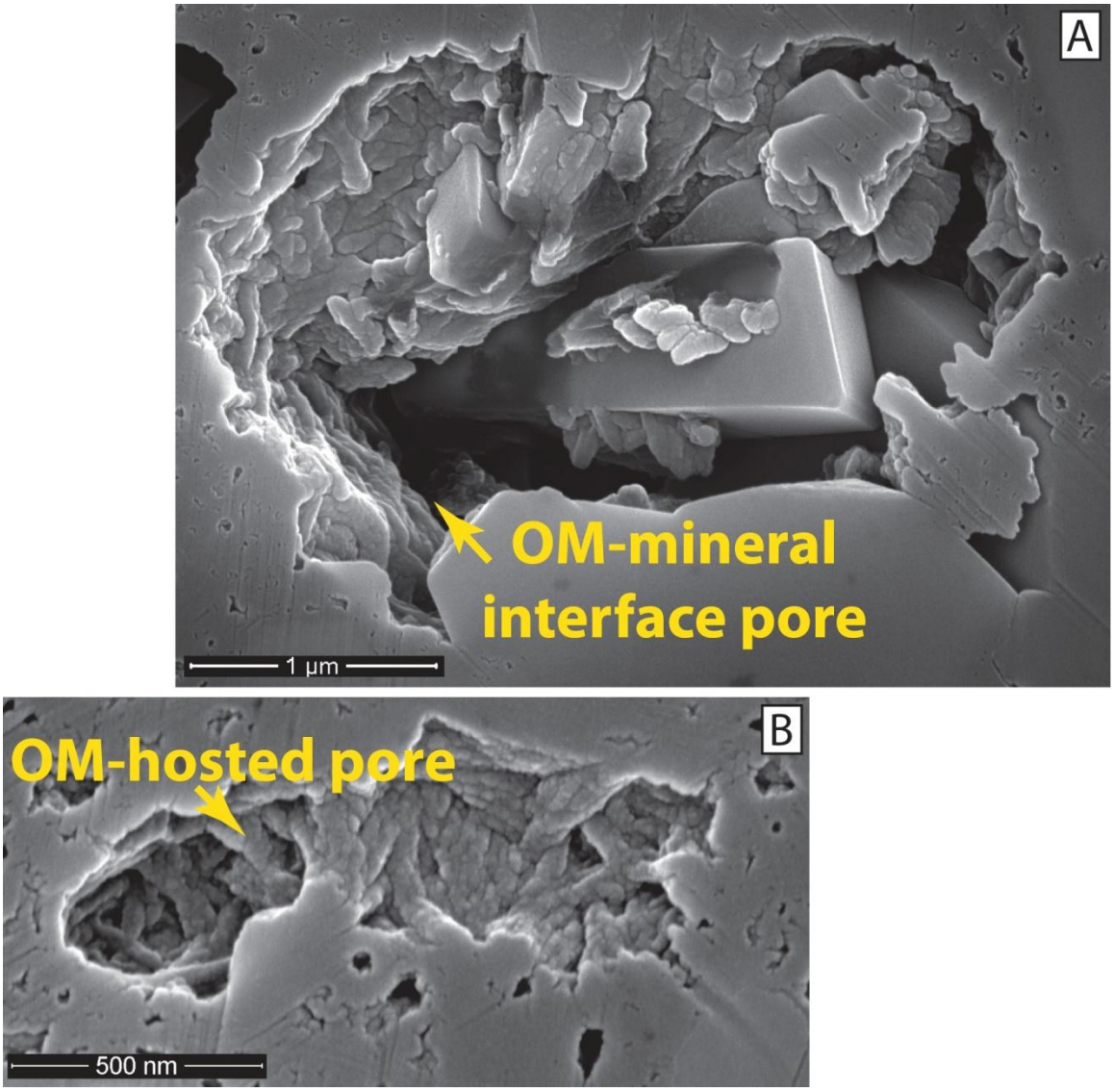

Figure 48: TLD images showing bitumen with vermicular or fibrous texture. Well 4 sample 1-80.

COMPACTION

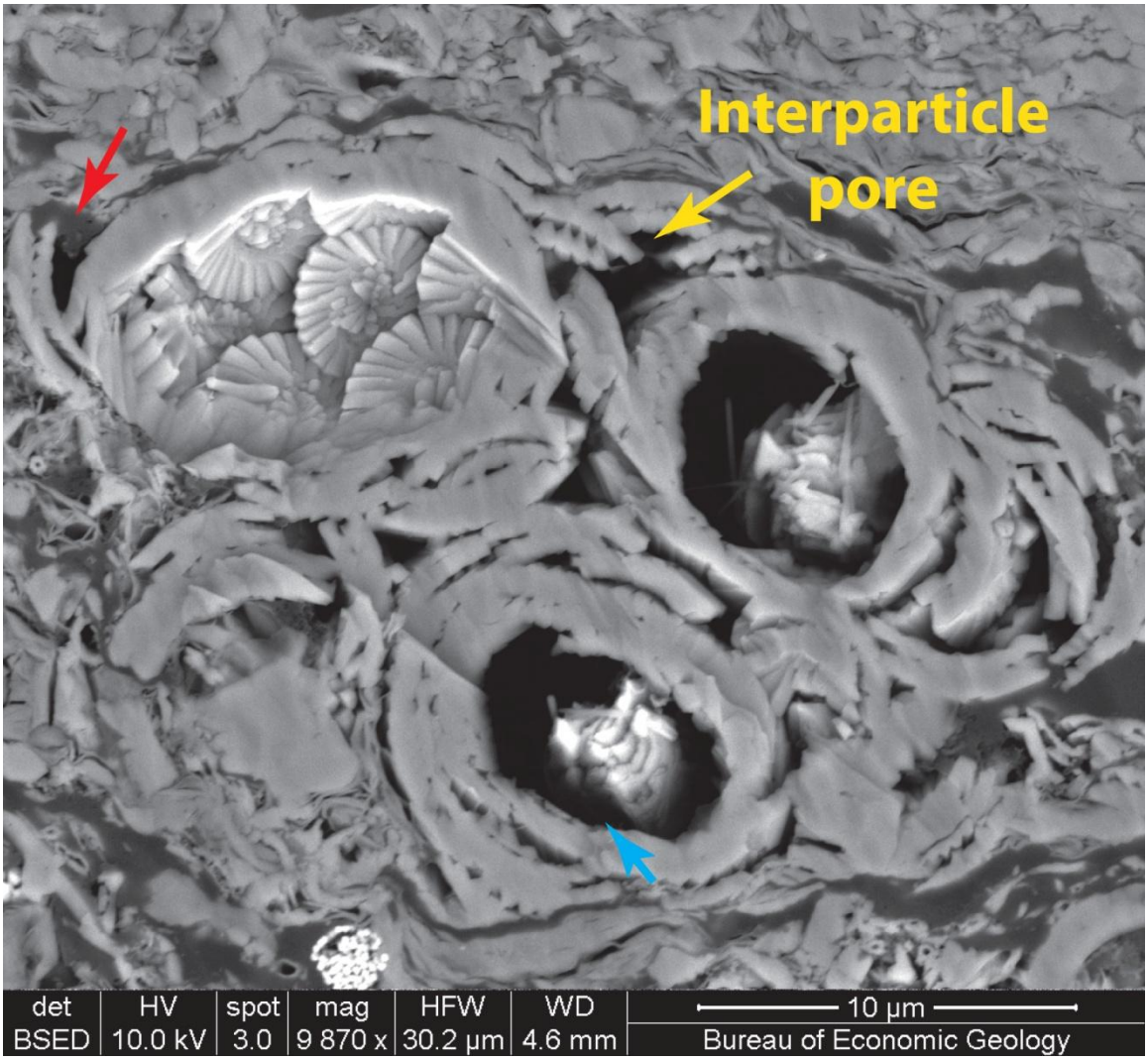

Figure 49: BSE image of crushed coccospheres with sheltered porosity (yellow arrow), primary intra-coccosphere pores (blue arrow), and kerogen being mashed into primary pore space (red arrow). Well 1 sample 16.

Lack of cementation, and large pores preserved between rigid coccolithic grains suggest that the majority of porosity loss within low-maturity samples occurs via compactional processes (Figure 37, 81, and 82). Strong correlations between porosity and pore size with abundance of ductile versus rigid components affirm this interpretation

(Figures 61, 63, and 73). As other studies have documented near-surface muds have porosity values up to ~80% that are strongly affected by early compaction and the structural character of the detrital grain assemblage (Mondol et al., 2007; Milliken et al., 2014; Schneider et al., 2011). Petrographic evidence of compaction in low-maturity samples includes:

- Most commonly deformation of kerogen and other ductile grains (Figure 28).
- Deformation and grain parallel alignment of clays near large grains (Figure 22A 49).
- Mechanical re-arrangement of coccolith plates within crushed coccospheres (Figure 49).
- Preservation of interparticle pores between rigid bioclastic debris (Figures 24, 49, 63, and 81).

Abundance and distribution of porosity is heavily dependent on structural properties of grains. Rigid, irregularly-shaped skeletal grains appear to resist physical compaction and likely undergo only minor mechanical re-arrangement. This preserves large, inter-particle, primary pores, up to ~26% within carbonate aggregates. Ductile components, such as OM and clay, appear to accommodate strain, and are compacted between more rigid grains, often showing alignment parallel to the grain surface (Figures 28 and 49).

It is unclear to what degree compaction has affected the pore network at high maturity. Inability to reliably distinguish authigenic and detrital components makes petrographic measurements of inter-granular volume (IGV) unreliable.

Pore Types

A wide variety of pore types were observed in this study. Interparticle and intraparticle pores are observed associated with both organic matter (OM) and mineral components. Pores include those arising from both primary and secondary processes. Porosity induced by sample preparation and beam damage during imaging are recognized and excluded from the database on natural pores. Objective parameters are used to characterize porosity for quantification, and are described below. Qualitatively, a more complex spectrum of pore types is interpreted than is described quantitatively.

Classified pore types include mineral-associated pores occurring between, around, or within mineral particles and OM-hosted pores occurring within OM. Mineral associated interparticle pores between mineral particles or mineral particles and OM are classified as: 1) inter-mineral pores between mineral particles, 2) OM-mineral interface pores between mineral particles and OM, and 3) clay-hosted pores between or within clay particles, including pores within clay-clasts. Intra-skeletal, inter-mineral, and OM-mineral interface pores that occur within aggregates of skeletal debris are given the modifier, "intra-pellet". Mineral-associated intraparticle pores within mineral grains are classified as one of the following: 1) inclusion pores, or small spherical artifacts that include fluids in a mineral cavity, 2) intra-skeletal pores or 3) moldic pores, where grains have been partially to fully dissolved. Pores within OM are classified as either simple or complex, on the basis of partitioning within the pore. Table 1 and Figure 50 summarize the pore type categories quantified in this study.

Table 1: Quantified Pore Types

Pore Type			Definition
Mineral-associated	Intraparticle	Inclusion	small, spherical, artifact of included fluid in mineral particle
		Intra-skeletal*	within skeletal cavity
		Moldic	anamalously large pore taking shape of partially to fully dissolved precursor
	Interparticle	Inter-mineral*	between mineral particles
		OM-mineral interface*	between mineral particle and OM
		Clay-hosted	between or within pyllosilicate particles (at least 2/3 of surrounding grains)
OM-hosted		Simple	within OM one chamber
		Complex	within OM, partitioned chamber

* inicates pore type where the modifier "intra-pellet" where it occurred within aggregate of skeletal debris

At the pore scale, the distribution of coccolith-size (micron-scale) particles is a primary control on matrix porosity. Mineral-associated pores within carbonate aggregates are distinguished and given the modifier "intra-pellet". They are, however, included in most calculations as a part of the inter-mineral, OM-mineral interface, and intra-skeletal populations. Likewise, clay-hosted porosity is considered largely interparticle. Distinct cases where one clay grain has bent and opened, creating a pore, are observed, though in most cases it is ambiguous as to whether clay pores are between or within clay particles. Distinction of aggregate boundaries and determination of which pores are intra-aggregate can be unclear and may be overly subjective during pore scale observation. The goal in the quantification process of this study was to encompass a sufficient area to account for pore distribution across small-scale rock fabric heterogeneity.

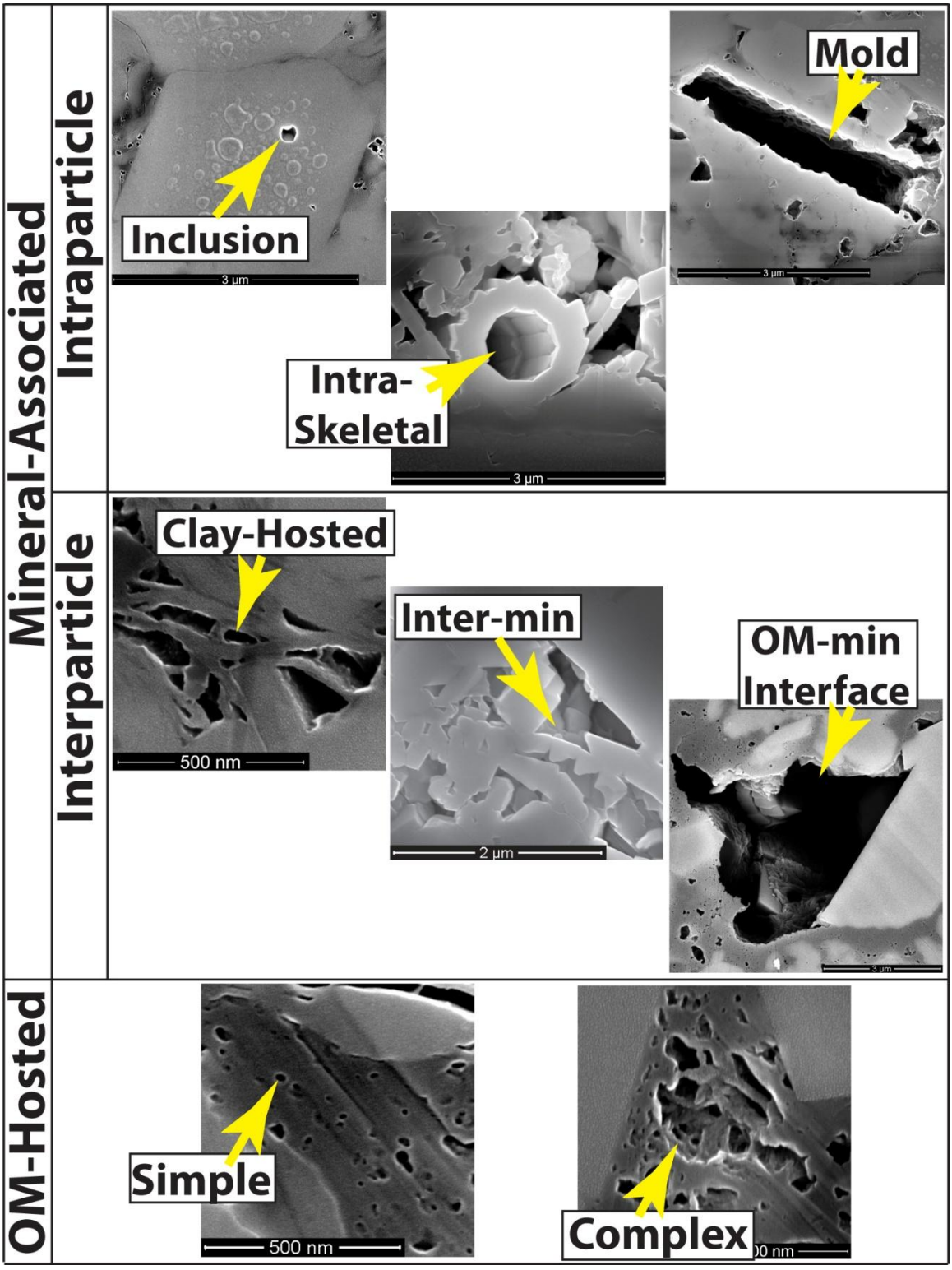
Mineral-Associated
Intraparticle
Inclusion
3 µm
Mold
3 µm
Intra-
Skeletal
3 µm
Interparticle
Clay-Hosted
500 nm
Inter-min
2 µm
OM-min
Interface
3 µm
OM-Hosted
Simple
500 nm
Complex

Figure 50

Figure 50: BSE and SE images of pore types quantified in this study including both mineral-associated and OM-hosted pores. Intraparticle mineral-associated pore types include: inclusion pores, moldic pores, and intra-skeletal pores. Inter-particle mineral associated pores include: inter-mineral pores, OM-mineral interface pores, and clay hosted pores. OM-hosted pore types include: simple pores, and complex pores with partitioned chambers. See Table 1 for more details.

INTERPARTICLE PORES

Pores between particles, or interparticle pores, are observed in all samples and are defined as being surrounded by multiple mineral particles or one or more mineral particles and OM. Pores surrounded by multiple mineral particles are classified as inter-mineral pores (Table 1; Figures 50 and 51). Pores surrounded by one or more mineral particles and OM are classified as organic matter-mineral interface pores (Table 1; Figures 50 and 52). Pores between clay particles, or clay-hosted pores, occur in all samples and are largely considered interparticle (Table 1; Figures 50 and 53).

Inter-mineral pores compose an average of 53.5% of the SEM visible porosity in low-maturity samples (Well 1, Ro~0.5%) and range in abundance from 0.02% to 9.12% bulk volume (Table 4; Figure 62). At high maturity, inter-mineral pores compose an average of 35.1% of the porosity in Well 3 and Well 4 (Table 4; Figure 62). Inter-mineral pores are relatively large and mean equivalent circular diameter ranges from 99.6 nm in Well 1, 50.9 in Well 3, and 49.0 in Well 4. Inter-mineral pores are most abundant in low-maturity samples associated with abundant coccolithic skeletal debris (Figure 51). Inter-mineral pores are primary and are present at deposition.

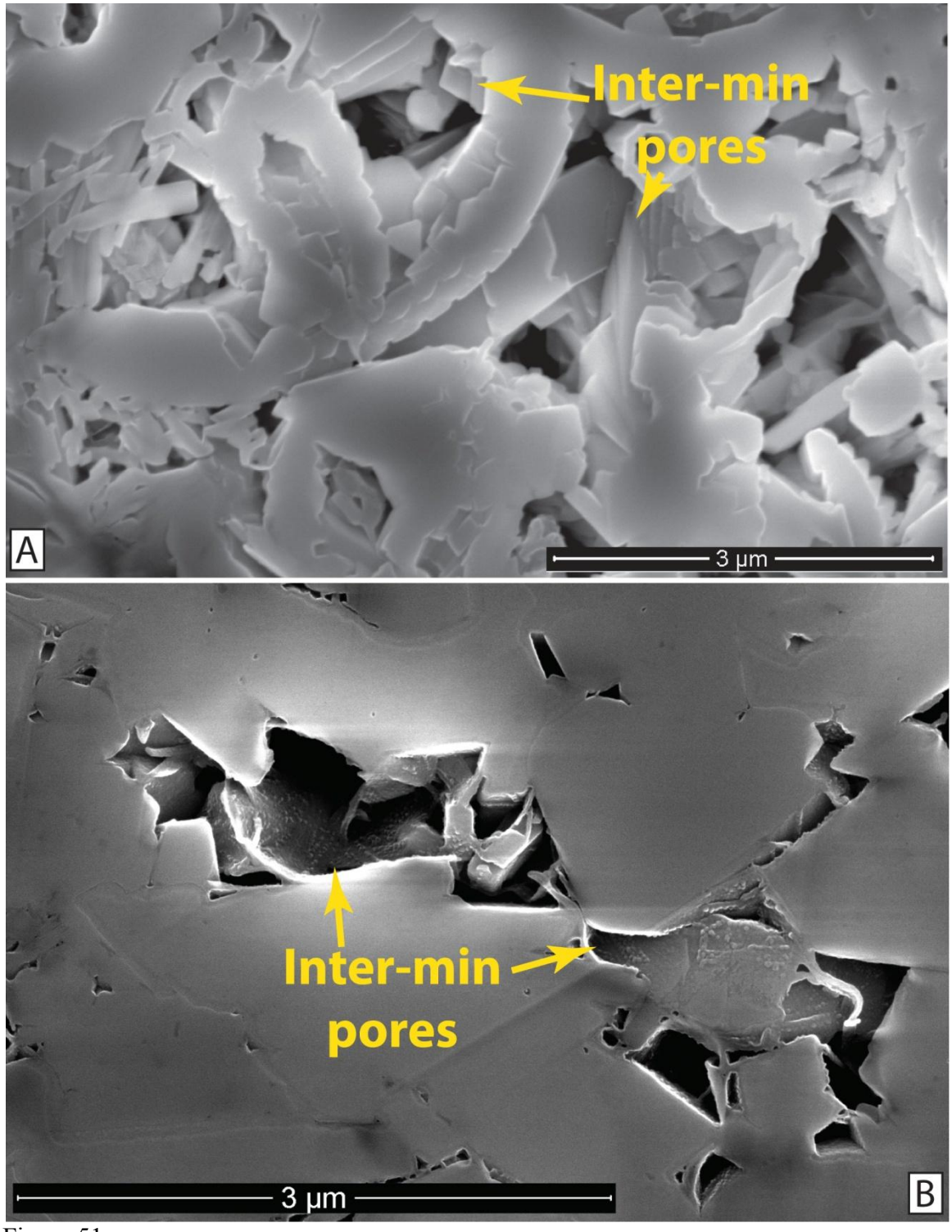

Figure 51

Figure 51: Examples of Inter-mineral pores including: A) large pores between coccolith debris (Well 1 sample 16), and B) inter-mineral pores between euhedral calcite crystals (Well 3 sample 1-66).

OM-mineral interface pores are volumetrically significant in both low and high-maturity samples, ranging in abundance from .09% -1.63% of the bulk volume in Well 1 and 0.27% - 5.53% in high-maturity samples (Table 1; Figures 47, 50, and 52). Genesis of these pores is attributed to several possible mechanisms: primary intergranular pores between OM and mineral particles, partial infill of primary pores by ductile kerogen, partial infill of primary pores by mobilized bitumen, and possible preferential bubble nucleation on a mineral surface during hydrocarbon maturation (Milliken et al. (2013)) (Figure 52). Subjective distinctions can be made between the four in exemplary cases. However, in most cases, the distinction is unclear. Milliken et al. (2013) classified similar pores as mineral-associated OM-hosted pores and included them as a part of the OM-hosted pore volume. For quantitative purposes in this study, interface pores are classified as interparticle, and are excluded from the OM-hosted pore volume. Observations that these pores occur in significant volumes, up to ~2.6% of the bulk volume, before and during hydrocarbon generation and are commonly associated with otherwise non-porous OM affirms that this is appropriate (Table 4; Figures 47 and 52). At high maturities where we observe porous OM, a large portion of interface pores can be attributed to preferential bubble nucleation, more analogous to the Milliken et al. (2013) report, which suggest a classification of intra-OM may be more appropriate in those cases.

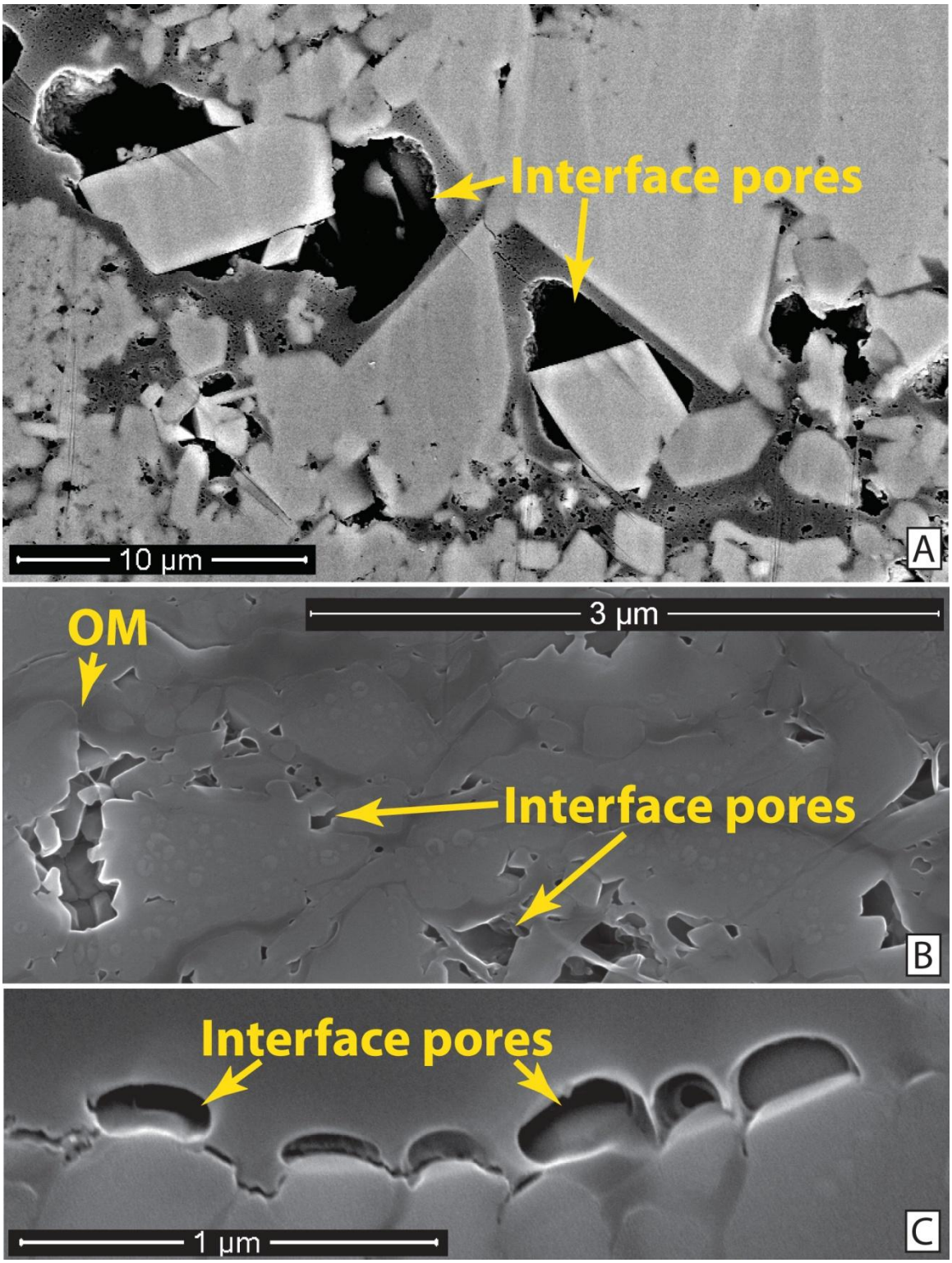
Interface pores
10 µm
A
OM
3 µm
Interface pores
B
Interface pores
1 µm
C
Figure 52

Figure 52: Examples of OM-mineral interface pores. A) Large, OM mineral interface pores resulting from partial OM fill. Note: calcite crystal growth appears to post-date bitumen fill (Well 4 sample 1-80). B) Interface pores between detrital kerogen and mineral particles (Well 1 sample 16). C) OM-mineral artifact pores between bitumen and a partially dissolve foraminifer test, pores are artifact of second fluid phase present during bitumen infill. (Well 1 sample 1).

Pores between phyllosilicate particles (clays and micas), or clay-hosted pores, are present at both low and high maturity, although abundance decreases with maturity (Table 4; Figure 62). Clay-hosted pores compose 0.03% - 1.08% of the bulk volume in Well 1, 0.09% - 0.61% of the bulk volume in Well 3, and 0.0% to 0.05% of the bulk volume in Well 3. These pores can be between clay plates along cleavage planes, within a clast, or between detrital grains (Figures 18, 19, and 53). Typically, this distinction is unclear. At low maturity, clay platelets are smectitic and are prone to generation of shrinkage pores attributed to sample preparation. This makes petrographic distinction of *in situ* and artifact clay-hosted pores both difficult and subjective in many cases. Shrinkage pores are anomalously large, and have a ragged "torn" appearance, and cut across, along, or around clay seams and clasts. At higher maturities (Well 3 Ro~1.2%), clay grains show fewer shrinkage artifacts and more distinct pores (Figure 53). Quantitatively, pores surrounded by at least 2/3 clay and/or mica grains are classified as clay-hosted pores (Table 1; Figure 50 and 53).

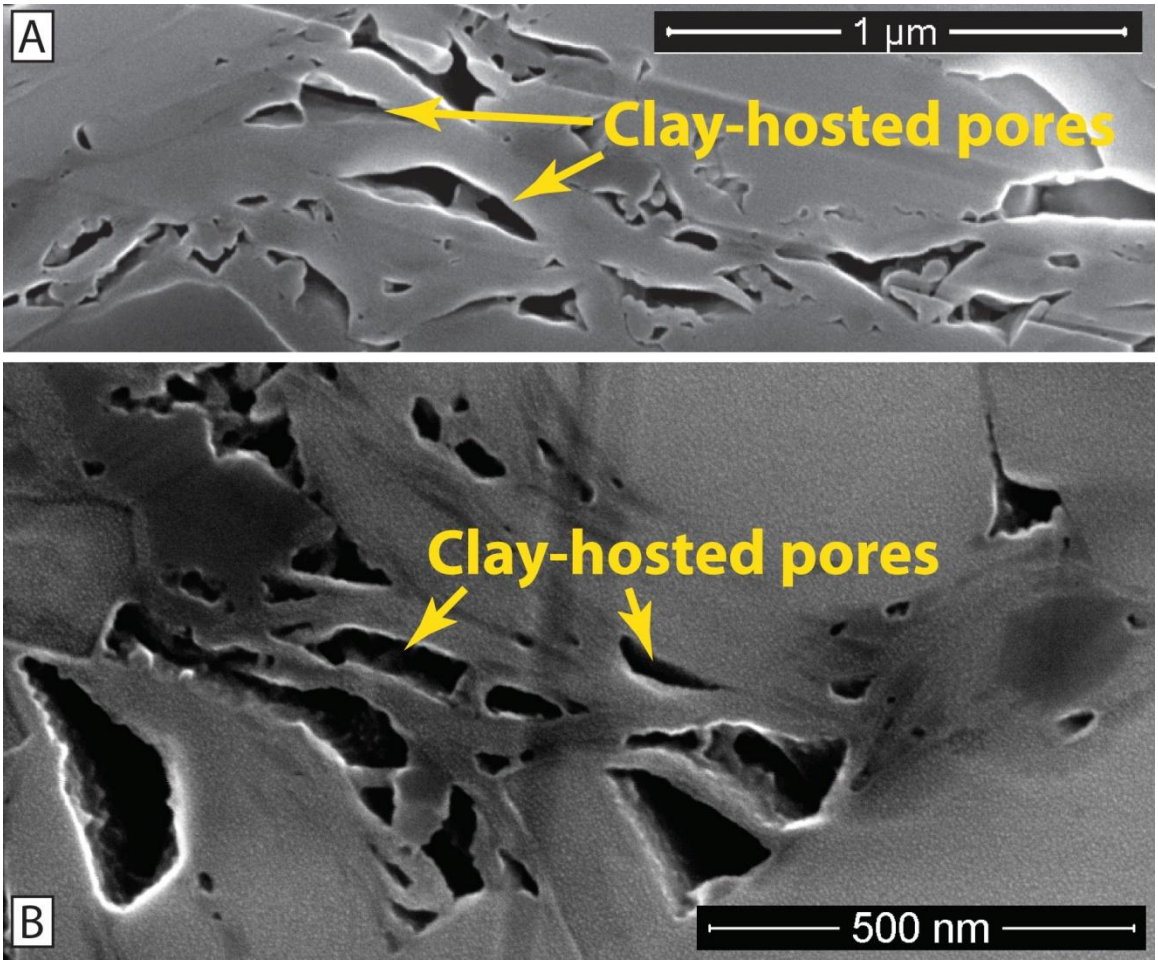

Figure 53: Pores between clay platelets. Well 1 sample 19 (A) and Well 3 sample 1-66 (B).

MINERAL-HOSTED INTRAPARTICLE PORES

Intraparticle pores are observed in all samples, and are defined in this study as pores contained within a single mineral particle. Primary, skeletal-hosted intraparticle pores, inclusion pores, and secondary pores were observed and attributed to grain dissolution.

Primary, skeletal-hosted intraparticle pores are observed in samples lacking pervasive bitumen infill (Table 4; Figures 54 and 62). These pores are most commonly

associated with coccolith and nannolith debris, particularly within coccolith spines (rhabdoliths). Mean equivalent circular diameter of intra-skeletal pores is ~427 nm in low-maturity samples. Small complex pores within phosphate grains were observed in a few samples, but do not contribute significantly to the matrix porosity (Figure 27C). The largest (~5 µm - 30 µm) pores in most samples are hosted within foraminifer tests but are excluded from quantification because they are too large to readily quantify with magnifications utilized here. These kinds of pores are common at low maturity; however cementation and bitumen infill are particularly destructive to these types of pores. (Figures 21, 22, 29, 33, 35, 46).

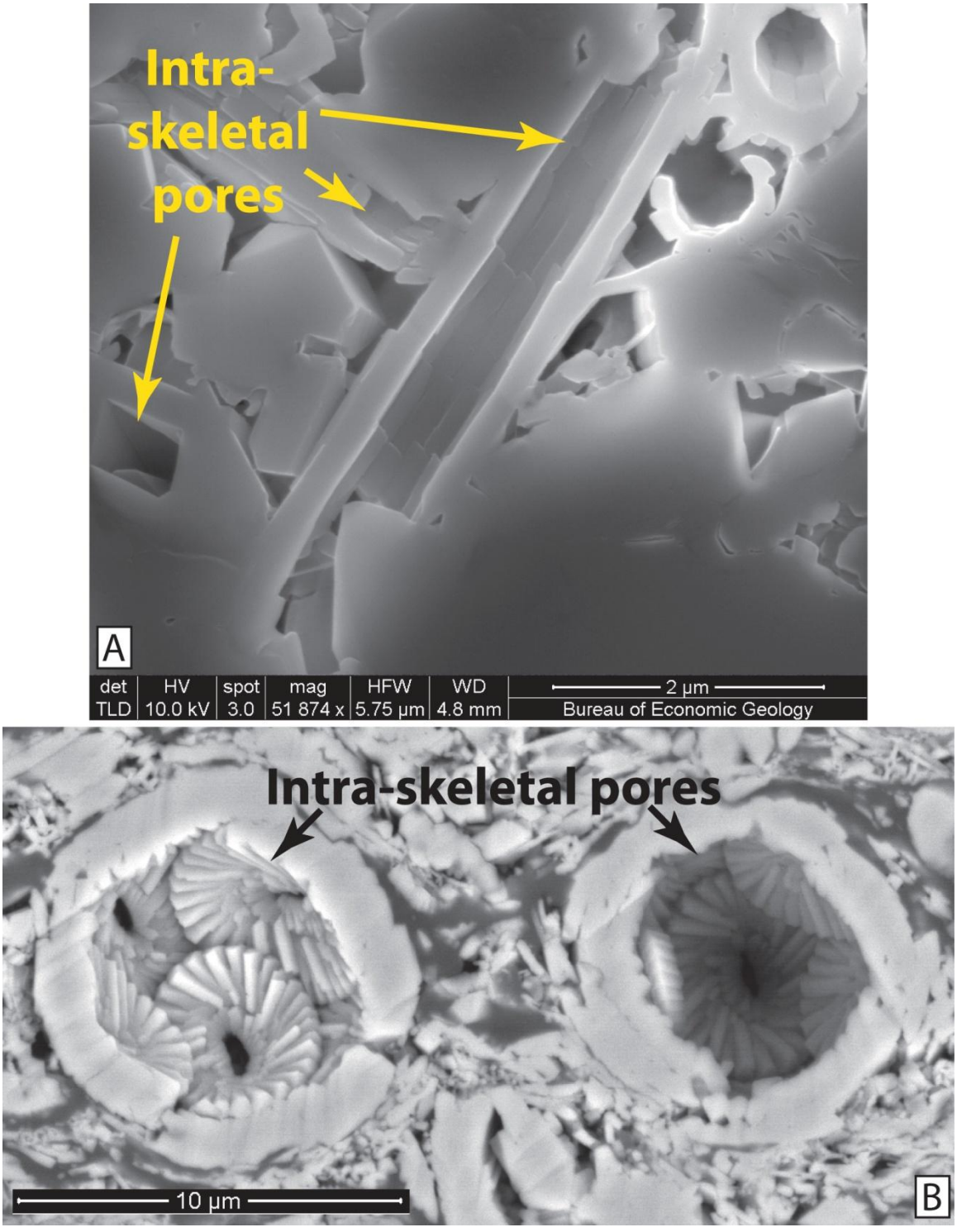

Figure 54: Examples of intra-skeletal pores including: A) pores within coccolith spines, and B) pores within two intact coccospheres. Well 1 sample 8.

Pores attributed to the presence of fluids, i.e., fluid inclusions, are observed in all samples typically composing less than ~0.1% of the bulk volume. These pores are very small (mean of ~27 nm), spherical (mean aspect ratio (length/width) ~1.4), and occur within skeletal debris and quartz. Inclusion pores are likely generated either from fluids caught during cementation or during growth of the skeleton.

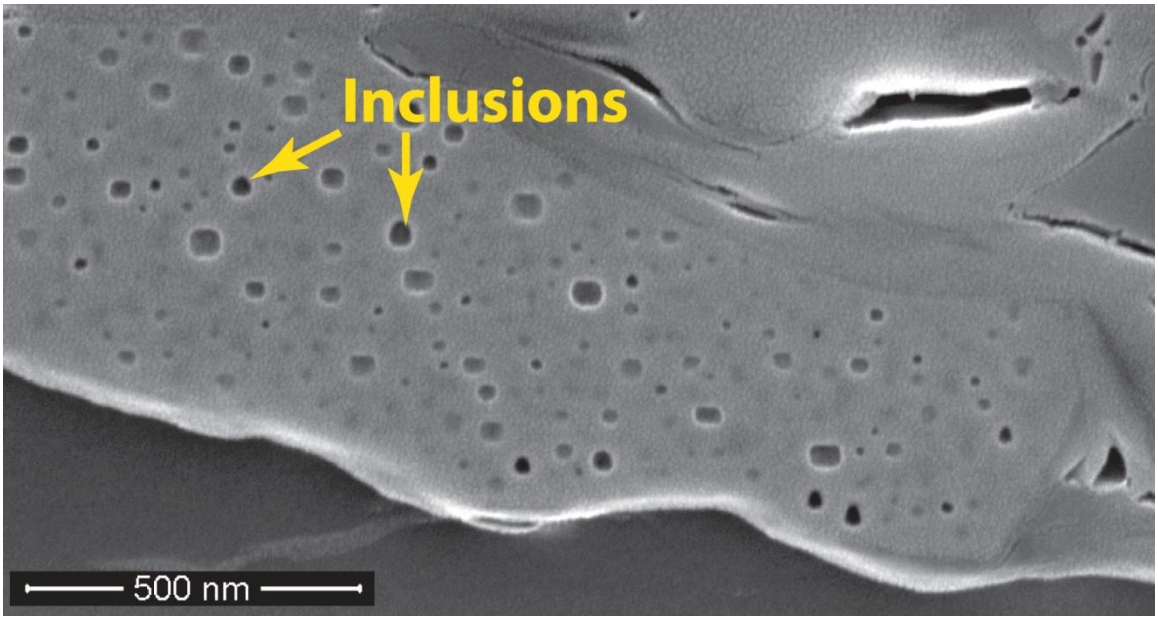

Figure 55: Example of inclusion pores within skeletal fragment. Well 1 sample 1.

Secondary pores attributed to grain dissolution are observed in several samples, and are commonly associated with grain replacement by albite. In Well 3 sample 1-136, secondary pores attributed to grain dissolution is associated with dissolved muscovite and/or kaolinite (Figure 56). These pores are recognizable from their shape, which mimics the morphology of the dissolved grain (Loucks et al., 2012), and can be replaced with authigenic albite and other cements. Possible dissolved primary grains can include

potassium feldspar and/or muscovite (Figure 56). Dissolution and replacement of feldspars is observed in low maturity and high-maturity samples, suggesting that it occurs throughout early burial. Dissolution of mica and/or kaolinite in Well 3 sample 1-136 occurred after microcrystalline apatite cementation and subsequent infill by porous bitumen. It is suspected that a large portion of OM-mineral interface pores in this sample were generated by partial dissolution, explaining the anomalously high volume (5.5% of the bulk volume).

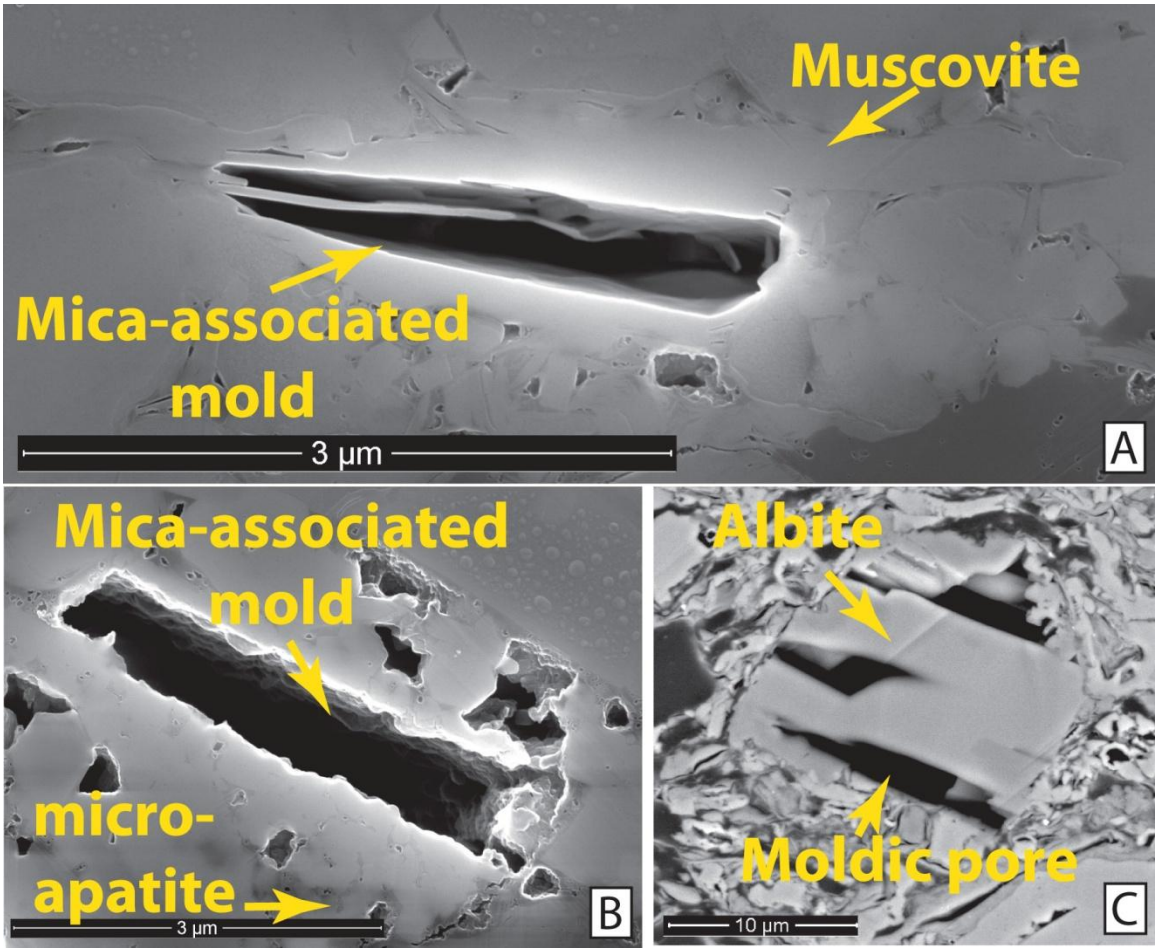

Figure 56: Examples of moldic pores resulting from partial or full dissolution. A) Partially dissolved muscovite/and or kaolinite, B) fully dissolved muscovite? C) Albite (as determined with EDS) replacing detrital grain with pores along cleavage plane. Well 3 sample 1-136 (A&B), Well 1 sample 16.

ORGANIC MATTER-HOSTED PORES

Pores within OM, or OM-hosted pores, are present in all high-maturity samples, as well as at low maturity within the Upper Eagle Ford, composing between 0% and 3.1% of the bulk volume in each sample. OM-hosted pores, typically 11.1 nm - 14.9 nm in size are significantly smaller than most mineral-associated pores, which range in median pore size from 20.3 nm - 68.1 nm. Quantitatively, these pores are subdivided into

complex and simple OM-hosted pores, distinguished by partitioning and the presence of "sub-chambers" within complex pores, implying connectivity to other OM-hosted pores (Milliken et al., 2013). The majority of these pores are interpreted as secondary and are a result of volatile expulsion during hydrocarbon generation, which accompanies a volume expansion (Lillico et al., 2001; Milliken et al., 2013; Seewald, 2013). OM-hosted pores present at low maturity (Ro ~0.5), however, are likely primary intra-kerogen pores.

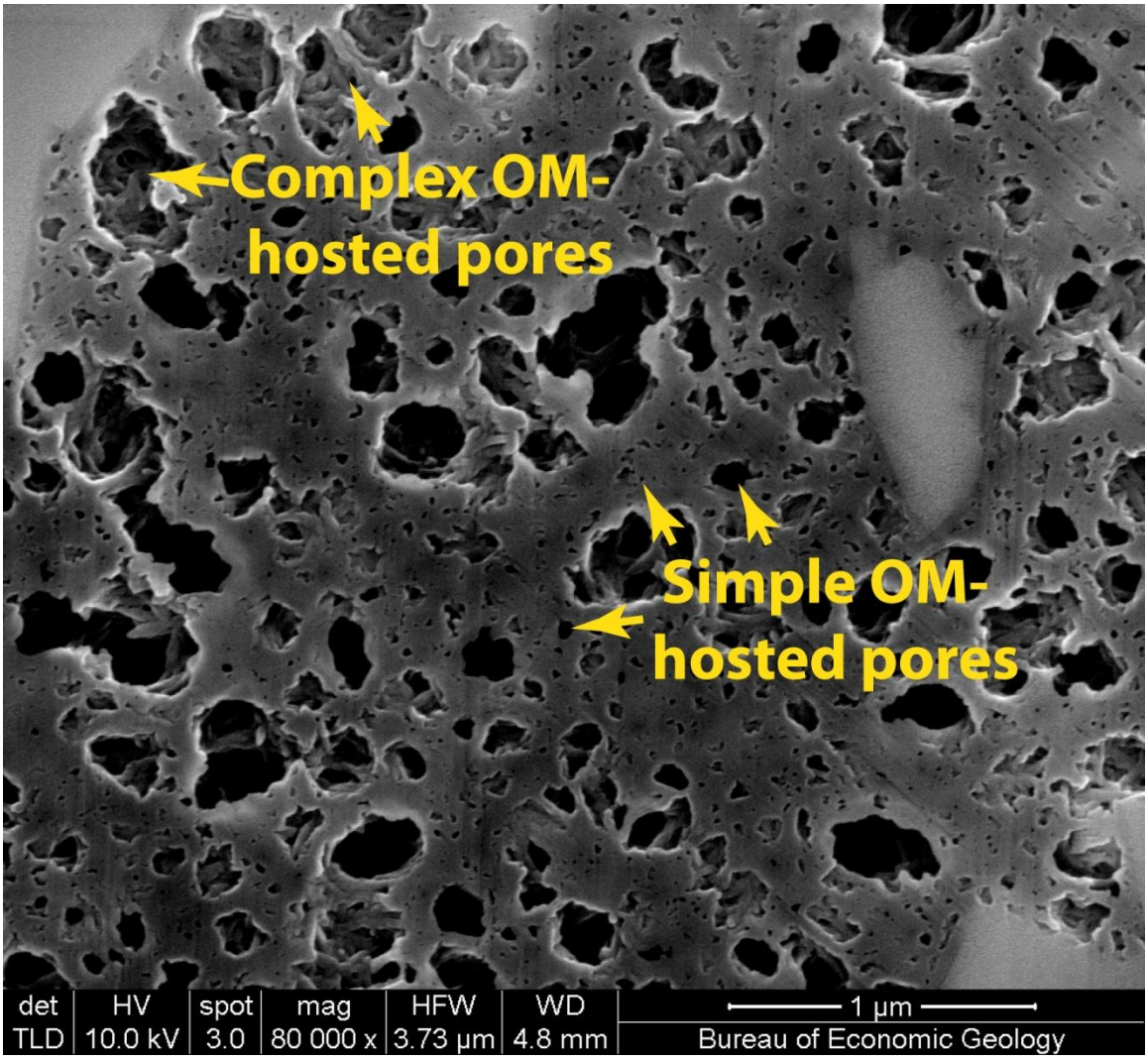

Figure 57: Secondary OM-hosted pores within bitumen infill of coccosphere. Well 3 sample 1-75.

Pores interpreted as primary within organic matter are observed within the Upper Eagle Ford at low and high maturity. Small, porous particles of OM are dispersed throughout clay seams are observed (Figure 18, 19A, 58A). These pores show a narrower size distribution and are, on average, larger than secondary OM-hosted pores (Figure 74). These pores show some heterogeneity in morphology; although general character, pore

size distribution and pore abundance is similar at both low and high maturity. This suggests that this kerogen is of a different composition and more inert (Table 4; Figures 58, and 62). Sun et al. (2014), shows, geochemically, that kerogen from this interval is more terrestrial in origin. Primary porosity within "woody" OM is present across maturities but is dispersed to distinct isolated particles.

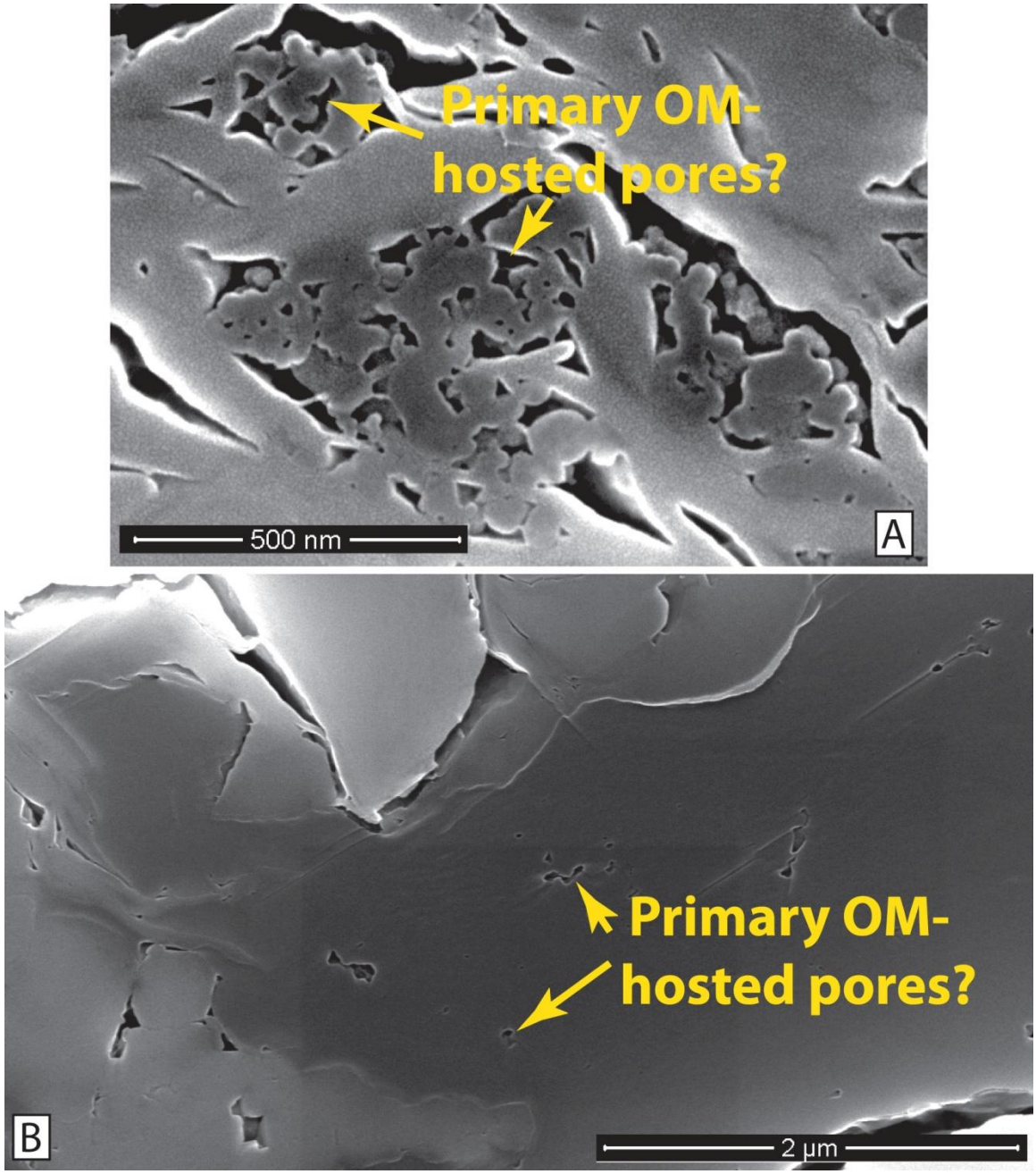

Figure 58: Examples of suspected primary OM-hosted pores from the UEF in Well 1. A) Porous OM interstitial with clay platelets, sample 19. B) Small, weakly developed pores in kerogen stringer, sample 23.

Secondary pores within OM, are present in significant volumes in the high-maturity samples, ranging from 0.02% - 3.60% (Table 4; Figure 62). Distribution, abundance, and morphology of secondary OM-hosted pores vary significantly between high-maturity samples. Observations, as well as comparison with point-count and trace data, suggest that OM-hosted pores develop in both kerogen and bitumen. These pores are likely controlled by a number of physical and chemical parameters including: OM type, distribution, and abundance. See *Porosity in the Wet-gas window* for more detail.

Artifact Pores

Identification of porosity induced by sample preparation and imaging is critical to the interpretation of in-situ porosity. Pores interpreted as artifacts are ignored in quantifications. Induced pores occur as shrinkage pores in clay and OM, as well as irregularities in sample coating.

QUANTITATIVE RESULTS

Point-count and manual-trace measurement of high-resolution SEM images yields compositional volume percentages, pore volume percentages, and pore size distributions. Pore volume and size measurements are presented for the cumulative measured pore population and by specific pore type within each sample, and well (Tables 2-7; Figures 52-77).

Modal Composition

Point counts and trace data (see *Quantitative Methods*) yield volumetric measurements of mineral composition, and OM. Trends in mineralogy and organic content (TOC) vary within each well and across maturity significantly impacting the pore network (Tables 2 and 3; Figures 61, 63, 64, 73 and 77). Samples are dominated by calcite, clay minerals, OM, and quartz. Dolomite, apatite, pyrite, titanium oxide, and feldspars are present in many samples (Table 2). Compositional controls on porosity are discussed in *Porosity Volume*, and *Pore Size Distribution.*

Burial diagenetic processes, both chemical and mechanical, have significantly altered the detrital grain assemblage. Distinction of detrital versus diagenetic heterogeneity is complicated by the challenge of discriminating authigenic and detrital components of clay size using petrographic methods. Interpretations are influenced by analogies to the architecture of sandstones and limestones (e.g., the notion that grain-shaped calcite is probably biogenic debris whereas intergrown rhombohedral calcite crystals contain a large portion of cement).

Calcite content determined by point counting increases from an average of 40.4% of the bulk volume in low maturity Well 1 (ranges from 18.6% - 54.3%) to an average of 50.3% in Well 4 (ranges from 40.3% - 57.0%) coincident with significant precipitation

of authigenic calcite (Table 2; Figure 37). Calcite content correlates inversely with clay at both low and high maturity, reflective of sediment mixing (Figure 1). Low-maturity samples show a weak inverse correlation between calcite and clay volume percent reflective of the volumetric significance of OM, which shows a strong inverse correlation with calcite volume (Figure 59).

TOC correlates inversely with calcite in low-maturity samples, and positively in high-maturity samples where significant infill of primary pore space by bitumen has occurred (Well 4), suggesting that volume of OM within high-maturity samples is strongly influenced by bitumen incursion (Figure 59). Well 1 has TOC values averaging 17.3% of the bulk volume (ranges from 4.9% to 37.9%), significantly greater than high-maturity samples which averaged 4.0% in Well 3 and 9.9% in Well 4. High-maturity samples with TOC values approaching those observed in the lower portion of Well 1 were not available for this study. It is unclear if this is due to deposition and/or sampling, or if there has been a volume loss in the detrital kerogen as bitumen and other hydrocarbons are generated.

Correlations between all parameters and clay volumes are weak. Clay composes an average of 26.2% of the bulk volume in Well 1 (ranges from 14.6% - 34.4%), whereas high-maturity samples had significantly lower proportions of clay. In high-maturity samples clay composes an average of 22.6% in Well 3 (ranges from 16.1% - 20.7%) and 18.2% in Well 4 (ranges from 2.3% - 31.9%) (Table 2). This 8% difference in well-averaged clay volume represents sedimentary and diagenetic processes. Differential proximity to extrabasinal and intrabasinal sediment supplies (e.g., rapid coccolithic "blooms" could differentially dilute extrabasinal input laterally) as well as hydro-dynamic "shoaling" of specific grain types can explain lateral heterogeneity. A decrease in volume occurs as a destruction of clay-hosted porosity which decreases from an average of 0.44%

of the bulk volume in Well 1 to 0.02% in Well 4 (Table 4; Figure 62). This would account for only a small portion of the ~8% difference in clay volume between Well 1 and Well 4. Reduction of clay volume potentially occurs through the illitization process. Awwiller (1993) described a volume loss of 15% throughout the illitization process in other Gulf Coast mudrocks.

A larger proportion of quartz occurs in high-maturity samples coincident with observed abundant crystalline quartz with euhedral crystal growth faces intergrown with calcite crystals (Table 2; Figures 38 and 59). Quartz composes an average of 5.2% of the bulk volume in Well 1 and 14.5% of the bulk volume in Well 4 (Table 2). Negative correlation between quartz abundance and calcite at low maturity reflects distinct extra-basinal and intra-basinal sediment sources and suggest that most quartz within Well 1 is detrital in origin (Figure 59). This suggests that the majority of the quartz at high maturity is likely authigenic in origin and precipitated during burial diagenesis. Weak positive correlations between quartz and calcite in high-maturity samples, suggest that quartz cement occurs in the greatest volumes where there was, or is an interparticle pore network (Figure 59, 60).

Other minerals occur in small amounts, typically less than 1%, and can compose as much as 8.9% of the bulk volume (Table 2). Low-maturity samples have significantly higher abundances of potassium-feldspar, and significantly lower abundance of albite (Table 2). Potassium-feldspar decreases from an average of 2.0% of the bulk volume in Well 1, and 0.1% - 0.2% of the bulk volume in Wells 3 and 4 respectively (Table 2). Albite increases from an average 1.1% of the bulk volume in Well 1 to averages of 2.2%-3.0% of the bulk volume in Wells 3 and 4 respectively (Table 2). Kaolinite is present in small amounts and decreases in abundance slightly across thermal maturity. Kaolinite composes 0.2% of the bulk volume in Well 1 and 0.1% - trace amounts in Wells 3 and 4

respectively, though a qualitative assement of foraminifer test filling cements is more revealing, and shows alteration of early kaolinite to Mg-rich phyllosilicate (clinochlore?) (Table 2; Figures 34, 35, and 39). Apatite is present locally in Well 3 sample 1-136 in significant volumes, up to 8.9% of the bulk volume, and also dispersed throughout the matrix in small amounts in high-maturity samples suggesting that it is a relatively late cement phase. Abundance and character of pyrite changes little across thermal maturity, reflective of its relatively early genesis.

Table #2: Point count measurments of mineral components

Well	Sample	Quartz (BV%)	Albite (BV%)	K-Feldspar (BV%)	Calcite (BV%)	Clay/ Mica (BV%)	Kaolinite (BV%)	Total Clay (BV%)	Dolomite (BV%)	Apatite (BV%)	Ti-Oxide (BV%)	Pyrite (BV%)	Other MIN (BV%)
1	23	4.6	0.3	2.0	44.7	25.3	0.1	25.4	0.0	0.0	0.0	0.7	0.0
1	19	0.9	0.7	5.6	54.3	21.0	0.0	21.0	0.0	0.0	0.0	0.0	0.6
1	16	2.4	0.1	0.7	51.6	24.4	0.3	24.7	0.0	0.0	0.0	0.0	0.0
1	11	4.6	1.4	1.4	42.0	34.4	0.0	34.4	0.0	0.0	0.0	0.0	0.0
1	8	1.7	2.1	2.4	39.3	28.6	0.7	29.3	5.7	0.0	0.1	0.0	0.0
1	4	13.9	3.3	1.1	32.7	14.6	0.0	14.6	0.7	0.0	0.0	1.9	0.1
1	1	8.1	0.0	0.6	18.6	33.9	0.0	33.9	0.0	0.6	0.0	0.4	0.1
3	1-31	6.1	3.9	0.3	51.9	27.3	0.0	27.3	0.0	0.0	0.0	0.1	0.0
3	1-61	10.7	7.3	0.0	48.4	26.0	0.0	26.0	0.3	0.0	0.0	0.4	0.0
3	1-66	17.9	0.6	0.0	56.4	16.1	0.0	16.1	0.0	0.0	0.0	0.0	0.0
3	1-136	5.9	0.3	0.0	48.9	20.7	0.3	21.0	0.0	8.9	0.1	0.0	0.0
4	1-5	7.6	4.0	0.6	40.3	31.9	0.0	31.9	2.6	1.7	1.7	0.4	0.0
4	1-10	19.9	0.7	0.0	53.7	14.0	0.0	14.0	0.0	0.0	0.0	1.6	0.0
4	1-75	11.4	1.7	0.2	57.0	16.3	0.0	16.3	0.1	0.3	0.0	0.5	0.1
4	1-80	17.9	0.1	0.0	59.4	2.3	0.0	2.3	3.0	0.0	0.0	0.0	0.0
4	1-90	21.7	0.9	0.0	46.1	15.3	0.1	15.4	0.9	0.1	0.0	0.1	0.0
4	1-100	8.1	3.6	0.1	47.1	29.7	0.0	29.7	0.3	0.0	0.0	0.6	0.0
4	1-123	14.9	4.3	0.6	48.4	17.7	0.0	17.7	0.0	0.0	0.3	1.0	0.0
1	avg	5.2	1.1	2.0	40.4	26.0	0.2	26.2	0.9	0.1	0.0	0.4	0.1
3	avg	10.1	3.0	0.1	51.4	22.5	0.1	22.6	0.1	2.2	0.0	0.1	0.0
4	avg	14.5	2.2	0.2	50.3	18.2	0.0	18.2	1.0	0.3	0.3	0.6	0.0

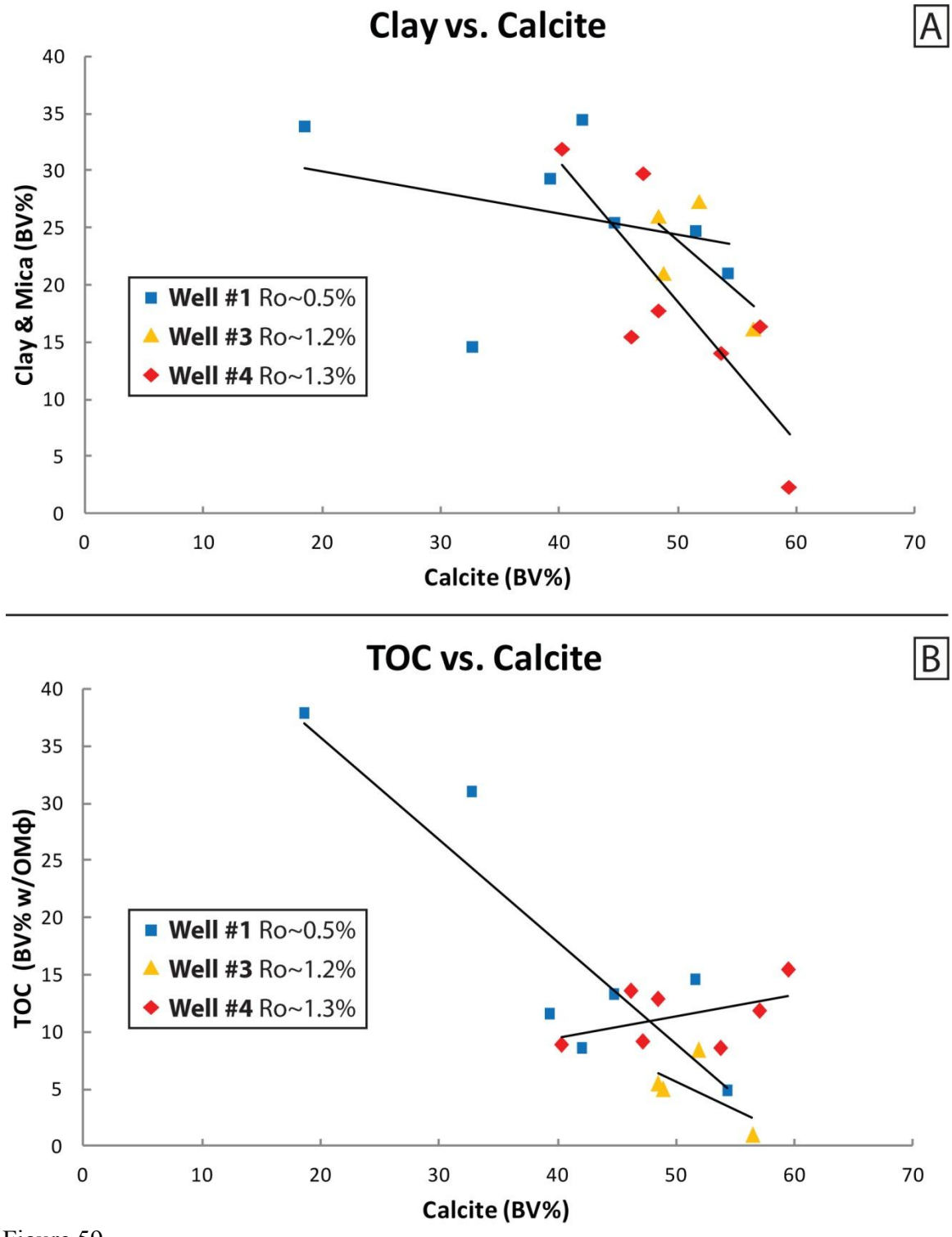
Clay vs. Calcite
A
Clay & Mica (BV%)
Calcite (BV%)
Well #1 Ro~0.5%
Well #3 Ro~1.2%
Well #4 Ro~1.3%
TOC vs. Calcite
B
TOC (BV% w/OMϕ)
Calcite (BV%)
Well #1 Ro~0.5%
Well #3 Ro~1.2%
Well #4 Ro~1.3%

Figure 59

Figure 59: Trends between components calculated by point-count analysis plotted as bulk volume percentages including: A) clay versus calcite values show a negative correlation between clay and calcite is observed at all maturities, however low-maturity samples with TOC values above 30% diverge from this trend. B) TOC versus calcite values. Note that samples with significant interparticle porosity (Well 1 and Well 3, see Table 4 and Figure 62) show strong negative correlations between TOC and calcite, whereas samples dominated volumetrically by OM-hosted pore networks (Well 4) show a positive correlation between TOC and calcite.

Table #3: Point count and trace measuremtns of porosity and OM volume

Well	Sample	Depth (ft)	TOC (Wt%)	TOC w/ OMφ (BV%)	TOC - OMφ (BV%)	φ Min (BV%)	φ of OM (BV%)	OM-Hosted φ (BV%)	φ visible (BV%)
1	23	186	2.8	13.3	13.1	9.0	1.5	0.2	9.2
1	19	267	2.1	4.9	4.5	12.1	7.3	0.4	12.5
1	16	322	5.9	14.6	14.6	5.9	0.0	0.0	5.9
1	11	379	5.5	8.6	8.6	7.6	0.0	0.0	7.6
1	8	423	7.2	11.6	11.6	7.7	0.0	0.0	7.7
1	4	459	12.5	31.0	31.0	0.7	0.0	0.0	0.7
1	1	498	13.6	37.9	37.9	0.1	0.0	0.0	0.1
3	1-31	8283	3.5	8.4	6.1	2.0	27.7	2.3	4.3
3	1-61	8313	3.6	5.5	4.5	1.3	18.0	1.0	2.3
3	1-66	8318	1.2	1.0	1.0	7.7	1.7	0.0	7.7
3	1-136	8388	3.5	5.0	4.5	10.0	10.5	0.5	10.5
4	1-5	9105	2.8	8.9	8.4	0.7	4.9	0.4	1.1
4	1-10	9109	1.3	8.6	8.3	1.6	2.8	0.2	1.8
4	1-75	9174	5.8	11.8	9.3	0.5	21.3	2.5	3.0
4	1-80	9179	2.7	15.4	12.9	1.9	16.5	2.5	4.4
4	1-90	9189	5.4	13.6	10.0	1.1	26.6	3.6	4.7
4	1-100	9199	3.1	9.1	8.0	0.6	12.3	1.1	1.7
4	1-123	9222	5.6	12.9	12.2	0.0	5.2	0.7	0.7
1	avg	362	7.1	17.4	17.3	6.2	1.3	0.1	6.2
3	avg	8326	2.9	5.0	4.0	5.3	14.5	1.0	6.2
4	avg	9168	3.8	11.5	9.9	0.9	12.8	1.6	2.5

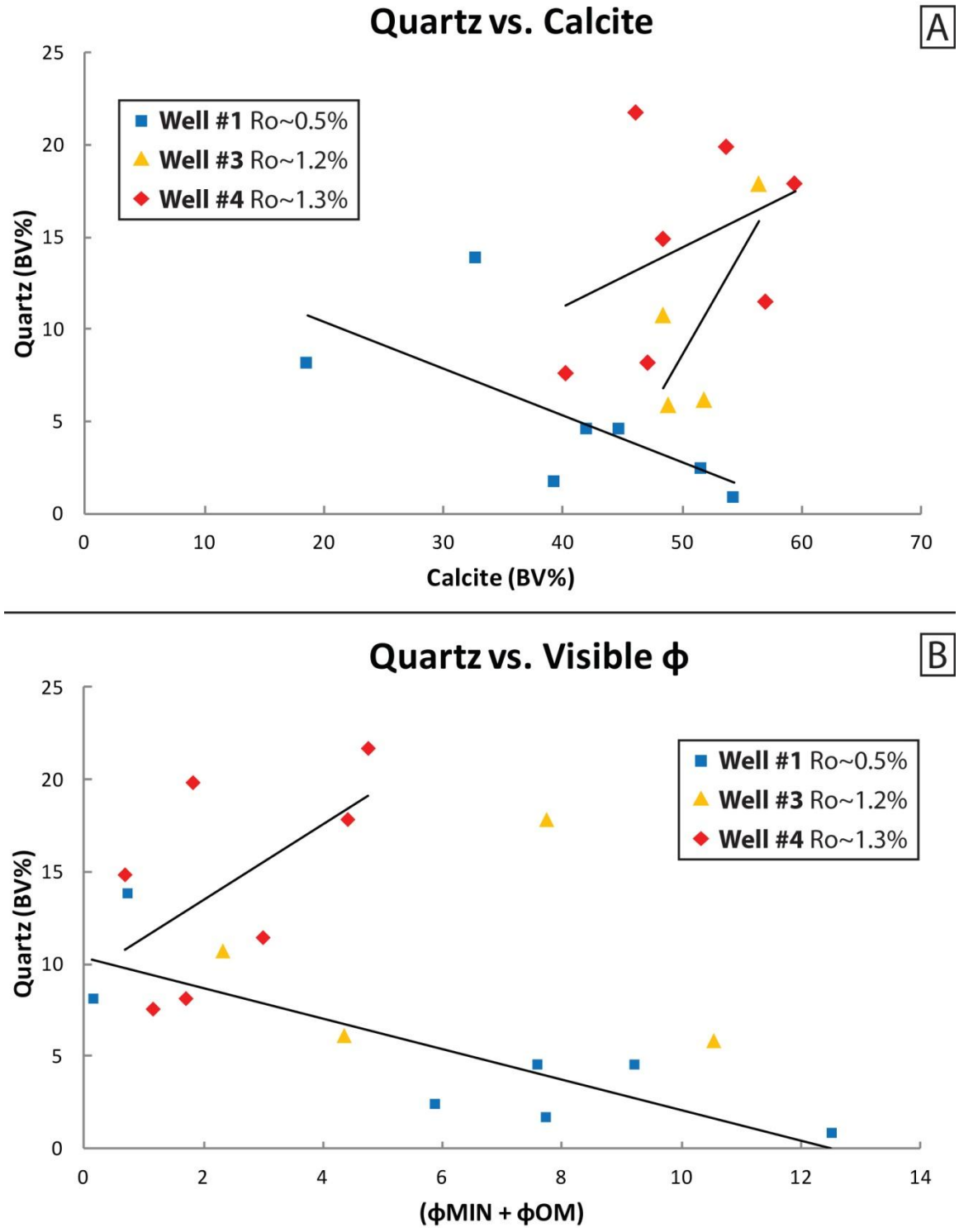
Quartz vs. Calcite
A
Well #1 Ro~0.5%
Well #3 Ro~1.2%
Well #4 Ro~1.3%
Quartz (BV%)
Calcite (BV%)
0
5
10
15
20
25
0
10
20
30
40
50
60
70
Quartz vs. Visible ϕ
B
Well #1 Ro~0.5%
Well #3 Ro~1.2%
Well #4 Ro~1.3%
Quartz (BV%)
(ϕMIN + ϕOM)
0
5
10
15
20
25
0
2
4
6
8
10
12
14

Figure 60

Figure 60: Cross-plots showing trends between mineral components calculated by point-count analysis and plotted as bulk volume percentages including: A) quartz versus calcite values show a negative correlation at low maturity and a positive correlation within high-maturity samples, and B) quartz versus visible porosity values in low-maturity samples show an inverse correlation (Well 1) but shows a weak positive correlation in Well 4, and no correlation in well 3.

Porosity Volume Measurements

Pore volume measurements are presented here for cumulative measured porosity by individual pore type within each sample, and as mean value of samples within each well. Measured pore volume percent ranges between 0.1% and 12.5% of the bulk volume within the data-set, with an average value of 4.8%. Total pore volume and volume of each pore type varies within each well and across burial conditions (i.e., between wells), as a function of mineral-associated and OM-hosted pore volumes (Table 3 and 4; Figures 61, 63, and 64). Both mineral-associated, and OM-hosted pore volumes vary with abundance and distribution of components, especially calcite and OM bulk volume percent (Figures 63 and 64). Abundance of clays, quartz, feldspars and other mineral componets show weak correlations with pore volume that are interpreted to be associative with calcite and OM abundance, (Table 2; Figure 59).

POROSITY VOLUMES IN WELL 1

Low-maturity samples from Well 1 have porosity values ranging between 0.1% and 12.5% of the bulk volume and average of 6.2%. Porosity values are strongly correlative with abundance of calcite, and inversely correlative with OM volume (Figure 61). Porosity is dominated by mineral-associated pores composing between 0.1% - 12.1% of the bulk volume, with an average of 6.2%. Mineral-associated pores that contribute significantly include: inter-mineral pores composing an average of 4.3% of the bulk volume, OM-mineral interface pores averaging 0.7% of the bulk volume, clay-hosted pores averaging 0.4% of the bulk volume, and intra-skeletal pores averaging 0.3% of the bulk volume (Table 4; Figure 62). Pores within carbonate aggregates, including inter-mineral, OM-mineral interface and intra-skeletal pores compose between 1.2% - 6.8% of the bulk volume in the five low-maturity samples where they occur (Table 4).

OM-hosted pores are present in low-maturity samples from Well 1 in small volumes, averaging 0.1% of the bulk volume, ranging from 0.2%-0.4% BV where present). However, at low maturity OM-hosted pores are not abundant and are restricted stratigraphically to the Upper Eagle Ford, composing an average of 0.28% of the bulk volume in samples where they occur (Table 4; Figure 62).

POROSITY VOLUMES IN WELL 3

High-maturity samples from Well 3 have visible porosity values composing an average of 2.3% - 10.5% of the bulk volume, averaging 6.2% (Tables 3 and 4). However only 4 samples all with relatively low TOC values, ranging from 1.0% - 6.1% of the bulk volume, were available to sample, and likely did not encompass enough heterogeneity in this well to be perfectly analogous to measurements from Well 1 and Well 4 (Table 3). Porosity within these samples shows a weak correlation with calcite and an inverse correlation with TOC (Figure 61), and consist of significant volumes of both OM-hosted porosity as well as relatively high proportions of mineral-associated porosity. Mineral-associated porosity in Well 3 composes 2.0% - 10.0% of the bulk porosity samples from Well 3 with an average of 5.3%. OM-hosted porosity composes trace amounts to 2.3% of the bulk volume. Samples 1-31 and 1-61 have pore networks dominated by OM-hosted pores, and OM-mineral interface pores, with some inter-mineral and clay-hosted porosity (Table 4; Figure 62). Sample 1-66 has very abundant inter-mineral pores, composing 7.3% of the bulk volume, and very small volumes of other pore types (note the TOC value is the lowest in the sample set, 1.0% of the bulk volume). Sample 1-136 has a pore network that is dominated volumetrically by OM-mineral interface pores, moldic pores associated with dissolution of muscovite and/or kaolinite and small portions of inter-mineral, clay-hosted and OM-hosted pores (Table 3; Figures 56 and 62). This sample

shows an unusually strong diagenetic overprint, with very abundant micro-crystalline apatite composing 8.9% of the bulk volume, bitumen, kaolinite, and mica-associated dissolution (Figure 33B, 40, and 56).

POROSITY VOLUMES IN WELL 4

High-maturity samples from Well 4 have porosity values ranging from 0.7% to 4.7% of the bulk volume with an average of 2.5%, significantly lower than Wells 1 & 2 (Table 3). Porosity in samples from Well 4 correlates positively with both TOC and calcite volume percent (Figure 61). Samples from Well 4 are dominated volumetrically by OM-hosted pores composing 0.2% - 3.6% of the bulk volume (average of 1.6%), and OM-mineral interface pores composing 0.0% - 1.8% of the bulk volume (average of 0.6%) (Table 3; Figure 62). Inter-mineral pores make up only 0.0% - 0.6% of the bulk volume (average of 0.2%), and visible clay-hosted porosity is present only in trace amounts in these samples (Table 3; Figure 62). Samples from the Upper Eagle Ford show significantly lower proportions of OM-hosted porosity than samples from the Lower Eagle Ford, as well as significant (0.6% of the bulk volume) inter-mineral porosity in sample 1-10 (Figure 62). Abundance of OM-interface porosity, and co-occurrence with OM-hosted pores (especially in sample 1-80) suggest that a significant proportion of pores between OM and mineral surfaces are resultant of secondary gas-bubble generation.

Well-averaged pore volumes decrease by an average of 3.7% across burial conditions. Across thermal maturity: an 85.4% overall decrease in mineral-associated pore volumes or a well-average difference of 5.3% of the bulk volume between Well 1 and 4, and an increase in OM-hosted pore volumes by an average of 1.5% between Well 1 and 4 is observed (Table 3; Figure 62).

Porosity loss of mineral-associated pore includes: inter-mineral pores with a 4.1% difference in average bulk volume between Well 1 and 4), clay-hosted pores with a 0.4% difference in average bulk volume between Well 1 and 4), and intra-skeletal with a 0.3% difference in average bulk volume between Well 1 and 4) (Table 3; Figure 62). OM-mineral interface pores maintain roughly the same average value in each well of 0.9% of the bulk volume (Table 3). Well-average mineral-associated porosity within fecal pellets decreases by 98.4%, suggesting that intra-pellet pores are especially susceptible to destruction (Table 3).

OM-hosted porosity increases significantly across thermal maturity (well-average increase of 1.5% of the bulk volume (Table 4; Figure 62). Very little OM-hosted porosity is present at low maturity, and it is interpreted as primary (Table 4; Figure 62). OM-hosted pore volumes vary significantly in high-maturity samples composing 0.04% - 3.6% of the bulk volume in Wells 3 & 4) and an average of 62.2% of porosity in Well 4 (Table 4; Figure 62). OM-hosted pore volumes correlate with both calcite and OM volume, however there are abundant outliers, suggesting other variables (e.g., OM type and chemistry) likely influence porosity generation within OM (Figure 64).

Table #4: Measured bulk volume perecentages of pore types.

Well	Sample	φ Visible (BV%)	φ MIN-Ass. (BV%)	φ OM-Hosted (BV%)	φ Inter-MIN (BV%)	φ Interface (BV%)	φ Clay-hosted (BV%)	φ Intra-Pellet* (BV%)	φ Intra-Skeletal (BV%)	φ Mica-Ass. Mold (BV%)	φ Inclusion (BV%)
1	23	9.2	9.0	0.20	7.15	0.42	0.96	3.78	0.16	0.00	0.01
1	19	12.5	12.1	0.35	9.12	1.18	0.68	5.96	0.69	0.00	0.00
1	16	5.9	5.9	0.00	2.68	1.63	0.15	2.03	0.42	0.00	0.07
1	11	7.6	7.6	0.00	5.39	0.85	1.08	1.17	0.07	0.00	0.00
1	8	7.7	7.7	0.00	5.23	0.10	0.12	6.85	0.43	0.00	0.02
1	4	0.7	0.7	0.00	0.19	0.46	0.04	0.00	0.00	0.00	0.02
1	1	0.1	0.1	0.00	0.02	0.09	0.03	0.00	0.00	0.00	0.00
3	1-31	4.3	2.0	2.34	0.75	0.97	0.25	0.01	0.00	0.00	0.03
3	1-61	2.3	1.3	0.99	0.55	0.66	0.09	0.00	0.00	0.00	0.02
3	1-66	7.7	7.7	0.02	7.30	0.27	0.13	0.00	0.00	0.00	0.01
3	1-136	10.5	10.0	0.52	0.54	5.53	0.61	0.08	0.02	3.20	0.02
4	1-5	1.1	0.7	0.43	0.04	0.32	0.03	0.00	0.00	0.00	0.00
4	1-10	1.8	1.6	0.24	0.61	1.05	0.01	0.00	0.04	0.00	0.01
4	1-75	3.0	0.5	2.52	0.17	0.14	0.03	0.10	0.04	0.00	0.03
4	1-80	4.4	1.9	2.54	0.03	1.81	0.00	0.00	0.00	0.00	0.02
4	1-90	4.7	1.1	3.60	0.09	0.67	0.04	0.23	0.00	0.00	0.11
4	1-100	1.7	0.6	1.12	0.24	0.27	0.05	0.00	0.00	0.00	0.01
4	1-123	0.7	0.0	0.67	0.00	0.00	0.00	0.00	0.00	0.00	0.00
1	avg	6.2	6.2	0.08	4.26	0.68	0.44	2.83	0.25	0.00	0.02
3	avg	6.2	5.3	0.97	2.28	1.86	0.27	0.02	0.00	0.80	0.02
4	avg	2.5	0.9	1.59	0.17	0.61	0.02	0.05	0.01	0.00	0.03

*note that Intra-Pellet pores are composed of Inter-MIN, Interface, and Intra-Skeletal pores

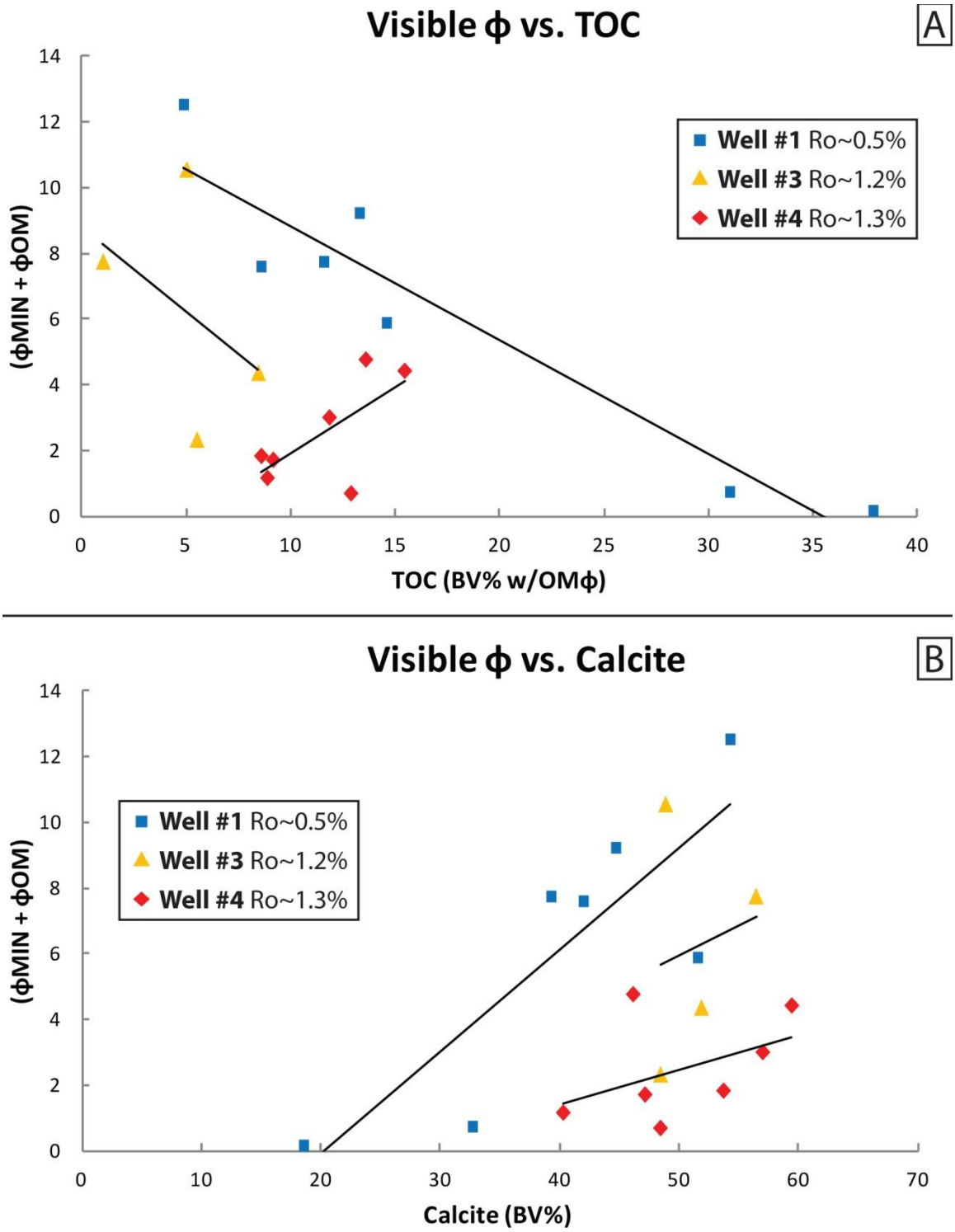
Visible ϕ vs. TOC
A
Well #1 Ro~0.5%
Well #3 Ro~1.2%
Well #4 Ro~1.3%
(ϕMIN + ϕOM)
TOC (BV% w/OMϕ)
0
2
4
6
8
10
12
14
0
5
10
15
20
25
30
35
40
Visible ϕ vs. Calcite
B
Well #1 Ro~0.5%
Well #3 Ro~1.2%
Well #4 Ro~1.3%
(ϕMIN + ϕOM)
Calcite (BV%)
0
2
4
6
8
10
12
14
0
10
20
30
40
50
60
70

Figure 61

Figure 61: Cross-plots showing between components and visible porosity calculated by point-count analysis and plotted as bulk volume percentages. A) Total visible pore volume percentage (ϕMIN + ϕ OM) versus volume percent OM (TOC) including OM-hosted porosity. B) Total visible pore volume percentage (ϕMIN + ϕ OM) versus volume percent calcite.

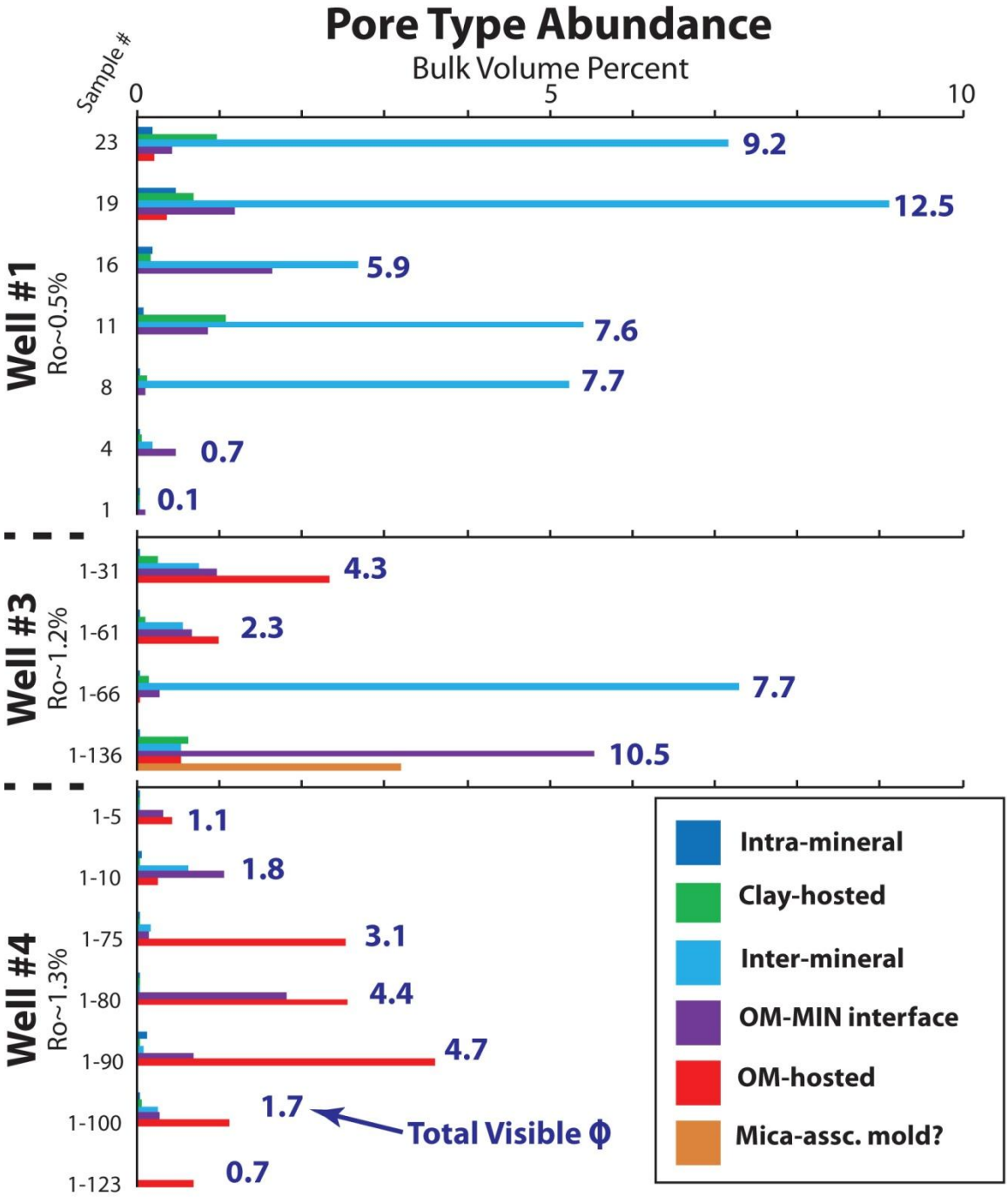
Pore Type Abundance
Bulk Volume Percent
Sample #
0
5
10
Well #1
Ro~0.5%
23
19
16
11
8
4
1
9.2
12.5
5.9
7.6
7.7
0.7
0.1
Well #3
Ro~1.2%
1-31
1-61
1-66
1-136
4.3
2.3
7.7
10.5
Well #4
Ro~1.3%
1-5
1-10
1-75
1-80
1-90
1-100
1-123
1.1
1.8
3.1
4.4
4.7
1.7
0.7
Total Visible ϕ
Intra-mineral
Clay-hosted
Inter-mineral
OM-MIN interface
OM-hosted
Mica-assc. mold?
Figure 62

Figure 62: Chart showing volume percentage of pore types per sample in Wells 1, 3, and 4. Samples organized stratigraphically but not to scale. Visible porosity in dark blue along left margin. Note Well1 is dominated by interparticle pores (inter-mineral and OM-interface), Well 4 is dominated by OM-hosted and OM-interface pores, and Well 3 has samples dominated by interparticle pores and by OM-hosted porosity. Moldic pores are present in Well 3 sample 1-136, likely resultant from dissolution of phyllosilicates (Figure 56). OM-hosted pores are present in high-maturity samples (Wells 3 and 4), as well as at low maturity in small abundances isolated to the Upper Eagle Ford.

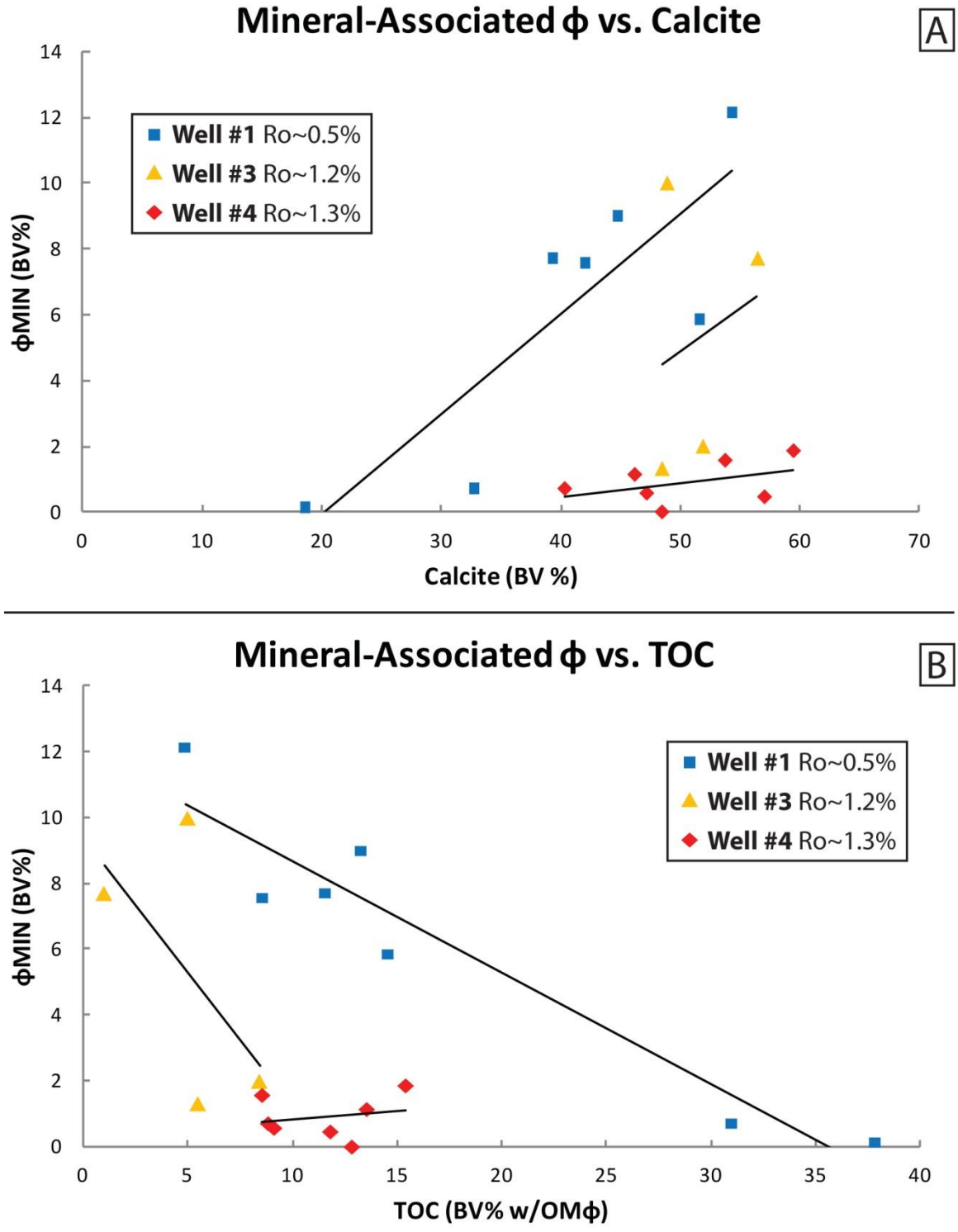
Mineral-Associated ϕ vs. Calcite
A
Well #1 Ro~0.5%
Well #3 Ro~1.2%
Well #4 Ro~1.3%
ϕMIN (BV%)
Calcite (BV %)
0
2
4
6
8
10
12
14
0
10
20
30
40
50
60
70
Mineral-Associated ϕ vs. TOC
B
Well #1 Ro~0.5%
Well #3 Ro~1.2%
Well #4 Ro~1.3%
ϕMIN (BV%)
TOC (BV% w/OMϕ)
0
2
4
6
8
10
12
14
0
5
10
15
20
25
30
35
40

Figure 63

Figure 63: Cross-plots showing between components and mineral-associated porosity calculated by point-count analysis and plotted as bulk volume percentages. A) Mineral-associated pore volume (ϕMIN) versus calcite volume percentage. B) ϕMIN versus total organic volume (TOC) including OM-hosted porosity. Note ϕMIN correlates positively with calcite at in all three wells, and as well as with TOC in Well 4. ϕMIN correlates inversely with TOC in Wells 1 and 3.

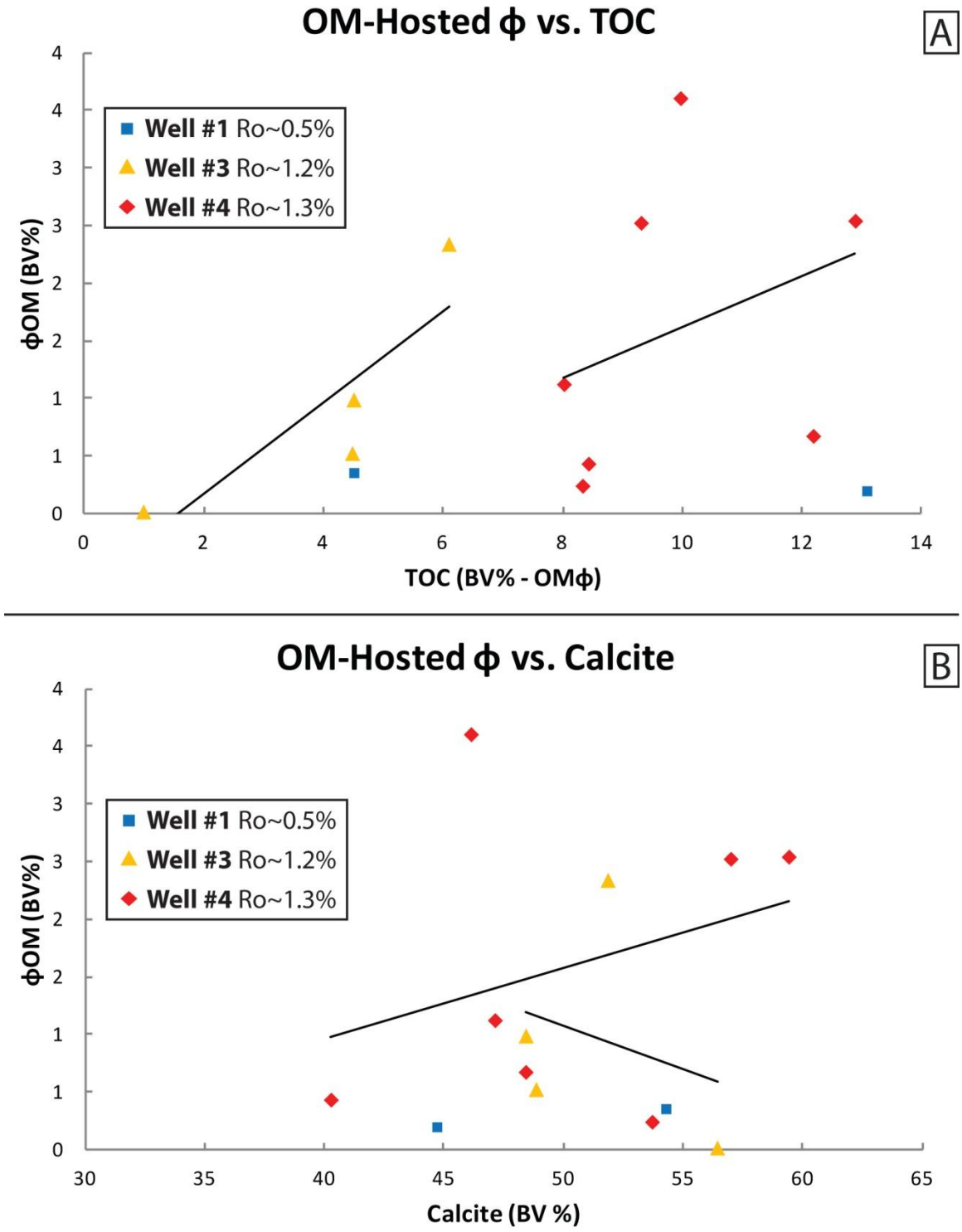
OM-Hosted ϕ vs. TOC
A
Well #1 Ro~0.5%
Well #3 Ro~1.2%
Well #4 Ro~1.3%
ϕOM (BV%)
TOC (BV% - OMϕ)
0
2
4
6
8
10
12
14
OM-Hosted ϕ vs. Calcite
B
Well #1 Ro~0.5%
Well #3 Ro~1.2%
Well #4 Ro~1.3%
ϕOM (BV%)
Calcite (BV %)
30
35
40
45
50
55
60
65

Figure 64

Figure 64: Cross-plots showing trends between components and OM-hosted porosity calculated by point-count analysis and plotted as bulk volume percentages. A) Total OM-hosted pore volume percentage (ϕOM) versus total organic content (TOC) excluding the volume of OM-hosted pores. B) ϕOM versus calcite volume percentage. Note that ϕOM correlates positively with TOC in both high maturity wells, as well as with calcite in Well 3. Well 3 shows a very weak inverse correlation with because sample 1-66 has abundant calcite (56.4% BV) and very little OM (1.0% BV), the three other samples show a positive correlation.

Pore Size Distributions

42,236 pores consisting of 20,708 mineral-associated pores and 21,528 OM-hosted pores were manually traced and classified at different magnifications within 18 samples from three wells, yielding a variety of size and shape measurements (Tables 5-7; Figures 65-77). Here, size data are presented for samples as: populations of all pores, OM-hosted pores, mineral-associated pores, and by specified type. Populations are presented for: within each sample, within each well, and as averaged-values in each well (Figures 65, 66-72, 74-76). Histograms (Figures 65, 67, 69, 71, and 75), binned to equivalent circular diameter (ECD) of 10 nm, are utilized to visually represent numerical distribution of relatively smaller pores (<300 nm), and to calculate cumulative distributions (as described in *Quantification of Pore Size Distributions*), whereas plots of cumulative area percent against equivalent circular diameter, are utilized to visually represent relative volumetric contribution of the population to pore type volumes (Figures 66, 68, 70, 72,74, and 76). As observed with pore volumes, pore size correlates best with volume of OM and calcite, suggesting they are primary controls on pore size at both low and high maturities (Figures 74 and 77).

Cumulative Pore Size Distributions

Total measured pores range in size from 3.6 nm to 3056.5 nm (ECD) with size distributions that vary dramatically within each sample and across thermal maturity. A decrease in the proportion of large pores and an increase in the proportion of small pores is measured across maturation from the early oil-window (Well 1 Ro~0.5%) to the gas window (Well 3 Ro~1.2, Well 4 Ro~1.3%) (Figure 65). The proportion of pores less than 20 nm increases from 11.8% of SEM visible porosity in Well 1, 44.6% in Well 3 and 67.5% in Well 4. Additionally, the proportion of pores larger than 20 nm decreases from

88.2% in Well 1, 55.4% in Well 3 and 32.5% in Well 4 (Figure 65). More specifically, high-maturity samples have smaller and volumetrically less abundant mineral-associated pores, as well as significantly more (numerically and volumetrically) small OM-hosted pores than low-maturity samples (Table 3; Figure 62, 67, 68, and 74). Within each well, cumulative pore size varies as a function of the size and abundance of OM-hosted and mineral-associated pores.

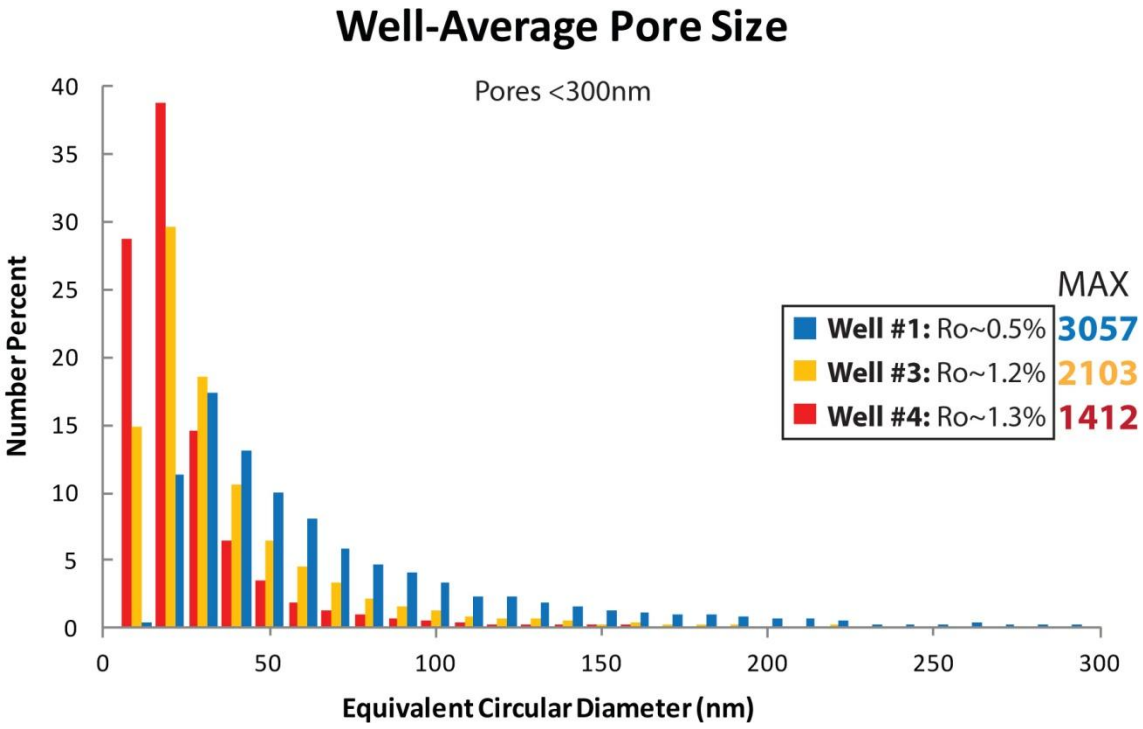

Figure 65: Histogram of the average pore-size distribution of each well binned by equivalent circular diameter values of 10 nm for pores less than 300 nm. Note the increased proportion of small (0-20 nm) and decreased proportion of pores larger than ~20 nm with maturation.

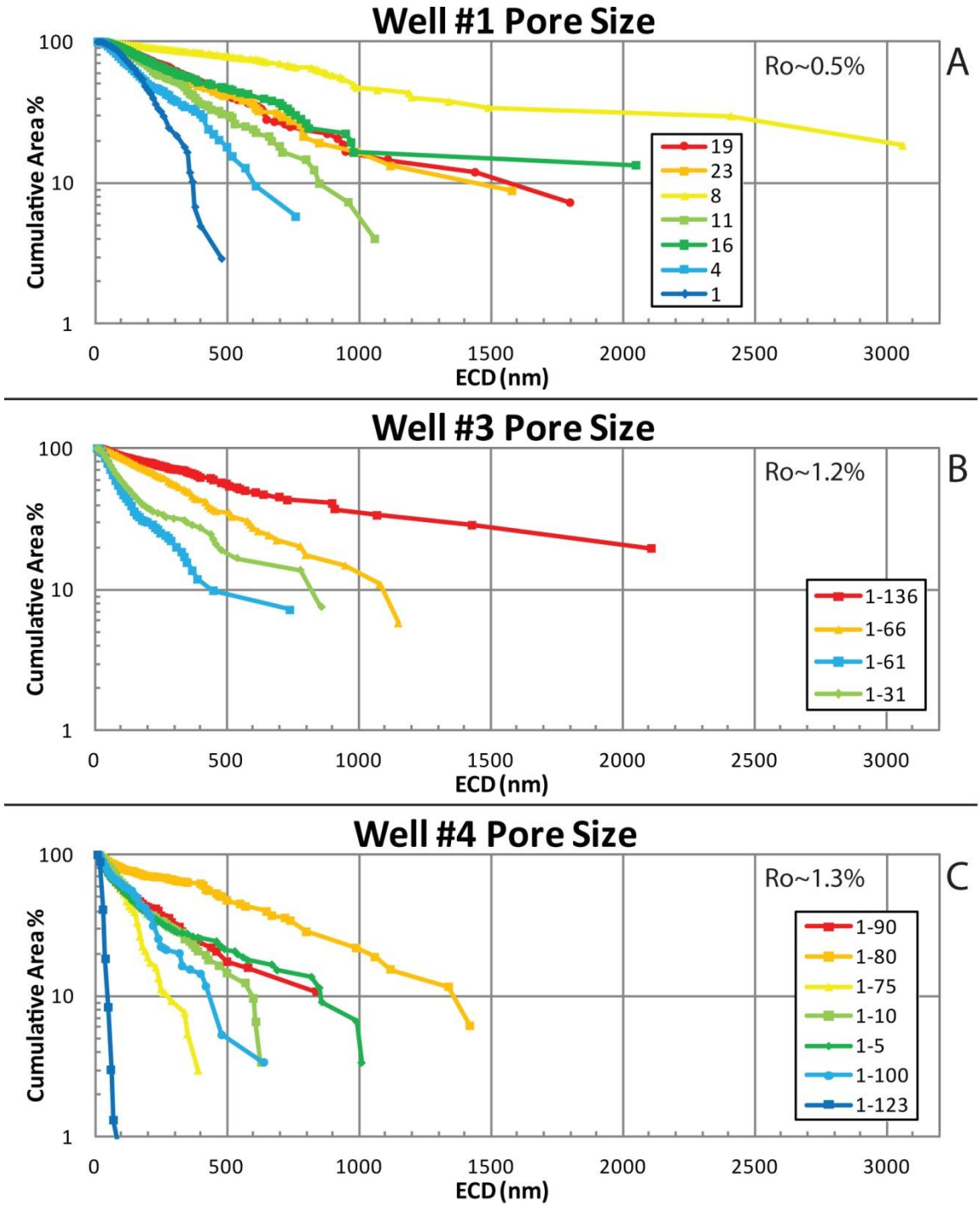
Well #1 Pore Size
Ro~0.5%
A
Cumulative Area %
ECD (nm)
19
23
8
11
16
4
1
Well #3 Pore Size
Ro~1.2%
B
1-136
1-66
1-61
1-31
Well #4 Pore Size
Ro~1.3%
C
1-90
1-80
1-75
1-10
1-5
1-100
1-123

Figure 66

Figure 66: Binned cumulative area percent plotted against equivalent circular diameter (ECD) for all samples in Wells 1, 3 and 4. Samples labeled and coded by porosity within each well (red is most porous, blue is least porous). Cumulative area percent is plotted on a logarithmic scale to amplify visual representations of differences.

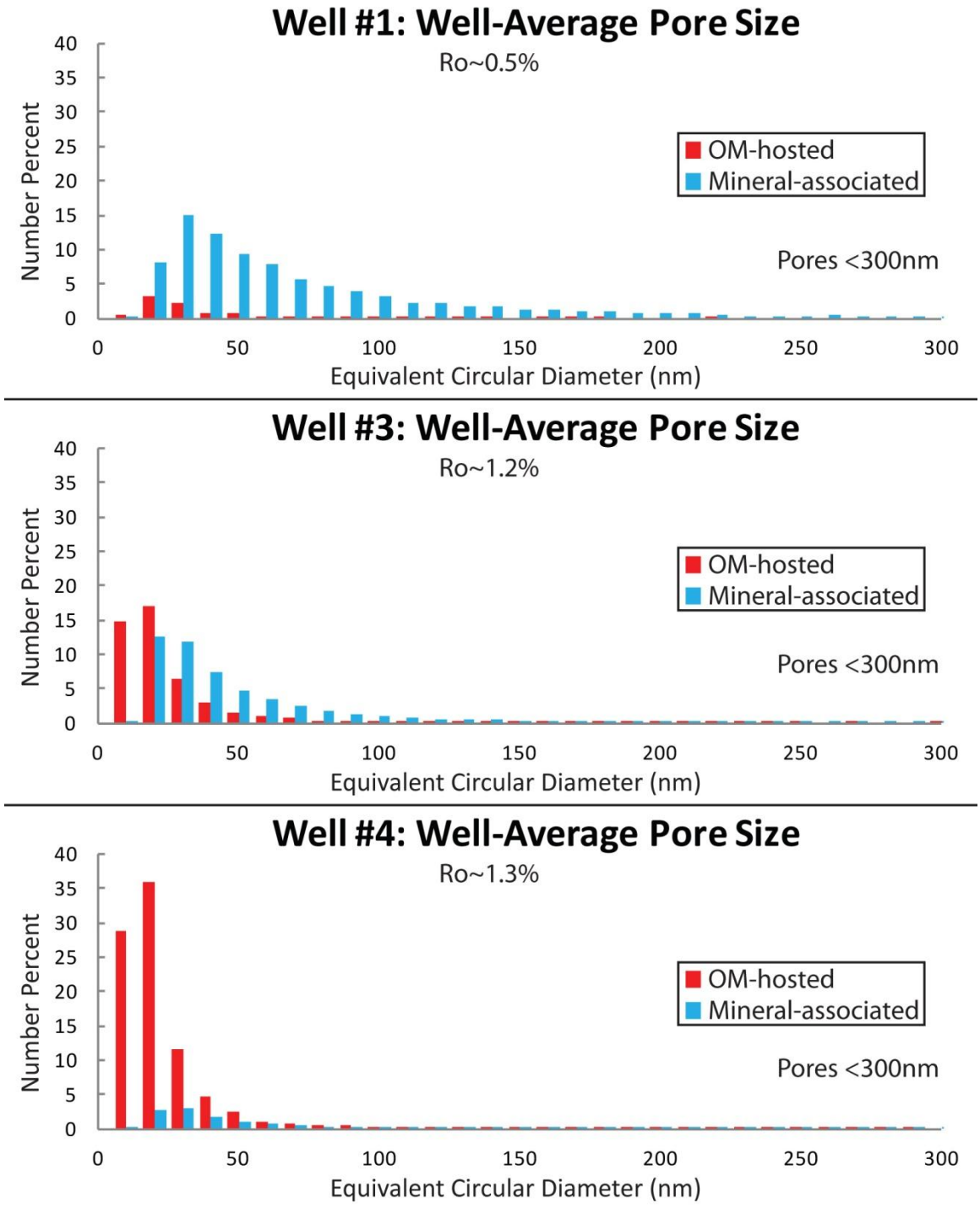
Well #1: Well-Average Pore Size
Ro~0.5%
Number Percent
OM-hosted
Mineral-associated
Pores <300nm
Equivalent Circular Diameter (nm)
Well #3: Well-Average Pore Size
Ro~1.2%
Number Percent
OM-hosted
Mineral-associated
Pores <300nm
Equivalent Circular Diameter (nm)
Well #4: Well-Average Pore Size
Ro~1.3%
Number Percent
OM-hosted
Mineral-associated
Pores <300nm
Equivalent Circular Diameter (nm)

Figure 67

Figure 67: Histograms of number percent of OM-hosted and mineral-associated pores scaled relative to measured proportions of porosity in 10 nm bins in Wells 1, 3 and 4. A decrease in abundance of large mineral-associated pores (greater than ~50 nm, the "tail") with depth (from Well 1 to Wells 3 and 4), and a decrease in the proportion of small (less than ~50 nm) mineral-associated pores in samples where significant porosity loss has occurred via bitumen infill (Well 4). High-maturity samples have significantly higher numerical proportions of smaller (mode~15 nm) OM-hosted pores.

Table #5: Calculated pore size measurements of all pores. Pore size is expressed as equivallent circular diameter (nm).

Well	Sample	# Total pores	Cum Max	CUM MIN	D10a CUM*	D50a CUM	D90a CUM	D10n CUM	D50n CUM	D90n CUM
1	23	1695	1573.3	8.4	1450	384	87	151	50	26
1	19	2480	1799.3	5.6	1587	413	100	167	50	25
1	16	1602	2049.9	10.4	**2050**	435	103	178	58	30
1	11	1458	1053.5	10.9	849	328	99	200	69	34
1	8	674	3056.5	14.3	**3056**	975	232	298	79	42
1	4	1349	754.4	8.7	603	200	58	116	46	25
1	1	857	471.1	8.1	371	187	71	159	52	27
3	1-31	4302	856.8	4.2	829	135	36	65	27	14
3	1-61	3074	730.2	4.5	445	100	34	67	29	16
3	1-66	1869	1149.5	5.5	1092	347	83	141	44	24
3	1-136	2665	2103.3	4.4	**2103**	576	86	90	33	16
4	1-5	2698	1007.4	4.2	856	132	26	44	17	13
4	1-10	2019	622.8	5.4	596	145	37	71	29	16
4	1-75	2562	380.2	4.5	273	115	35	70	27	14
4	1-80	2525	1411.8	4.1	1364	484	50	58	27	14
4	1-90	4151	836.8	3.6	**837**	149	32	54	25	13
4	1-100	1988	632.7	5.0	436	158	30	51	26	14
4	1-123	4268	142.3	4.4	48	28	19	33	22	12
1	avg	1445	1536.9	9.5	1423.6	417.5	107.2	181.2	57.8	29.9
3	avg	2978	1209.9	4.6	1117.2	289.5	59.6	90.7	33.5	17.6
4	avg	2887	719.2	4.5	630.0	172.9	32.8	54.5	24.6	13.7
Total	avg	2346	1146.2	6.5	1046.9	293.9	67.7	111.8	39.5	20.8
Total	max	4302	3056.5	14.3	3056.5	975.1	232.3	298.0	78.5	41.8
Total	min	674	142.3	3.6	48.3	28.1	19.3	33.2	17.2	12.4
Total	sum	42236								

*bold values indicate samples for which the D10 value was exceeded by a single pore. The size of the largest pore is listed.

MINERAL-ASSOCIATED PORE SIZE DISTRIBUTIONS

Measured mineral-associated pores range in size from 8.1 nm to 3056.5 nm (ECD), the size distribution of which varies significantly across thermal maturity and within each well dependent on many factors. Within each well, abundance and distribution of OM and/or calcite appear to be major controls on mineral-associated pore size, and porosity (Figures 63 and 65). Abundance of clays, quartz, feldspars and other mineral componets show very weak correlations with pore size that are interpreted to be associative with TOC and calcite abundance, (similar interpretation made in *Pore Volume Measurements*). Mineral-associated pore size correlates strongly with calcite within low-maturity samples, suggesting that rigid calcite grains shelter the largest pores (Figure 15). Correlations are much weaker in high-maturity samples, where there is significant diagenetic influence on mineral-associated pore size (Figure 15). Similarly, mineral-associated pore size correlates strongly inversely against OM volume at all maturities (Figure 73A). This suggest that primary pore size (and volume) decrease occurs from: differential compaction of ductile kerogen especially during early diagenesis as described in Milliken et al. (2014b)), as well as infill of primary pore space by mobilized bitumen (see Discussion).

More specifically: inter-mineral, OM-mineral interface, and clay-hosted pores exhibit a decrease of the proportion pores larger than 50 nm and an increase of the proporiton of inter-mineral pores smaller than 50 nm across burial conditions (Figures 69-72). Intraparticle inclusion pores maintain similar size distributions and volume (Figures 71 and 72). Intra-pellet and intra-skelal pores show a smaller fraction of large

pores, but suffer a more significant loss of the majority of their pore volume and population with bitumen infill (Table 4; Figure 72).

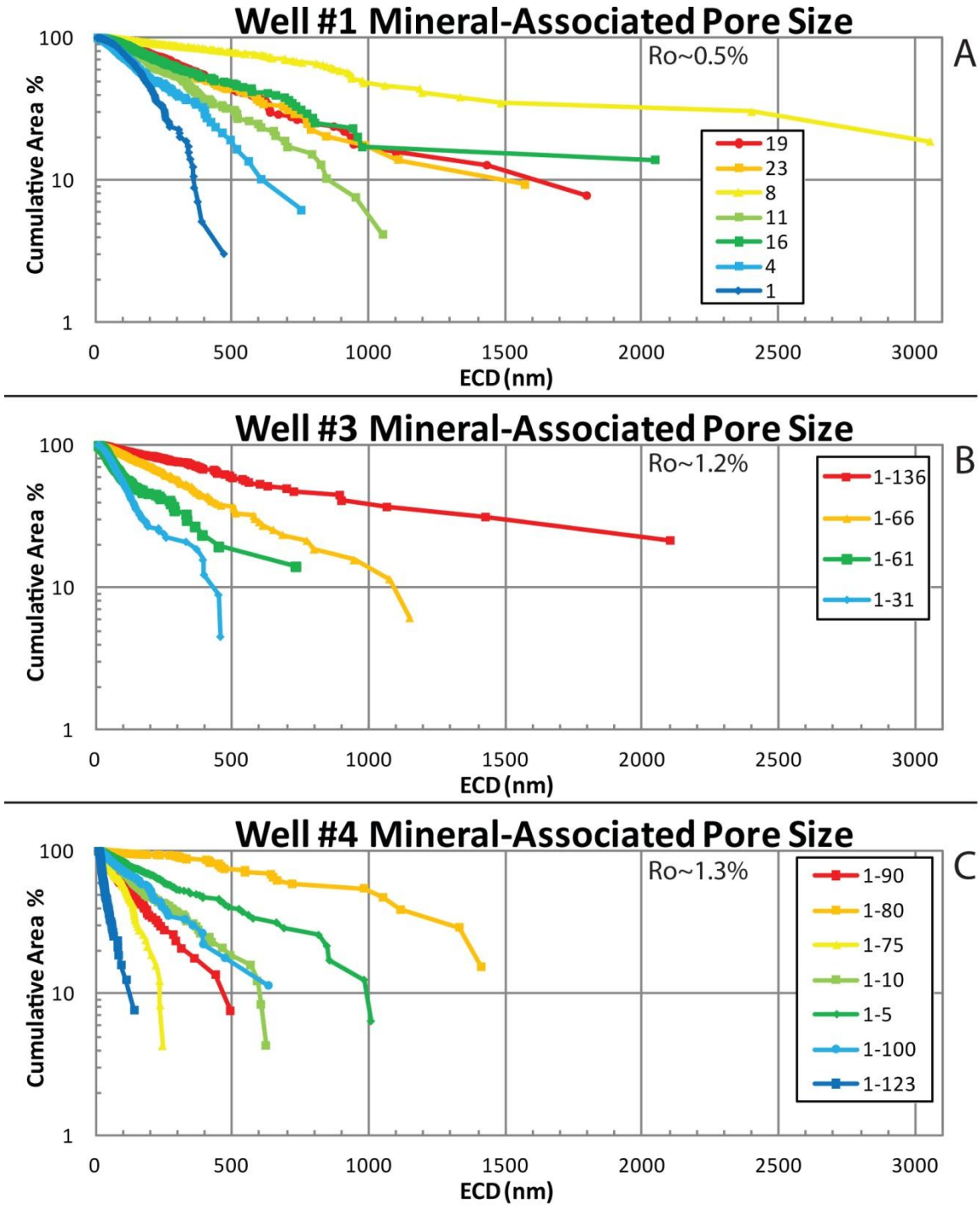

Figure 68: Cumulative area percent plotted against equivalent circular diameter (ECD) of mineral-associated pores in Wells 1, 3 and 4. Samples labeled and color coded in order of porosity (red is most porous, blue is least).

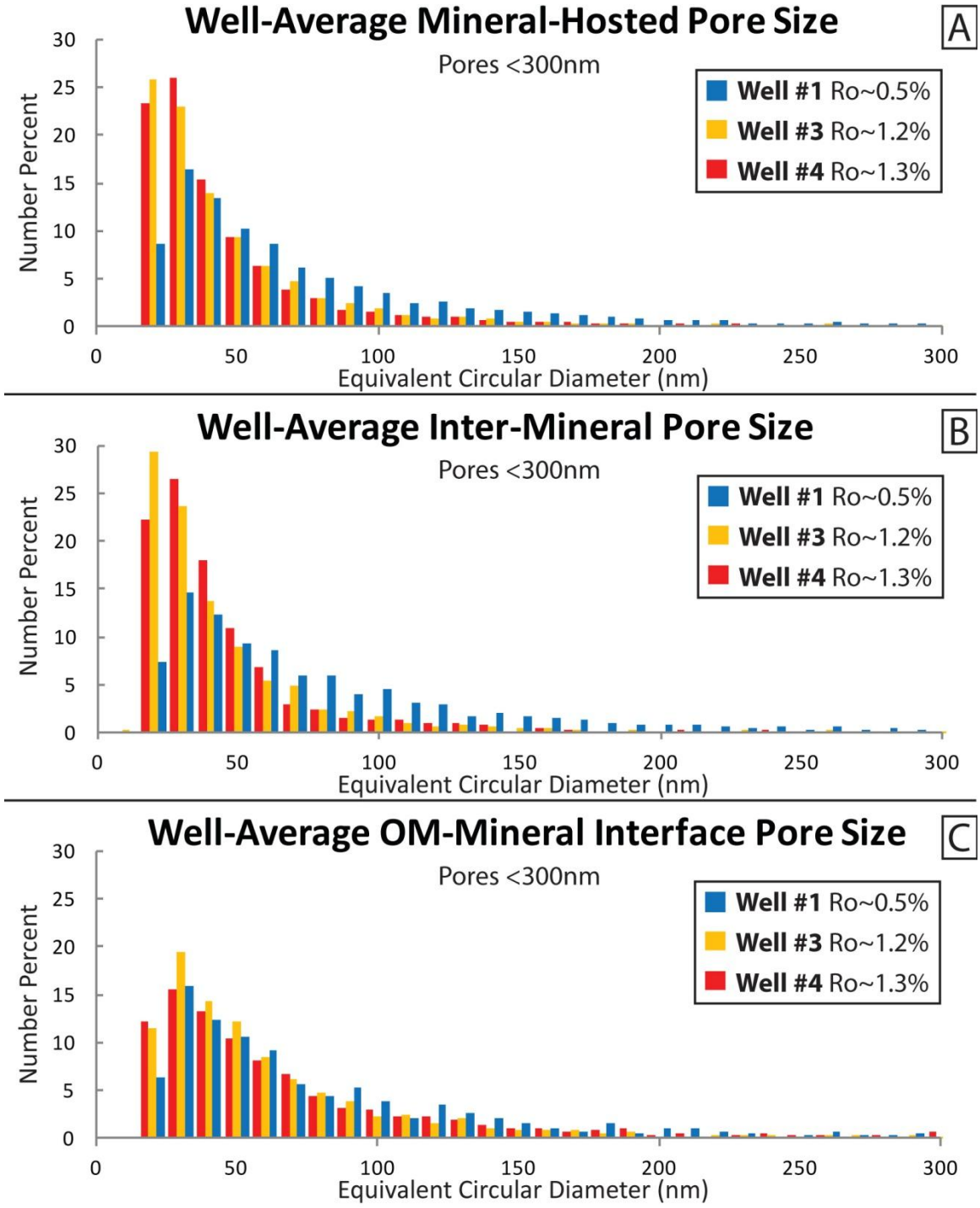
Well-Average Mineral-Hosted Pore Size
A
Pores <300nm
Well #1 Ro~0.5%
Well #3 Ro~1.2%
Well #4 Ro~1.3%
Number Percent
Equivalent Circular Diameter (nm)
Well-Average Inter-Mineral Pore Size
B
Pores <300nm
Well #1 Ro~0.5%
Well #3 Ro~1.2%
Well #4 Ro~1.3%
Number Percent
Equivalent Circular Diameter (nm)
Well-Average OM-Mineral Interface Pore Size
C
Pores <300nm
Well #1 Ro~0.5%
Well #3 Ro~1.2%
Well #4 Ro~1.3%
Number Percent
Equivalent Circular Diameter (nm)

Figure 69

Figure 69: Histograms of mineral-associated pores smaller than 300 nm averaged for each well. Pore types include: A) all mineral-associated pores, B) inter-mineral pores, C) OM-mineral interface pores. Note increased proportion of smaller (less than ~ 40 nm ECD) inter-mineral pores, and decreased abundance of larger pores (greater than ~50 nm, the "tail"). OM-mineral interface weakly show a similar trend.

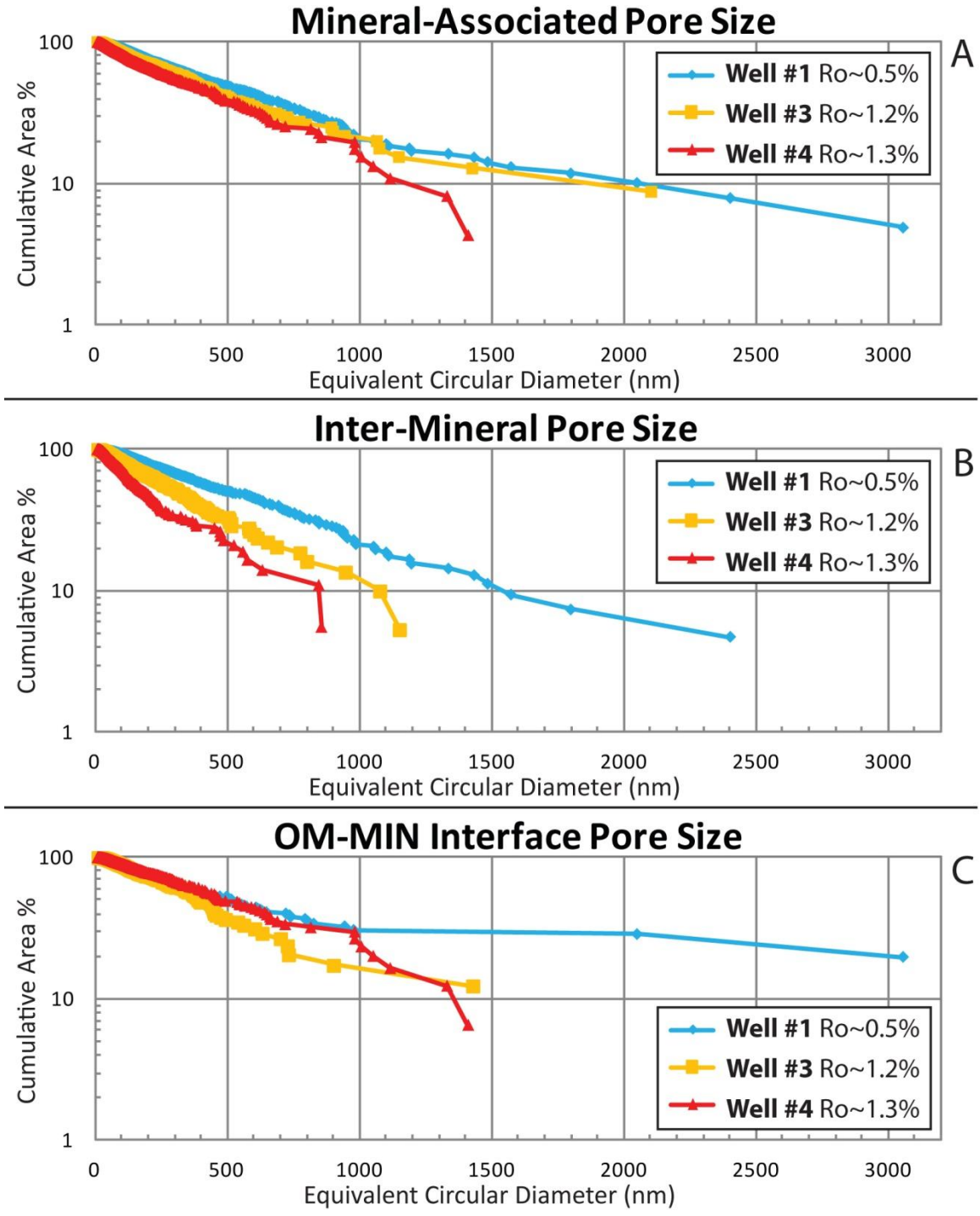
Mineral-Associated Pore Size
A
Cumulative Area %
100
10
1
0
500
1000
1500
2000
2500
3000
Equivalent Circular Diameter (nm)
Well #1 Ro~0.5%
Well #3 Ro~1.2%
Well #4 Ro~1.3%
Inter-Mineral Pore Size
B
Cumulative Area %
100
10
1
0
500
1000
1500
2000
2500
3000
Equivalent Circular Diameter (nm)
Well #1 Ro~0.5%
Well #3 Ro~1.2%
Well #4 Ro~1.3%
OM-MIN Interface Pore Size
C
Cumulative Area %
100
10
1
0
500
1000
1500
2000
2500
3000
Equivalent Circular Diameter (nm)
Well #1 Ro~0.5%
Well #3 Ro~1.2%
Well #4 Ro~1.3%

Figure 70

Figure 70: Cumulative area percent of mineral-associated pore types plotted against equivalent circular diameter as populations within each well. Pore types include: A) all mineral-associated, B) inter-mineral, and C) OM-mineral interface pores. Note the increased abundance of smaller inter-mineral pores, and a decrease in the proportion of large pores accompanies thermal maturation. OM-mineral interface pores show a loss of the largest pores, and a slight increase in of the contribution of smaller pores.

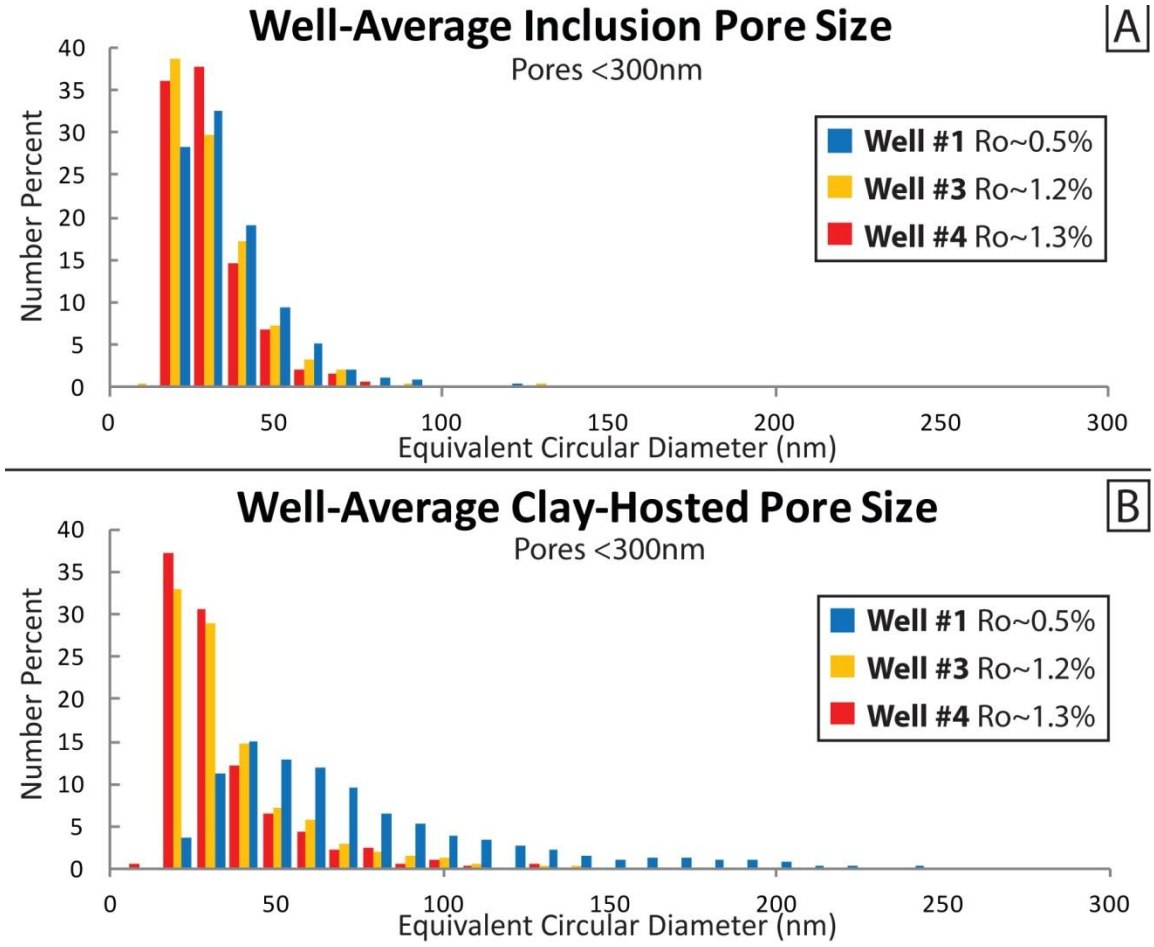

Figure 71: Histograms of mineral-associated pores smaller than 300 nm averaged for each well. Pore types include: A) intraparticle inclusion (inclusion), B) clay-hosted pores.

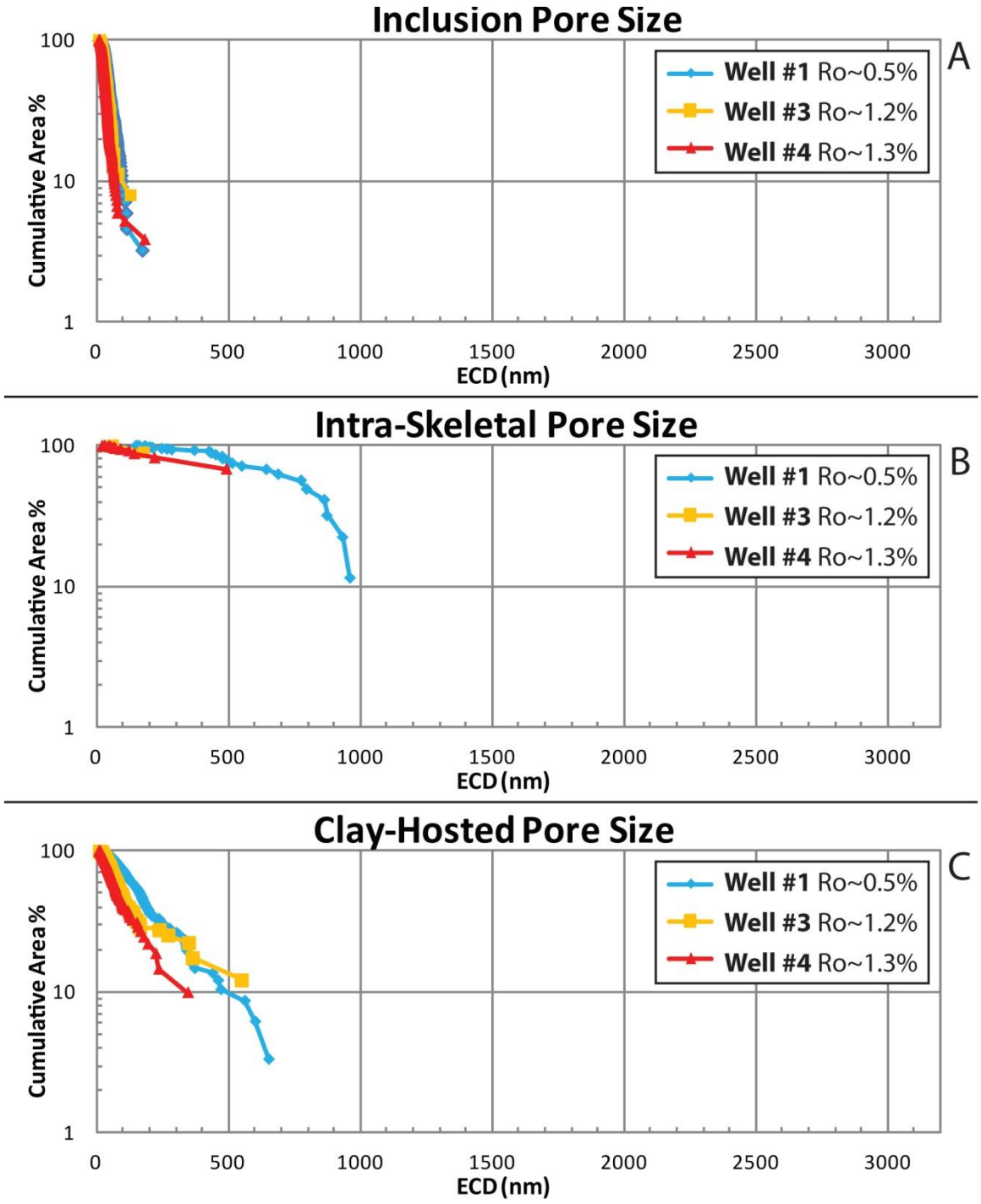
Inclusion Pore Size
A
Well #1 Ro~0.5%
Well #3 Ro~1.2%
Well #4 Ro~1.3%
Cumulative Area %
100
10
1
0
500
1000
1500
2000
2500
3000
ECD (nm)
Intra-Skeletal Pore Size
B
Well #1 Ro~0.5%
Well #3 Ro~1.2%
Well #4 Ro~1.3%
Cumulative Area %
100
10
1
0
500
1000
1500
2000
2500
3000
ECD (nm)
Clay-Hosted Pore Size
C
Well #1 Ro~0.5%
Well #3 Ro~1.2%
Well #4 Ro~1.3%
Cumulative Area %
100
10
1
0
500
1000
1500
2000
2500
3000
ECD (nm)

Figure 72

Figure 72: Cumulative area percent of mineral-associated pore types plotted against equivalent circular diameter as populations within each well. Pore Types include: A) intraparticle inclusion pores, B) intra-skeletal pores (note small population at high maturity), and C) clay-hosted pore.

Table#6: Pore size measurments of mineral-associated pores. Pore size is expressed as equivallent circular diameter (nm).

Well	Sample	#Min pores	Std Dev MIN	Max MIN	Min MIN	D10a MIN*	D50a MIN	D90a MIN	D10n MIN	D50n MIN	D90n MIN
1	23	1461	105.9	1573.3	11.8	1506.1	411.6	94.3	168.5	52.7	23.0
1	19	1769	121.4	1799.3	9.9	1637.0	424.2	113.4	200.4	54.4	22.0
1	16	1602	110.3	2049.9	10.4	**2049.9**	436.5	100.0	166.3	48.5	20.5
1	11	1458	99.3	1053.5	10.9	857.8	323.6	93.8	190.6	59.1	23.9
1	8	674	233.6	3056.5	14.3	**3056.5**	978.9	242.0	288.5	68.1	32.5
1	4	1349	62.4	754.4	8.7	577.7	212.6	55.5	106.6	35.9	16.8
1	1	857	64.1	471.1	8.1	361.2	182.5	69.4	148.9	42.3	17.7
3	1-31	1464	38.9	456.5	9.3	432.5	109.8	35.6	77.0	28.3	14.7
3	1-61	1247	40.8	730.2	9.9	**730.2**	148.5	33.2	63.5	26.2	15.1
3	1-66	1762	89.5	1149.5	9.9	1095.9	354.5	83.4	133.2	35.9	16.8
3	1-136	1128	118.2	2103.3	9.3	**2103.3**	685.5	117.7	123.4	35.7	16.8
4	1-5	1387	85.2	1007.4	8.7	992.6	362.5	72.2	123.8	40.7	18.0
4	1-10	1484	57.8	622.8	9.9	599.2	182.3	50.8	103.8	34.3	16.4
4	1-75	451	36.8	244.4	9.3	235.7	117.5	34.3	85.5	28.6	15.4
4	1-80	426	159.1	1411.8	11.8	**1411.8**	1028.5	311.1	110.7	25.7	16.1
4	1-90	1196	37.6	492.9	9.3	471.5	135.7	30.3	65.9	25.0	14.3
4	1-100	663	54.9	632.7	10.4	**632.7**	205.2	44.5	88.4	32.1	16.8
4	1-123	330	14.3	142.3	11.4	128.3	34.9	18.0	36.4	20.3	15.1
1	avg	1310.0	113.8	1536.9	10.6	1435.2	424.3	109.8	181.4	51.6	22.3
3	avg	1400.3	71.8	1109.9	9.6	1090.5	324.6	67.5	99.3	31.5	15.8
4	avg	848.1	63.7	650.6	10.1	638.8	295.2	80.2	87.8	29.5	16.0
Total	avg	1150.4	85.0	1097.3	10.2	1048.9	351.9	88.9	126.8	38.5	18.4
Total	max	1769.0	233.6	3056.5	14.3	3056.5	1028.5	311.1	288.5	68.1	32.5
Total	min	330.0	14.3	142.3	8.1	128.3	34.9	18.0	36.4	20.3	14.3
Total	sum	20708									

*bold values indicate samples for which the D10 value was exceeded by a single pore. The size of the largest pore is listed.

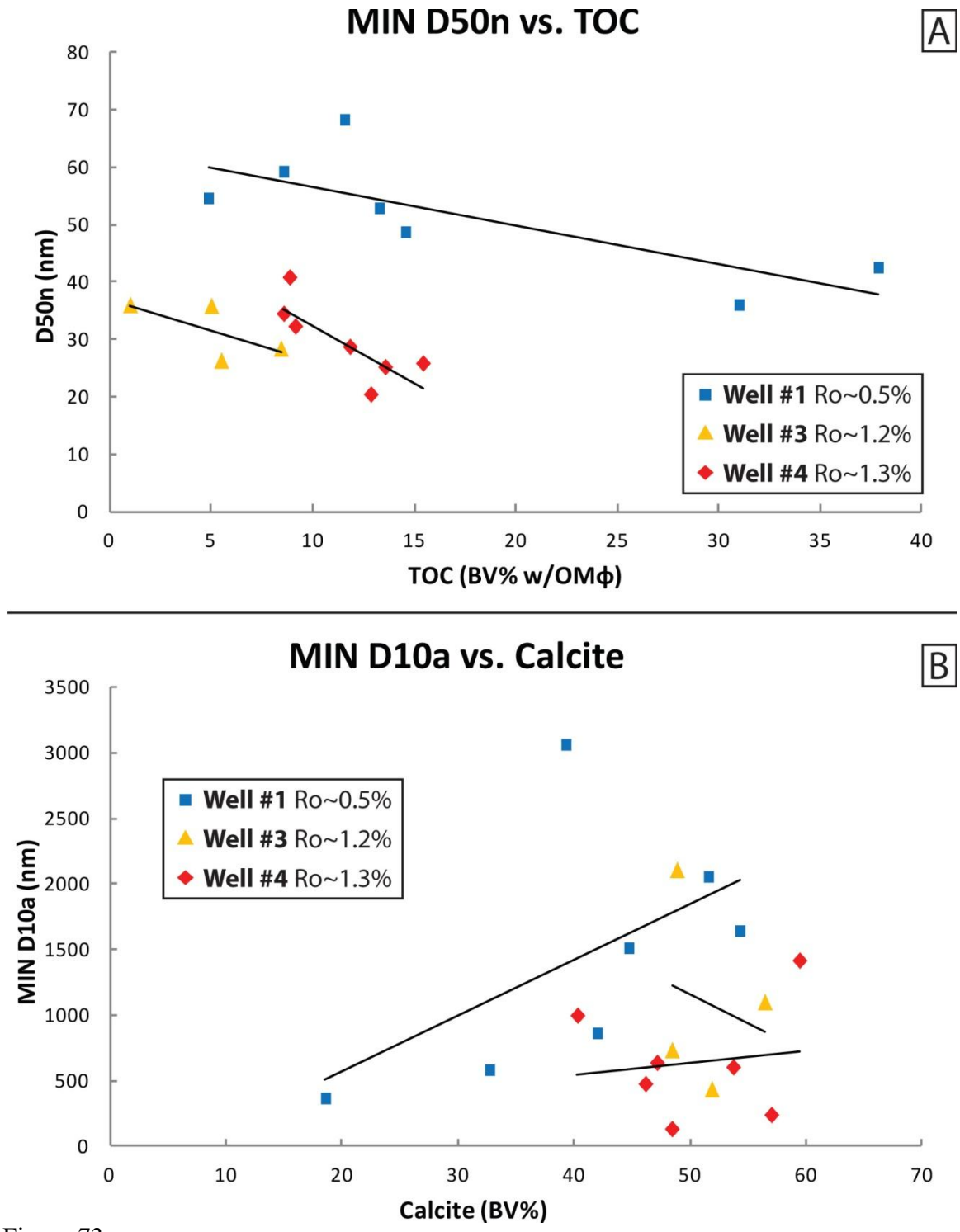
MIN D50n vs. TOC
A
D50n (nm)
TOC (BV% w/OMϕ)
Well #1 Ro~0.5%
Well #3 Ro~1.2%
Well #4 Ro~1.3%
MIN D10a vs. Calcite
B
MIN D10a (nm)
Calcite (BV%)
Well #1 Ro~0.5%
Well #3 Ro~1.2%
Well #4 Ro~1.3%

Figure 73

Figure 73: Cross-plots showing between components and mineral-associated pore size calculated by point-count and trace analysis, plotted as pore size (ECD) against bulk volume percent. Illustrates controls on mineral-associated pores size including: A) mean mineral-associated pore size (D50n) versus ON volume (TOC) including the OM-hosted porosity (ϕOM) for all three wells and B) the pore diameter for which 10% of the pores are larger versus volume percent calcite for all three wells.

OM-HOSTED PORE SIZE DISTRIBUTIONS

OM-hosted pore size distribution varies significantly within high maturity wells and across thermal maturity. Measured OM-hosted pores range in diameter (ECD) from 3.6 nm - 856.8 nm. Controls on OM-hosted pore size distribution are complex and more poorly understood than controls on mineral-associated pore size.

Relatively few OM-hosted pores were observed in low-maturity samples and are interpreted as primary (Table 4; Figure 67: see *OM-Hosted Pores* for more detail). OM-hosted pores within the low maturity Upper Eagle Ford (samples 19 and 23) show size distributions and OM-hosted pore volumes very similar to those observed in the Upper Eagle Ford of Well 4, suggesting that the OM-hosted pore network in samples from the Upper Eagle Ford is relatively inert (Tables 3 and 7; Figures 62 and 74).

Secondary OM-hosted pores observed in all high-maturity samples, show diverse pore size distributions (Table 7; Figure 74). Controls on OM-hosted pore size likely include chemistry of OM, and volume available within OM for bubble growth (Figure 77). As shown in Milliken et al 2013, the size distribution of OM-hosted pores within the gas window does not change significantly with maturation from Well 3 to Well 4 (Table 7; Figures 74, 75, and 76). OM-hosted pore size does correlate positively with OM volume in Wells 3 and 4, and positively with calcite volume in Well 4 where the pore network is dominated by OM-hosted pores (Figure 77). Anamalously low pore size distribution in sample 1-123 from the lower, OM-rich portion of Well 4 (Figure 86).

A few subtle trends between complex and simple OM-hosted pores are observed between the high maturity Well 3 (Ro~1.2%) and the high maturity Well 4 (Ro~1.3%).

In particular, the complex OM-hosted pore popuation has a higher proportion of pores larger than ~70 nm in samples from Well 4 than samples from Well 3. However, this could be an artifact of the relatively small sample population in Well 3. In Addition, numerically the population of simple OM-hosted pores below ~100 nm in diameter (ECD), changes little between Well 3 and Well 4 (Figure 17), however in the cumulative area plot shows that there is a significantly larger contribution of a few large simple pores (greater than ~120 nm) in Well 4. It is uncertain if these trends are related to increased thermal maturity in Well 4, or (more likely) that large OM-hosted pores did not have room to grow. There is significantly less OM in Well 3, and bitumen has not permeated the mineral-associated pore network in Well 3 as pervasively into the mineral-associated pore network.

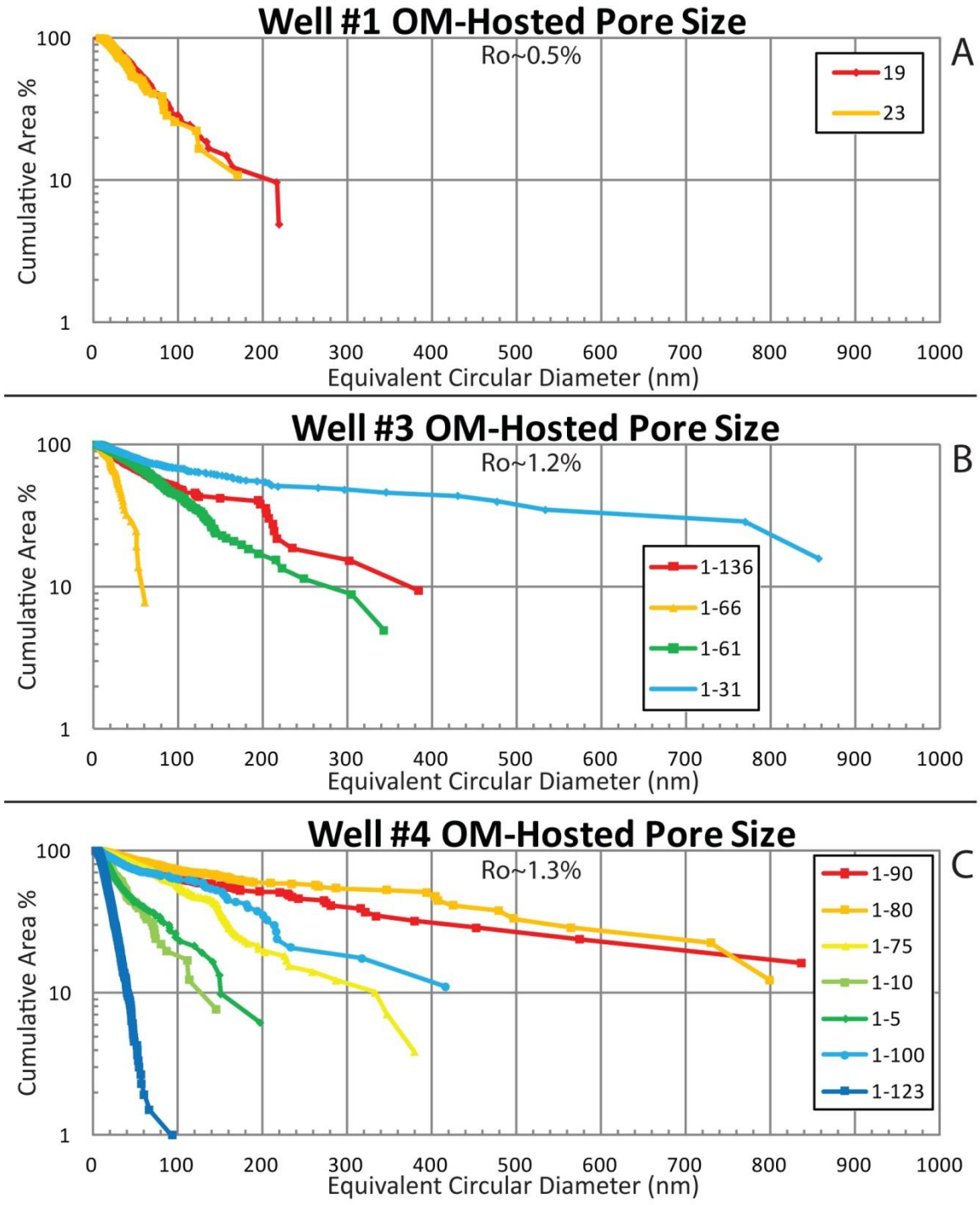

Figure 74: Cumulative area percent plotted against equivalent circular diameter (ECD) of OM-hosted pores in Wells 1, 3 and 4. Samples labeled and color coded in order of porosity (red is most porous, blue is least).

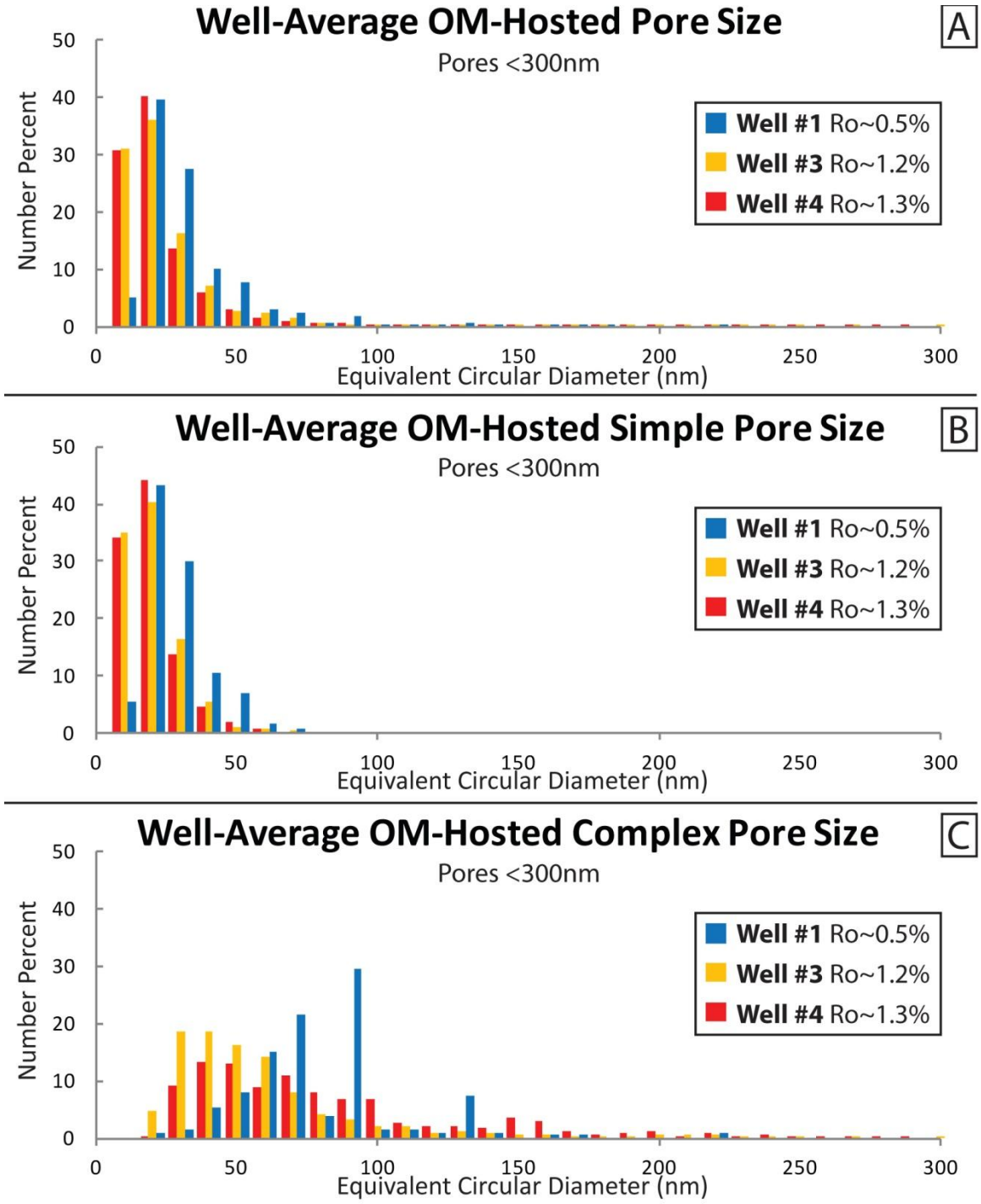

Figure 75: Histograms of OM-hosted pores smaller than 300 nm ECD averaged for each well. Pore types include: A) all OM-hosted, B) simple OM-hosted, and C) complex OM-hosted pores.

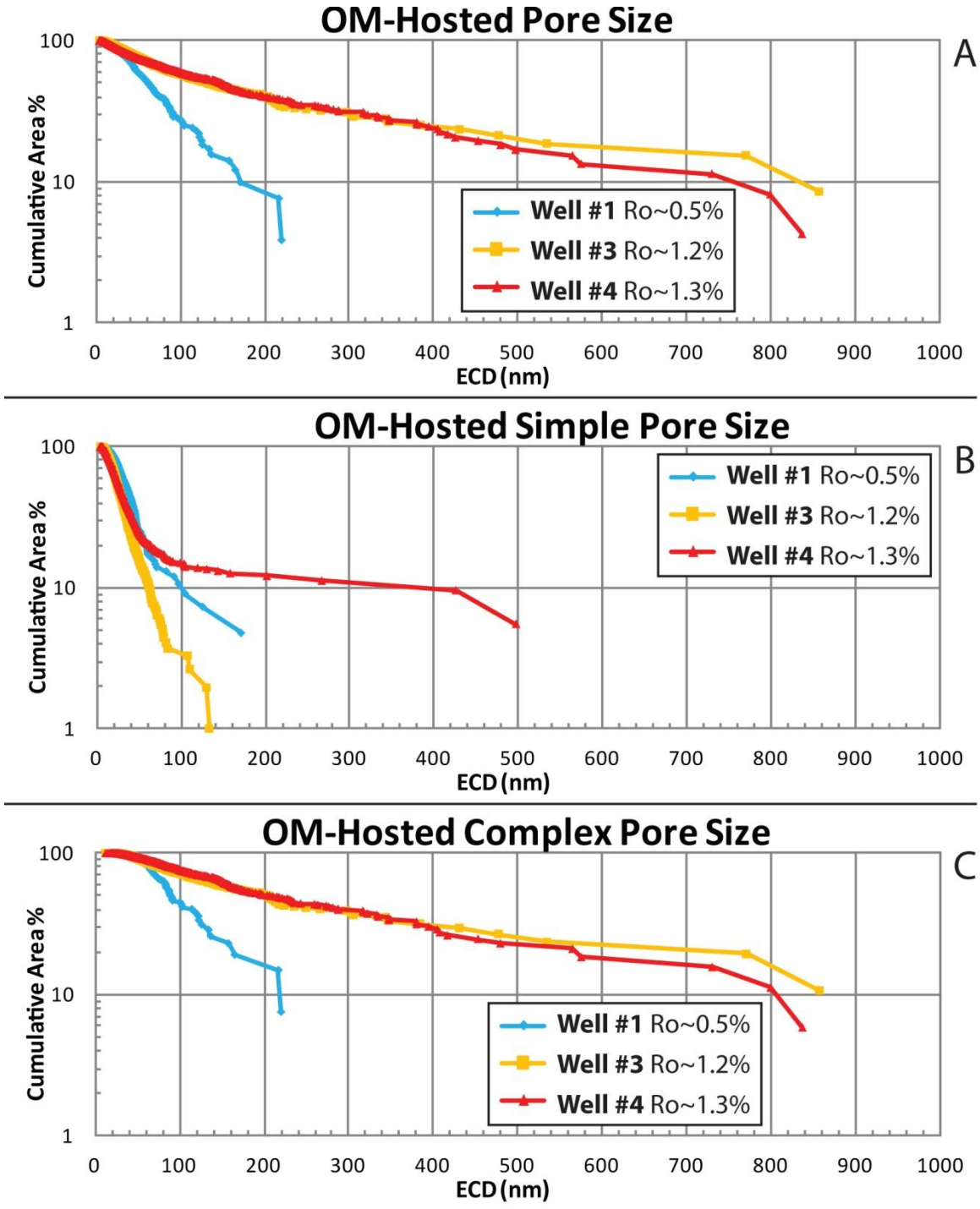

Figure 76: Cumulative area percent of OM-hosted pore types plotted against equivalent circular diameter as populations within each well. Pore types include: A) all OM-hosted, B) simple OM-hosted, and C) complex OM-hosted.

Table #7: Pore size measurments of OM-hosted pores. Pore size is expressed as equivallent circular diameter (nm).

Well	Sample	#OM pores	Std Dev OM	Max OM	Min OM	D10a OM*	D50a OM	D90a OM	D10n OM	D50n OM	D90n OM
1	23	234	20.4	170.9	8.4	**170.9**	57.9	20.7	45.6	21.1	11.9
1	19	711	23.3	219.9	5.6	210.9	64.0	23.3	54.8	22.1	11.5
1	16	0	-	-	-	-	-	-	-	-	-
1	11	0	-	-	-	-	-	-	-	-	-
1	8	0	-	-	-	-	-	-	-	-	-
1	4	0	-	-	-	-	-	-	-	-	-
1	1	0	-	-	-	-	-	-	-	-	-
3	1-31	2838	34.6	856.8	4.2	**856.8**	256.9	29.6	40.3	12.5	6.5
3	1-61	1827	26.7	343.4	4.5	280.8	85.0	23.5	51.4	15.5	7.6
3	1-66	107	11.4	61.2	5.5	58.5	13.3	13.3	33.6	13.3	7.7
3	1-136	1537	24.7	384.5	4.4	376.8	97.7	20.4	36.8	13.3	7.3
4	1-5	1311	14.6	197.9	4.2	151.4	40.6	12.8	27.4	12.4	7.7
4	1-10	535	14.4	145.9	5.4	130.6	40.1	12.9	32.7	12.8	8.1
4	1-75	2111	32.8	380.2	4.5	333.8	114.6	30.7	57.2	14.9	7.1
4	1-80	2099	42.8	799.3	4.1	**799.3**	397.6	37.6	45.6	14.5	7.7
4	1-90	2955	32.2	836.8	3.6	**836.8**	229.7	27.2	39.6	12.2	6.8
4	1-100	1325	27.5	416.7	5.0	**416.7**	155.2	21.4	34.2	12.9	7.7
4	1-123	3938	7.1	94.3	4.4	41.3	19.4	9.5	21.9	11.1	7.1
1	avg	135.0	21.8	195.4	7.0	190.9	60.9	22.0	50.2	21.6	11.7
3	avg	1577.3	24.4	411.5	4.6	393.2	113.2	21.7	40.5	13.6	7.3
4	avg	2039.1	24.5	410.2	4.5	387.1	142.5	21.7	36.9	13.0	7.5
Total	avg	1196.0	24.0	377.5	4.9	358.8	120.9	21.8	40.1	14.5	8.1
Total	max	3938.0	42.8	856.8	8.4	856.8	397.6	37.6	57.2	22.1	11.9
Total	min	0.0	7.1	61.2	3.6	41.3	13.3	9.5	21.9	11.1	6.5
Total	sum	21528									

*bold values indicate samples for which the D10 value was exceeded by a single pore. The size of the largest pore is listed.

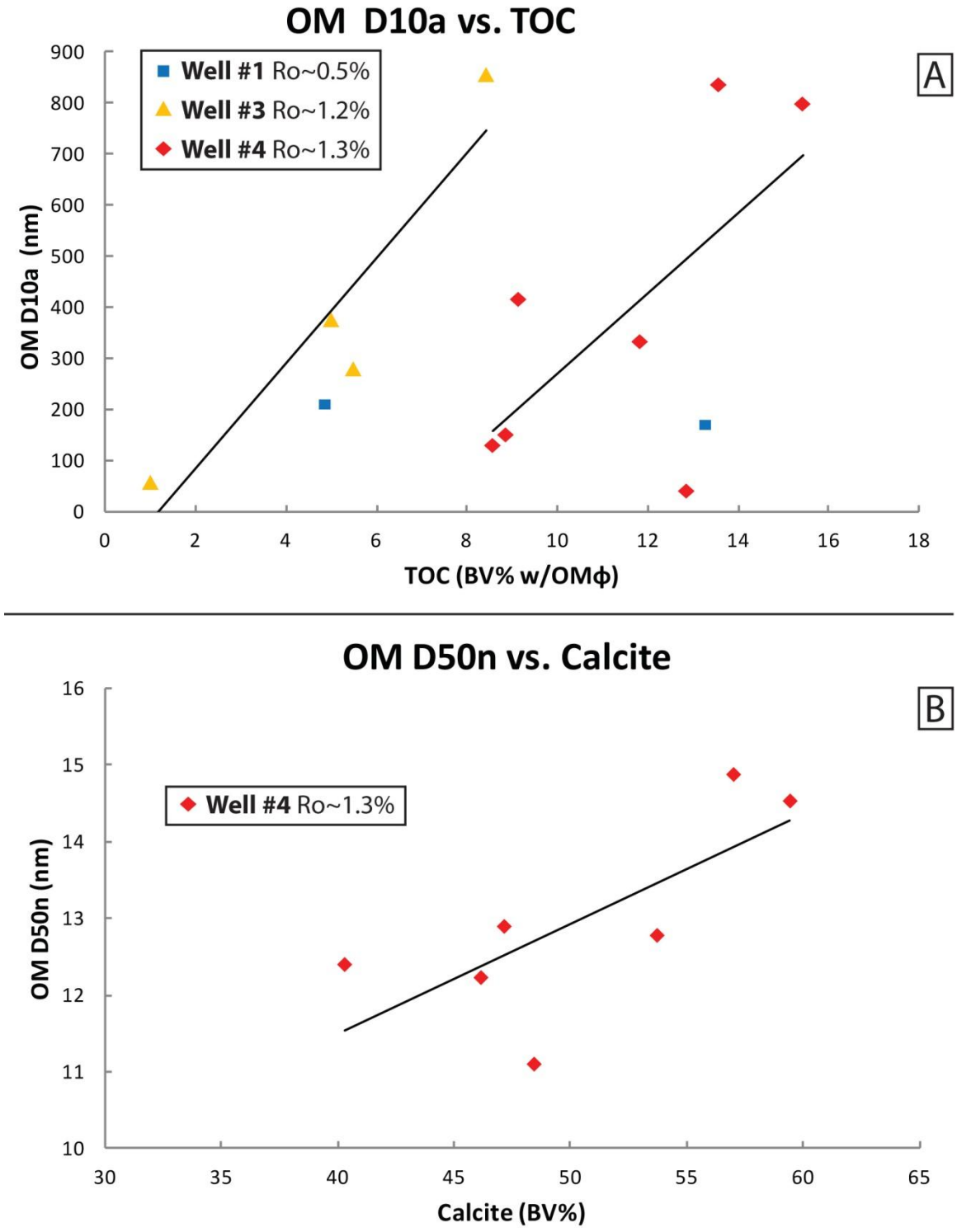
OM D10a vs. TOC
A
Well #1 Ro~0.5%
Well #3 Ro~1.2%
Well #4 Ro~1.3%
OM D10a (nm)
TOC (BV% w/OMϕ)
0
100
200
300
400
500
600
700
800
900
0
2
4
6
8
10
12
14
16
18
OM D50n vs. Calcite
B
Well #4 Ro~1.3%
OM D50n (nm)
Calcite (BV%)
10
11
12
13
14
15
16
30
35
40
45
50
55
60
65

Figure 77

Figure 77: Cross-plots showing between components and mineral-associated pore size calculated by point-count and trace analysis, plotted as pore size (ECD) against bulk volume percent. Illustrates controls on pore OM-hosted pore size including: A) the pore diameter for which 10% of OM-hosted pores (by area) are greater in area versus OM volume (TOC) including OM-hosted porosity (ϕOM), and B) Mean value of all OM-hosted pores (D50n) versus volume percent calcite.

DISCUSSION: PORE NETWORK EVOLUTION

The dominant changes in the character of the Eagle Ford pore system from the early oil-window (Ro~0.5%) to the gas window (Ro~1.2% - 1.3%) are: 1) a decrease in the abundance and size of primary mineral-associated pores, and 2) an increase in the abundance of small secondary OM-hosted pores (Table 4; Figures 62, 67, 68-70, 75 and 76). Compaction, cementation, and infill of pore space with secondary OM destroy mineral-associated porosity at all stages of maturity (Figures 78-85). Significant volumes of secondary porosity develop within OM as volatiles are generated and expelled (Figures 79, 84-86).

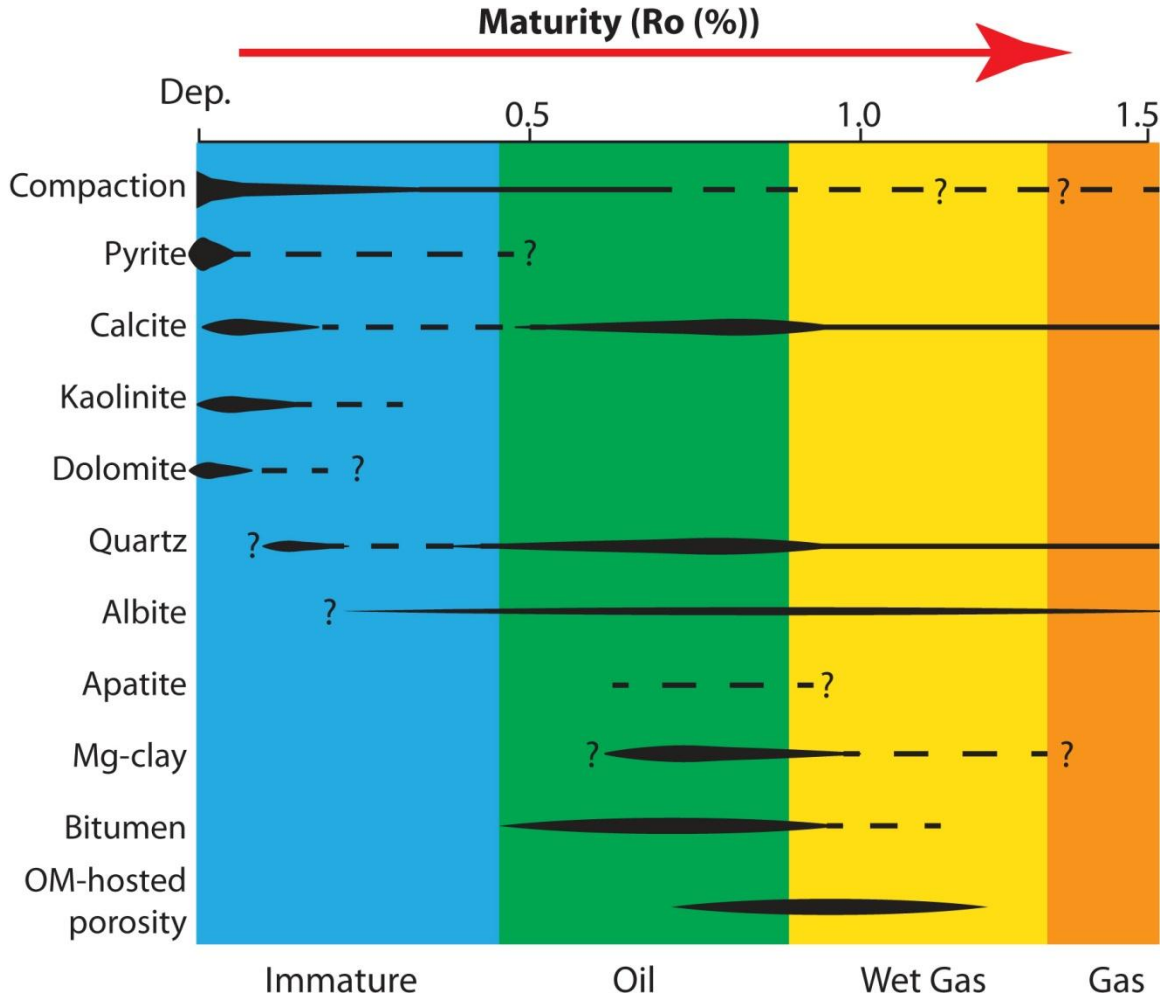

Figure 78: Interpreted paragenetic "spindle diagram" of processes effecting South Texas Eagle Ford sediments integrating data from this study, Ergene (2014), Fishman (2013), Milliken et al. (2014b), Sun et al. (2014), Zhang, (2014). Thermal maturity is plotted along the horizontal axis and chemical/physical processes occurrence along the vertical axis. Spindle thickness reflects relative occurrence of chemical or mechanical processes (e.g., cement generation or compaction). This diagram is a simplification of complex processes which differentially effect different grain assemblages across maturity.

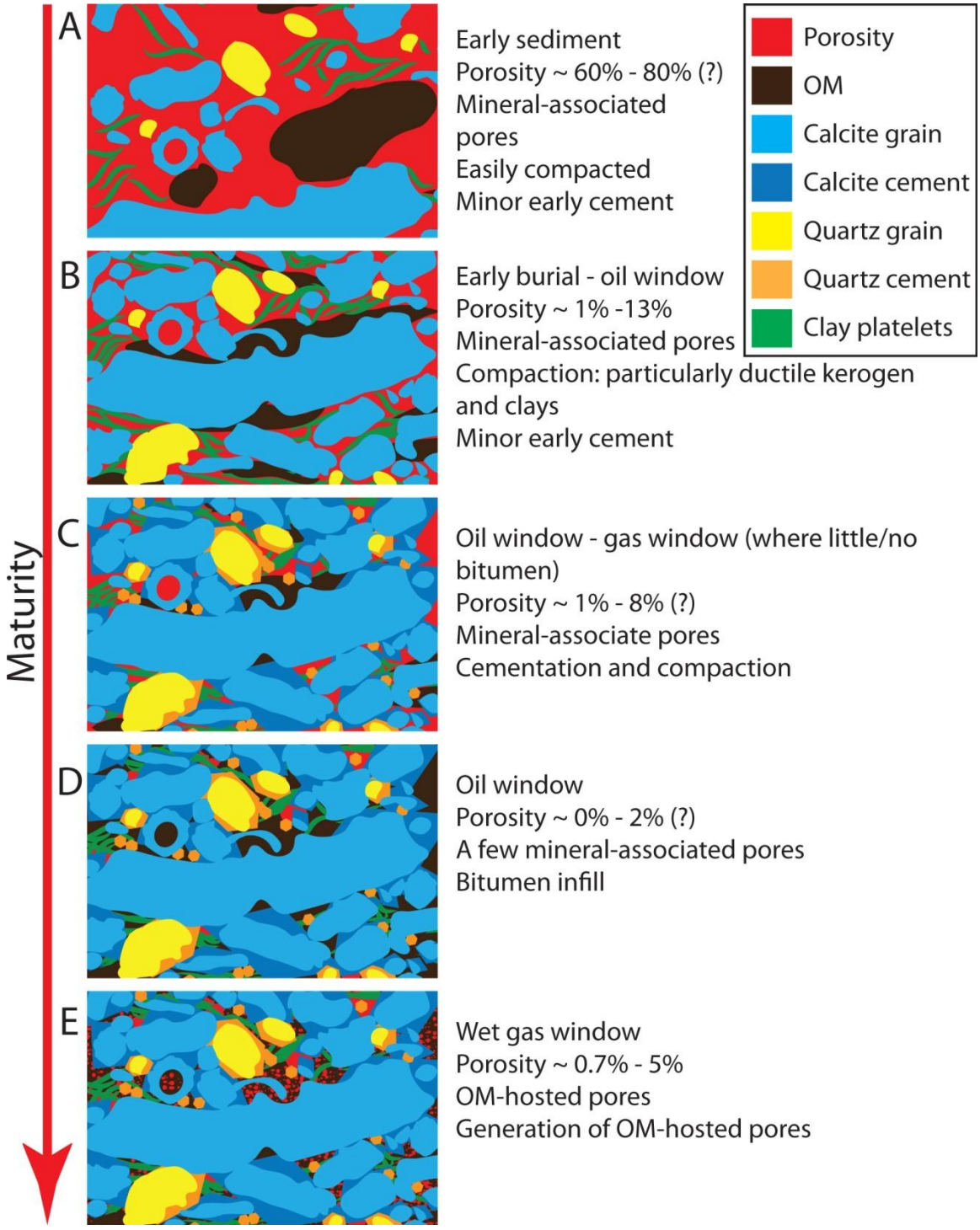
A
B
C
D
E
Maturity
Early sediment
Porosity ~ 60% - 80% (?)
Mineral-associated pores
Easily compacted
Minor early cement
Early burial - oil window
Porosity ~ 1% -13%
Mineral-associated pores
Compaction: particularly ductile kerogen and clays
Minor early cement
Oil window - gas window (where little/no bitumen)
Porosity ~ 1% - 8% (?)
Mineral-associate pores
Cementation and compaction
Oil window
Porosity ~ 0% - 2% (?)
A few mineral-associated pores
Bitumen infill
Wet gas window
Porosity ~ 0.7% - 5%
OM-hosted pores
Generation of OM-hosted pores
Porosity
OM
Calcite grain
Calcite cement
Quartz grain
Quartz cement
Clay platelets
Figure 79

Figure 79: Simplified cartoon displaying common diagenetic pathways of coccolithic Eagle Ford sediments, emphasizing processes with the greatest effects on porosity. Porosity values are inferred from point-count and trace data (Table 3). Early cements are not shown, as they typically do not significantly impact coccolithic debris. Five interpreted "stages" of diagenesis most significantly affecting the distribution and abundance of porosity include: A) early, un-compacted sediment that is strongly prone to compaction (Milliken et al. 2014), B) low maturity sediments under early burial conditions where most porosity has been lost by compaction, C) sediments that have developed "late" calcite and quartz overgrowths as well as micro-crystalline quartz and further compaction, but have not have had pore space in-filled by bitumen, D) sediments in the oil-window where bitumen has pervaded into primary pore space, and E) sediments in the wet-gas window that have developed abundant, small secondary pores within OM. Note that the effects of diagenesis are highly variable, two samples from similar maturities may or may not have undergone the processes in the order described above (e.g., early bitumen infill can inhibit later cementation).

Porosity in the Early Oil-Window

Samples from the early oil-window (Ro~0.5) contain pore networks dominated volumetrically by relatively large mineral-associated pores with median sizes ranging from 35.9 nm - 52.7 nm (Tables 4 and 6; Figure 81). Specifically, in low-maturity samples, pore volumes are dominated by inter-mineral pores and OM-mineral interface pores with mean diameters of 99.6 nm and 79.7 nm respectively (Table 4; Figures 62, 69, and 70).

Physical stability of the grain assemblage strongly impacts pore size and abundance during early diagenesis. Positive correlation between calcite abundance porosity volume and pore size suggests that rigid skeletal calcite grains are resistant to compaction, preferentially sheltering porosity between, within, and around grains. Negative correlation between OM abundance porosity and pore size suggest detrital OM behaves in a ductile manner and is especially susceptible to compaction, particularly during early diagenesis (Milliken et al., 2014). Additionally, bitumen has permeated into primary porosity where sulphur-rich OM is abundant (Figure 82). Large pores, with a mean pore diameter of 154.5 nm, occur within aggregates of skeletal debris contributing up to 88.7% of visible porosity or 6.9% of the bulk volume (Table 4, Figure 81). Mineral-associated pores within carbonate aggregates, can be inter-mineral, OM-mineral interface and/or intra-skeletal (Figure 24).

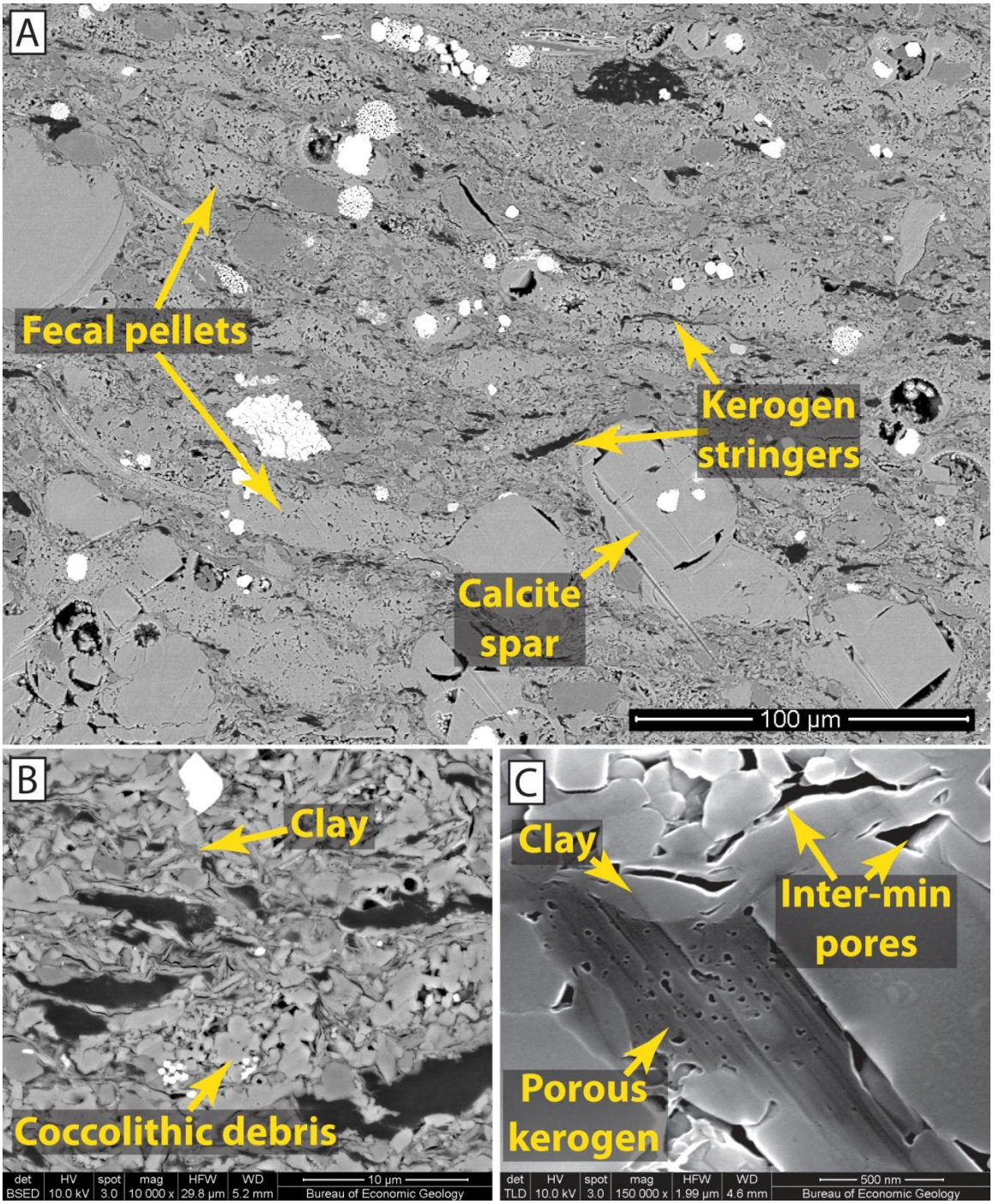
A
Fecal pellets
Kerogen stringers
Calcite spar
100 µm
B
Clay
Coccolithic debris
det HV spot mag HFW WD
BSED 10.0 kV 3.0 10 000 x 29.8 µm 5.2 mm
10 µm
Bureau of Economic Geology
C
Clay
Inter-min pores
Porous kerogen
det HV spot mag HFW WD
TLD 10.0 kV 3.0 150 000 x 1.99 µm 4.6 mm
500 nm
Bureau of Economic Geology
Figure 80

Figure 80: BSE and SE images of low-maturity sample including: A) low-magnification BSE image showing spatial isolation of kerogen stringers and early cements, as well as fecal pellet distribution, B) BSE image area within A showing grain assemblage is dominated by coccolithic debris, clay and non-porous kerogen stringers, and C) SE image of area within B showing abundance of inter-mineral pores and what is possibly primary pores within clay-associated kerogen. Well 1 sample 23.

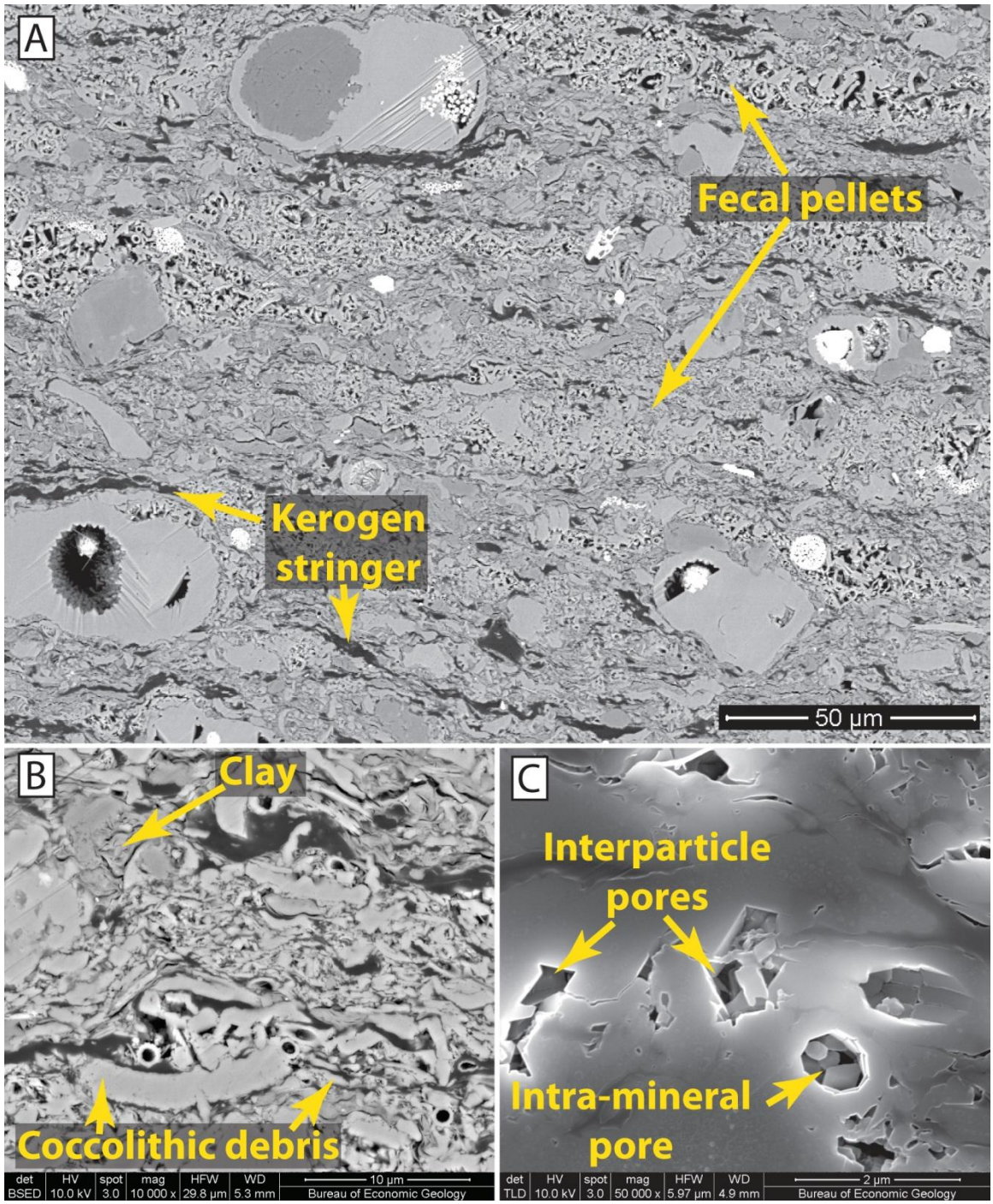
A
Fecal pellets
Kerogen stringer
50 µm
B
Clay
Coccolithic debris
det HV spot mag HFW WD
BSED 10.0 kV 3.0 10 000 x 29.8 µm 5.3 mm
10 µm
Bureau of Economic Geology
C
Interparticle pores
Intra-mineral pore
det HV spot mag HFW WD
TLD 10.0 kV 3.0 50 000 x 5.97 µm 4.9 mm
2 µm
Bureau of Economic Geology
Figure 81

Figure 81: BSE and SE images of low-maturity sample including: A) low-magnification BSE image showing spatial isolation of kerogen stringers and early cements, as well as fecal pellet distribution, note fecal pellets host abundant porosity, B) BSE image area within A showing grain assemblage is dominated by coccolithic debris, clay and non-porous kerogen, and C) SE image of area within B showing abundance of inter-particle pores and intra-mineral pores. Well 1 sample 16.

Chemical stability of detrital components impacts the pore network at low maturity in addition to the aforementioned constraints. Components such as low-Mg calcite coccoliths, K-clay, quartz, feldspar, and low-S OM appear relatively stable at low-maturities. Cementing and replacing minerals such as kaolinite, pyrite, early calcite, and albite occur, but are typically isolated spatially and do not impact porosity as strongly as compaction at low maturity (Figure 80, 81).

Pore-filling bitumen occurs in high TOC samples from the Lower Eagle Ford of Well 1 where sulphur-rich OM is present (Figure 82) (Sun et al., 2014). It is yet unclear what proportion of OM volume is bitumen in these samples. An inverse correlation between volumes of calcite and OM (Figure 59), as well as observations of OM character suggest that the distribution of OM in Well 1 is controlled dominantly by primary depositional processes. Primary OM-hosted porosity in low-maturity samples is restricted to the Upper Eagle Ford and occurs in very small proportions, contributing less than 3% of the total porosity, or 0.20% to 0.35% of the bulk volume in Well 1 samples 19 and 23 (Table 4; Figure 62, 80).

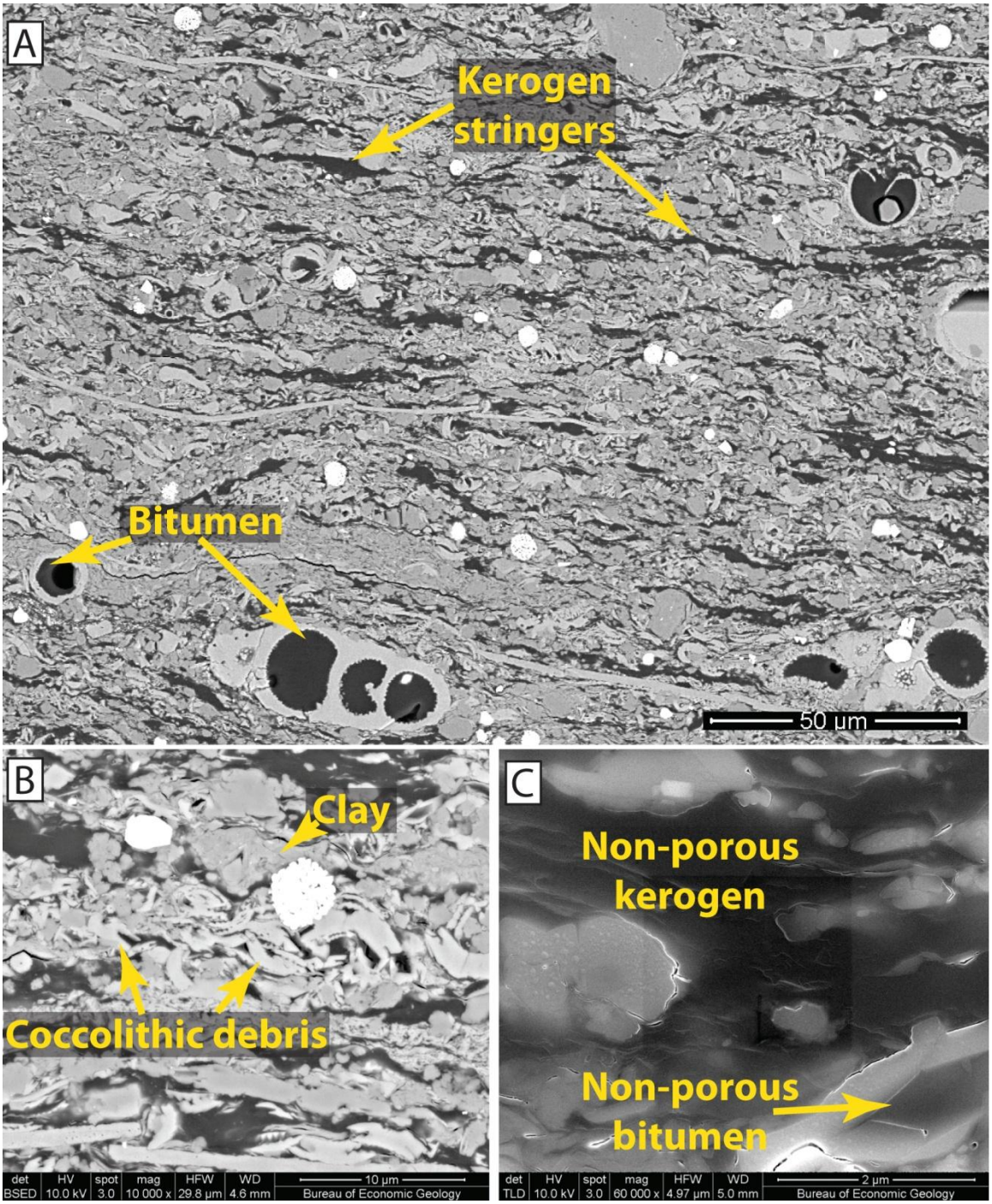
A
Kerogen stringers
Bitumen
50 µm
B
Clay
Coccolithic debris
det HV spot mag HFW WD
BSED 10.0 kV 3.0 10 000 x 29.8 µm 4.6 mm
10 µm
Bureau of Economic Geology
C
Non-porous kerogen
Non-porous bitumen
det HV spot mag HFW WD
TLD 10.0 kV 3.0 60 000 x 4.97 µm 5.0 mm
2 µm
Bureau of Economic Geology
Figure 82

Figure 82: BSE and SE images of low-maturity sample including A) low-magnification BSE image showing abundance of detrital kerogen stringers, and bitumen that has filled into primary intra-particle pore space, B) BSE image within A showing abundance of coccolithic grains, clay and kerogen, and C) SE image of non-porous kerogen and pore-filling bitumen. Well 1 sample 4.

Porosity in the Wet-Gas Window

Most samples from the gas window (Ro~1.2% - 1.3%) contain pore networks dominated volumetrically by small secondary pores within OM, to the point where visible porosity is correlative with OM volume in Well 4 (Tables 4 and 7; Figures 61, 62, 67, 74, 75, and 84-86). Results indicate that: 1) compaction, cementation, and infill of pore space with bitumen are destructive of primary, mineral associated porosity, and 2) secondary porosity within OM has been generated between the early oil-window and the wet-gas window (Tables 4 and 6; Figures 61, and 84-86).

A decrease in mineral-associated pore size and volumes occurs with increasing burial conditions. An average 86% less mineral-associated porosity occurs in Well 4 than in Well 1. Median mineral-associated pore size decreases from 51.6 nm in Well 1 to 29.5 nm in Well 4. The relative degree to which porosity was lost by compaction and cementation after early burial is uncertain in the absence of quantitative data on intergranular volumes.

In calcite-rich samples, preservation of a significant portion of relatively large pores and pore-shaped spaces occupied by OM suggests that compaction plays a limited role in later diagenesis. Additionally, It is unclear if compaction continues to affect organic components during hydrocarbon maturation. Residual kerogen could potentially accommodate additional strain as a consequence of volume loss during and after expulsion of mobile bitumen and volatiles, especially in OM-rich samples that can have TOC values of up to 37.9% of the bulk volume (Table 3).

Cementation has had an undeniable effect on porosity loss within high-maturity samples. General observations suggest that the magnitude of porosity loss through cementation may be significant. Interlocking euhedral calcite and quartz crystals are

abundant in high-maturity samples with abundant calcite grains (Figures 38, and 83-85), suggesting that cementation likely preferentially influenced samples with high initial porosity. Well 4 sample 1-123 shows a lack of cementation, suggesting that pore space was destroyed prior to "late" cementation (Figure 86).

A large portion of OM at high maturity is diagenetic in origin, filling what was pore space, distributed evenly throughout what was a pore network (Figures 37, 46B, 84 and 85). OM occupies spaces similar in size and morphology to primary interparticle pores, coats euhedral crystals (probable cements), and fills intraparticle volume (including inter-particle pores within fecal pellets) (Figure 82). This observation in synthesis with the positive correlation between calcite and OM volumes in samples with dominantly OM-hosted pore networks suggests that that the distribution of OM at high maturity is controlled by where bitumen has space into which it can permeate. These observations implies that the OM pore network exists within what was previously the mineral-associated pore network, suggesting connectivity of OM is significantly higher than within low-maturity samples, where OM consist of more spatially isolated "stringers" (Figures 80-82, and 84-86).

Mineral-associated pores are present in all high-maturity samples, but are typically smaller than in the low maturity well and occur in significantly lower abundances (Tables 4 and 6; Figures 62, 68, and 69). Median pore sizes of mineral-associated pores in high-maturity samples range from 20.3 nm - 40.6 nm, and they compose an average of 5.3% of the bulk volume in Well 3 and 0.9% of the bulk volume in Well 4 (Tables 4 and 6).

In most high-maturity samples, mineral-associated pores are dominantly OM-mineral interface pores that compose an average of 1.06% of the bulk volume (Table 4; Figures 46, 52, and 62). OM-mineral interface pores can be primary spaces between

grains, inter-mineral pores that were partially filled with OM, or nucleation sites for bubbles along mineral surfaces (Figure 46 and 52). Inter-mineral pores are present in high-maturity samples, but are significantly smaller and volumetrically less abundant (Table 4; Figures 62, 69, and 70). Mean inter-mineral porosity decreases from 4.26% of the bulk volume in Well 1 to 2.28% in Well 3 and only 0.17% in Well 4 (Table 4; Figure 62). Mean inter-mineral pore size decreases from 99.6 nm in Well 1 to 50.9 nm in Well 3 and 48.9 nm in Well 4.

Locally, in Well 3 (Ro~1.2%), mineral-associated pores dominate both volumetrically and numerically in low-TOC samples where bitumen has not pervaded into large portions of the mineral-associated pore volume, as observed in Well 3 sample 1-66 (Figure 84), or where dissolution of unstable components such as muscovite and/or kaolinite, generate secondary moldic pores after bitumen fill (Well 3 sample 1-136) (Figure 56).

Pores within carbonate aggregates are especially susceptible to effects of "late" chemical processes. Average mineral-associated porosity within carbonate aggregates decreases from 2.83% of the bulk volume in Well 1, to 0.02% in Well 3, and 0.05% in Well 4 (Table 4). Similarly, maximum mineral-associated pore volume within carbonate aggregates decreases from 6.9% in Well 1 to 0.6% in Well 3, and 0.2% in Well 4 (Table 4). Abundant calcite cement, some quartz cement, near pervasive OM-fill of most fecal pellets into spaces the same size and shape as primary pores, suggest that primary pores within carbonate aggregates are strongly affected by chemical processes during "late" diagenesis (Figures 37 and 84).

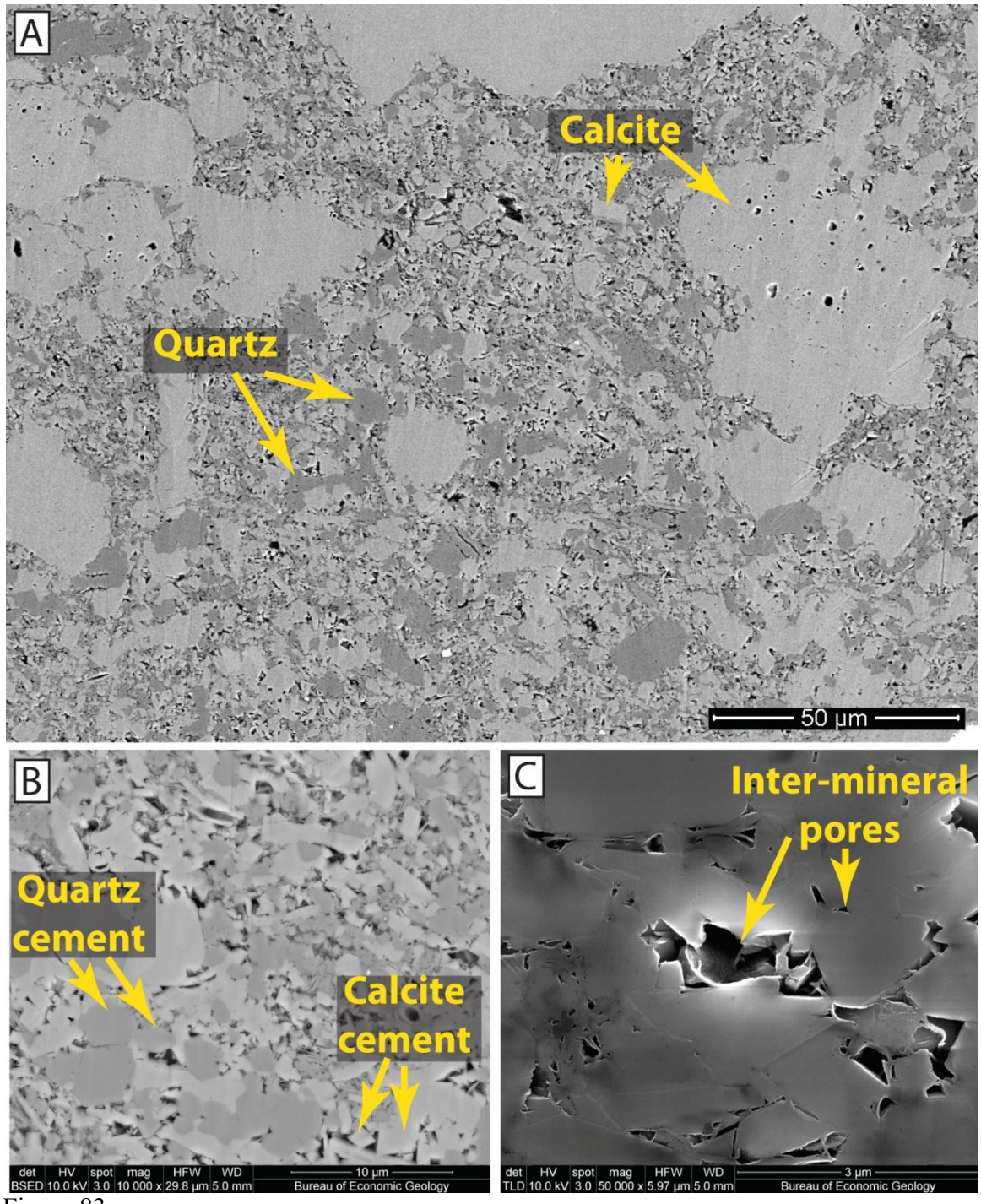
A
Calcite
Quartz
50 µm
B
Quartz cement
Calcite cement
det HV spot mag HFW WD
BSED 10.0 kV 3.0 10 000 x 29.8 µm 5.0 mm
10 µm
Bureau of Economic Geology
C
Inter-mineral pores
det HV spot mag HFW WD
TLD 10.0 kV 3.0 50 000 x 5.97 µm 5.0 mm
3 µm
Bureau of Economic Geology
Figure 83

Figure 83: BSE and SE images of high-maturity sample including: A) low-magnification BSE image to show spatial distribution of components and lack of distinct fabric, B) BSE image within A to show abundance of calcite and quartz cement, and C) SE image to show preserved inter-mineral pores. Interpretations of mineralogy based on BSE intensity, morphology and EDS signal. Well 3 sample 1-66.

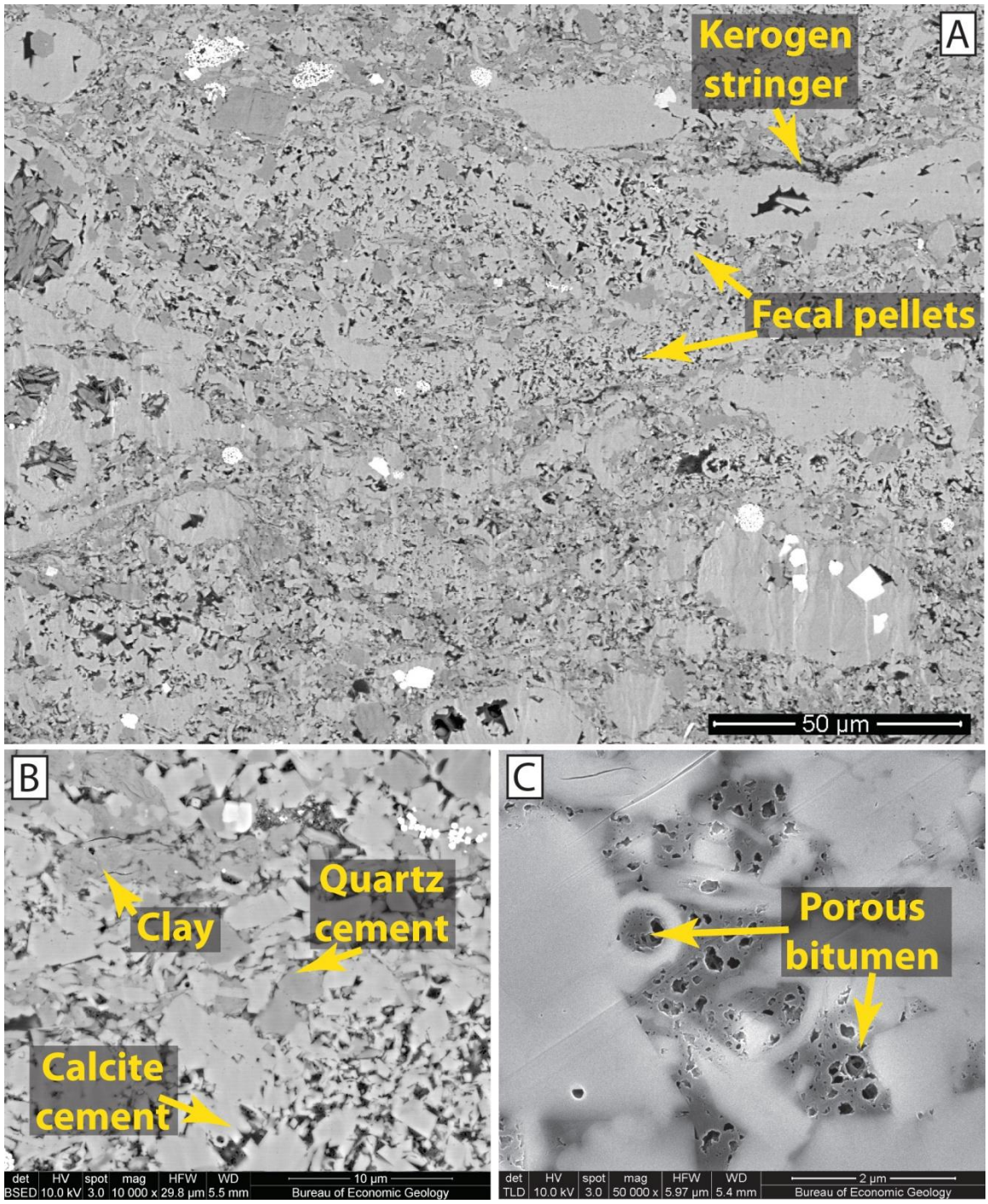
A
Kerogen stringer
Fecal pellets
50 µm
B
Clay
Quartz cement
Calcite cement
det HV spot mag HFW WD
BSED 10.0 kV 3.0 10 000 x 29.8 µm 5.5 mm
10 µm
Bureau of Economic Geology
C
Porous bitumen
det HV spot mag HFW WD
TLD 10.0 kV 3.0 50 000 x 5.97 µm 5.4 mm
2 µm
Bureau of Economic Geology
Figure 84

Figure 84: BSE and SE images of high-maturity sample including: A) low-magnification BSE image showing spatial distribution of fecal pellets and OM dispersed throughout what was an interparticle pore network, B) BSE image within A showing abundance of calcite and quartz cement, and C) SE image of bitumen that has in-filled primary intra-particle pore space, coated euhedral crystal growth faces and developed OM-hosted porosity. Interpretations of mineralogy based on BSE intensity, morphology and EDS signal. Well 4 sample 1-75.

Secondary pores are generated within OM compose an average of 62.2% of the porosity or 1.59% of the bulk volume in Well 4 and 25.5% of the porosity or 0.97% of the bulk volume in Well 3. Median pore sizes of OM-hosted pores range from 11.1 nm - 14.9 nm (Table 7). OM-hosted porosity and pore size is covariant with calcite abundance and TOC in samples dominated by OM-hosted porosity, suggesting that larger OM-hosted pores occur within samples with larger inter-granular volumes and more OM where bubbles have more room to grow within OM (Figures 63, and 77). Alternatively, or in conjunction with the previous possibility, larger and more volumetrically abundant pores preferentially occur in bitumen, as opposed to kerogen.

Data outliers from trends suggest that OM type and chemistry influences secondary porosity generation within OM. Examples of this include relatively inert OM within the Upper Eagle Ford (Well 1 samples 19 and 23, Well 4 samples 1-5 and 1-10), and OM with anomalously low pore sizes and volumes for samples with relatively high OM volumes (Well 4 sample 1-123) (Tables 2, 3, and 7, Figure 86). The sample in the latter case is from a stratigraphic interval that is rich in kerogen (TOC values up to 37.9% of the bulk volume) and prone to early bitumen generation at low maturity, suggesting that a large portion of the OM in this sample is residual kerogen.

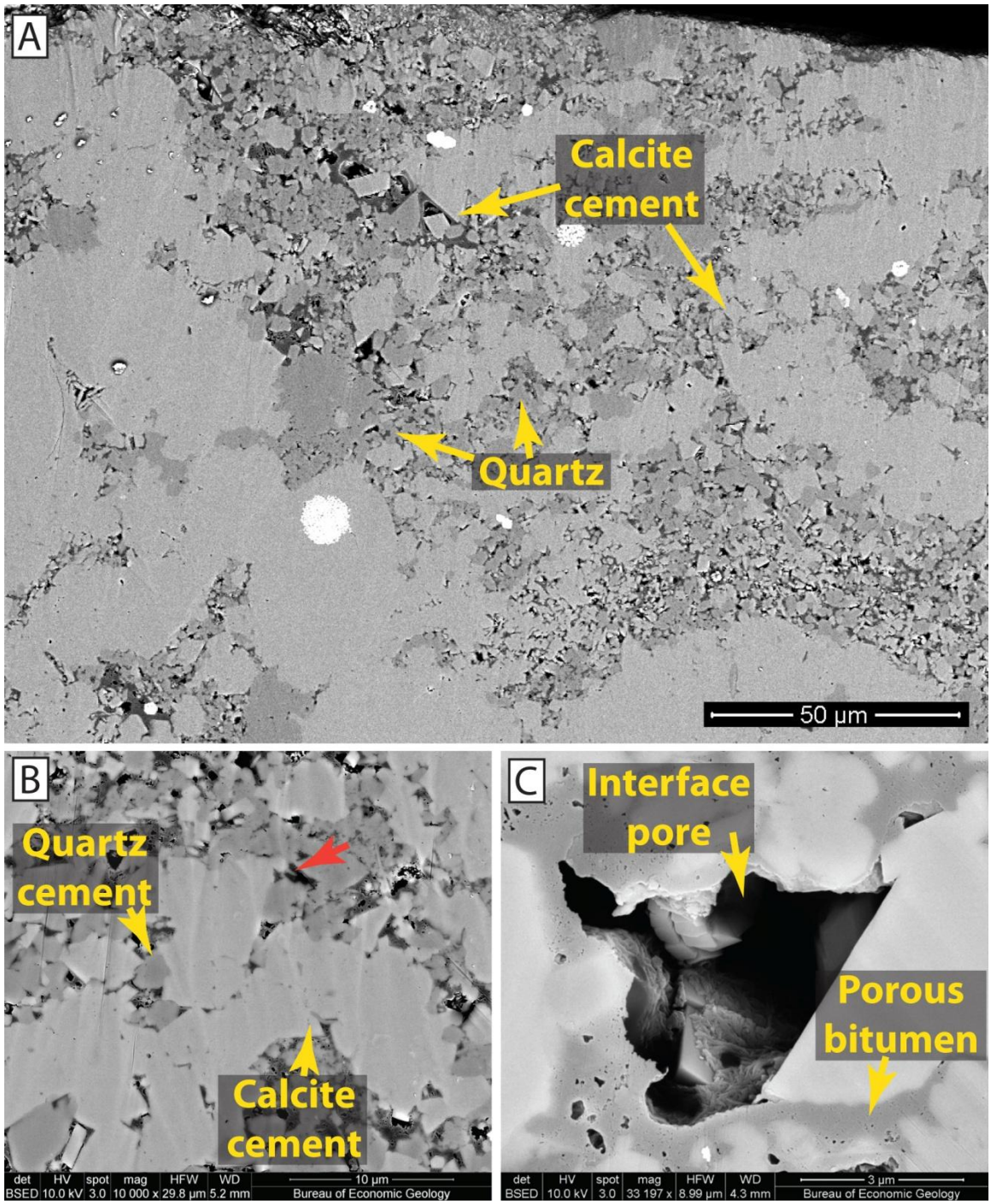
A
Calcite cement
Quartz
50 µm
B
Quartz cement
Calcite cement
det HV spot mag HFW WD
BSED 10.0 kV 3.0 10 000 x 29.8 µm 5.2 mm
10 µm
Bureau of Economic Geology
C
Interface pore
Porous bitumen
det HV spot mag HFW WD
BSED 10.0 kV 3.0 33 197 x 8.99 µm 4.3 mm
3 µm
Bureau of Economic Geology
Figure 85

Figure 85: BSE and SE images of high-maturity sample including: A) low-magnification BSE image to show spatial distribution of components and abundant cementation, B) BSE image within A to show abundance of large, interlocking calcite crystals and quartz cement, red arrow points to bitumen fill of secondary pore within a dolomite crystal, and C) SE image to show porous bitumen coating authigenic mineral growth faces. OM-mineral interface pores occur where bitumen has partially filled primary mineral-associated pore space. Interpretations of mineralogy based on BSE intensity, morphology and EDS signal. Well 4 sample 1-80.

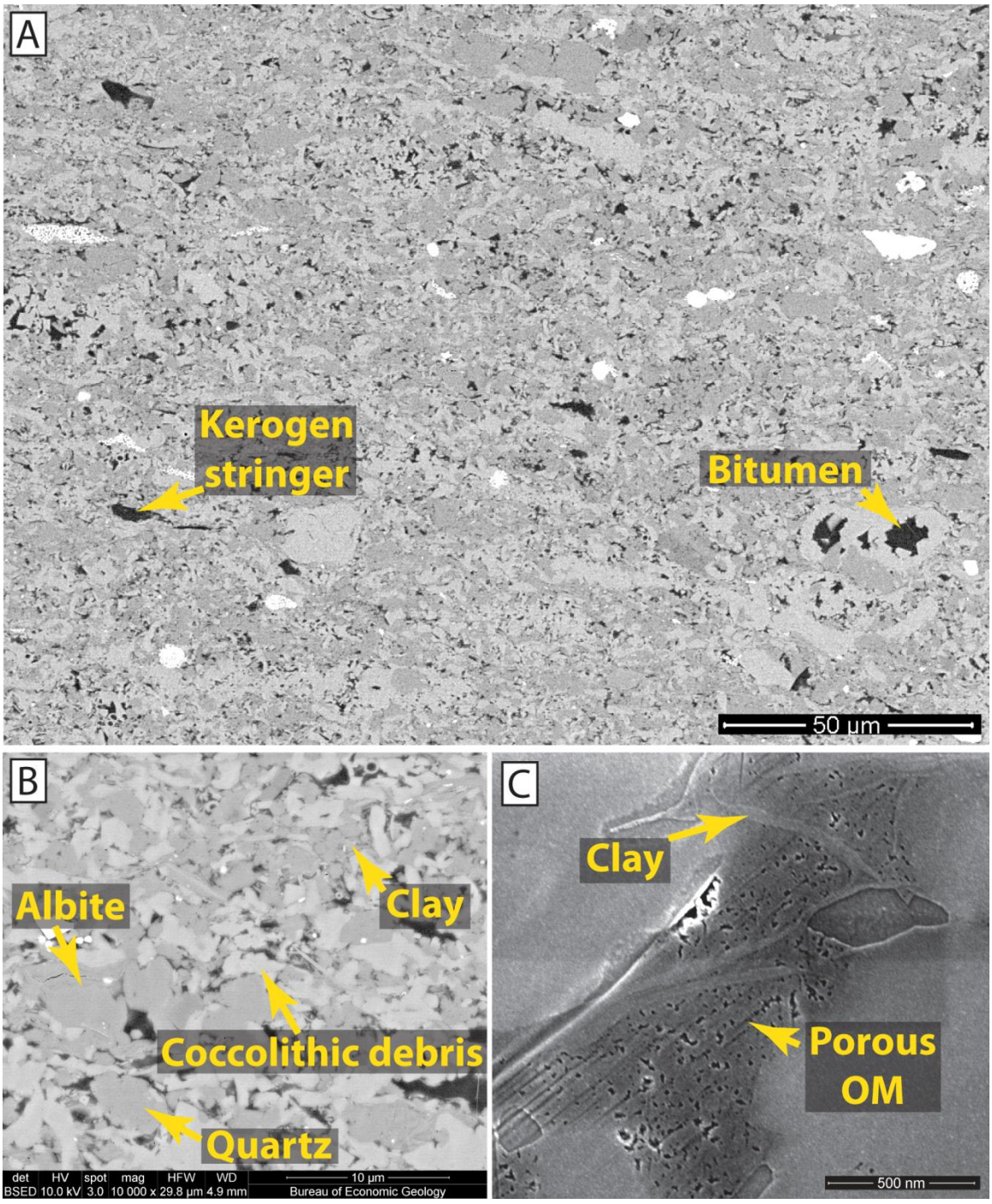
A
Kerogen stringer
Bitumen
50 µm
B
Albite
Clay
Coccolithic debris
Quartz
det HV spot mag HFW WD
BSED 10.0 kV 3.0 10 000 x 29.8 µm 4.9 mm
10 µm
Bureau of Economic Geology
C
Clay
Porous OM
500 nm
Figure 86

Figure 86: BSE and SE images of high-maturity sample including: A) low-magnification BSE image to show spatial distribution of components and lack of distinct fabric, B) BSE image within A to show lack of pore-filling cements and porosity suggesting pore space was destroyed by compaction prior to "late" cementation, and C) SE image to show porous OM with diminutive pore size distribution, possibly residual kerogen. Interpretations of mineralogy based on BSE intensity, morphology and EDS signal. Well 4 sample 1-123.

Application of Other Methods

Mineral-associated pores <10 nm and OM-hosted pores <4 nm are beyond detection with the methods applied in this study, limiting conclusions accordingly. Pores below this detection limit are quantified by Zhang et al. (2014), who applies N-adsorption techniques to the same sample set, quantifying pore abundances up to 300 nm in size. The next phase of this study will focus on the integration of pore measurements reported here with N-adsorption data.

CONCLUSIONS

As in sandstones, carbonates, and other mudrocks, porosity evolution in the Eagle Ford Formation, South Texas, is driven by compaction, cementation, and generation of secondary porosity. The evolution of the pore network is a direct response of the detrital grain assemblage to changing physical and chemical conditions in the subsurface.

Destruction of porosity in low-maturity samples (Ro~0.5%) is strongly controlled by the relative physical and chemical stabilities of the grain assemblage to early diagenetic processes. More rigid bioclastic debris shelters large, volumetrically abundant, pores from strain. In contrast, ductile components, e.g., kerogen and clays, are strongly influenced by the effects of early compaction. This results in lower porosity and pore size values in OM-rich samples and higher porosity and pore size values in calcite-rich samples. A minor degree of primary porosity loss from chemical processes, e.g., cementation and bitumen infill, is interpreted to have occurred in low-maturity samples, reflecting the relative chemical stability of components under early burial conditions.

Similarly, destruction of primary porosity and generation of secondary porosity in high-maturity samples (Ro~1.2% - 1.3%) is controlled by the relative physical and chemical stabilities of the grain assemblage and early diagenetic components, e.g., kaolinite and early bitumen to later burial diagenetic processes. Data and observations suggest that chemical processes at high maturity have a much stronger effect on pore networks in high-maturity samples than physical processes such as compaction. Significant loss of porosity within high-maturity samples has occurred through infill by secondary OM (bitumen) and cementation. Corresponding to a decrease in mineral-associated porosity, significant volumes of smaller pores have been generated within OM in most high-maturity samples making up to 3.9% of the bulk volume.

Across thermal maturity, from the early oil-window (Ro~0.5%) to the gas window Ro~1.2%-1.3%) the dominant changes in the character of the Eagle Ford pore system are a decrease in the abundance and size of primary mineral-associated pores and an increase in the abundance of small secondary OM-hosted pores. Pore networks as we find them today reflect responses of the detrital grain assemblage to the changing physical and chemical conditions in the subsurface.

REFERENCES

Adelseck, C. G., Geehan, G. W., & Roth, P. H. (1973). Experimental evidence for the selective dissolution and overgrowth of calcareous nannofossils during diagenesis. Geological Society of America Bulletin, 84(8), 2755-2762.

Ahn, J. H., & Peacor, D. R. (1985). Transmission electron microscopic study of diagenetic chlorite in Gulf Coast argillaceous sediments. Clays and Clay Minerals, 33(3), 228-236.

Ambrose, R., Hartman, R., Diaz Campos, m., Akkutlu, I. Y., & Sondergeld, C. (2010). New Pore-scale Considerations for Shale Gas in Place Calculations. Paper presented at the SPE Unconventional Gas Conference.

Ambrose, R., Hartman, R., Diaz-Campos, M., Akkutlu, I. Y., & Sondergeld, C. (2012). Shale Gas-in-Place Calculations Part I: New Pore-Scale Considerations. SPE Journal, 17(1), 219-229.

Arthur, M. A. (2005). Sea-level control on source-rock development: perspectives from the Holocene Black Sea, the mid-Cretaceous Western Interior Basin of North America, and the Late Devonian Appalachian Basin.

Awwiller, D. (1993). Illite/smectite formation and potassium mass transfer during burial diagenesis of mudrocks: a study from the Texas Gulf Coast Paleocene-Eocene. Journal of Sedimentary Research, 63(3).

Baker, P. A., & Bloomer, S. H. (1988). The origin of celestite in deep-sea carbonate sediments. Geochimica et Cosmochimica Acta, 52(2), 335-339.

Barrett, E. P., Joyner, L. G., & Halenda, P. P. (1951). The determination of pore volume and area distributions in porous substances. I. Computations from nitrogen isotherms. Journal of the American Chemical society, 73(1), 373-380.

Bernard, S., Brown, L., Wirth, R., Schreiber, A., Schulz, H.-M., Horsfield, B., . . . Mathia, E. J. (2013a). FIB-SEM and TEM Investigations of an Organic-rich Shale Maturation Series from the Lower Toarcian Posidonia Shale, Germany: Nanoscale Pore System and Fluid-rock Interactions. Electron Microscopy of Shale Hydrocarbon Reservoirs: AAPG Memoir 102, 102, 53.

Bernard, S., Horsfield, B., Schulz, H.-M., Wirth, R., Schreiber, A., & Sherwood, N. (2012a). Geochemical evolution of organic-rich shales with increasing maturity: A STXM and TEM study of the Posidonia Shale (Lower Toarcian, northern Germany). Marine and Petroleum Geology, 31(1), 70-89. doi: 10.1016/j.marpetgeo.2011.05.010

Bernard, S., Wirth, R., Schreiber, A., Schulz, H.-M., & Horsfield, B. (2012b). Formation of nanoporous pyrobitumen residues during maturation of the Barnett Shale (Fort Worth Basin). International Journal of Coal Geology, 103, 3-11. doi: 10.1016/j.coal.2012.04.010

Berner, R. A. (1970). Sedimentary pyrite formation. American Journal of Science, 268(1), 1-23.

Berner, R. A., Leeuw, J. W. D., Spiro, B., Murchison, D. G., & Eglinton, G. (1985). Sulphate Reduction, Organic Matter Decomposition and Pyrite Formation [and Discussion]. Philosophical Transactions of the Royal Society A: Mathematical, Physical and Engineering Sciences, 315(1531), 25-38. doi: 10.1098/rsta.1985.0027

Bolton, A. J., Maltman, A. J., & Fisher, Q. (2000). Anisotropic permeability and bimodal pore-size distributions of fine-grained marine sediments. Marine and Petroleum Geology, 17(6), 657-672.

Bown, P. (1998). Calcareous nannofossil biostratigraphy: Chapman and Hall; Kluwer Academic.

Bralower, T. J. (1988). Calcareous nannofossil biostratigraphy and assemblages of the Cenomanian-Turonian boundary interval: Implications for the origin and timing of oceanic anoxia. Paleoceanography, 3(3), 275-316.

Burdine, N., Gournay, L., & Reichertz, P. (1950). Pore size distribution of petroleum reservoir rocks. Journal of Petroleum Technology, 2(7), 195-204.

Burton, J., Krinsley, D., & Pye, K. (1987). Authigenesis of kaolinite and chlorite in Texas Gulf Coast sediments. Clays and Clay Minerals, 35(4), 291-296.

Clarkson, C., Wood, J., Burgis, S., Aquino, S., Freeman, M., & Birss, V. (2012). Nanopore Structure Analysis and Permeability Predictions for a Tight Gas/Shale Reservoir Using Low-Pressure Adsorption and Mercury Intrusion Techniques. Paper presented at the SPE Americas Unconventional Resources Conference.

Curtis, M., Ambrose, R., Sondergeld, C., & Sondergeld, C. (2010). Structural characterization of gas shales on the micro-and nano-scales. Paper presented at the Canadian Unconventional Resources and International Petroleum Conference.

Curtis, M. E., Cardott, B. J., Sondergeld, C. H., & Rai, C. S. (2012a). Development of organic porosity in the Woodford Shale with increasing thermal maturity. International Journal of Coal Geology.

Curtis, M. E., Sondergeld, C. H., Ambrose, R. J., & Rai, C. S. (2012b). Microstructural investigation of gas shales in two and three dimensions using nanometer-scale resolution imaging. AAPG Bulletin, 96(4), 665-677. doi: 10.1306/08151110188

Deer, W. A., Howie, R. A., & Zussman, J. (1992). An introduction to the rock-forming minerals (Vol. 2): Longman Scientific & Technical Hong Kong.

Desbois, G., Urai, J., & Kukla, P. (2009). Morphology of the pore space in claystones–evidence from BIB/FIB ion beam sectioning and cryo-SEM observations. eEarth Discussions, 4(1), 1-19.

Donovan, A., & Staerker, T. (2010). Sequence Stratigraphy of the Eagle Ford (Boquillas) Formation in the Subsurface of South Texas and Outcrops of West Texas: Gulf Coast Association of Geological Societies Transactions, v. 60.

Driskill, B., Garbowicz, A., Govert, A., & Suurmeyer, N. (2012). Reservoir Description of the Subsurface Eagle Ford Formation, Maverick Basin Area, South Texas, USA (SPE 154528). Paper presented at the 74th EAGE Conference & Exhibition.

Driskill, B., Walls, J., DeVito, J., & Sinclair, S. W. (2013). Applications of SEM Imaging to Reservoir Characterization in the Eagle Ford Shale, South Texas, USA. Electron Microscopy of Shale Hydrocarbon Reservoirs: AAPG Memoir 102, 102, 115.

Energy Information Association, 2010. Eagle Ford Shale Play, Western Gulf Basin, South Texas, <http://www.eia.gov/oil_gas/rpd/shaleusa9.pdf> accessed March 4, 2014.

Ergene, S.M., (2014). Lithologic Heterogeneity of the Eagle Ford Formation, Central Texas. University of Texas at Austin.

Fairbanks, M. D. (2012). High Resolution Stratigraphy and Facies Architecture of the Upper Cretaceous (Cenomanian-Turonian) Eagle Ford Group, Central Texas. University of Texas at Austin.

Fishman, N., Guthrie, J., & Honarpour, M. (2013). The Stratigraphic Distribution of Hydrocarbon Storage and its Effect on Producible Hydrocarbons in the Eagle Ford Formation, South Texas. Paper presented at the Unconventional Resources Technology Conference.

Fishman, N. S., Hackley, P. C., Lowers, H. A., Hill, R. J., Egenhoff, S. O., Eberl, D. D., & Blum, A. E. (2012). The nature of porosity in organic-rich mudstones of the Upper Jurassic Kimmeridge Clay Formation, North Sea, offshore United Kingdom. International Journal of Coal Geology, 103, 32-50. doi: 10.1016/j.coal.2012.07.012

Folk, R. L. (1980). Petrology of sedimentary rocks: Hemphill Pub. Co.(Austin, Tex.).

Hall, P., Mildner, D., & Borst, R. (1983). Pore size distribution of shaley rock by small angle neutron scattering. Applied Physics Letters, 43(3), 252-254.

Harbor, R. L. (2011). Facies characterization and stratigraphic architecture of organic-rich mudrocks, Upper Cretaceous Eagle Ford Formation, South Texas.

Houben, M., Desbois, G., & Urai, J. (2013a). A comparative study of representative 2D microstructures in Shaly and Sandy facies of Opalinus Clay (Mont Terri, Switzerland) inferred form BIB-SEM and MIP methods. Marine and Petroleum Geology.

Houben, M., Desbois, G., & Urai, J. (2013b). Pore morphology and distribution in the Shaly facies of Opalinus Clay (Mont Terri, Switzerland): Insights from representative 2D BIB–SEM investigations on mm to nm scale. Applied Clay Science, 71, 82-97.

Honjo, S. (1976). "Coccoliths: production, transportation and sedimentation." Marine Micropaleontology 1: 65-79.

Huang, J., Cavanaugh, T., & Nur, B. (2013). An Introduction to SEM Operational Principles and Geologic Applications for Shale Hydrocarbon Reservoirs. Electron Microscopy of Shale Hydrocarbon Reservoirs: AAPG Memoir 102, 102, 1.

Ji, L., Zhang, T., Milliken, K. L., Qu, J., & Zhang, X. (2012). Experimental investigation of main controls to methane adsorption in clay-rich rocks. Applied Geochemistry, 27(12), 2533-2545. doi: 10.1016/j.apgeochem.2012.08.027

Kaneko, K. (1994). Determination of pore size and pore size distribution: 1. Adsorbents and catalysts. Journal of Membrane Science, 96(1), 59-89.

Kate, J., & Gokhale, C. (2006). A simple method to estimate complete pore size distribution of rocks. Engineering geology, 84(1), 48-69.

Klaver, J., Desbois, G., Urai, J. L., & Littke, R. (2012). BIB-SEM study of the pore space morphology in early mature Posidonia Shale from the Hils area, Germany. International Journal of Coal Geology, 103, 12-25. doi: 10.1016/j.coal.2012.06.012

Knackstedt, M. A., Latham, S., Madadi, M., Sheppard, A., Varslot, T., & Arns, C. (2009). Digital rock physics: 3D imaging of core material and correlations to acoustic and flow properties. The Leading Edge, 28(1), 28-33.

Kuila, U., & Prasad, M. (2013). Specific surface area and pore- size distribution in clays and shales. Geophysical Prospecting.

Kuila, U., Prasad, M., Derkowski, A., & McCarty, D. (2012). Compositional Controls on Mudrock Pore-Size Distribution: An Example from Niobrara Formation. Paper presented at the SPE Annual Technical Conference and Exhibition.

Land, L. S., Mack, L. E., Milliken, K. L., & Leo Lynch, F. (1997). Burial diagenesis of argillaceous sediment, south Texas Gulf of Mexico sedimentary basin: A reexamination. Geological Society of America Bulletin, 109(1), 2-15.

Lillico, D., Babchin, A., Jossy, W., Sawatzky, R., & Yuan, J.-Y. (2001). Gas bubble nucleation kinetics in a live heavy oil. Colloids and Surfaces A: Physicochemical and Engineering Aspects, 192(1), 25-38.

Loucks, R. G., Reed, R. M., Ruppel, S. C., & Hammes, U. (2012). Spectrum of pore types and networks in mudrocks and a descriptive classification for matrix-related mudrock pores. AAPG Bulletin, 96(6), 1071-1098. doi: 10.1306/08171111061

Loucks, R. G., Reed, R. M., Ruppel, S. C., & Jarvie, D. M. (2009). Morphology, Genesis, and Distribution of Nanometer-Scale Pores in Siliceous Mudstones of the Mississippian Barnett Shale. Journal of Sedimentary Research, 79(12), 848-861. doi: 10.2110/jsr.2009.092

Lovley, D. R. (1991). Dissimilatory Fe (III) and Mn (IV) Reduction. Microbiological Reviews, 55(2), 259.

Macquaker, J. H. S., Keller, M. A., & Davies, S. J. (2010). Algal Blooms and "Marine Snow": Mechanisms That Enhance Preservation of Organic Carbon in Ancient Fine-Grained Sediments. Journal of Sedimentary Research, 80(11), 934-942. doi: 10.2110/jsr.2010.085

Mapstone, N. (1975). Diagenetic history of a North Sea chalk. Sedimentology, 22(4), 601-614.

Mazzullo, S. (2000). Organogenic Dolomitization in Peritidal to Deep-Sea Sediments: Perspectives. Journal of Sedimentary Research, 70(1).

Milliken, K., & Day-Stirrat, R. (2013). Cementation in mudrocks: Brief review with examples from Cratonic Basin Mudrocks. Chatellier, J.¬ Y., and Jarvie, DM, eds., Critical Assessment of Shale Resource Plays, 5.

Milliken, K.L., Ko, Lucy, T., Pommer, Maxwell, E., Marsaglia, Kathleen, M. (2014). Mediterranean Sapropels: Analogures for Petrographic Assesment of Organic Matter in Oil and Gas Shales. AAPG Annual Convention and Exhibition Houston, Tx.

Milliken, K., & Land, L. (1993). The origin and fate of silt sized carbonate in subsurface Miocene—Oligocene mudstones, south Texas Gulf Coast. Sedimentology, 40(1), 107-124.

Milliken, K., McBride, E., & Land, L. (1989). Numerical assessment of dissolution versus replacement in the subsurface destruction of detrital feldspars, Oligocene Frio Formation, South Texas. Journal of Sedimentary Research, 59(5), 740-757.

Milliken, K. L. (1992). Chemical behavior of detrital feldspars in mudrocks versus sandstones, Frio Formation (Oligocene), South Texas. Journal of Sedimentary Research, 62(5), 790-801.

Milliken, K. L., Day-Stirrat, R. J., Papazis, P. K., & Dohse, C. (2012). Carbonate Lithologies of the Mississippian Barnett Shale, Fort Worth Basin, Texas.

Milliken, K. L., Esch, W. L., Reed, R. M., & Zhang, T. (2012). Grain assemblages and strong diagenetic overprinting in siliceous mudrocks, Barnett Shale (Mississippian), Fort Worth Basin, Texas. AAPG Bulletin, 96(8), 1553-1578. doi: 10.1306/12011111129

Milliken, K. L., Rudnicki, M., Awwiller, D. N., & Zhang, T. (2013). Organic matter-hosted pore system, Marcellus Formation (Devonian), Pennsylvania. AAPG Bulletin, 97(2), 177-200. doi: 10.1306/07231212048

Mondol, N. H., Bjørlykke, K., Jahren, J., & Høeg, K. (2007). Experimental mechanical compaction of clay mineral aggregates—Changes in physical properties of mudstones during burial. Marine and Petroleum Geology, 24(5), 289-311.

Nelson, P. H. (2009). Pore-throat sizes in sandstones, tight sandstones, and shales. AAPG Bulletin, 93(3), 329-340.

Passier, H. F., Middelburg, J. J., de Lange, G. J., & Böttcher, M. E. (1997). Pyrite contents, microtextures, and sulfur isotopes in relation to formation of the youngest eastern Mediterranean sapropel. Geology, 25(6), 519-522.

Pevear, D., Klimentidis, R., & Robinson, G. (1991). Petrogenetic significance of kaolinite nucleation and growth on pre-existing mica in sandstones and shales. LPI Contributions, 773, 125.

Pittman, E. D. (1992). Artifact porosity in thin sections of sandstones. Journal of Sedimentary Research, 62(4), 734-737.

Pollastro, R. M. (1981). Authigenic kaolinite and associated pyrite in chalk of the Cretaceous Niobrara Formation, eastern Colorado. Journal of Sedimentary Research, 51(2).

Reed, R., & Loucks, R. (2007). Imaging nanoscale pores in the Mississippian Barnett Shale of the northern Fort Worth Basin. Paper presented at the AAPG Annual Convention Abstracts.

Reed, R. M., Loucks, R. G., & Ruppel, S. C. (2013). Comment on "Formation of nanoporous pyrobitumen residues during maturation of the Barnett Shale (Fort Worth Basin)" by Bernard et al. (2012). International Journal of Coal Geology.

Roduit, N., 2008, JMICROVISION Version 1.2.7: Image analysis toolbox for measuring and quantifying components of high-definition images: http://www.jmicrovision.com (accessed November 1, 2012).

Schneider, J., Flemings, P. B., Day-Stirrat, R. J., & Germaine, J. T. (2011). Insights into pore-scale controls on mudstone permeability through resedimentation experiments. Geology, 39(11), 1011-1014.

Scholle, P. A. (1977). Chalk diagenesis and its relation to petroleum exploration: oil from chalks, a modern miracle. Am. Assoc. Pet. Geol. Bull.;(United States), 61(7).

Schoonen, M. A. (2004). Mechanisms of sedimentary pyrite formation. Special Papers-Geological Society of America, 117-134.

Seewald, J. S. (2003). Organic–inorganic interactions in petroleum-producing sedimentary basins. Nature, 426(6964), 327-333.

Sondergeld, C., Ambrose, R., Rai, C., & Moncrieff, J. (2010). Micro-Structural Studies of Gas Shales. Paper presented at the SPE Unconventional Gas Conference.

Suits, N. S., & Wilkin, R. T. (1998). Pyrite formation in the water column and sediments of a meromictic lake. Geology, 26(12), 1099-1102.

Sun, Xun et al., (2014). Geochemical Characterization of Organic Matter from the Eagle Ford Formation and Indications of Thermal Maturity and Depositional Redox Conditions. AAPG Annual Conference and Exhibition, Houston Tx., Abstracts, April 6-9.

Taylor, K., & Macquaker, J. (2000). Early diagenetic pyrite morphology in a mudstone-dominated succession: the Lower Jurassic Cleveland Ironstone Formation, eastern England. Sedimentary Geology, 131(1), 77-86.

Turner, J. T. (2002). Zooplankton fecal pellets, marine snow and sinking phytoplankton blooms. Aquatic Microbial Ecology, 27(1), 57-102.

Turner, J. T., & Ferrante, J. G. (1979). Zooplankton fecal pellets in aquatic ecosystems. BioScience, 670-677.

Van der Plas, L., & Tobi, A. (1965). A chart for judging the reliability of point counting results. American Journal of Science, 263(1), 87-90.

Wignall, P., & Newton, R. (1998). Pyrite framboid diameter as a measure of oxygen deficiency in ancient mudrocks. American Journal of Science, 298(7), 537-552.

Wilkin, R., Barnes, H., & Brantley, S. (1996). The size distribution of framboidal pyrite in modern sediments: An indicator of redox conditions. Geochimica et Cosmochimica Acta, 60(20), 3897-3912.

Workman, S. J., & Grammer, G. M. (2013). Integrating Depositional Facies and Sequence Stratigraphy in Characterizing Unconventional Reservoirs in the Cretaceous (Cenomanian-Turonian) Eagle Ford Shale, South Texas.

Yortsos, Y. C., & Stubos, A. K. (2001). Phase change in porous media. Current opinion in colloid & interface science, 6(3), 208-216.

Young, J. R., Bergen, J. A., Bown, P. R., Burnett, J. A., Fiorentino, A., Jordan, R. W., . . . Von Salts, K. (1997). Guidelines for coccolith and calcareous nannofossil terminology. Palaeontology, 40(4), 875-912.

Zhang et al., et al. (2014). Pore Characterization of Eagle Ford Shales by N2 Adsorption and Desorption Isotherms and Pore Evolution in Organic Matter During Thermal Maturation. AAPG Annual Conference and Exhibition, Houston Tx., Abstracts, April 6-9.